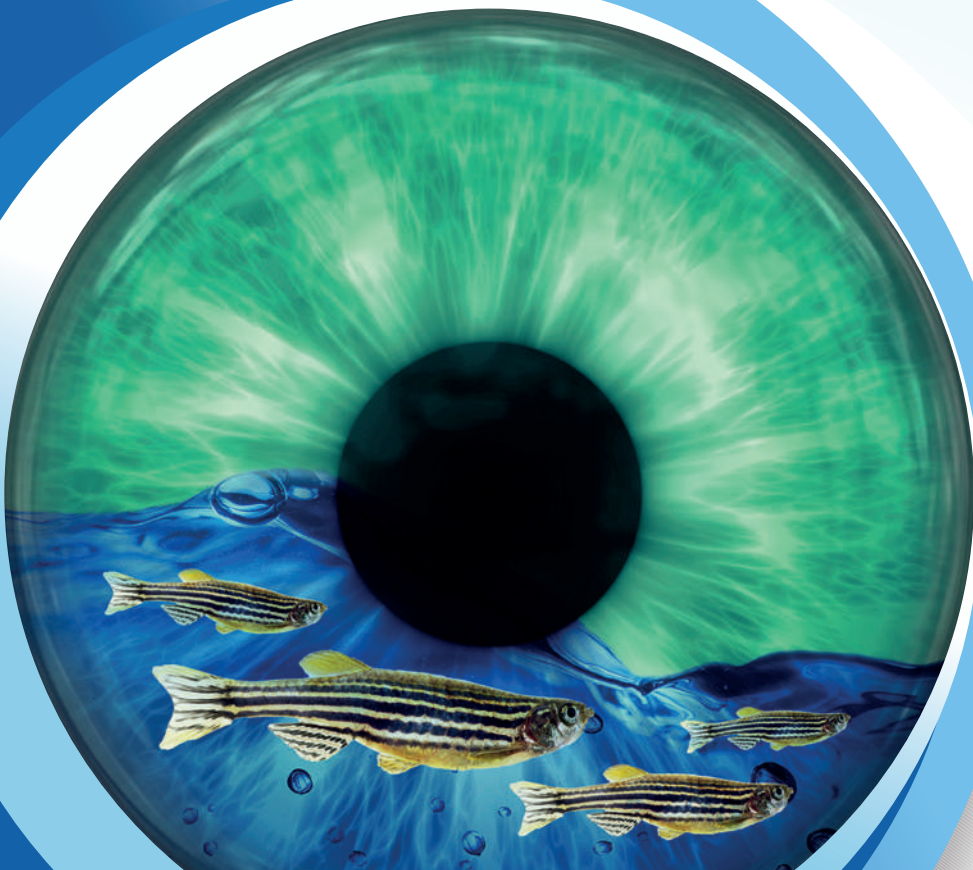# Towards gene therapy for *USH2A*-associated retinitis pigmentosa

Fishing for answers

Margo Dona

Towards gene therapy for
USH2A-associated retinitis pigmentosa
~Fishing for answers~

Margo Anne Dona

Towards gene therapy for *USH2A*-associated retinitis pigmentosa

~Fishing for answers~

Proefschrift

ter verkrijging van de graad van doctor
aan de Radboud Universiteit Nijmegen
op gezag van de rector magnificus prof. dr. J.H.J.M. van Krieken,
volgens besluit van het college van decanen
in het openbaar te verdedigen
op donderdag 29 november 2018
om 12.30 uur precies

door

Margo Anne Dona
geboren op 28 december 1987
te 's-Hertogenbosch

Promotoren:
Prof. dr. J.M.J. Kremer
Prof. dr. J.E.E. Keunen

Copromotor:
Dr. H.A.R. van Wyk

Manuscriptcommissie:
Prof. dr. P.M.T. Deen (voorzitter)
Prof. dr. J.H.L.M. van Bokhoven
Ass. Prof. dr. A. El-Amraoui (Institut Pasteur, Frankrijk)

TABLE OF CONTENTS

LIST OF ABBREVIATIONS

a.u.	arbitrary units
a.a.	amino acid
AAV	adeno associated virus
Adgrv1	Adhesion G protein-coupled receptor V1
AONs	Antisense oligonucleotides
AOS	Accessory outer segments
arRP	Autosomal recessively inherited nonsyndromic RP
atgMO	Translation-blocking Morpholino
Bodipy	Boron-dipyrromethene
bp	Base pairs
CamK	Calmodulin-dependent protein kinase
CBA	Chicken beta actin
CC	Connecting cilium
cc2d2a	Coiled-coil and C2-domains containing protein 2a
COS	Cone outer segment
CP	Calyceal processes
D.r.	Danio rerio
dB	Decibel
DD	Development delay
DEC	Dier experimenten commissie
DMD	Duchenne Muscular Dystrophy
DNA	Deoxyribonucleic acid
dpf	Days post fertilization
dync1h1	Dynein cytoplasmic dynein motor complex 1
DZANK1	Double Zinc Ribbon and Ankyrin Repeat domains 1
EPASIS	Elution profile analysis of SDS-induced sub-complexes
er	endoplasmic reticulum
ERG	Electroretinogram
ESRF	End-stage renal failure
FN3	Fibronectin type 3
G	Golgi system
GCL	Ganglion cell layer
GST	Glutathione S-transferase
H.s.	Homo Sapiens

HEK293T	Human embryonic kidney 293T
hTERT-RPE1	Human telomerase reverse transctriptase-transformed retinal pigment epithelium
IB	Immunoblot
IF	Intermediate filament
INL	Inner nuclear layer
IP	Immunoprecipitation
IPL	Inner plexiform layer
iPSC	Induced pluripotent stem cell
IRES	Internal ribosomal entry site
IS	Inner segment
iso	Isoform
JBTS	Joubert syndrome
kDa	Kilo Dalton
L	Lysosomes
lamG	Laminin G
LCA	Leber Congential Amaurosis
LCA5	Leber's Congenital amaurosis type 5
LV	Lentiviral
m	Mitochondria
MICAL3	Microtubule-associated Monooxygenase, Calponin and LIM domain containtint 3
MIP	molecular inversion probes
MO	Morpholino
mpf	Months post fertilization
Mq	MilliQ
MS	Mass spectrometry
MTS	Molar Tooth sign
n	Nucleus
nbl	non blastema mutant
ncp	night cap mutant
NINL	ninein-like protein
OKR	Optokinetic response
ONL	Outer nuclear layer
OPL	Outer plexiform layer
OS	Outer segments

PBM	PDZ-binding motif
PEI	Polyethylenimine
PFA	Paraformaldehyde
pg	patiënten groep
RD	Retinal degeneration
ROS	Rod outer segment
RP	Retinitis pigmentosa
RPE	Retinal pigment epithelium
RT-PCR	Reverse transcriptase polymerase chain reaction
SEM	Standard error of the mean
SILAC	Stable isotope labeling of amino acids in cell culture
som	Somites
spMO	Splice-blocking Morpholino
TAP	Tandem Affinity Purification
TEM	Transmission electron microscopy
TGN	Trans-Golgi network
TLF	Tupfel Long fin
TM	Transmembrane domain
TRIDs	Translational read-through inducing drugs
Ush2a	Usher syndrome type 2a
UV	Ultraviolette
v	vescicular structures
VMR	Visual motor response
WES	Whole exome sequencing
wt	wild-type
ZFIN	Zebrafish information network
ZIRC	Zebrafish international resource center
ZOP	Zebrafish opsin promotor

Chapter 1

General introduction

1

1. GENERAL INTRODUCTION

1.1 History and prevalence of Usher Syndrome

Usher syndrome is a devastating genetic condition characterized by hearing impairment and a progressive loss of visual function as a consequence of retinitis pigmentosa (RP). The combination of hearing loss and visual impairment was first reported by the German ophthalmologist Albrecht von Graefe in 1858, when he described three affected brothers who had been studied by his own cousin, Alfred Graefe [1]. As these cases were relatives, a hereditary defect was suspected. The German ophthalmologist Richard Liebreich recognized the condition in the hearing impaired population of Berlin [2], and in 1880 Arthur Hartmann, a German otologist, introduced a recessive pattern of inheritance for the combination of deafness and RP [3]. The first descriptions of combined deaf-blindness in the Dutch population were by De Wilde in 1919. Finally, 77 years after the first description, the syndrome was named after the Scottisch ophthalmologist Charles Howard Usher in 1935 [4]. Although Usher syndrome is the most common cause of hereditary deaf-blindness in man, it is still classified as a rare disease. The prevalence of Usher syndrome is estimated to range from 4.4 to 6.2 per 100,000 inhabitants, with a variable distribution in different populations and between the different clinical types of Usher syndrome [5,6].

1.2 Clinical classification of Usher syndrome

Currently, three clinical types of Usher syndrome are distinguished based on the severity and progression of the hearing impairment, the presence of vestibular dysfunction and the age at which RP is diagnosed (**Table 1**) [7,8]. The initial sign of visual dysfunction in Usher syndrome patients is often night blindness, which is followed by a progressive loss of peripheral vision that generally results in legal blindness in the sixth or seventh decade of life [9]. In addition, atypical forms of Usher syndrome, such as congenital severe-to-profound hearing loss combined with late onset or subclinical RP, have been reported [10-12]. It has been postulated that environmental factors or modifier genes might influence the observed clinical outcome in patients with atypical Usher syndrome. Usher syndrome type 1 is the most severe form of Usher syndrome characterized by congenital severe to profound hearing loss, vestibular dysfunction and a pre-pubertal onset of the retinal degeneration. Usher syndrome type 2 is the most common type of Usher syndrome (>50% of the patients). As shown in **Table 1**, patients with Usher syndrome type 2 have an intact vestibular function, congenital hearing impairment and a progressive loss of visual function, as a consequence of RP [13]. The RP is generally diagnosed during or after puberty. Usher syndrome type 3 is the most variable form of Usher syndrome with stable, progressive or profound hearing loss, variable vestibular

function, and progressive vision loss. Other symptoms noticed in Usher syndrome patients are reduced fertility, mental deficiencies, cerebral atrophy, ataxia, bronchiectasis and immotile nasal cilia [14-21]. Further research is needed to determine whether or not these symptoms are also part of the clinical spectrum of Usher syndrome.

USH type	Hearing impairment	Visual impairment	Vestibular function
Usher syndrome type 1	Congenital; severe to profound	Onset of RP before puberty; progressive	Absent
Usher syndrome type 2	Congenital; moderate to severe	Onset of RP around puberty; progressive	Intact
Usher syndrome type 3	Variable age of onset; progressive	Variable age of onset of RP; progressive	Variable

Table 1. Clinical classification of Usher syndrome

2. HEARING AND HEARING REHABILITATION IN USHER SYNDROME PATIENTS

2.1 The ear: organ for hearing and balance

Sound is an important aspect of communication. The (inner) ear is the organ for hearing and balance. Sound waves are captured by the ear and converted into electrical signals that lead to the perception of sound by the brain. Besides that, the inner ear also contains the vestibular system or balance organ [22].

2.2 Anatomy of the human ear

The ear consists of three main parts: the outer, middle and inner ear (**Figure 1**). Sound waves are captured by the pinna and travel to the tympanic membrane via the external auditory canal. The three auditory ossicles in the middle ear; the malleus, incus and stapes, transmit these vibrations to the inner ear. The inner ear consists of the cochlea and the vestibular system. The increase in pressure in the cochlear fluid caused by inward movement of the stapes also displaces fluid in the inner ear. As a consequence, the basilar membrane moves in vertical direction resulting in an increased pressure within the scala tympani. The enhanced pressure results in displacement of cochlear fluid in the scala media and finally in displacement of the sensory epithelium in the organ of Corti. The sensory epithelium contains approximately 16,000 hair cells that convert mechanical stimuli into electrical signals. Inner hair cells convert the amplified mechanical signal into electrical responses, whereas the outer hair cells receive and amplify sound-evoked vibrations of the sensory epithelium. At the apical part of the hair cells, 10 to 50 actin based protrusions are present, the stereocilia, which are anchored

in the cuticular plate. Stereocilia are organized in a staircase-like pattern and connected to each other by fibrous links. Every hair bundle contains one true, microtubule-based, cilium that is known as the kinocilium. In mammals, the kinocilium is required for proper hair bundle formation and orientation and disappears at the end of hair cell development in the cochlea. Finally, action potentials are transmitted via the auditory nerve to the primary auditory cortex. In general, healthy young individuals are capable of hearing frequencies between 20 and 20,000 Hertz (Hz). Sound of different frequencies can be distinguished because of difference in shape of the basilar membrane, the organ of Corti and the tectorial membrane from base to apex. High frequency sounds are optimally detected in the more basal part of the cochlea, and sounds with low frequencies in the more apical part of the cochlea.

2.3   Vestibular system

The vestibulum or balance organ, is part of the inner ear and consists of semicircular canals and the otolith organs (the utricle and saccule) (**Figure 1**). The semicircular canals register rotational movements and the otoliths register linear accelerations. The ear stones (otoconia) ballast the otolith membrane, making it heavier than the surrounding endolymph. When the head rotates, the force on the hair cell-containing sensory epithelium changes which leads to a deflection of stereocilia. As a result, mechanotransduction channels are opened, resulting in the depolarization of the cell and neurotransmitter release onto the vestibular nerve.

2.4   Hearing impairment in Usher syndrome patients and rehabilitation

Hearing impairment is defined as the loss in the ability of hearing sounds of more than 26 decibels (dB) for an average of four frequencies (0.5, 1, 2 and 4kHz) (www. who.int). Patients with Usher syndrome type 1 have a severe to profound hearing loss from birth with occasionally only residual hearing at the lower frequencies [23,24]. For these patients, cochlear implantation is so far the only effective treatment. A cochlear implant is an electronic device that replaces the function of the damaged inner ear sensory epithelium. Bilateral cochlear implantation can also improve identification of the direction of sound. Detection of sound can be achieved with implantation late in life, but speech recognition appears only possible in patients that had a previous stimulation of the auditory system, since it depends on the development of hearing skills and the maturation of the auditory pathways [25]. Although, the level of hearing rehabilitation after implantation varies significantly among patients.

Typical for Usher syndrome type 2 is congenital moderate-to-severe bilateral hearing impairment, with the high frequencies being most severely affected [24,26-29]. Patients with Usher syndrome type 3 present with an onset of progressive hearing loss mainly in the

first and second decade of life. Rapid progression in the first two decades (≥ 25 dB per decade) is followed by a period of relative stability [30]. For both Usher syndrome type 2 and type 3 patients, bilateral hearing aids are provided from birth or at first detection of hearing loss. Hearing aids can amplify the signal, however they are incapable of truly correcting hearing loss. Modern devices use sophisticated digital signal processing to try and improve speech recognition. However, further research, especially on sound localization and speech intelligibility in noise, is necessary to improve hearing aids and hearing aid fitting [31]. In some patients with Usher syndrome type 2 and 3 the severe progression of hearing impairment leads to insufficient speech intelligibility with hearing aids. These patients are often provided with a cochlear implant [31-33].
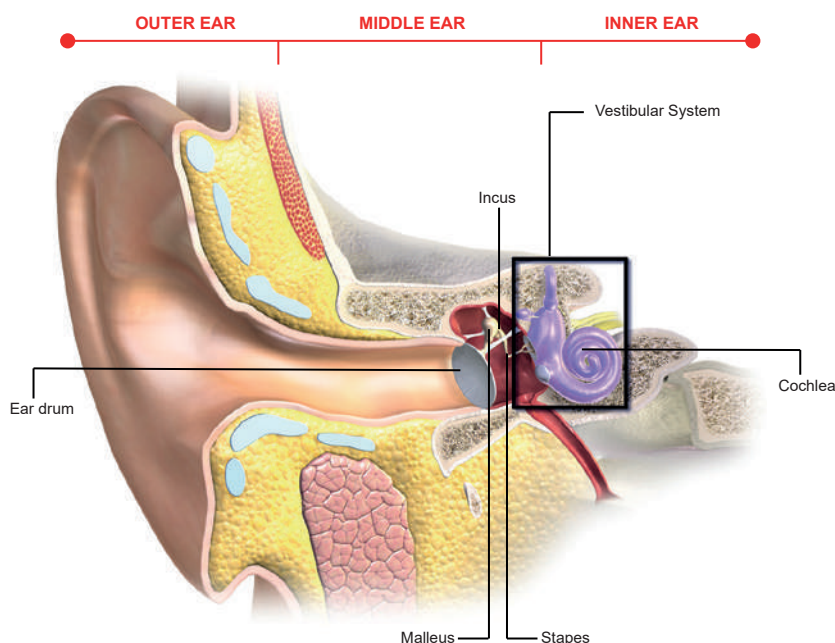

Figure 1. Schematic representation of the outer, middle and inner ear. The inner ear is pointed out with the square. The vestibular system, the balance organ, is part of the inner ear.
© Adobe Stock.

3.   VISION AND VISUAL IMPAIRMENT IN USHER SYNDROME PATIENTS

3.1   Human visual perception

Visual perception is the ability to interpret the world around us using light in the visible spectrum reflected by the objects in the environment. The most primitive eyes originate

1

from 550 million years ago and are described as patches of photoreceptor proteins in unicellular organisms [34]. Throughout evolution, the human eye developed into a highly specialized and sophisticated system that is responsible for our vision.

3.2   Anatomy of the human eye

The human eye is composed of three main layers: the outer layer, the middle layer and the inner layer (**Figure 2**). The outer layer is made up of the sclera and the cornea. The sclera is the outermost layer of the eye that maintains the shape of the eye and serves as protector of the inner parts of the eye from bacterial invasions. The cornea functions as a window that controls the entry of light into the eye. The middle layer is formed by the choroid, ciliary body and iris. The choroid has a dark pigment, melanin that facilitates the absorption of light whereas the ciliary body is responsible for controlling the shape of the lens and the production of aqueous humor. The choroid is mainly composed of blood vessels and therefore this layer is also referred to as uvea or vascular tunic. The inner layer, the retina, contains the sensory epithelium. Based on its cellular components, the retina can be divided in three nuclear layers separated by two synaptic layers (**Figure 3**). The ganglion cell layer (GCL) contains the cell bodies of the retinal ganglion cells. At the inner plexiform layer (IPL) the synaptic connections between ganglion cells and secondary neurons (horizontal, amacrine and bipolar cells) are made. The inner nuclear layer (INL) contains the nuclei and part of the cell bodies of these three secondary neurons and the cell bodies of the Müller glia cells. In the outer plexiform layer (OPL) the synaptic connections between the photoreceptor cells and the secondary neurons are situated. The outer nuclear layer (ONL) contains the nuclei and part of the cell bodies of the light-sensitive photoreceptor cells. In the human retina, two types of photoreceptor cells can be distinguished: the rods and the cones (**Figure 3**). A human eye approximately contains 6.4 million cones and 110-125 million rods. The density of cones is the highest in the fovea situated near the center of the macula. Cones are conically-shaped cells that are responsible for color vision and enable us to see during daytime. Humans have a trichromatic visual system consisting of three different type of cones varying in spectral sensitivity: the L-cones (red), M-cones (green) and S-cones (blue). In contrast, rods are cylindrically-shaped cells that enable us to see during night. Rods contain more visual pigment than cones, and multiple rods are connected to a single bipolar cell. Therefore, rods are able to amplify light signals much stronger than cones in dim light situations. Both types of photoreceptors have the same basic structure (**Figure 3**). In both rods and cones, the conversion of light into electrical signals (phototransduction), takes place in the outer segments (**Figure 3**) [35]. The outer segment is regarded to be a highly specialized non-motile primary cilium with the connecting cilium as the ciliary transition zone. Proteins involved in outer segment

formation and function, such as proteins involved in the phototransduction cascade, are synthesized in the inner segment and actively transported to the outer segment via the connecting cilium. The outer segments of the photoreceptor cells are embedded in the multifunctional Retinal Pigment Epithelium (RPE). The RPE offers protection, reduces the reflection of light, and is involved in phagocytation of photoreceptor outer segment membranes [36].

3.3   Retinal degeneration in Usher syndrome patients

Progressive blindness caused by RP is considered to be a rare disorder (www.nei.nih.gov). The term "retinitis" suggests an inflammatory process, however this is misleading as RP is not an inflammation, but an inherited, slow-paced degeneration of the retina. The term "pigmentosa" refers to the characteristic pigmentary deposits in the retina.

In the early stages of RP, rods are more severely affected than cones. Function of rods gradually deteriorates and vision in dim light becomes more difficult. During later stages of RP, the visual field starts to narrow down. Only a small area of central vision remains, along with slight peripheral vision. The visual field decrease results in tunnel vision and finally leads to total blindness. The pathophysiology underlying Usher syndrome-associated photoreceptor degeneration is still largely unknown. Unfortunately, no treatment options are currently available for the progressive retinal degeneration in Usher syndrome patients.
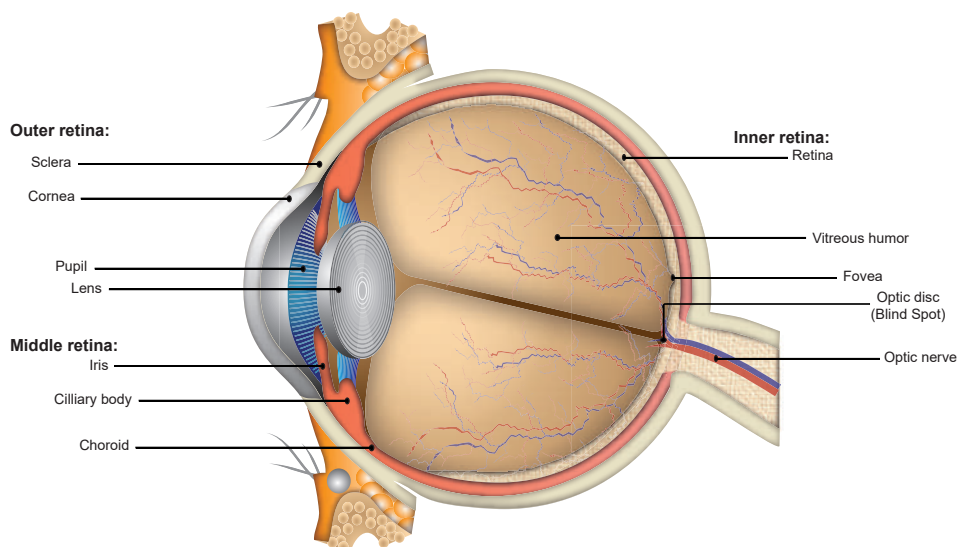
Outer retina:
Sclera
Cornea

Pupil
Lens

Middle retina:
Iris
Cilliary body

Choroid

Inner retina:
Retina

Vitreous humor

Fovea
Optic disc
(Blind Spot)

Optic nerve

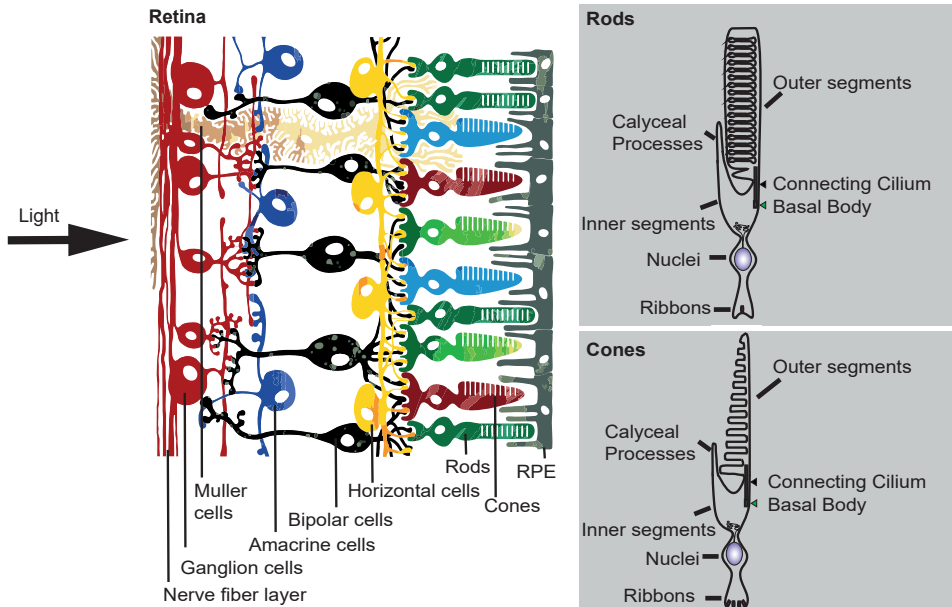**Figure 2**. Anatomy of the human eye.
© Adobe Stock.

Figure 3. Schematic representation of the retina and light-sensitive photoreceptor cells.

The light enters the eye via the lens and reaches the photoreceptor cells after passing the different layers of the retina.

4. GENES AND PROTEINS INVOLVED IN USHER SYNDROME

Usher syndrome is inherited as an autosomal recessive trait and is not only clinically but also genetically heterogeneous (**Table 2**). So far, nine genetic loci and six different genes (*MYO7A*, *USH1C*, *CDH23*, *PCDH15*, *USH1G* and *CIB2*) have been identified to be involved in Usher syndrome type 1. Mutations in *USH2A*, *ADGRV1* and *WHRN* result in Usher syndrome type 2, and defects in *USH3A* lead to Usher syndrome type 3. In addition, mutations in *PDZD7* can act as a modifier of RP in Usher syndrome type 2a patients and together with *ADGRV1* mutations contribute to digenic Usher syndrome [37]. Mutations in *HARS* are associated with Usher syndrome type 3b [38], and a combination of mutations in *CEP250* and *C2ORF71* are associated with atypical Usher syndrome [39].

4.1 Mutations in *USH2A* are the most frequent cause of Usher syndrome

Usher syndrome type 2 is the most common type of Usher syndrome and has been reported to represent around two-thirds of Usher syndrome cases [40], of whom 57-85% can be explained by mutations in *USH2A* (ENSG00000042781) [41,42]. Also, mutations in *USH2A* are the most frequent cause of autosomal recessively inherited nonsyndromic RP (arRP), accounting for 7-23% of arRP cases [42].

USH2A encodes usherin and to date, two different isoforms have been identified (**Figure 4**). The originally identified human *USH2A* transcript is composed of 21 exons and encodes a presumably secreted protein of 1,551 amino acids (usherin[isoA]) [43]. In 2004, van Wijk *et al.* identified 51 additional exons of *USH2A* that altogether encode a transmembrane protein of 5,202 amino acids (usherin[isoB]) [44]. In addition to the domains present in usherin[isoA] (an N-terminal signal peptide, a Lam-G like domain, a LamNT domain, 10 EGF-lam domains and 4 FN3 domains), usherin[isoB] contains two laminin G domains (LamG), 28 FN3 domains, a transmembrane domain and a short intracellular region with a C-terminal class I PDZ-binding motif (**Figure 4**). In 2005, a novel inner ear-specific exon was identified, adding 24 additional amino acids to the intracellular region of the protein [45]. In mouse retina, usherin[isoB] is reported to be the most prevalent isoform which is mainly located at the photoreceptor periciliary membrane and the synaptic region of photoreceptor cells [46-49]. At the periciliary region, usherin is thought to be part of a protein complex that is involved in transport and docking of vesicles from the inner to the outer segment of photoreceptor cells [50].
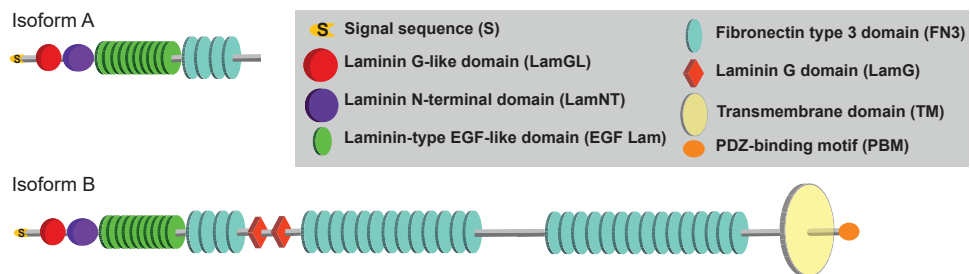
Usherin

Figure 4. Schematic representation of usherin protein isoform A and isoform B visualizing the different domains.

4.2 Usher proteins function in highly dynamic protein networks

Usher proteins are members of protein families with very diverse functions [22]. Despite the predicted variety in protein function, the clinical similarities in patients suggest that the associated proteins play a role in the same processes or pathways. Indeed, Usher proteins have been shown to interact and to function in highly dynamic multiprotein networks (**Figure 5**) [22]. These protein networks function in different compositions at different subcellular locations during different stages of inner ear and retinal development and thereafter [47,51].

1

Table 2. Types of Usher syndrome and associated genes and proteins, with the corresponding animal models.

USH Type	Locus	Location	Gene/Protein	Fruit fly	Animal Model Mouse	Zebrafish	Therapeutic progress
USH1	USH1b	11q13.5	MYO7A / myosin VIIa	Crinkled	Shaker-1 (sh-1)	Mainer	- Transsplicing therapy in mice - Gene augmentation in mice - Clinical trial, phase I/II (UshStat®)
	USH1c	11p15.1	USH1C/ harmonin	CG5921 uncharacterized	Deaf circler (dfcr); deaf circler 2 Jackson (dfcr-2J)	ush1c^fh293	- Gene augmentation in mice - Splice correction in mice - Translational read-through inducing drugs (TRIDs) in vivo - Gene correction in vitro
	USH1d	10q22.1	CDH23/ cadherin-23	Cad88c uncharacterized	Waltzer (v)	Sputnik; eye n/a	
	USH1e	21q21	unknown				
	USH1f	10q21.1	PCDH15/ protocadherin-15	Cad99C	Ames waltzer (av)	Orbiter	
	USH1g	17q25.1	USH1G/ SANS	Sans	Jackson shacker (js)		- TRIDs in vitro
	USH1h	15q22-q23	unknown				
	USH1j	15q25.1	CIB2/ CIB2				
	USH1k	10p11.21-q21.1	unknown				
USH2	USH2a	1q41	USH2A/ usherin		Ush2a-/- late onset, mild	ush2a^tj1245 ush2a^rmc1 ear n.d.	- Splice correction in vitro and in zebrafish - Gene augmentation in zebrafish
	USH2c	5q14.3	ADGRV1/ ADGRV1		gpr98-/-; vlgr1/del7TM; Frings/Mass1^BUB/BsJ	MO: ear n.d.	
	USH2d	9q32	WHRN/ whirlin		Whirler (wi)'; whirlin long isoform^-1,2		- Gene augmentation in mice
USH3	USH3a	3q25.1	CLRN1/ clarin-1		Clrn1-/-; Clrn1^N48K/N48K	hCLRN1^N48K eye n/a	- Small molecules
	USH3b	20q	HARS/ HARS				
USH modifier	-	10q24.31	PD2D7/ PD2D7			MO:	

N/a is not available, n.d. not determined. [eye symbol] is visual impairment detected, [crossed-ear symbol] is hearing loss detected. In case of the whirlin mouse models the observed phenotypes are different per model. The following numbers indicate the specific phenotype per model. 1, hearing impaired; 2, visual impaired.

In photoreceptor cells, Usher proteins predominantly localize in the region of the connecting cilium, more specifically at the basal body, the accessory centriole, the calyceal processes and the periciliary membrane (**Figure 6**)[22,50,52]. It has been postulated that in this region Usher proteins are important for providing structural support. Besides that, evidence is accumulating for a major role of these proteins in the transport and docking of vesicles that contain essential proteins for outer segment formation, maintenance and function[47,53,54]. Another important subcellular location where Usher proteins have been identified, is in the synaptic regions of both photoreceptors and inner ear hair cells (**Figure 6**)[50]. Multiple studies have elucidated an important role for the Usher protein network in inner ear hair cell and photoreceptor synapse formation and function[49,52,55,56]. Finally, Usher mouse mutants exhibit severe defects in the inner ear hair bundle morphology (**Table 2**) and Usher proteins have been detected in the hair bundle, indicating an essential role in hair bundle development and maintenance[50]. However, despite all suggested and indicated functions, more research is needed to unravel the full function of the Usher proteins and the associated network(s) in both inner ear and retina.
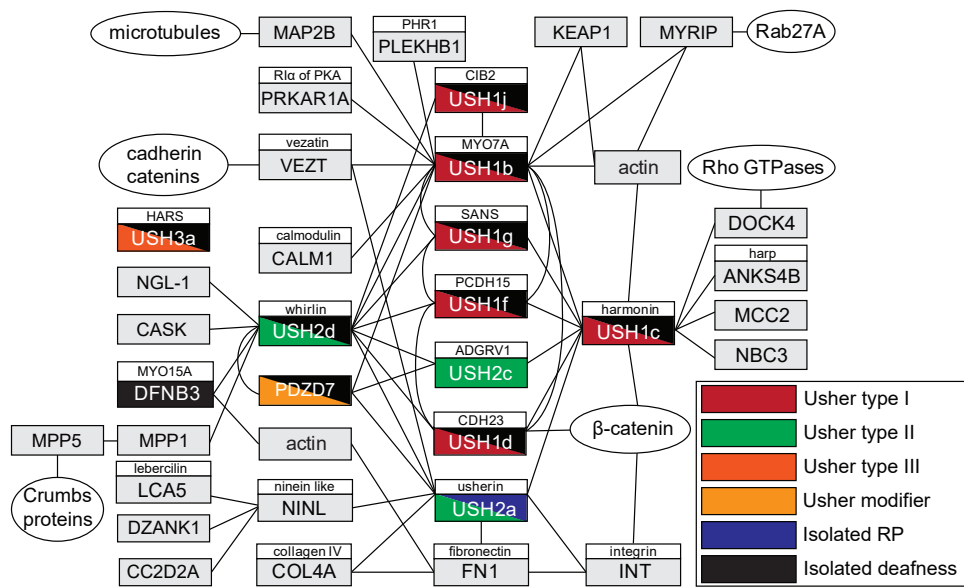
Figure 5. The Usher protein network.
Identified protein-protein interactions are indicated. The red and green boxes represent Usher syndrome-associated proteins. Black boxes indicate association with isolated deafness and orange boxes represent modifiers for Usher syndrome (Adapted with permission from thesis E. van Wijk).
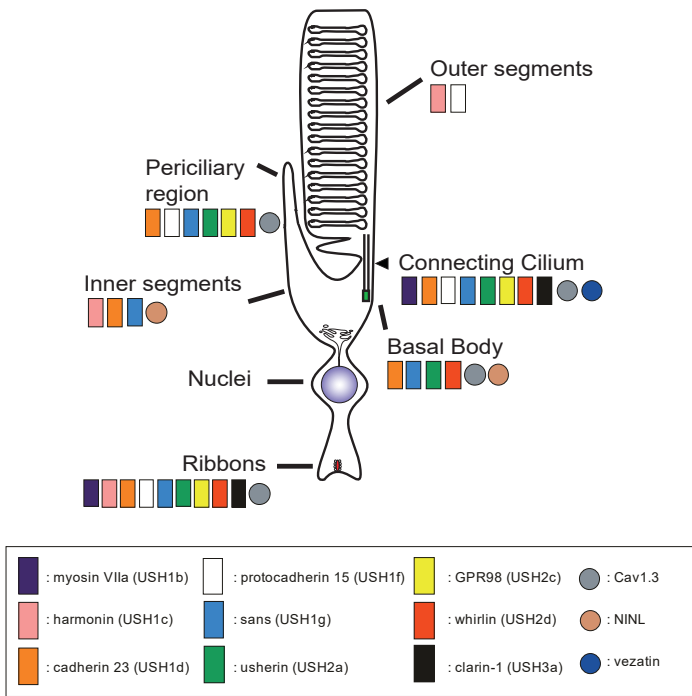
Figure 6. Localization of USH proteins in the photoreceptor
(Figure adapted with permission [50]).

5.   CELLULAR AND ANIMAL MODELS FOR USHER SYNDROME

Suitable cellular or animal models are essential to gain more insight into the molecular mechanisms underlying photoreceptor and hair cell dysfunction in Usher syndrome patients and to evaluate the therapeutic strategies that are currently under development. Here, we describe an overview of existing models for Usher syndrome (**Table 2**).

5.1   Human cellular models

The accessibility of human material for studying Usher protein function is limited since these proteins are mostly expressed in retina, brain and inner ear. However, human nasal epithelium or hair roots also express Usher proteins and can be collected from Usher patients semi-invasively [57,58]. In addition, patient-specific induced pluripotent stem cell (iPSC)-derived otic and retinal progenitor cells may be useful in unraveling the mechanisms underlying the disease [59-61]. iPSCs can be generated directly from fibroblasts or keratinocytes. Otic progenitors derived from iPSCs were used to study the function of MYO7A. Compound heterozygous mutations in *MYO7A* led to mechanotransduction

channel dysfunction, and abnormal electrophysiological activity of iPSC-derived hair cell-like cells [62]. The lack of photoreceptor outer segments and RPE in cultured iPSC-derived photoreceptor precursor cells and the impossibility to measure visual acuity in cell models remain a challenge at this moment. Therefore, animal models are crucial to gain insight into the pathophysiological effects of a mutated gene and to assess the efficacy of novel potential therapies at the level of visual function.

5.2   Fruit fly (*Drosophila melanogaster*)

For more than 100 years, studies in fruit flies yielded new and exciting insights in the field of genetics [63]. The *Drosophila* compound eye consists of a retina and four optic ganglia. It is a highly organized and stereotypic organ in which it is easy to detect phenotypes that disrupt this regular pattern of organization [64]. However, the retina comprises approximately 700-800 ommatidia, or facets. Each ommatidium contains eight photoreceptor cells that are associated with a rhabdomere. Fruit fly mutants for the orthologues Usher genes *MYO7A, PCDH15, USH1G, CDH23* and *USH1C* have been generated (**Table 2**). Although some defects in the auditory Johnston's organ were reported, no defects in visual function were observed.

5.3   Mouse (*Mus Musculus*)

Mutant mouse models are commonly used to study inherited retinal dystrophies, including RP [65]. Mice are more closely related to humans than fruit flies and have a greater genetic complexity. However, the available Usher knock-out models do not fully recapitulate the phenotype of Usher syndrome patients (**Table 2**). Hearing impairment and vestibular dysfunction is observed in the majority of knock-out models for Usher genes, whereas the retinal degeneration as observed in Usher syndrome patients is only sporadically seen as shown in **Table 2**. Compared to human photoreceptors, mouse photoreceptors have no calyceal processes and an underdeveloped periciliary membrane [66]. These anatomical differences could possibly explain the observed discrepancy in phenotype, since the calyceal processes and the periciliary membrane are the most prominent subcellular locations in photoreceptor cells where USH1 and USH2 proteins have been found [47,66-68].

5.4   Zebrafish (*Danio Rerio*)

5.4.1   *Using the zebrafish as model to study retinal degeneration*

Zebrafish, *Danio Rerio,* are tropical freshwater fish native to the Southern part of Asia, where they live in shallow, slow-flowing water. The vertebrate zebrafish are teleosts and belong to the family of Cyprinidae and class of Actinopterygii. In the 1970s the

American molecular biologist George Streisinger and his colleagues at the University of Oregon introduced the zebrafish as a laboratory animal [69]. The zebrafish has emerged as an eminent model organism in scientific research thanks to numerous advantageous characteristics like their small size, ease of maintenance and genetic manipulation, high fecundity, rapid *ex vivo* development and transparency during embryogenesis [70] (**Figure 7**). Challenges in using the zebrafish as a model organism for human retinal disorders are their largely duplicated genome, the absence of a macula, the distribution of rods and cones and their ability to regenerate retinal cells upon injury.

Functional vision is crucial for the survival of zebrafish larvae, soon after hatching the larvae must be able to search for food and to avoid predators. Using the behavioral optokinetic response (OKR) assay and the electrophysiological electroretinogram (ERG), retinal function can be assessed in zebrafish larvae from 5 dpf onwards [71].
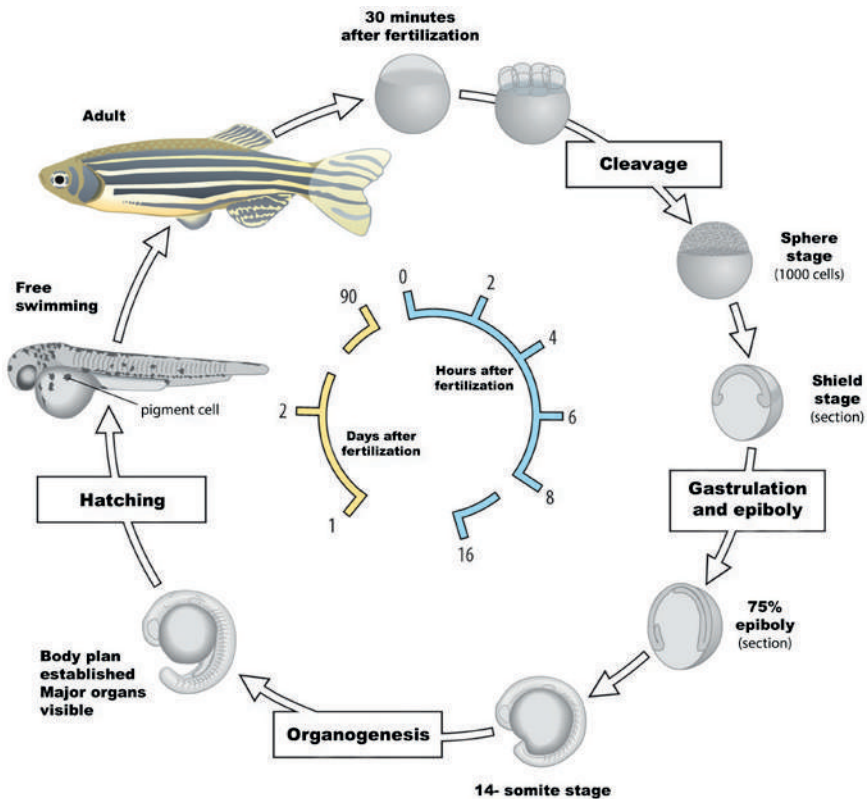
Figure 7. Life cycle and development of the zebrafish.

In total, 4 stages can be distinguished: embryonic stage (up to 3 days post fertilization), larval stage (3-27 days post fertilization), juvenile stage (approximately 27-60 days post fertilization) and adult stage (> 90 days post fertilization).

A dedicated online database containing information on zebrafish genetics and development is available (Zebrafish Information Network (ZFIN) (www.zfin.org)). The Zebrafish International Resource Center (ZIRC) is a resource from where more than 34,000 different mutant and transgenic zebrafish lines can be purchased (www.zebrafish.org).

5.4.2 *Zebrafish Usher knockdown and knock-out models*

In contrast to the existing mouse models for Usher genes, several morphant and mutant zebrafish models for Usher syndrome display early-onset retinal dysfunction (**Table 2**)[72]. Due to an ancient genome duplication in teleost fish, orthologs of approximately ~30% of the mammalian genes are present in two copies. For instance, zebrafish have two copies of the *MYO7A* gene, *myo7aa* and *myo7ab*. *Myo7aa* is expressed in the sensory hair cells of the inner ear, the neuromasts, and in photoreceptors[73-75]. Recently, impaired visual function and photoreceptor degeneration have been observed in *myo7aa* mutants[73]. Similar to what has been observed in *Myo7a* mouse mutants, opsins like rhodopsin and blue cone opsin are not correctly localized in photoreceptors of *myo7aa* mutants. In 5 day old *ush1c* mutants, maturation of the photoreceptor ribbon synapse is abnormal, leading to a decrease in synaptic transmission and, as a consequence, to an impaired visual function[76,77]. *Cdh23* (USH1d) was shown to be expressed in GABAergic amacrine cells but not in photoreceptors of larval zebrafish eyes[78]. Auditory and vestibular defects were detected[79], although no defects in visual function were reported for the existing *cdh23* mutant alleles[78,80]. Zebrafish also have two *PCDH15* (USH1f) orthologs, *pcdh15a* and *pcdh15b*. *Pcdh15a* is expressed in mechanosensory hair cells and brain, whereas *pcdh15b* is expressed in photoreceptors, the brain and weakly in the inner ear and neuromasts[81]. The *pcdh15a* mutant *orbiter* shows vestibular dysfunction but intact visual function. In contrast, vestibular function is normal in *pcdh15b*, whereas visual function is impaired. For Usher syndrome type 3a, the conserved role of *USH3A* in hearing and balance is demonstrated in *clrn1* morphants and mutants[82,83]. Although clarin1 is described to be present in larval and adult eyes, no analysis of retinal function was performed[84]. For *USH2* genes no knock-out models have been generated and characterized yet. However, *ush2a* or *adgrv1* (USH2c) morphants exhibit signs of early photoreceptor death[37,72,85]. In contrast with USH1 and USH3 models[86-89], so far no vestibular defects were described for the USH2 models. Taken together, the observed photoreceptor defects in *ush2a* morphants and *ush1* mutants suggest that the zebrafish could be a suitable model to study *USH2A*-associated RP (**Chapter 4**).

6.   OUTLINE AND AIM OF THIS THESIS

The main purpose of the research in this thesis is to obtain a better understanding of the pathophysiology underlying *USH2A*-associated retinal degeneration, and to design, develop and evaluate therapeutic strategies for the future treatment of this condition. In **chapter 2**, the retinal function of ninein-like protein (NINL), a key interaction partner of usherin[isoB] is studied. With the use of proteomics, Double Zinc Ribbon and Ankyrin Repeat domains 1 (DZANK1) has been identified as a novel interaction partner of NINL (**chapter 2A**). Furthermore, we show that NINL and DZANK1 co-function in the cytoplasmic dynein1-mediated transport of Trans-Golgi network (TGN)-derived vesicles in zebrafish photoreceptor cells. In **chapter 2B** the physical and genetic interaction between CC2D2A and NINL is described. The association of NINL with both the cytoplasmic dynein 1-dynactin motor complex (**chapter 2A**) and MICAL3 supports a role for NINL in the initial transport of trans-Golgi network-derived RAB8A-MICAL3 coated vesicles towards the base of the photoreceptor cilium, while the association of NINL with CC2D2A provides a docking point for these incoming vesicles at the entrance of the ciliary compartment (**chapter 2B**).

To evaluate future therapeutic strategies that could potentially halt the progression of the devastating Usher syndrome, an animal model that mimics the human phenotype is needed. In **chapter 3A** we describe the generation and characterization of two *ush2a* knock-out zebrafish models. In contrast with *Ush2a* knock-out mouse models, the zebrafish models display an early-onset retinal phenotype. In addition, in **chapter 3B** we investigate the sensitivity of different behavioral assays to detect retinal dysfunction in zebrafish larvae. We have optimized the semi high-throughput visual motor response (VMR) assay and propose a new workflow to analyze visual performance in zebrafish larvae.

Chapter 4 highlights our efforts in the development of therapeutic strategies for *USH2A*-associated RP. For this purpose, we have generated two different *Tol2*-based transgenic zebrafish lines that express human *miniUSH2A* genes in the *ush2a[rmc1]* background. We demonstrate that expression of either *miniUSH2A* gene results in significant rescue of the retinal phenotype observed in *ush2a[rmc1]* larvae. Finally, **chapter 5** provides the general discussion of this thesis, and implications for future research on this topic.

REFERENCES

1. Von Graefe, A. Exceptionelles Verhalten des Gesichtsfeldes bei Pigmententartung der Netzhaut. *Archiv für Ophtalmologie* 4, 441-445, (1858).

2. Liebreich, R. Abkunft aus Ehen unter Blutverwandten als Grund von Retinitis Pigmentosa. *Dtsch. Arch. Klin. Med.* 13, 53-55, (1861).

3. Hartmann, A. Taubstummheit und Taubstummenbildung nach den vorhanden Quellen sowie nach eigenen Beobachtungen und Erfahrungen. *Stuttgart: Verlag Fernidand Enke.*, (1880).

4. Usher, C. Bowman Lecture: On a few hereditary eye affections. . *Trans Ophthalmol. Soc. UK*, 164-245, (1935).

5. Rosenberg, T., Haim, M., Hauch, A. M. & Parving, A. The prevalence of Usher syndrome and other retinal dystrophy-hearing impairment associations. *Clin Genet* 51, 314-321, (1997).

6. Spandau, U. H. & Rohrschneider, K. Prevalence and geographical distribution of Usher syndrome in Germany. *Graefes Arch Clin Exp Ophthalmol* 240, 495-498, (2002).

7. Smith, R. J. *et al.* Clinical diagnosis of the Usher syndromes. Usher Syndrome Consortium. *Am J Med Genet* 50, 32-38, (1994).

8. Davenport, S. a. O., GS. The heterogeneity of Usher syndrome. . *Fifth international conference on birth defects. Amsterdam. Excerpta Medica*, 87-88, (1977).

9. Sandberg, M. A. *et al.* Disease course in patients with autosomal recessive retinitis pigmentosa due to the USH2A gene. *Invest Ophthalmol Vis Sci* 49, 5532-5539, (2008).

10. Khateb, S. *et al.* A homozygous nonsense CEP250 mutation combined with a heterozygous nonsense C2orf71 mutation is associated with atypical Usher syndrome. *J Med Genet* 51, 460-469, (2014).

11. Bashir, R., Fatima, A. & Naz, S. A frameshift mutation in SANS results in atypical Usher syndrome. *Clin Genet* 78, 601-603, (2010).

12. Liu, X. Z. *et al.* Mutations in the myosin VIIA gene cause a wide phenotypic spectrum, including atypical Usher syndrome. *Am J Hum Genet* 63, 909-912, (1998).

13. Bonnet, C. & El-Amraoui, A. Usher syndrome (sensorineural deafness and retinitis pigmentosa): pathogenesis, molecular diagnosis and therapeutic approaches. *Curr Opin Neurol* 25, 42-49, (2012).

14. Zrada, S. E., Braat, K., Doty, R. L. & Laties, A. M. Olfactory loss in Usher syndrome: another sensory deficit? *Am J Med Genet* 64, 602-603, (1996).

15. Schaefer, G. B., Bodensteiner, J. B., Thompson, J. N., Jr., Kimberling, W. J. & Craft, J. M. Volumetric neuroimaging in Usher syndrome: evidence of global involvement. *Am J Med Genet* 79, 1-4, (1998).

16. Mangotich, M. & Misiaszek, J. Atypical psychosis in Usher's syndrome. *Psychosomatics* 24, 674-675, (1983).

17. Hunter, D. G., Fishman, G. A., Mehta, R. S. & Kretzer, F. L. Abnormal sperm and photoreceptor axonemes in Usher's syndrome. *Arch Ophthalmol* 104, 385-389, (1986).

18. Hess-Rover, J., Crichton, J., Byrne, K. & Holland, A. J. Diagnosis and treatment of a severe psychotic illness in a man with dual severe sensory impairments caused by the presence of Usher syndrome. *Journal of intellectual disability research : JIDR* 43 (Pt 5), 428-434, (1999).

19. Drouet, A., Swalduz, B., Guilloton, L., Faivre, A. & Felten, D. [Usher syndrome: a case report]. *Rev Neurol (Paris)* 159, 323-325, (2003).

1

20. Bonneau, D. *et al.* Usher syndrome type I associated with bronchiectasis and immotile nasal cilia in two brothers. *J Med Genet* 30, 253-254, (1993).

21. Domanico, D., Fragiotta, S., Cutini, A., Grenga, P. L. & Vingolo, E. M. Psychosis, Mood and Behavioral Disorders in Usher Syndrome: Review of the Literature. *Medical hypothesis, discovery & innovation ophthalmology journal* 4, 50-55, (2015).

22. Mathur, P. & Yang, J. Usher syndrome: hearing loss, retinal degeneration and associated abnormalities. *Biochim Biophys Acta* 1852, 406-420, (2015).

23. Kumar, A., Fishman, G. & Torok, N. Vestibular and auditory function in Usher's syndrome. *The Annals of otology, rhinology, and laryngology* 93, 600-608, (1984).

24. Wagenaar, M. *et al.* Hearing impairment related to age in Usher syndrome types 1B and 2A. *Arch Otolaryngol Head Neck Surg* 125, 441-445, (1999).

25. Hoshino, A. C., Echegoyen, A., Goffi-Gomez, M. V., Tsuji, R. K. & Bento, R. F. Outcomes of Late Implantation in Usher Syndrome Patients. *International archives of otorhinolaryngology* 21, 140-143, (2017).

26. Pennings, R. J. *et al.* Pure tone hearing thresholds and speech recognition scores in Dutch patients carrying mutations in the USH2A gene. *Otology & neurotology : official publication of the American Otological Society, American Neurotology Society [and] European Academy of Otology and Neurotology* 24, 58-63, (2003).

27. van Aarem, A. *et al.* Stable and progressive hearing loss in type 2A Usher's syndrome. *The Annals of otology, rhinology, and laryngology* 105, 962-967, (1996).

28. Sadeghi, M. *et al.* Audiological findings in Usher syndrome types IIa and II (non-IIa). *International journal of audiology* 43, 136-143, (2004).

29. Hartel, B. P. *et al.* A combination of two truncating mutations in USH2A causes more severe and progressive hearing impairment in Usher syndrome type IIa. *Hearing research* 339, 60-68, (2016).

30. Sadeghi, M., Cohn, E. S., Kimberling, W. J., Tranebjaerg, L. & Moller, C. Audiological and vestibular features in affected subjects with USH3: a genotype/phenotype correlation. *International journal of audiology* 44, 307-316, (2005).

31. Hartel, B. P. *et al.* Hearing aid fitting for visual and hearing impaired patients with Usher syndrome type IIa. *Clinical otolaryngology : official journal of ENT-UK ; official journal of Netherlands Society for Oto-Rhino-Laryngology & Cervico-Facial Surgery* 42, 805-814, (2017).

32. Hartel, B. P. *et al.* Cochlear Implantation in Patients With Usher Syndrome Type IIa Increases Performance and Quality of Life. *Otology & neurotology : official publication of the American Otological Society, American Neurotology Society [and] European Academy of Otology and Neurotology* 38, e120-e127, (2017).

33. Pietola, L. *et al.* Speech recognition and communication outcomes with cochlear implantation in Usher syndrome type 3. *Otology & neurotology : official publication of the American Otological Society, American Neurotology Society [and] European Academy of Otology and Neurotology* 33, 38-41, (2012).

34. Lamb, T. D., Collin, S. P. & Pugh, E. N., Jr. Evolution of the vertebrate eye: opsins, photoreceptors, retina and eye cup. *Nature reviews. Neuroscience* 8, 960-976, (2007).

35. Ebrey, T. & Koutalos, Y. Vertebrate photoreceptors. *Progress in retinal and eye research* 20, 49-94, (2001).

36. Strauss, O. in *Webvision: The Organization of the Retina and Visual System* (eds H. Kolb, E. Fernandez, & R. Nelson) (1995).

37. Ebermann, I. *et al*. PDZD7 is a modifier of retinal disease and a contributor to digenic Usher syndrome. *J Clin Invest* 120, 1812-1823, (2010).

38. Puffenberger, E. G. *et al*. Genetic mapping and exome sequencing identify variants associated with five novel diseases. *PLoS One* 7, e28936, (2012).

39. Abbott, J. A. *et al*. The Usher Syndrome Type IIIB Histidyl-tRNA Synthetase Mutation Confers Temperature Sensitivity. *Biochemistry* 56, 3619-3631, (2017).

40. Millan, J. M. *et al*. An update on the genetics of usher syndrome. *Journal of ophthalmology* 2011, 417217, (2011).

41. Yan, D. & Liu, X. Z. Genetics and pathological mechanisms of Usher syndrome. *Journal of human genetics* 55, 327-335, (2010).

42. McGee, T. L., Seyedahmadi, B. J., Sweeney, M. O., Dryja, T. P. & Berson, E. L. Novel mutations in the long isoform of the USH2A gene in patients with Usher syndrome type II or non-syndromic retinitis pigmentosa. *J Med Genet* 47, 499-506, (2010).

43. Eudy, J. D. *et al*. Mutation of a gene encoding a protein with extracellular matrix motifs in Usher syndrome type IIa. *Science* 280, 1753-1757, (1998).

44. van Wijk, E. *et al*. Identification of 51 novel exons of the Usher syndrome type 2A (USH2A) gene that encode multiple conserved functional domains and that are mutated in patients with Usher syndrome type II. *Am J Hum Genet* 74, 738-744, (2004).

45. Adato, A. *et al*. Usherin, the defective protein in Usher syndrome type IIA, is likely to be a component of interstereocilia ankle links in the inner ear sensory cells. *Hum Mol Genet* 14, 3921-3932, (2005).

46. Liu, X. *et al*. Usherin is required for maintenance of retinal photoreceptors and normal development of cochlear hair cells. *Proc Natl Acad Sci U S A* 104, 4413-4418, (2007).

47. Maerker, T. *et al*. A novel Usher protein network at the periciliary reloading point between molecular transport machineries in vertebrate photoreceptor cells. *Human molecular genetics* 17, 71-86, (2008).

48. van Wijk, E. *et al*. The DFNB31 gene product whirlin connects to the Usher protein network in the cochlea and retina by direct association with USH2A and VLGR1. *Hum Mol Genet* 15, 751-765, (2006).

49. Reiners, J. *et al*. Scaffold protein harmonin (USH1C) provides molecular links between Usher syndrome type 1 and type 2. *Hum Mol Genet* 14, 3933-3943, (2005).

50. Cosgrove, D. & Zallocchi, M. Usher protein functions in hair cells and photoreceptors. *Int J Biochem Cell Biol* 46, 80-89, (2014).

51. Sorusch, N. *et al*. Characterization of the ternary Usher syndrome SANS/ush2a/whirlin protein complex. *Hum Mol Genet*, (2017).

52. Kremer, H., van Wijk, E., Marker, T., Wolfrum, U. & Roepman, R. Usher syndrome: molecular links of pathogenesis, proteins and pathways. *Hum Mol Genet* 15 Spec No 2, R262-270, (2006).

53. Roepman, R. & Wolfrum, U. Protein networks and complexes in photoreceptor cilia. *Sub-cellular biochemistry* 43, 209-235, (2007).

54. van Wijk, E. *et al*. Usher syndrome and Leber congenital amaurosis are molecularly linked via a novel isoform of the centrosomal ninein-like protein. *Hum Mol Genet* 18, 51-64, (2009).

55. Reiners, J., Nagel-Wolfrum, K., Jurgens, K., Marker, T. & Wolfrum, U. Molecular basis of human Usher syndrome: deciphering the meshes of the Usher protein network provides insights into the pathomechanisms of the Usher disease. *Exp Eye Res* 83, 97-119, (2006).

1

56. Overlack, N., Maerker, T., Latz, M., Nagel-Wolfrum, K. & Wolfrum, U. SANS (USH1G) expression in developing and mature mammalian retina. *Vision Res* 48, 400-412, (2008).

57. Nakanishi, H. *et al.* Hair roots as an mRNA source for mutation analysis of Usher syndrome-causing genes. *Journal of human genetics* 55, 701-703, (2010).

58. Vache, C. *et al.* Nasal epithelial cells are a reliable source to study splicing variants in Usher syndrome. *Hum Mutat* 31, 734-741, (2010).

59. Tucker, B. A. *et al.* Patient-specific iPSC-derived photoreceptor precursor cells as a means to investigate retinitis pigmentosa. *eLife* 2, e00824, (2013).

60. Wu, A. Y. & Daniel, M. G. Using stem cell biology to study and treat ophthalmologic and oculoplastic diseases. *Taiwan journal of ophthalmology* 7, 77-81, (2017).

61. Li, Y., Chan, L., Nguyen, H. V. & Tsang, S. H. Personalized Medicine: Cell and Gene Therapy Based on Patient-Specific iPSC-Derived Retinal Pigment Epithelium Cells. *Adv Exp Med Biol* 854, 549-555, (2016).

62. Tang, Z. H. *et al.* Genetic Correction of Induced Pluripotent Stem Cells From a Deaf Patient With MYO7A Mutation Results in Morphologic and Functional Recovery of the Derived Hair Cell-Like Cells. *Stem cells translational medicine* 5, 561-571, (2016).

63. Bellen, H. J., Tong, C. & Tsuda, H. 100 years of Drosophila research and its impact on vertebrate neuroscience: a history lesson for the future. *Nature reviews. Neuroscience* 11, 514-522, (2010).

64. Kumar, J. P. The fly eye: Through the looking glass. *Dev Dyn*, (2017).

65. Campochiaro, P. A. & Mir, T. A. The mechanism of cone cell death in Retinitis Pigmentosa. *Progress in retinal and eye research*, (2017).

66. Sahly, I. *et al.* Localization of Usher 1 proteins to the photoreceptor calyceal processes, which are absent from mice. *J Cell Biol* 199, 381-399, (2012).

67. Sorusch, N. *et al.* Characterization of the ternary Usher syndrome SANS/ush2a/whirlin protein complex. *Human molecular genetics* 26, 1157-1172, (2017).

68. May-Simera, H., Nagel-Wolfrum, K. & Wolfrum, U. Cilia - The sensory antennae in the eye. *Progress in retinal and eye research* 60, 144-180, (2017).

69. Streisinger, G., Walker, C., Dower, N., Knauber, D. & Singer, F. Production of clones of homozygous diploid zebra fish (Brachydanio rerio). *Nature* 291, 293-296, (1981).

70. Huang, P., Zhu, Z., Lin, S. & Zhang, B. Reverse genetic approaches in zebrafish. *Journal of genetics and genomics = Yi chuan xue bao* 39, 421-433, (2012).

71. Emran, F. *et al.* OFF ganglion cells cannot drive the optokinetic reflex in zebrafish. *Proc Natl Acad Sci U S A* 104, 19126-19131, (2007).

72. Blanco-Sanchez, B., Clement, A., Phillips, J. B. & Westerfield, M. Zebrafish models of human eye and inner ear diseases. *Methods Cell Biol* 138, 415-467, (2017).

73. Wasfy, M. M., Matsui, J. I., Miller, J., Dowling, J. E. & Perkins, B. D. myosin 7aa(-/-) mutant zebrafish show mild photoreceptor degeneration and reduced electroretinographic responses. *Exp Eye Res* 122, 65-76, (2014).

74. Ernest, S. *et al.* Mariner is defective in myosin VIIA: a zebrafish model for human hereditary deafness. *Hum Mol Genet* 9, 2189-2196, (2000).

75. Hodel, C. *et al.* Myosin VIIA is a marker for the cone accessory outer segment in zebrafish. *Anatomical record* 297, 1777-1784, (2014).

76. Blanco-Sanchez, B., Clement, A., Fierro, J., Jr., Washbourne, P. & Westerfield, M. Complexes of Usher proteins preassemble at the endoplasmic reticulum and are required for trafficking and ER homeostasis. *Disease models & mechanisms* 7, 547-559, (2014).

77. Phillips, J. B. *et al.* Harmonin (Ush1c) is required in zebrafish Muller glial cells for photoreceptor synaptic development and function. *Disease models & mechanisms* 4, 786-800, (2011).

78. Glover, G., Mueller, K. P., Sollner, C., Neuhauss, S. C. & Nicolson, T. The Usher gene cadherin 23 is expressed in the zebrafish brain and a subset of retinal amacrine cells. *Mol Vis* 18, 2309-2322, (2012).

79. Nicolson, T. *et al.* Genetic analysis of vertebrate sensory hair cell mechanosensation: the zebrafish circler mutants. *Neuron* 20, 271-283, (1998).

80. Mo, W., Chen, F., Nechiporuk, A. & Nicolson, T. Quantification of vestibular-induced eye movements in zebrafish larvae. *BMC neuroscience* 11, 110, (2010).

81. Seiler, C. *et al.* Duplicated genes with split functions: independent roles of protocadherin15 orthologues in zebrafish hearing and vision. *Development* 132, 615-623, (2005).

82. Ogun, O. & Zallocchi, M. Clarin-1 acts as a modulator of mechanotransduction activity and presynaptic ribbon assembly. *J Cell Biol* 207, 375-391, (2014).

83. Gopal, S. R. *et al.* Zebrafish Models for the Mechanosensory Hair Cell Dysfunction in Usher Syndrome 3 Reveal That Clarin-1 Is an Essential Hair Bundle Protein. *J Neurosci* 35, 10188-10201, (2015).

84. Phillips, J. B. *et al.* The cone-dominant retina and the inner ear of zebrafish express the ortholog of CLRN1, the causative gene of human Usher syndrome type 3A. *Gene expression patterns : GEP* 13, 473-481, (2013).

85. Slijkerman, R. W. *et al.* The pros and cons of vertebrate animal models for functional and therapeutic research on inherited retinal dystrophies. *Progress in retinal and eye research* 48, 137-159, (2015).

86. Emptoz, A. *et al.* Local gene therapy durably restores vestibular function in a mouse model of Usher syndrome type 1G. *Proc Natl Acad Sci U S A* 114, 9695-9700, (2017).

87. Pan, B. *et al.* Gene therapy restores auditory and vestibular function in a mouse model of Usher syndrome type 1c. *Nature biotechnology* 35, 264-272, (2017).

88. Vijayakumar, S. *et al.* Rescue of peripheral vestibular function in Usher syndrome mice using a splice-switching antisense oligonucleotide. *Hum Mol Genet* 26, 3482-3494, (2017).

89. Geng, R. *et al.* Usher syndrome IIIA gene clarin-1 is essential for hair cell function and associated neural activation. *Hum Mol Genet* 18, 2748-2760, (2009).

Chapter 2

Dissecting the *USH2A*-associated protein
network: unraveling function of key
interaction player NINL

2
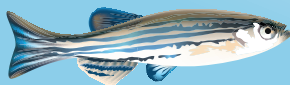
Dona M[1], Bachmann-Gagescu R[2], Texier Y[3], Toedt G[4], Hetterschijt L[5], Tonnaer EL[6], Peters TA[6], van Beersum SE[5], Bergboer JG[7], Horn N[3], de Vrieze E[1], Slijkerman RW[1], van Reeuwijk J[5], Flik G[8], Keunen JE[9], Ueffing M[3], Gibson TJ[4], Roepman R[5], Boldt K[3], Kremer H[10], van Wijk E[1]

[1] Department of Otorhinolaryngology, Radboud University Medical Centre, Nijmegen, the Netherlands; Radboud Institute for Molecular Life Sciences, Radboud University Nijmegen, Nijmegen, the Netherlands; [2] Institute of Molecular Life Sciences, University of Zurich, Zürich, Switzerland; Institute of Medical Genetics, University of Zurich, Zürich, Switzerland; [3] Division of Experimental Ophthalmology, and Medical Proteome Center, Centre for Ophthalmology, Eberhard Karls University Tuebingen, Tübingen, Germany; [4] Structural and Computational Biology Unit, European Molecular Biology Laboratory, Heidelberg, Germany; [5] Radboud Institute for Molecular Life Sciences, Radboud University Nijmegen, Nijmegen, the Netherlands; Department of Human Genetics, Radboud University Medical Centre, Nijmegen, the Netherlands; [6] Department of Otorhinolaryngology, Radboud University Medical Centre, Nijmegen, the Netherlands; [7] Department of Human Genetics, Radboud University Medical Centre, Nijmegen, the Netherlands; [8] Department of Organismal Animal Physiology, Institute for Water and Wetland Research, Radboud University Nijmegen, Nijmegen, The Netherlands; [9] Department of Ophthalmology, Radboud University Medical Centre, Nijmegen, the Netherlands; [10] Department of Otorhinolaryngology, Radboud University Medical Centre, Nijmegen, the Netherlands; Radboud Institute for Molecular Life Sciences, Radboud University Nijmegen, Nijmegen, the Netherlands; Department of Human Genetics, Radboud University Medical Centre, Nijmegen, the Netherlands

Chapter 2.1

NINL and DZANK1 co-function in
vesicle transport and are essential for
photoreceptor development in zebrafish

2.1

ABSTRACT

Ciliopathies are Mendelian disorders caused by dysfunction of cilia, ubiquitous organelles involved in fluid propulsion (motile cilia) or signal transduction (primary cilia). Retinal dystrophy is a common phenotypic characteristic of ciliopathies since photoreceptor outer segments are specialized primary cilia. These ciliary structures heavily rely on intracellular minus-end directed transport of cargo, mediated at least in part by the cytoplasmic dynein 1 motor complex, for their formation, maintenance and function. Ninein-like protein (NINL) is known to associate with this motor complex and is an important interaction partner of the ciliopathy-associated proteins lebercilin, USH2A and CC2D2A. Here, we scrutinize the function of NINL with combined proteomic and zebrafish in vivo approaches. We identify Double Zinc Ribbon and Ankyrin Repeat domains 1 (DZANK1) as a novel interaction partner of NINL and show that loss of Ninl, Dzank1 or both synergistically leads to dysmorphic photoreceptor outer segments, accumulation of trans-Golgi-derived vesicles and mislocalization of Rhodopsin and Ush2a in zebrafish. In addition, retrograde melanosome transport is severely impaired in zebrafish lacking Ninl or Dzank1. We further demonstrate that NINL and DZANK1 are essential for intracellular dynein-based transport by associating with complementary subunits of the cytoplasmic dynein 1 motor complex, thus shedding light on the structure and stoichiometry of this important motor complex. Altogether, our results support a model in which the NINL-DZANK1 protein module is involved in the proper assembly and folding of the cytoplasmic dynein 1 motor complex in photoreceptor cells, a process essential for outer segment formation and function.

2.1

1. INTRODUCTION

Dysfunction of cilia is the underlying defect in a growing group of pleiotropic genetic disorders, the ciliopathies. Cilia are ubiquitous microtubule-based organelles involved in fluid propulsion (motile cilia) or signal transduction (primary cilia) and ciliopathy-associated proteins localize to various ciliary sub-compartments. Retinal dystrophy is a common clinical feature of ciliopathies where the primary affected retinal cell type is the photoreceptor, which contains a highly specialized primary cilium, consisting of the connecting cilium and axoneme serving as a backbone to the outer segment. For propagation of visual excitation, outer segments are composed of stacks of membranous discs, which are densely packed with the light-sensitive transmembrane receptor rhodopsin and its associated photo-transduction machinery. The membranous discs are organized around the axoneme that is continuous with the connecting cilium. The entire outer segment can thus be regarded as a highly specialized primary cilia compartment. The connecting cilium literally connects the outer segment to the inner segment of the photoreceptor and is the equivalent of a canonical ciliary transition zone. This proximal region of the cilium ensures a tight control of protein access into the ciliary compartment [1–5] through a gate-keeper function, involving several ciliopathy-associated proteins such as NPHP's [4] and Meckel and Joubert syndrome proteins [6], importins and Ran GTPases [7, 8]. Given the daily renewal of about 10% of the total length of the outer segments in humans [9], photoreceptor cells require intense intracellular trafficking to build their outer segments and to replenish the shed discs. Transmembrane proteins, such as rhodopsin and Usherin are synthesized in the inner segment and subsequently moved from the trans-Golgi network (TGN) towards the base of the ciliary compartment via microtubule-based vesicular transport [10]. This transport involves motor proteins such as the ATPases kinesin and dynein [11, 12]. Specifically, the cytoplasmic dynein 1 motor complex, which consists of two 530 kDa heavy chains, responsible for force production, a group of 74 kDa intermediate chains, 53 to 57 kDa light intermediate chains, and 8 to 21 kDa light chains [13], has been implicated in minus-end directed transport of post-Golgi-derived rhodopsin-containing vesicles [14]. During its transport, the carboxy-terminal domain of rhodopsin binds to the dynein light chain Tctex-type DYNLT1 [14]. In the absence of rhodopsin, small rudimentary photoreceptor outer segments are formed during the first few postnatal weeks. After this period the outer segments vanish and photoreceptors die rapidly. As a consequence, photo-transduction is impaired leading to defects in visual function [15, 16]. A similar defect in photoreceptor morphology and function is observed in the zebrafish cannonball mutant, in which the cytoplasmic dynein motor complex 1 is dysfunctional due to a mutation in the dynein cytoplasmic 1 heavy chain 1 (dync1h1) gene [17]. These findings emphasize the importance of the cytoplasmic dynein motor

complex 1 for intracellular trafficking which is essential for photoreceptor development and function. However, the structure of this complex has not been fully elucidated to date. Previously, we described a retinal ciliopathy-associated protein module consisting of Usherin, Lebercilin (Leber's congenital amaurosis type 5) and NINLisoB (ninein-like protein isoform B) present at the base of the connecting cilium [18]. In addition, we now identified a physical interaction between NINLisoB and the ciliopathy protein CC2D2A, involved in Joubert and Meckel syndrome, two important ciliopathies (Bachmann-Gagescu, et al co-submission). Furthermore, NINL was found to associate with several members of the cytoplasmic dynein 1-dynactin motor complex and polo-like kinase 1 and was found to function in microtubule nucleation by recruitment of gamma-tubulin ring complexes [19]. However, the function of NINL in photoreceptors is still elusive.

In the current study, we investigate the role of NINL and its associated protein complex in the retina using a combination of proteomics and in vivo studies in zebrafish. We identify a central role for NINL and its novel interaction partner DZANK1 in vesicle transport towards the photoreceptor outer segments. Knockdown in zebrafish larvae of either ninl or dzank1 or synergistically at sub-phenotypic doses, leads to abnormal outer segment morphology, mislocalization of rhodopsin, accumulation of vesicular structures and consequently, loss of visual function. We further demonstrate that NINL and DZANK1 associate with complementary subunits of the cytoplasmic dynein 1 motor complex, which is essential for proper transport of vesicle-bound proteins towards the base of the photoreceptor connecting cilium and, as a consequence, photoreceptor development in zebrafish. Together, our findings shed light onto the assembly and structure of the cytoplasmic dynein 1 motor complex and link it to several ciliopathy proteins located at the entrance to the ciliary compartment.

2.   RESULTS

2.1   DZANK1 interacts with NINLisoB in the retina

Previously, NINL[isoB] was identified as a key connector of three large retinal ciliopathies [18] (Bachmann-Gagescu et al, co-submission). Its function within the retina, however, has not yet been deciphered. To get insight into the function of NINL, we screened a random-primed bovine retina cDNA library to identify interaction partners for the previously predicted intermediate filament (IF) domain (538-825aa) of NINL[isoB] [18]. Approximately 70% of the positive clones (> 1,000 clones), could be identified as DZANK1 (double zinc ribbon and ankyrin repeat domains 1), a protein with a yet unknown function. To elaborate on this finding, three overlapping cDNA fragments were cloned: one encoding full length DZANK1 (752aa) and two different deletion constructs, encoding either the zinc finger domains as found in Ran binding proteins

(ZNF_RBZ, SMART accession number SM00547, 244-317aa) or the ankyrin repeats known to be involved in protein-protein interactions (ANK, SMART accession number SM00248, 595-681aa) (SMART database; http://smart.embl-heidelberg.de) (Fig 1a). To test whether the interactions of DZANK1 with NINL are isoform-specific, both isoforms of NINL were tested. The transcript encoding NINL[isoB] lacks exon17 of the originally described NINL gene (encoding NINLisoA), resulting in the in-frame skipping of 349 amino acids after residue 734 [18]. Using dedicated binary yeast two-hybrid assays, we were able to pinpoint the interaction to the ZNF_RBZ domains of DZANK1 and both isoforms of NINL (Fig 1b). Since NINL[isoB] was originally found in the yeast-two hybrid screen, we continued with this isoform for further confirmations. We performed several in vitro and in vivo binding assays to conclusively validate the interaction between DZANK1 and NINL[isoB]. In a glutathione S-transferase (GST) pull-down assay, we identified that full-length Strep/FLAG-tagged DZANK1 was pulled down from HEK293T cell lysates by GST-fused NINLisoB_538-825aa and not by GST alone (Fig 1c). To confirm this interaction in cellulo, HEK293T cells were co-transfected with plasmids encoding full length HA-tagged NINL[isoB] and Strep/FLAG-tagged DZANK1 for immunoprecipitation (IP) assays. With anti-HA antibodies, NINLisoB consistently co-immunoprecipitated with full length DZANK1, but not with the control protein LRRK2 (Fig 1d). Reciprocal IP experiments with anti-FLAG antibodies for IP confirmed these results (Fig 1d'). In addition we performed GST pull-down assays from biologically relevant bovine retinal extracts followed by mass spectrometry (LC-MS/MS) analysis. In total, 445 different proteins were identified of which 59 passed the stringent filtering criteria. GST-fused human NINLisoB_aa538-825 was able to consistently pull-down endogenous bovine DZANK1 (in 4 out of 4 assays) whereas unfused GST (in 0 out of 3 assays) was not, which further confirmed the interaction (S1 Table). Further confirmation of the interaction was obtained through co-localization of eGFP- and mRFP-tagged DZANK1 and NINL[isoB] in hTERT-RPE1 cells. In singly transfected cells, NINL[isoB] and DZANK1 were both present at the ciliary base, partially co-localizing with the basal body and the ciliary marker polyglutamylated tubulin (anti-GT335) (Fig 2a and 2b"). DZANK1 also localized along the microtubule network of the cells. Co-expression of NINL[isoB] and DZANK1 resulted in the co-localization of both proteins, thereby fully retaining the latter to the basal body (Fig 2c", yellow signal). Importantly, co-localization of endogenous NINL and DZANK1 was also observed by immunohistochemistry in rat retina where NINL was demonstrated at the region of the connecting cilium [18]. Using a specific anti-DZANK1 antibody we show that NINL and DZANK1 co-localize in this region (Fig 2d–2f').
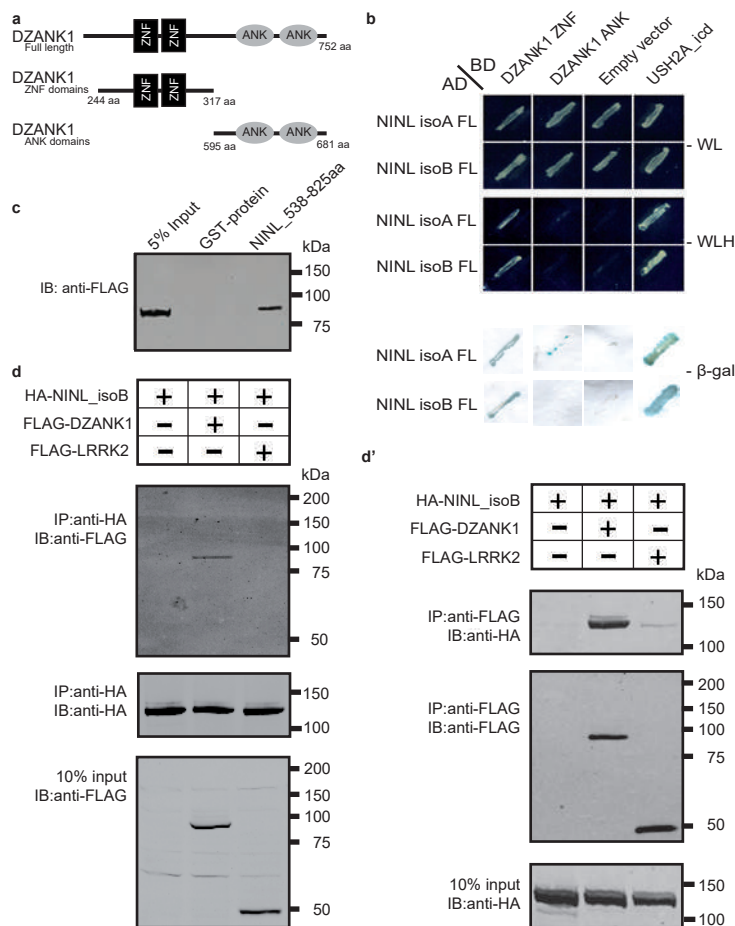
Figure 1. Protein-protein interaction studies

(a) Schematic protein structure of DZANK1. Two different deletion constructs of DZANK1, one consisting of the ZNF_RBZ domains (244-317aa) and the other of the ANK domains (595-681aa), were used for co-transformation in yeast. (b) Results of the cotransformation in yeast. Yeast transformants were selected on low (SD/-Trp/-Leu/-His) and high-stringency (SD/-Trp/-Leu/-His-/-Ade) medium with observed growth, indicating interaction of the tested bait and prey proteins. In addition, the β-galactosidase filter lift assay was performed. The USH2A_intracellular region was used as a positive control. Empty prey vector was used as a negative control. Yeast-two-hybrid analysis revealed a specific interaction between DZANK1 ZNF_RBZ domains and both NINLisoA/B. (c) GST pull-down assays, showing that Strep/FLAG-tagged DZANK1 was efficiently pulled down by GSTfused NINLisoB, but not by GST alone. The first lane shows 5% input of the protein lysate. (d) Co-immunoprecipitation of DZANK1 Full Length (FL) with NINLisoB, but not with LRRK2. The immunoblot (IB) in the top panel shows that HA-tagged NINL co-immunoprecipitated with Strep/FLAG-tagged DZANK1 (lane 2), whereas unrelated FLAG-tagged LRRK2 (lane 3) did not. The anti-HA immunoprecipitates are shown in the middle panel; protein input is shown in the bottom panel. (d') Reciprocal IP experiments using anti-FLAG antibodies confirmed the co-immunoprecipitation of HA-tagged NINLisoB with Strep/FLAGtagged DZANK1 (lane 2) and not with LRRK2 (lane 3) shown in the top panel. The anti-FLAG immunoprecipitations are shown in the middle panel; protein input is shown in the bottom panel. ANK: ankyrin repeat domain; ZNF_RBZ: Zinc Finger domain like in Ran-binding proteins; aa: amino acids.

2.1
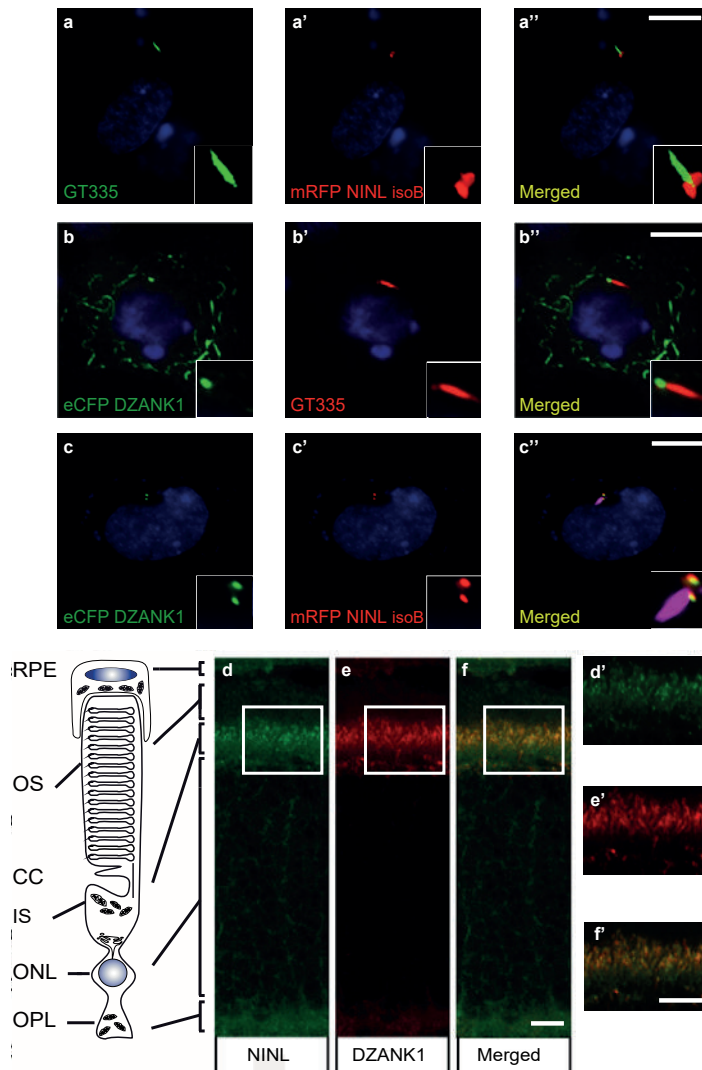
Figure 2. NINL and DZANK1 co-localize at the base of cilia in RPE cells and rat retina.

(a-c) Centrosomal co-localization of NINLisoB and DZANK1 in hTERT-RPE1 cells. When expressed alone, mRFP-NINLisoB (red signal in, a-a'' and c-c'') was localized to both centrioles at the base of the cilia marked with GT335 (green signal in a'-a'' and red signal in b-b''), whereas eYFP–DZANK1 was localized to the basal body and to the microtubule network of the cell (green signal in b-b''). After co-expression of NINLisoB and DZANK1, both proteins were localized at the basal body of the cilia in the centrosome (cilia marked by GT335, cyanid signal), supporting an interaction between the two proteins (c-c''). Nuclei were stained with DAPI (blue signal). (d-f) Co-localization of endogenous NINLisoB and DZANK1 in rat retina. (d-e) Co-immunostaining of NINL and DZANK1 in radial cryo-sections of adult (P20) rat retina with anti-NINL antibodies (green signal; d) and antiDZANK1 antibodies (red signal; e) showing co-localization (yellow signal: f) in the inner segment (IS) and in the region of the connecting cilium (CC). (d'-f') show details of the subcellular (co-) localization of NINL and DZANK1 in, respectively, d, e and f. Scale bars represent 10 μm (a-c''), 5 μm (f) and 1 μm (f').

2.2 Ninl and dzank1 genetically interact in photoreceptor outer segment morphogenesis and function

To investigate the biological role of NINL and DZANK1 in the retina, we first addressed the suitability of zebrafish as an animal model. tBLASTn searches of the zebrafish genome, using the amino acid sequence of human NINL and DZANK1, revealed a single ortholog for both genes. Although extensive RT-PCR analyses were performed, we were not able to detect the transcript encoding zebrafish Ninl isoform A in RNA obtained from zebrafish larvae (5 days post fertilization (dpf)). Therefore we conclude that under the given conditions the ninl transcript that shows the highest degree of homology with the human NINL^{isoB} encoding transcript is the most prominent. The presence of shorter or alternative transcripts encoding additional zebrafish Ninl isoforms cannot be ruled out, as no 5'- and 3'-RACE experiments were performed. Subsequently, the effect of ninl and dzank1 knockdown during zebrafish embryonic development was investigated, using gene-specific translation-blocking (atgMOs) and splice-blocking morpholinos (spMOs)**.**

Control MO-injected larvae (10 ng/nl; n = 300 from 2 biological replicates) appeared morphologically normal, and could not be distinguished from uninjected larvae (WT) during the studied developmental period of 4 to 5 dpf (Fig 3a and 3d). In contrast, injection of ninl atgMO revealed a concentration-dependent spectrum of phenotypes (n>200/group from 2 biological replicates; Bachmann-Gagescu et al., companion manuscript). Injection of the optimal concentration of 2 ng/nl ninl atgMO resulted in severe morphological defects including ventrally curved body axis, ventriculomegaly, pronephric cysts, expanded melanophores, small eyes and circling swimming behavior at 4 dpf (n = 300 from 2 biological replicates; Fig 3b and Bachmann-Gagescu et al., companion manuscript). In addition, we observed significantly shorter photoreceptor outer segments (OS) on retinal cryosections from 4dpf ninl morphant larvae stained with boron-dipyrromethene (bodipy) to mark the outer segment membrane discs (mean OS length 1.6+/-0.26 μm in morphants compared to 3.9+/-0.32 μm in wild-type, p<0.0001, unpaired Student's t-test, n>10 larvae from each group in each of 2 biological replicates) (Bachmann-Gagescu et al, companion manuscript). Co-injection of 150 pg/nl capped MO-resistant mRNA encoding human NINL^{isoB} with 2 ng/nl of ninl atgMO rescued the observed body curvature phenotype (curved body shape in 71% of ninl atgMO injected larvae (n = 207) versus 36% in ninl atgMO + ninl mRNA injected larvae (n = 203), data pooled from 2 biological replicates, p<0.0001, two-tailed Fisher's exact test) and the OS length (mean OS length in rescued larvae 3.8+/-0.25 μm, p<0.0001, Student's t-test, n = 10 larvae) (Bachmann-Gagescu et al, co-submission). In addition, the specificity of the observed phenotypes is further confirmed by the fact that a second morpholino against ninl targeting the splice site at the intron14/exon15 junction causing aberrant

splicing led to similar phenotypes, including ventriculomegaly, expanded melanophores (4 ng/nl, n = 200) and shortened photoreceptor outer segments as compared to control MO-injected larvae. Finally, using an anti-ninl antibody, we observed substantial decrease of Ninl protein on Western blots and on immuno-histochemistry of retinal cryosections for the ninl atgMO-injected larvae and milder decrease in both assays for the ninl ex15 spMO-injected larvae (Bachmann-Gagescu et al, companion manuscript). Injection of increasing amounts of a splice-blocking morpholino targeting dzank1 exon8 resulted in small eyes and severe pericardial edema at 4 dpf (S1a Fig, Fig 3c). In addition, dzank1 morphants showed impaired ambulatory activity as predicted before [20]. Based on the incidence of the observed phenotypes and non-quantitative RT-PCR analysis on RNA from morphant larvae (harvested at 2 and 4dpf; S1a and S1g Fig.) we determined that the optimal dose of the dzank1 ex8 spMO was 6 ng/nl. Co-injection of 150 pg/nl capped MO-resistant mRNA encoding human DZANK1 with 6 ng/nl dzank1 ex8 spMO rescued the observed ambulatory activity phenotype (n = 105, 2 biological replicates; S1b and S1e Fig). This observed ambulatory activity phenotype could be fully recapitulated by a second splice blocking morpholino targeting dzank1 exon4 (6 ng/nl, n = 162 out of 200 injected larvae from 2 biological replicates; S2 Fig), further indicating the specificity of the used morpholino. Subsequently, we evaluated the retinal morphology of dzank1 ex8 spMO-treated larvae (4 dpf; n = 40). While retinal lamination was unaffected, significantly shortened photoreceptor outer segments (OS) were observed as compared to controls, as highlighted by boron-dipyrromethene (bodipy) staining of membranes (Fig 3a'-3c' and 3h) (mean OS length 2.1+/-0.39 µm in morphants compared to 4.9+/-0.27 µm in wild-type, p<0.0001, unpaired Student's t-test, n> 10 larvae from each group in each of 2 biological replicates). The observed photoreceptor outer segment defects fully coincided with the ambulatory activity defects observed in dzank1 ex8 spMO-treated larvae and could be rescued as well (mean OS length in rescued larvae 3.0+/-0.36 µm as compared to 1.9+/-0.25 µm in dzank1 morphants (P = 0.01, unpaired Student's t-test, n = 13 larvae each group) and 3.5+/-0.25 µm in uninjected larvae (P = 0.3 (NS), unpaired Student's t-test, n = 12 larvae) (S1 Fig). These phenotypes could also be recapitulated by a second splice blocking MO targeting ninl ex15 or dzank1 ex4 (Bachmann-Gagescu et al., companion manuscript; S2 Fig). These observations are indicative for an essential role of both Ninl and Dzank1 in OS formation and/or maintenance.

To investigate whether there is a functional relationship between Ninl and Dzank1 in this process, sub-effective doses of dzank1 ex8 spMO (1 ng/nl) and ninl atgMO (0.5 ng/nl) were co-injected. While single injections with these sub-phenotypic amounts of MOs caused no discernible phenotypes (no body curvature defects or abnormal swimming behavior for ninl atgMO-injected larvae or no defects in ambulatory activity in dzank1
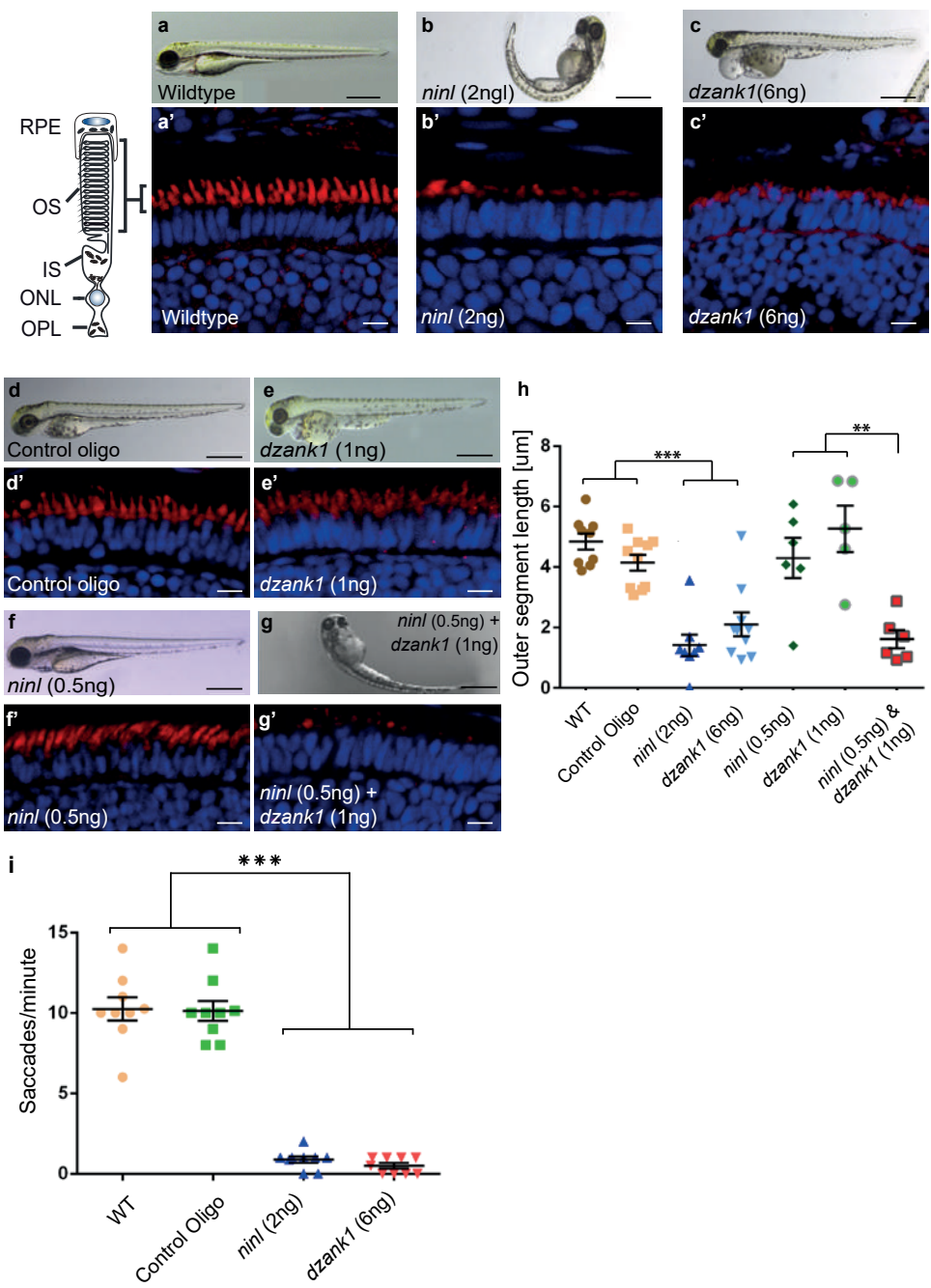
Figure 3. Morphological, functional and epistatic effects of ninl and dzank1 knockdown in zebrafish retina.

2.1

(a-c) Images of 4 dpf living zebrafish. Un-injected controls (WT) appear morphologically normal (a), while embryos injected with 2 ng of ninl atgMO display morphological defects, including ventrally curved body axis and small eyes (b). Embryos injected with 6 ng dzank1 ex8 spMO resulted in expanded melanophores, small eyes and severe pericardial edema (c) (a'-c') Retinal histology of 4 dpf zebrafish morphants examined by cryosections, where bodipy highlights the OS (red) and nuclei are stained with DAPI (blue) in all panels. Outer segments were shortened and dysmorphic in ninl and dzank1 morphants compared to wildtype larvae. (d-g) Ninl interacts genetically with dzank1. Injection of sub-effective dzank1 (1 ng/nl) MO (e') or ninl (0.5 ng/nl) MO (f') shows normal OS shape and length in morphologically normal appearing larvae, which could not be distinguished from un-injected embryos (WT) or control MO-injected larvae (d'). Combined injection of sub-effective concentrations of ninl (0.5 ng/nl) and dzank1 (1 ng/nl) MO together results in almost complete absence of OS (g'). (h) Quantification of Outer Segment length, shown as a scatter graph where each datapoint represents the mean OS length in one larva, revealed a significantly decreased length of outer segments in ninl (2ng/nl), dzank1 (6ng/nl) and ninl/dzank1 double morphants as compared to controls. Bars represent the mean value for each treatment group with the Standard error of the mean (SEM) ***P< 0.0001, ** P< 0.001, unpaired Student's t-test. (i) Analysis of the Opto Kinetic Response (OKR) showing severely decreased responses in larvae injected with 2 ng ninl atgMO or 6 ng dzank1 ex8 spMO (*** p< 0.0001, Student's t-test). Scale bars represent 500 μm (a-c and e-h) and 15 μm (a'-c' and e'-h'). RPE, retinal pigment epithelium; OS, Outer Segment; IS, Inner Segment; ONL, Outer Nuclear Layer; OPL, Outer Plexiform Layer.

ex8 spMO-injected larvae) (n = 200/group, 2 biological replicates; Fig 3e and 3f)), co-injection of both MOs resulted in a severely enhanced phenotype including defects in swimming behavior, small eyes and curved tails (Fig 3d–3g). Furthermore, photoreceptor outer segment length measurements on transverse sections of bodipy-stained retina demonstrated significantly impaired OS formation in double morphants (ninl atgMO 0.5 ng/nl + dzank1 ex8 spMO 1ng/nl; mean OS length 1.6+/-0.3 μm, n = 6), as compared to low dose single ninl atgMO-injected (0.5 ng/nl;mean OS length 4.3+/-0.66 μm, n = 6) and dzank1 ex8 spMO-injected larvae (1ng/nl; mean OS length 5.2+/-0.76 μm, n = 5), and as to control MO-injected (mean OS length 4.2+/-0.26 μm, n = 10) and uninjected (WT) larvae (mean OS length 4.8+/-0.28 μm, n = 9) (Fig 3a', 3d', 3e', 3f', 3g' and 3h; P<0.001, unpaired Student's t-test for pairwise comparison between double morphants and each low dose single morphant). These retinal defects in double morphants were similar to those quantified in larvae injected with the optimal doses of dzank1 spMO (6 ng/nl; 2.1+/-0.39 μm, n = 10; Fig 3c' and 3h) or ninl atgMO (2 ng/nl; 1.6+/-0.26 μm, n = 8; Fig 3b' and 3h) alone. The functional impact of these morphological changes in the morphant retinas was confirmed by measurements of the optokinetic response (OKR) [21, 22], which tests the ability of zebrafish larvae to visually track rotating stripes [23]. At 4 dpf, ninl and dzank1 morphant larvae displayed a grossly impaired OKR response (0–2 saccades per minute), in contrast to the normal OKR response (5–15 saccades per minute) of control morphants and un-injected larvae from the same clutch (mean number of saccades per minute = 10.3 +/- 0.7 in uninjected wild-type, 10.1 +/- 0.6 in control oligo injected, 0.5 +/- 0.2 in dzank1 morphant and 0.9 +/- 0.2 in ninl morphant larvae, n = 9/group; P<0.0001 for pairwise comparisons wildtype/control oligo vs each morphant, unpaired Student's t-test) (Fig 3h). Since spontaneous eye movements in the absence of a stimulus were occasionally registered in all MO-injected larvae, the loss of OKR response is not due to a defect in ocular muscular contraction, but to impaired visual function.
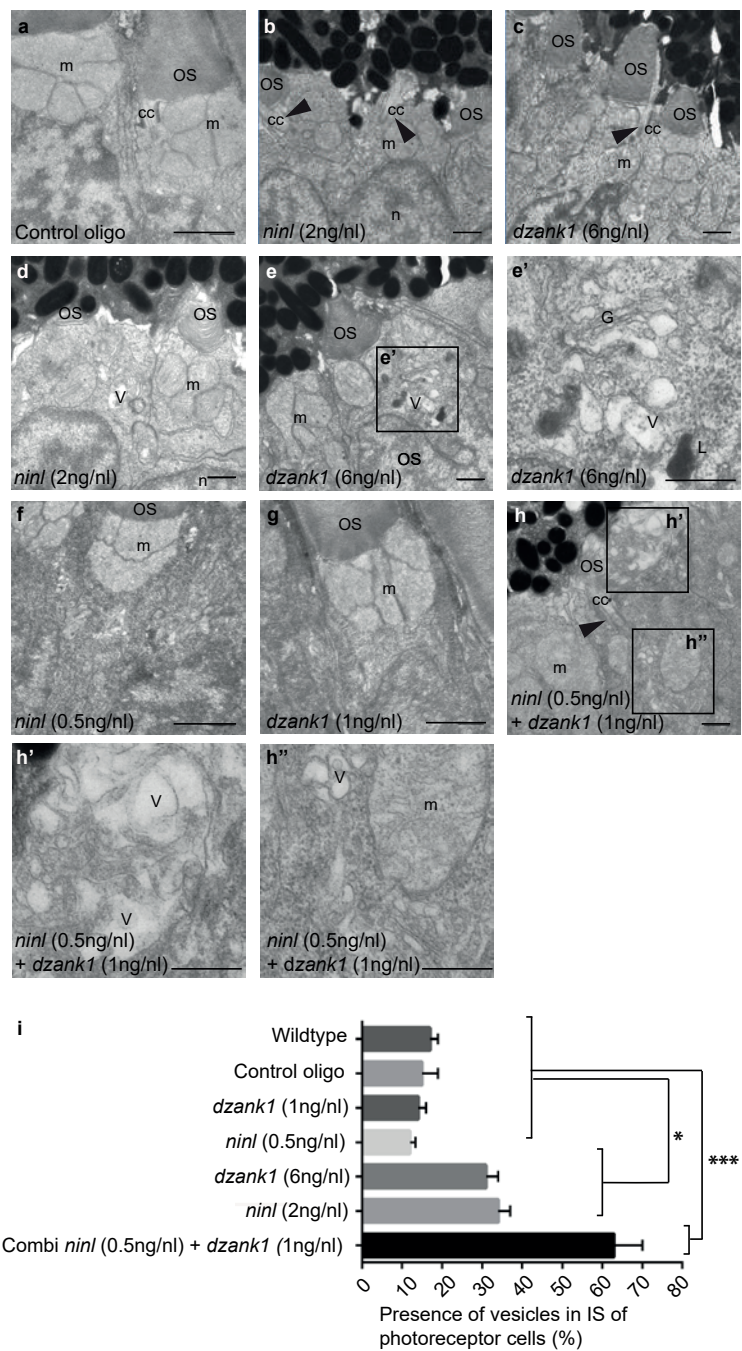
Figure 4. dzank1 and ninl knockdown leads to accumulation of vesicles and vacuoles in zebrafish photoreceptors.

Transmission electron microscopy of control (a), ninl knockdown larvae (b,d) and dzank1 knockdown larvae (c,e). Ninl and dzank1 morphants (b-e) demonstrate absent or shortened and dysmorphic outer segments (OS), whereas connecting cilia (CC) are still intact (arrowheads in b-c,h), and accumulation of vesicular structures (v), highlighted in the boxed area in e (e'). Sub-effective concentration of ninl (f) and dzank1 (g) MO-injection leads to a normal phenotype compared to control MO-injected larvae (a) and uninjected controls. Injection of combined sub-effective concentrations of dzank1 and ninl (h) MO leads to increased vesicle accumulation in OS (h') and inner segment (h''). (i) Analysis of the presence of vesicles in inner segments of photoreceptor of cells (%). On the Y—axis the different classes are indicated (minimum of 6 eyes per group). (* $P<0.01$ and *** $P<0.001$ Student's t-test). Larvae in all panels are 4 dpf. Scale bars represent 0.5 μm. OS: outer segment, CC: connecting cilium, m: mitochondria, n: nucleus, v: vesicular structures, G: Golgi system, L: lysosome.

2.3 Knockdown of *ninl* and *dzank1* leads to vesicle accumulation in photoreceptor cells

To obtain a more detailed insight into the role of Ninl and Dzank1 in OS morphogenesis, the retinal ultra-structure of ninl, dzank1 morphants and control larvae was studied by transmission electron microscopy (TEM) (for numbers see S5 Table). In control MO-injected embryos (4 dpf), the photoreceptor inner segments (IS) displayed compact ellipsoid regions with clustered mitochondria, a narrow myoid with a Golgi apparatus, while OS presented well-organized, nicely stacked disc structures (Fig 4a), as described for wild-type uninjected larvae [17, 24]. In contrast, in both ninl and dzank1 morphants, IS malformations were found including swollen Golgi complexes with enlarged and distended cisternae, accumulation of vesicle-like structures throughout the IS, large vacuoles and dispersed mitochondria. Occasionally, lysosomal structures were observed (Fig 4e'). OS were either absent, or disrupted. Ultra-structural characteristics of deviant OS were hampered elongation, accumulation of vesicles, polarization defects and deformed discs (Fig 4d and 4e'). Statistical analyses of these defects were based on quantification of the proportion of photoreceptor cells presenting with vesiculated inner segments in the different experimental groups (Fig 4i). No significant difference could be demonstrated between vesiculation in IS of larvae injected with sub-phenotypic doses of dzank1 (1 ng/nl) or ninl (0.5 ng/nl) MO (Fig 4f and 4g) as compared to control MO-injected (10 ng/nl) or wildtype (WT) zebrafish larvae. The percentage of IS in photoreceptors with vesicular structures and/or swollen Golgi complexes in dzank1 (6 ng/nl MO), ninl (2 ng/nl MO) as well as combined (dzank1 1 ng/nl and ninl 0.5 ng/nl) MO-injected zebrafish groups was significantly increased compared to WT and control MO-injected larvae ($P<0.01$, Student's t-test). The most significant vesicular increase was observed in the combined MO-injected (dzank1 and ninl) group (Fig 4h and 4h'') ($P<0.001$, Student's t-test).

2.4   NINL and DZANK1 associate specifically with complementary subunits of the cytoplasmic dynein 1 motor complex

Mass spectrometry (MS)-based quantitative proteomics was employed to gain further insights into the molecular basis of the defects observed in ninl and dzank1 morphants. N-terminally fused Strep/FLAG-tagged NINL$^{isoA/B}$ and DZANK1 together with their associated, native protein complexes were tandem-affinity-purified from HEK293T cells and the complex components identified by liquid chromatography coupled to tandem mass spectrometry (LC-MS/MS). Besides six actin-binding proteins (ARP1, ARP1B, ARP10, CAPZA1, CAPZA2 and CAPZB) and three subunits of Ca^{2+}/calmodulin-dependent protein kinase II (CaMKII) (CAMK2A, CAMK2D, and CAMK2G), the NINL-associated interactome contained multiple subunits of the cytoplasmic dynein 1-dynactin motor complex (DYNC1H1, DYNC1LI1, DYNC1LI2, DYNCI2, DYNLRB1, DCTN1-4, and DCTN6), which is involved in minus end–directed, microtubule-associated transport (Fig 5a, S2 Table). These results were confirmed by the GST pull-down from bovine retinal extracts in which DZANK1, several subunits of the cytoplasmic dynein 1-dynactin motor complex (DYNC1H1, DYNC1LI1, DCTN1, DCTN2 and DCTN4) and five dynactin-associated actin-binding proteins (ARP1B, ARP10, CAPZA1, CAPZA2 and CAPZB) were found to associate with GST-fused NINL^{isoB}_aa538-825 (S1 Table). We thus confirmed the previously described association of NINL with several subunits of the cytoplasmic dynein 1-dynactin motor complex [19]. Intriguingly, the DZANK1-associated protein complex exclusively contained the two cytoplasmic dynein 1 light chains, DYNLL1 and DYNLL2, which were absent from the NINL interactome. We confirmed the identified interaction between DZANK1 with DYNLL1 and DYNLL2 by reciprocal co-IP experiments in HEK293T cells. In addition, co-expression of mRFP-tagged DYNLL1 or DYNLL2 with eCFP-tagged DZANK1 in ciliated hTERT-RPE1 cells resulted in recruitment of the latter to the basal body and accessory centriole (S3 and S4 Figs). These results suggest that the cytoplasmic dynein 1 motor complex is composed of at least two sub-complexes: one DZANK1-associated sub-complex containing DYNLL1 and DYNLL2, and another NINL-associated sub-complex containing at least DYNC1H1, DYNC1LI1, DYNC1LI2, DYNCI2 and DYNLRB1. In order to better understand the orchestration and dynamics of the NINL-associated motor complex, we performed an elution profile analysis of SDS-induced sub-complexes by quantitative mass spectrometry (EPASIS) [25]. SF-TAP-tagged NINL$^{isoA/isoB}$ was over-expressed in HEK293T cells and affinity-purified using the FLAG moiety of the fusion tag. The native protein complex was sequentially treated with increasing SDS-concentrations to destabilize the interactions and thereby induce the elution of sub-complexes. Besides the dynactin submodule, which showed the most stable association with the NINL complex (S5c Fig; complete elution at ≥ 0.005% SDS) a second sub-module consisting of proteins from the cytoplasmic dynein 1 motor complex

[26] was identified (S5c Fig c; elution between 0.001 and 0.01% SDS). This dynein sub-module may dissociate in two additional sub-modules but this finding lacked statistical significance (S5–S8 Figs, S3 and S4 Tables). In addition, CLIP1 (= CLIP-170), PAFAH1B1 (= LIS1), ACAD11 and MRPS27 co-eluted with the dynein module, making them potentially novel candidate components of the dynein 1 motor complex.

2.1

2.5   Zebrafish Ninl and Dzank1 are required for intracellular dynein-based transport

Dynein 1 heavy chain 1 (dync1h1), encoding a subunit of the cytoplasmic dynein 1 motor complex which mediates minus-end-directed post-Golgi vesicle trafficking towards the basal body, is mutated in the zebrafish cannonball mutant [17]. Similar to our findings in ninl and dzank1 morphants, cannonball mutants form short rudimentary photoreceptor OS, show organelle positioning defects and display a severe accumulation of vesicles in the photoreceptor IS and OS and this phenotype could be recapitulated by a translation blocking morpholino against dync1h1 [17]. Sub-effective concentrations of this previously published dync1h1 MO (1 ng/nl) [17] in combination with the ninl atgMO (0.5 ng/nl) were co-injected and compared to single injected morphants, control MO-injected larvae and uninjected controls (n = 300/group from 2 biological replicates). At 4 dpf, quantification of OS lengths in each group was performed on bodipy-stained cryosections and revealed significantly shortened OS in larvae in the dync1h1 (3 ng/nl; mean OS length 1.95+/-0.4 µm, n = 5; Fig 5d', 5d" and 5h) and dync1h1/ninl morphant groups (1ng/nl + 0.5 ng/nl; mean OS length 1.413+/-0.2 µm, n = 13; Fig 5g', 5g" and 5h) as compared to uninjected controls (mean OS length 4.8+/-0.27 µm, n = 9; Fig 5b', 5b" and 5h), control MO-injected (10 ng/nl; mean OS length 4.2+/-0.26 µm, n = 10; Fig 5c', 5c" and 5h) and to both low-dose single dync1h1 MO-injected (1 ng/nl; mean OS length 3.6+/-0.44 µm, n = 13; Fig 5f', 5f" and 5h) and ninl atgMO-injected (0.5 ng/nl; mean OS length 4.3+/-0.66 µm, n = 6; Fig 5e', 5e" and 5h) groups (P<0.001; two tailed, unpaired Student's t-test on pairwise comparisons between double morphants and each of the single low-dose morphants), demonstrating a genetic interaction between ninl and dync1h1 and supporting a role for Ninl in cytoplasmic dynein 1-driven intracellular vesicle transport. In addition, localization of rhodopsin, which should be restricted to the OS, was aberrantly observed in the photoreceptor cell body in both ninl and dzank1 morphants (S9 Fig and Bachmann-Gagescu et al. co-submission.). The observed mislocalization of rhodopsin in these morphants could be explained by defects in intracellular transport. However it could also be the result of defects in OS development and a consequence of the absence of this structure. Although the OS of ninl morphants are severely affected, the connecting cilium of photoreceptor cells in ninl, dzank1 and ninl-dzank1 double morphants was found to be intact (arrow heads in Fig 4b, 4c and 4h), providing the
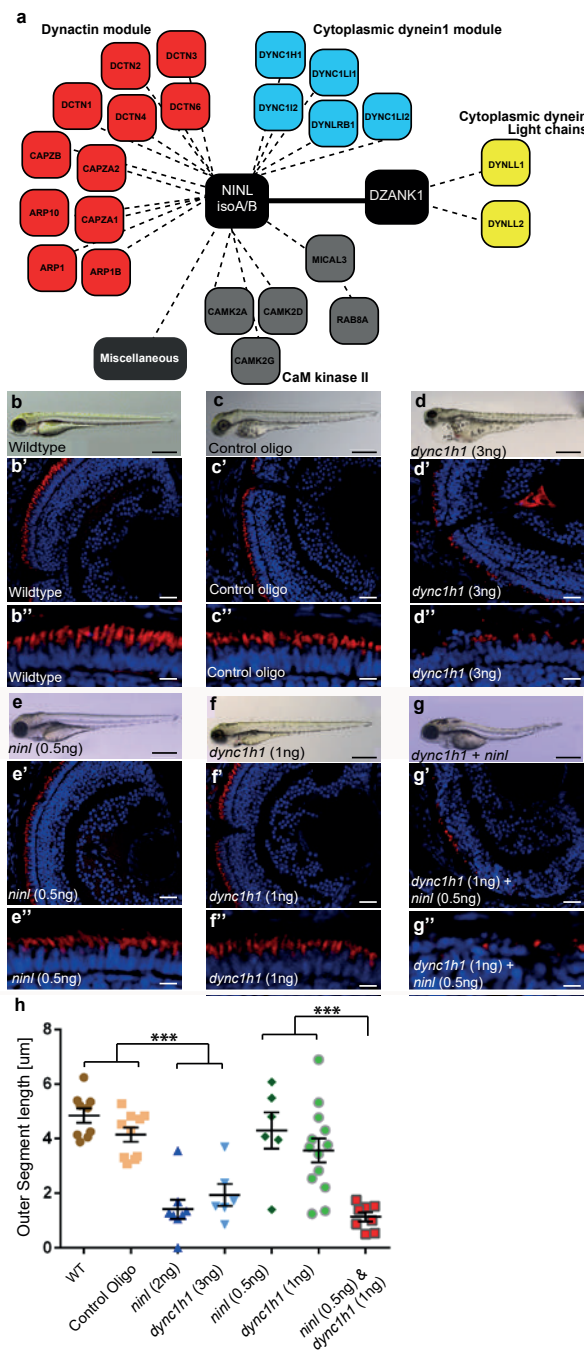
Figure 5. NINL and DZANK1 associate specifically with complementary subunits of the cytoplasmic dynein 1 motor complex.

2.1

(a) Strep-SILAC and TAP experiments show that DZANK1 interacts specifically with DYNLL1 and DYNLL2 (yellow). NINL associates with components of the dynactin complex (red) and with most components of the dynein 1 motor complex (blue), except for DYNLL1 and DYNLL2. The solid line between NINL and DZANK1 symbolizes a direct interaction, whereas the dashed lines stand for interactions determined by immune and affinity purifications. (b-g") Genetic interaction between ninl and dync1h1. MO-injection with a high concentration of dync1h1 (3 ng/nl) shows larvae with pericardial edema, small eyes and short OS (d-d"). MO-injection of sub-effective concentrations of ninl (0.5 ng/nl) (e-e") or dync1h1 (1 ng/nl) (f-f") generates larvae with a normal phenotype and normal OS length, compared to wildtype larvae (b-b") and control MO-injected larvae (c-c"). The combination of sub-effective MO concentrations of ninl (0.5 ng/nl) and dync1h1 (1 ng/nl) results in short larvae and virtual absence of outer segments (g-g"). All larvae are 4 dpf. Panels b'-d" and e'-g" are retinal cryo-sections stained with bodipy (red) to highlight the outer segments and DAPI to stain the nuclei. (h) Quantification of photoreceptor outer segment length revealed a significantly decreased length of outer segments in dync1h1 (3ng/nl) and dync1h1/ninl double morphants as compared to controls (*** P< 0.0001; two-tailed, unpaired Student's t-test). Scale bars represent 500 μm (b-g), 50 μm (b'- g') and 15 μm (b"-g").

opportunity to test the localization of proteins to this ciliary compartment regardless of the presence of an outer segment. USH2A, a previously published interaction partner of NINL, is a transmembrane protein that is synthesized in the IS and subsequently transported in TGN-derived vesicles towards the base of the connecting cilium. USH2A was previously shown to localize in the peri-ciliary region, which should be independent of the presence of the OS [27]. Therefore, a defect in USH2A localization would likely be due to impaired post-Golgi dynein-based trafficking. Using a zebrafish-specific anti-Ush2a antibody, we observed a strongly reduced immunofluorescent signal in ninl and dzank1 morphants (4 dpf), as compared to control MO-injected larvae (4 dpf) (Fig 6a'–6d'). The localization of centrin, which was used as a marker for the connecting cilium, was unaffected in both controls and morphants (Fig 6a'''–6d'''). Together, these data indicate a defect in the transport of vesicle-bound transmembrane proteins in ninl and dzank1 morphants.

To determine whether Ninl and/or Dzank1 are required for other dynein-based intracellular transport processes, we monitored dynein 1-mediated melanosome transport in zebrafish skin. Zebrafish alter their skin pigmentation by trafficking melanosomes within melanophores. The melanosome, a lysosome-related organelle, can be shuttled bi-directionally between the cell periphery and the peri-nuclear region by two microtubule-based molecular motors, kinesin II (anterograde) and dynein 1 (retrograde). Pigment aggregation (retrograde transport) can be stimulated within minutes upon treatment with epinephrine [28]. In the melanosome transport assay, 5 dpf larvae are dark-adapted to display maximum melanophore dispersion (Fig 7a). After addition of epinephrine, the melanosomes rapidly contract and can be visually evaluated for reduction in pigment dispersion (Fig 7a'–7a"). The endpoint is apparent when pigmentation pattern reflects peri-nuclear accumulation of melanosomes (Fig 7a'). A rapid melanosome contraction was seen in control MO-injected and un-injected larvae (Fig 7a–a" and 7d) ($\Delta T = 1.55$ min and $\Delta T = 1.30$ min respectively; n = 20/group), whereas ninl and dzank1 morphants demonstrated significantly delayed dynein

1-mediated melanosome retraction (ΔT = 15.42 min and ΔT = 23.62, n = 20; P<0.001; Student's t-test (two tailed, unpaired), Fig 7b–7c‴ and 7d), which is indicative for impaired dynein 1-mediated retrograde transport. Taken together, our findings suggest that the Ninl-Dzank1-cytoplasmic Dynein 1 complex is required for the intracellular transport of organelles and vesicles, and is essential for the photoreceptor's OS formation, maintenance and function.
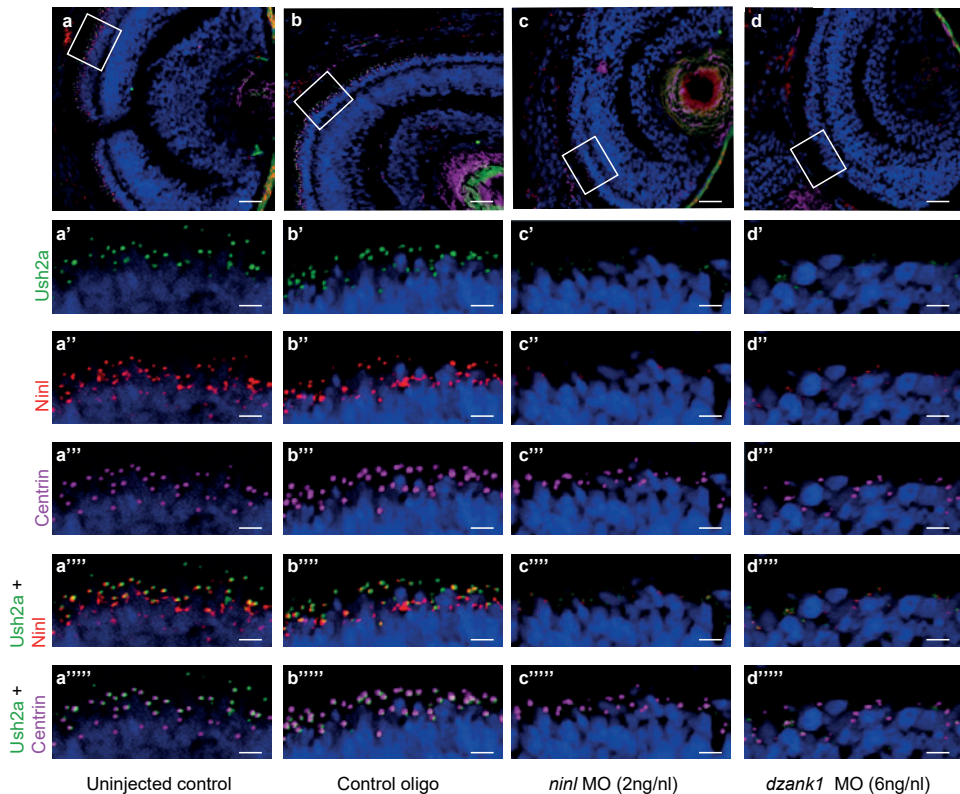
Figure 6. Impaired Ush2a transport in dzank1 and ninl morphants.

(a-d) Overview of Ninl and Ush2a localization in cryo-sections of 4 dpf zebrafish retina using anti-Ninl (red signal), anti-Ush2a (green signal) and the basal body marker anti-Centrin (cyanid signal). In all images the nuclei are counterstained with DAPI (blue signal). (a-a‴') Un-injected wildtype, (b-b‴') 10 ng/nl control MO-injected, (c-c‴') 2 ng/nl ninl MO-injected and (d-d‴') 6 ng/nl dzank1 MO-injected zebrafish retinas. (a'-d') Anti-Ush2a staining (green signal) is strongly reduced in dzank1 and ninl morphants (c'-d'), while Ush2a is clearly present in wildtype and control MO-injected larvae. (a''-d''). Specific Ninl-immunofluorescence (red signal) was largely abolished in ninl morphants and reduced in dzank1 morphants. (a‴-d‴) Centrin (cyanide signal) was observed in wildtype, un-injected control and in both ninl and dzank1 morphants. (a‴'-d‴') Co-localization of Ush2a and Ninl (yellow signal) was observed in wildtype and control MO-injected larvae. (a‴''-d‴'') Co-localization of Ush2a and Centrin (yellow signal) was seen in all images (WT, Control Oligo, ninl and dzank1 morphants), despite strong reduction of Ush2a immunofluorescence in ninl and dzank1 morphants. Scale bars represent 15 μm, except for (a-d) in which the scale bars represent 50 μm.

2.1
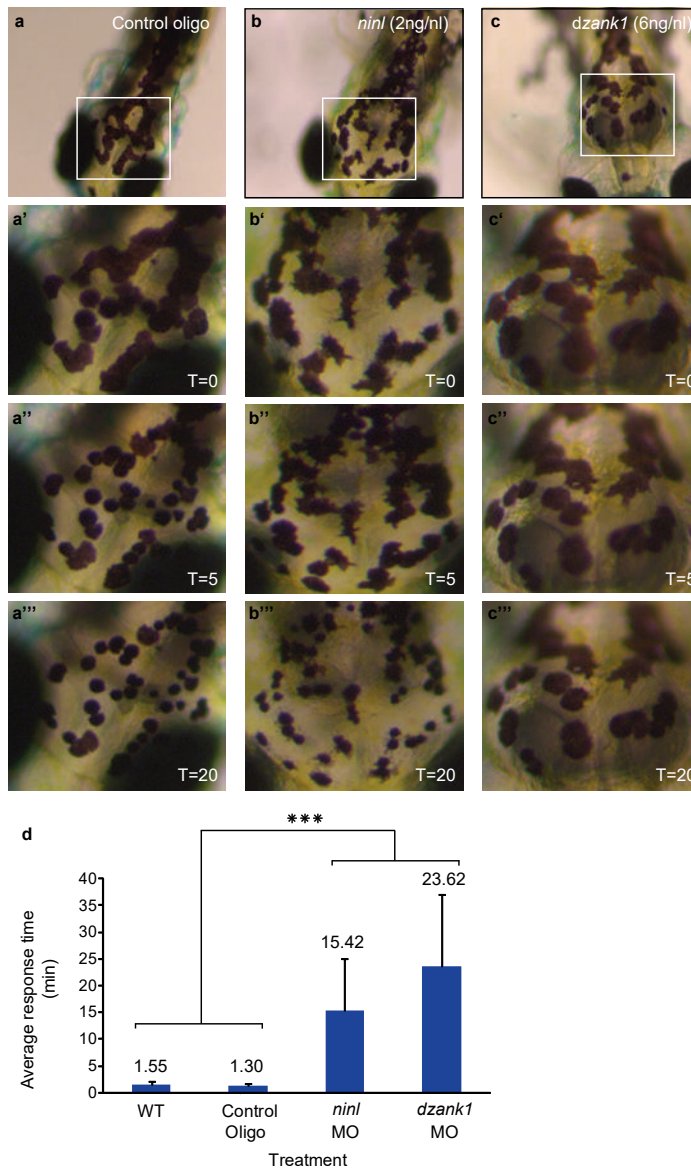
Figure 7. ninl and dzank1 knockdown results in epinephrine-induced melanosome retraction delay.

Control MO-injected larvae (10 ng/nl; n = 20) at 5 dpf (a-a'''), ninl morphant (2 ng/nl; n = 20) (b-b''') and dzank1 morphant (6 ng/nl; n = 20) (c-c'''). White Box denotes the area at higher magnification (40x) (a'-c''). (a-c') Melanosome pattern of the different larvae before treatment, (a''-c'') 5 min after epinephrine addition and (a'''- c''') 20 min after epinephrine addition, t represents time in minutes. (d) Graphical representation with error bars (standard deviation) demonstrating a significant delay of epinephrine-induced melanosome retrograde trafficking compared with wild-type and control MO-injected (10 ng/nl) larvae. Treatment (control, ninl- or dzank1-morphants) is noted on the x-axis and average response time in minutes is noted on the Y-axis. ***: P<0.001 (two-tailed, unpaired Student's t-test).

3. DISCUSSION

In this study, a central role for NINL and its novel interaction partner DZANK1 is identified in vesicle transport in photoreceptor cells. We demonstrate that NINL and DZANK1 associate with complementary subunits of the cytoplasmic dynein 1 motor complex and that this complex consists of at least two submodules. In photoreceptor cells, this motor complex has been implicated in post-Golgi vesicle trafficking and organelle positioning [14, 17]. In line with this function, in vivo studies in the zebrafish demonstrate defects in post-Golgi trafficking as revealed by delayed cytoplasmic dynein 1-regulated melanosome transport, defective photoreceptor outer segment formation, abnormal vesicle accumulation within the photoreceptor inner segments and mislocalization of rhodopsin and Ush2a in both ninl and dzank1 morphants.

Cytoplasmic dynein 1 is fundamentally important for embryonic development. Dynein 1 heavy chains are essential for the formation of the motor complex and their absence leads to very early embryonic lethality in mice before E8.5 [29]. In contrast, larvae of the zebrafish cannonball (cnb) mutant lacking Dync1h1 undergo relatively normal early development and remain indistinguishable from wild-type siblings until approximately 3.5 dpf. This remarkable difference between mouse and zebrafish mutants may be explained by the presence of wild-type maternally-derived (yolk-associated) mRNA in zebrafish embryos [30]. Cnb larvae eventually show a reduced eye size, present with small rudimentary photoreceptor outer segments and expanded skin melanophores, show severe organelle positioning defects and die between 6 and 8 dpf [17]. The phenotype of zebrafish depleted for Ninl is remarkably similar to that of the cnb mutant, with small eyes, mispositioned organelles, retinal dystrophy, and expanded melanophores. These overlapping phenotypic characteristics in combination with the observed genetic interaction in the retina between ninl and dync1h1 suggest that the ninl morphant phenotype is caused by dysfunctional cytoplasmic dynein 1-mediated transport.

Mice lacking Dync1li1, a light-intermediate chain subunit of dynein 1, which is structurally less important than heavy chains, survive into adulthood [31]. Their photoreceptors do, however, lack outer segments due to blocked transport of TGN-derived vesicles towards the basal body. In contrast to the ninl morphants, dzank1 morphants show a much milder phenotype and do not present curved bodies or major early developmental defects. DZANK1 associates specifically with two structurally less important dynein 1 light chains, which might explain the less severe phenotype of dzank1 morphant zebrafish larvae. Nonetheless, photoreceptor cells of both ninl and dzank1 morphant zebrafish larvae display severely shortened outer segments, disruption of mitochondria organisation and accumulation of vesicles within the inner segments. Given that photoreceptors have extremely high transport requirements due to the significant daily renewal of their outer segments, they are predicted to be more sensitive to defects in

intracellular transport, which could explain why loss of dzank1 results predominantly in a photoreceptor phenotype.

The physical position and role of NINL and DZANK1 in the cytoplasmic dynein 1 motor complex remains unknown. Up to now, tandem affinity purification assays from HEK293T cells using different subunits of this motor complex as bait never identified peptides of NINL or DZANK1 (S2 Table). The most likely explanation for this is that NINL and DZANK1 are not expressed in these cells or are expressed only at very low levels. To get the first insights into the dynamics and orchestration of the NINL-associated dynein 1 motor complex, we performed an elution profile analysis of SDS-induced sub-complexes by quantitative mass spectrometry (EPASIS). Despite the fact that the dynein module shows a tendency of being built up of two distinct sub-modules, the statistical significance is lacking. CLIP1 (= CLIP-170), PAFAH1B1 (= LIS1), ACAD11 and MRPS27 co-eluted with the dynein module, making them potentially novel candidate components of the dynein 1 motor complex. LIS1 was previously found to interact with cytoplasmic dynein 1-dynactin [32] and CLIP1 [33] in order to keep dynein in a persistent microtubule-bound state [34]. The role of ACAD11 and MRPS27 in dynein 1 function or dynamics needs to be determined. The dynactin complex was identified as a distinct sub-complex which was most strongly associated with NINL in the EPASIS essay. The lack of clear OS defects in zebrafish mok/dctn1a and dctn1b mutants [17, 35, 36] however, implies that dynein 1 functions independently of dynactin in outer segment morphogenesis. Indeed it was reported that the binding of dynactin1 to dynein 1 is non-essential for the ability of dynein 1 to bind stably to rhodopsin transport vesicles in vitro [14]. Therefore it can be concluded that the ocular phenotypes observed in the ninl morphant are most likely caused by a non-functional dynein 1 complex rather than dysfunction of the dynactin complex.

We previously described the association of NINL[isoB] with USH2A [18], a protein known to be essential for photoreceptor homeostasis in mice [27, 37]. The retinal defects observed in ninl morphants are more severe than those observed in the Ush2a knockout mouse model, which displays intact outer segments and late-onset mild photoreceptor degeneration [27]. This comparison suggests a transport function for NINL[isoB] upstream of USH2A towards the apical inner segment. The absence of Ush2a at the photoreceptor periciliary region of ninl morphants is in line with this hypothesis.

DZANK1 protein sequence analysis predicted the presence of two ZNF_RBZ domains and their interaction with RanGDP rather than their involvement in transcription. Ran is an abundant Ras-like GTPase, which plays a role in multiple cellular processes, including modulation of nucleo-cytoplasmic transport of macromolecules larger than ~40 kDa across the nuclear envelope [38]. Further, it has been proposed that a similar complex, consisting of Ran, Ran-binding proteins and importins/exportins plays a role

in regulating import of cargo at the base of the cilium [39] and that RanBP2 is involved in processing or transport of opsin [40]. Since the ZNF domains of DZANK1 are highly homologous to the functional domains of RanBP2, DZANK1 might be involved in transport of opsin as well. The observed mislocalization of rhodopsin in photoreceptor cells of dzank1 morphant zebrafish larvae is in line with this. Moreover, a role for DZANK1 in opsin transport and subsequent ciliary entry creates an attractive functional connection between DZANK1 and the Usher protein network, members of which have been suggested to act in opsin vesicle docking at the periciliary region and subsequent transport in the connecting cilium and calyceal processes [41, 42].

In summary, our study provides a deeper insight into the tissue-specific dynamics of the cytoplasmic dynein 1 motor complex, and supports an essential role for this complex in close connection to NINL and DZANK1 in post-Golgi vesicle transport of selective cargo in zebrafish photoreceptor cells.

4. METHODS

4.1 Ethics statement

Animal experiments were conducted in accordance with the Dutch guidelines for the care and use of laboratory animals, with the approval of the Animal Experimentation Committee (Dier Experimenten Commissie [DEC]) of the Royal Netherlands Academy of Arts and Sciences (Koninklijke Nederlandse Akademie van Wetenschappen [KNAW] (Protocol # RU-DEC 2012–301).

4.2 Yeast two-hybrid interaction assay

To identify the interacting regions between DZANK1 and NINL[isoA/B], a GAL4-based Y2H screen (HybriZAP, Stratagene, La Jolla, CA, USA) was used as previously described [43, 44]. Accession IDs: NINL[isoA] (Q9Y2I6), NINL[isoB] (XP_005260736), DZANK1 (Q9NVP4), DYNLL1 (NP_001032584), DYNLL2 (Q96FJ2).

4.3 Localization studies in cells

The cellular (co)-localization of DZANK1, NINL[isoB], DYNLL1 and DYNLL2 was determined by co-transfecting hTERT-RPE1 cells on glass slides, with pcDNA3-mRFP and pcDNA3-eCFP. DZANK1 FL, NINL[isoB], DYNLL1 and DYNLL2 were transfected using Effectene Transfection Reagent (Qiagen, Netherlands) according to manufacturer's instructions. After 48 hours transfection, cells were washed with PBS, fixed with 4% paraformaldehyde (PFA) and mounted with Vectashield containing DAPI (Vector Laboratories, Inc., UK). Images were taken with an Axioplan2 Imaging fluorescence microscope (Zeiss) and processed using Adobe Photoshop version 8.0 (Adobe Systems, USA).

4.4   GST pull-down

The GST-fusion proteins were produced by transforming Escherichia coli BL21-DE3 with plasmid pDEST15-NINL (538aa to 825aa), as previously described [43]. Strep/FLAG-tagged DZANK1 or Strep/FLAG-tagged NINL[isoB] were produced by transfecting HEK293T cells with plasmids encoding N-SF-TAP-hsDZANK1 or NINL[isoB], respectively, using the transfection reagent (PEI; Polyethylenimine), according to the manufacturer's instructions. The GST pull-down assay was performed as described previously [43]. For GST pull-down experiments from retinal extracts, retinas were dissected from fresh bovine eyes obtained from the local slaughter house. Retinas were homogenated by sonication on ice for two times 30 s in extraction buffer [10 mM HEPES (pH 7.9), 10 mm NaCl, 3 mm $MgCl_2$, freshly added 1 mm DTT, 1 mm Na_3VO_4], supplemented with complete protease inhibitor cocktail (Roche Diagnostic). Retinal extracts were incubated overnight at 4°C with the GST fusion proteins immobilized on glutathione sepharose 4B beads. GST fusion proteins were eluted from the glutathion sepharose 4B beads with 100 mM reduced Glutathione (GSH) in 50mM TRIS-HCl (pH 8.0) overnight. Proteins were subsequently precipitated and analyzed by mass spectrometry analysis as described below.

4.5   Co-immunoprecipitation in HEK293T cells

HA-tagged NINL and DYNLL1 were expressed by using the mammalian expression vector pcDNA3-HA/DEST, the 3xHA-tagged DYNLL2 by using p3xHA_CMV/DEST, Strep/FLAG-tagged DZANK1 by using pSF-NTAP/DEST and LRRK2 by using p3xFLAG/DEST from the Gateway cloning system (Invitrogen, USA). HEK293T cells were co-transfected, using Effectene Transfection Reagent (Qiagen, USA) according to the manufacturer's instructions. Twenty-four hours after transfection, the cells were washed with PBS and subsequently lysed in IP lysis buffer (50 mM Tris-HCL pH 7.5, 150 mM NaCl, 1% Triton-X-100 supplemented with complete protease inhibitor cocktail (Roche, Germany)) on ice. HA-tagged molecules were immune-precipitated from cleared lysates at 4°C overnight. Protein-antibody complexes were coupled to ProtA/G beads (Santa Cruz) for 2 hours at 4°C. After incubations, the beads were pelleted and washed three times with lysis buffer. Beads were boiled and proteins were resolved on SDS-PAGE. For western blotting, proteins were electrophoretically transferred into nitrocellulose membranes, blocked with 5% non-fat dry milk (Biorad) in PBS-T (PBS supplemented with 0.1% Tween) and analyzed with the appropriate primary and secondary antibodies in 0.5% non-fat dry milk in PBS-T. After 4 washes in lysis buffer, the protein complexes were analyzed on immunoblots using the Odyssey Infrared Imaging System (LI-COR, USA). As secondary antibodies, IRDye800 goat-anti-mouse IgG and Alexa Fluor 680 goat-anti-rabbit IgG were used.

4.6   Antibodies

The monoclonal antibodies directed against Centrin (1:100), Millipore, lot nr: 04–162 and the polyclonal antibodies directed against the cytoplasmic region of USH2A^{isoB} (1:100), Novus Biological, lot nr: T00620A02 have been described previously [43, 45]. For the rhodopsin staining anti-rhodopsin, clone 4D2 Millipore lot nr: 2038649 (1:1000) was used.

For Western blot and immunohistochemical analyses, antibodies directed against human NINL (aa406-455) were purchased from LSBio, cat. No. LS-C201509 (1:100). Antibodies against the C-terminal region of zebrafish Ninl, which were raised in guinea pigs against a GST-fusion protein, encoding a peptide consisting of 403aa to 591aa (Genbank NP_001268727) were used for immunohistochemical analyses. The cDNA, encoding this peptide was amplified by using the forward and reverse primers 5'-GACCAAGCCTGTCAAGAGCG-3' and 5'-GCCCTGAGACTTCAACAAC-3', respectively. The secondary antibodies were goat anti-guinea pig Alexa Fluor 488 and Alexa Fluor 568, goat anti-rabbit Alexa Fluor 488, goat anti-mouse Alexa Fluor 488, Alexa Fluor 568 and Alexa Fluor 647; (all used at a dilution of 1:500, all from Molecular Probes-Invitrogen Carlsbad, CA, USA). The latter were diluted together with DAPI in block buffer (2% BSA and 10% Normal Goat serum in PBS).

4.7   Zebrafish

Experimental procedures were conducted in accordance with international and institutional guidelines. Wild type adult Tupfel Long fin (TLF) zebrafish were used. The zebrafish eggs were obtained from natural spawning of wild-type breeding fish. Larvae were maintained and raised by standard methods [46]. Translation-blocking ninl (5'-CATCCTCGTCCATCCCACCACATAC-3'), exon15 splice-blocking ninl (5'-CCCAACACTAAAGAGATACACCAAT-3'), exon4 splice-blocking dzank1 (5'-CGGCCATCACTGCATCACATTACAA-3') exon8 splice-blocking dzank1 (5'- AGGACATCTTTAGAATGATAGACGT-3') and translation blocking dync1h1 (5'- CGCCGCTGTCAGACATTTCCTACAC-3') morpholinos (MOs) were designed by Gene Tools Inc. (USA) and diluted to the appropriate concentration in deionized, sterile water, supplemented with 0.5% phenol red. To determine the most effective dose of the ninl, dzank1 and dync1h1 MOs, 1 nl of diluted MO (containing 2,4,6,8 and 10 ng) was injected into the yolk of one- to two-cell-stage embryos using a Pneumatic Picopump pv280 (World Precision Instruments). A minimum sample size of 50 larvae was used for every condition. After injection, embryos were cultured in E3 embryo medium (5 mM NaCl, 0.17 mM KCl, 0.33 mM CaCl$_2$, 0.33 mM MgSO$_4$, supplemented with 0.1% methylene blue) at 28°C and subsequently phenotyped at 4 dpf (days post fertilization). Injected embryos were classified into two classes of phenotypes based on the relative severity as compared to age-matched, standard control (5'-CCTCTTACCTCAGTTACA

2.1

ATTTATAC-3'; Gene Tools Inc, USA) MO-injected (10 ng) embryos of the same clutch. Images were taken with an Axioplan2 Imaging fluorescence microscope (Zeiss, Germany) equipped with a DC350FX camera (Zeiss, Germany). To determine the efficiency of splice-blocking, RNA was isolated from 50 control MO injected and 50 dzank1- (and ninl-) splice MO-injected embryos (2 dpf) using the RNeasy mini kit (Qiagen) according to manufacturer's instructions. Here, 500 ng of total RNA was used to produce first-strand cDNA. Reverse transcription was performed using the Superscript III cDNA synthesis kit (Life Technologies) according to the manufacturer's instructions. Subsequently, PCR analysis was performed. Primers used for the analysis of ninl exon15 morphants are 5'-AAGTATGATGGCCTGGATGC-3' and 5'-GAGATGTCCTTCCGCTCAAC-3'; primers used for the analysis of dzank1 exon4 morphants are 5'-GGCAGCACCTCAAATAATCC-3' and 5'-CTGAAGGTCGATGGCTAAGG-3'; primers used for the analysis of dzank1 exon8 morphants are 5'-CTCGCTTGACAGCACAAAAC-3' and 5'-AAAACAGGTCTGGCTTGTCG-3'. Obtained fragments were extracted from a 1% agarose gel using the Nucleospin gel extraction kit (Machery Nagel, USA) and Sanger sequenced. For histological analysis of zebrafish, larvae were fixed in 4% PFA in PBS at 4°C overnight. Embryos were rinsed with PBS and infiltrated in 10% sucrose solution in PBS for two hours. Embryos were positioned (ventral side downwards) in Tissue Tek (Sakura), rapidly frozen in melting isopropyl alcohol and sections (7 μm thickness along the lens/optic nerve axis) were made. Immunohistochemistry was performed using retina sections, derived from four-to-six day old morphants and age-matched control oligo MO-injected zebrafish. The bodipy staining was performed on 5 day old larvae. The sections were washed twice in PBS for 5 minutes, permeabilized with 0.5% triton-x-100 in PBS for two times 10 minutes and followed by three washing steps with PBS for 5 minutes. Sections were then incubated for 10 minutes with bodipy (1:100), DAPI and phalloidin/actin (monoclonal Actin, Abcam lotnr: Ab328–500 (1:400)) diluted in PBS. Subsequent photoreceptor outer segment length measurements were performed blinded as to their injection status (using ImageJ). Equivalent single confocal sections through each eye were selected and the outer segments from 10 adajcent photoreceptors were measured and averaged for each larvae. P-values were calculated using Student's t-test (two tailed, unpaired).

4.8   Affinity purifications of protein complexes

HEK293T cells were cultured as described previously [47]. For SILAC experiments, HEK293T cells were grown in SILAC DMEM (PAA), supplemented with 3 mM L-Glutamine (PAA), 10% dialyzed fetal bovine serum (PAA), 0.55 mM lysine and 0.4 mM arginine. Light SILAC medium was supplemented with $^{12}C_6$, $^{14}N_2$ lysine and $^{12}C_6$, $^{14}N_4$ arginine. Heavy SILAC medium was supplemented with either $^{13}C_6$ lysine and $^{13}C_6$, $^{15}N_4$ arginine or $^{13}C_6$, $^{15}N_2$ lysine and $^{13}C_6$, $^{15}N_4$ arginine. 0.5 mM proline was added to all SILAC media to

prevent arginine to proline conversion. All amino acids were purchased from Silantes. For DNA transfections, HEK293T cells were seeded, grown overnight, and then transfected using PEI.

4.9   Tandem affinity purification

HEK293T (human embryonic kidney, ATCC) cells were transfected for 48 hours with either SF-TAP-NINL, SF-TAP-DZANK1, using polyethyleneimine (PEI, Polysciences) as a transfection reagent. Following transfection, cells were lysed in lysis buffer containing 30 mM Tris–HCl (pH 7.4), 150 mM NaCl, 0.5% Nonidet-P40 (NP40), freshly supplemented with protease inhibitor cocktail (Roche), phosphatase inhibitor cocktail II and III (Sigma), for 20 minutes at 4°C. The Streptavidin- and FLAG-based tandem affinity purification steps were performed as previously described [47, 48]. 5% of the final eluate was evaluated by SDS-PAGE followed by silver staining, according to standard protocols, while the remaining 95% were subjected to protein precipitation with chloroform and methanol. Protein precipitates were subsequently subjected to mass spectrometry analysis and peptide identification as previously described [25].

4.10   One-step Strep affinity purification

For SILAC experiments, one step Strep purifications of SF-TAP-tagged proteins and associated protein complexes was performed as described earlier [49]. HEK293T cells, transiently expressing the SF-TAP-tagged constructs were lysed in lysis buffer, containing 0.5% Nonidet-P40, protease inhibitor cocktail (Roche) and phosphatase inhibitor cocktails II and III (Sigma-Aldrich) in TBS (30 mM Tris-HCl (pH 7.4), 150 mM NaCl), for 20 minutes at 4°C. After sedimentation of nuclei at 10,000 x g for 10 minutes, the protein concentration was determined by a Bradford assay, before equal amounts of each lysate were transferred to Strep-Tactin-Superflow beads (IBA) and were incubated for one hour at 4°C on an end-over-end shaker. Then, the resin was washed three times with wash buffer (TBS containing 0.1% NP-40, phosphatase inhibitor cocktail II and III). The protein complexes were eluted by incubation for 10 minutes in Strep-elution buffer (IBA). The eluted samples were concentrated using 10 kDa cut-off VivaSpin 500 centrifugal devices (Sartorius Stedim Biotech) and pre-fractionated using 1D-SDS-Page. Afterwards, the samples were subjected to in-gel tryptic cleavage as described elsewhere [50].

4.11   Protein complex destabilisation

For EPASIS, SF-TAP-tagged NINL was over-expressed in HEK293T cells as described above. After 48 hours, cells were lysed as described for SF-TAP analysis and the cleared lysates were incubated with anti-FLAG-M2 agarose resin for 1h. After three washes

with wash buffer (TBS containing 0.1% Tergitol-type NP-40 and phosphatase inhibitor cocktails II and III, Sigma-Aldrich), the resin was incubated at 4°C for three minutes with each concentration of SDS (0.001%, 0.005%, 0.01% and 0.02%) in SDS-elution buffer (TBS containing phosphatase inhibitor cocktails II and III). Afterwards, a final elution step with FLAG peptide (200 μg/ml; Sigma-Aldrich) in wash buffer was performed. After every elution step a single wash step was performed. The flow-through was collected and precipitated by methanol-chloroform, before being analyzed by LC-MS/MS.

4.12 Mass spectrometry and data analysis

LC-MS/MS analysis was performed on an Ultimate3000 nano RSLC system (Thermo Scientific) coupled to a LTQ Orbitrap Velos or to an LTQ OrbitrapXL mass spectrometer (Thermo Scientific) by a nano spray ion source. Tryptic peptide mixtures were automatically injected and loaded at a flow rate of 6 μl/min in 0.1% trifluoroacetic acid in HPLC-grade water onto a nano trap column (75 μm internal diameter (i.d.) × 2 cm, packed with Acclaim PepMap100 C18, 3 μm, 100 Å; Thermo Scientific). After five minutes, peptides were eluted and separated on the analytical column (75 μm i.d. × 25 cm, Acclaim PepMap RSLC C18, 2μm, 100 Å; Thermo Scientific) by a linear gradient from 2% to 35% of buffer B (80% aceto-nitrile and 0.08% formic acid in HPLC-grade water) in buffer A (2% aceto-nitrile and 0.1% formic acid in HPLC-grade water) at a flow rate of 300 nl/min over 33 minutes for EPASIS samples, respectively over 80 minutes for SF-TAP and SILAC samples. Remaining peptides were eluted by a short gradient from 35% to 95% buffer B in 5 minutes. The eluted peptides were analyzed by a LTQ Orbitrap Velos or a LTQ Orbitrap XL mass spectrometer. From the high resolution MS pre-scan with a mass range of 300 to 1500, the ten most intense peptide ions were selected for fragment analysis in the linear ion trap if they exceeded an intensity of at least 200 counts and if they were at least doubly charged. The normalized collision energy for CID was set to a value of 35% and the resulting fragments were detected with normal resolution in the linear ion trap. The lock mass option was activated; the background signal with a mass of 445.12002 as lock mass. Every ion selected for fragmentation, was excluded for 20 seconds by dynamic exclusion. Non-quantitative MS/MS data were analyzed, using Mascot (version 2.4, Matrix Science, Boston, MA, USA). Mascot was set up to search the human subset of the Swiss Prot database (Release 2013_12, 20274 entries), assuming trypsin as the digestion enzyme. Mascot was searched with a fragment ion mass tolerance of 0.5 Da and a parent ion tolerance of 10.0 PPM. Oxidation of methionine and was specified as variable modification, iodoacetamide derivative of cysteine as fixed. The Mascot results were loaded in Scaffold (version Scaffold_4, Proteome Software Inc., Portland, OR) to validate MS/MS based peptide and protein identifications. Peptide identifications were accepted if they could be established at greater than 95.0% probability as specified by

the Peptide Prophet algorithm [51]. Protein identifications were accepted if they could be established at greater than 99.0% probability and contained at least two identified peptides. Protein probabilities were assigned by the Protein Prophet algorithm [52]. Proteins, which contained similar peptides and could not be differentiated based on MS/MS analysis alone, were grouped to satisfy the principles of parsimony.

For SILAC experiments, all acquired spectra were processed and analyzed, using the MaxQuant software [53] (version 1.3.0.5) and the human subset of the human proteome reference set, provided by SwissProt (release 2012_01 534,242 entries) was used for peptide and protein identification. Cysteine carbamidomethylation was selected as fixed modification, methionine oxidation and protein acetylation were allowed as variable modifications. The peptide and protein false discovery rates were set to 1%. Contaminants like keratins were removed. Proteins, identified and quantified by at least two unique peptides were considered for further analysis. The significance values were determined by Perseus tool (part of MaxQuant), using significance A. Label-free quantification and statistical analysis of the EPASIS data were performed as previously described [25] using MaxQuant (version 1.3.0.5). The human subset of the human proteome reference set, provided by SwissProt (Release 2012_01 534,242 entries) was used for peptide and protein identification. Seven biological replicates with five fractions each were performed for the NINL experiment and three biological replicates for the control experiment, resulting in a total number of 50 individual samples being measured. Proteins had to be present in at least 4/7 (57%) repeated experiments to be considered for further analysis. The reproducibility of the experiments was analyzed as already described [25] and is shown in S6 and S7 Figs To assign the proteins to the pre-defined sub-complexes (S4 Table [26, 54]), the EPD threshold was determined by a stepwise parameter search (n = 1000), which resulted in a value of 0.089 (S8 Fig).

4.13 Transmission electron microscopy (TEM)

Zebrafish (4 dpf) were fixed at 4°C overnight in a freshly prepared mixture of 2,5% glutaraldehyde and 2% PFA in 0.1 M sodium cacodylate buffer (pH 7.4). After rinsing in buffer, specimens were post-fixated in a freshly prepared mixture, containing 1% osmium tetroxide and 1% potassium ferrocyanide in 0.1 M sodium cacodylate buffer (pH 7.4), at room temperature during 2 hours. After rinsing, tissues were dehydrated through a graded series of ethanol and embedded in epon. Ultrathin (rostrocaudally) sections (70 nm), comprising zebrafish eyes at the optic nerve level, were collected on Formvar coated grids, subsequently stained with 2% uranyl acetate and Reynold's lead citrate, and examined with a Jeol1010 electron microscope. Using Adobe Photoshop version 8.0, TEM images were adjusted for brightness and contrast. To compare the degree of

vesiculation in the inner segments of the various experimental groups, quantitative TEM analysis was accomplished. To this end, 8000x magnification images of the central retina (50% middle arc length) were acquired. For each zebrafish group, several eyes and fields of view in the retina were evaluated (S5 Table). For each field of view, the total number of photoreceptor cells was counted. Finally, each photoreceptor cell was evaluated for presence of vesicles. The statistical significance of differences between two groups was assessed using the independent samples Student's t-test (SPSS 20.0). Morphant groups were analyzed and compared versus the wild type group, as well as versus the mock-injected group. The statistical significance was set at $p < 0.05$. Data are presented as means ± SEM.

4.14 Zebrafish OKR assay

The OKR was measured by a previously described method [55]. Zebrafish larvae were mounted in an upright position in 3% methylcellulose in a small Petri dish. The Petri dish was placed on a platform surrounded by a rotating drum 8 cm in diameter. A pattern of alternating black and white vertical stripes was displayed on the drum interior (each stripe subtended an angle of 36°C). Larvae (4 dpf) were visualized through a stereomicroscope positioned over the drum and illuminated with fiberoptic lights. Eye movements were recorded while larvae were optically stimulated by the rotating stripes. Larvae were subjected to a protocol of a 30 seconds counterclockwise rotation, a 10 seconds rest, and a 30 seconds clockwise rotation.

4.15 Melanosome transport assay

To induce melanosome retraction P5 larvae were exposed to epinephrine (Sigma E4375) at a final concentration of 500 µg/ml. Melanosome retraction was continuously monitored under the microscope and the endpoint was scored when all melanosomes in the head (and the trunk) were perinuclear [28]. P-values were obtained using Student's t-test (two tailed, unpaired).

4.16 Statistical analyses

For all quantifications of zebrafish experiments, the Graphpad Prism6 software (http://www.graphpad.com/scientific-software/prism/) was employed to generate scatter plots, calculate mean values and SEM values, and perform statistical tests. Continuous data was analyzed using two-tailed, unpaired Student's t-test and categorical data was analyzed using Fisher's exact test.

SUPPLEMENTAL DATA
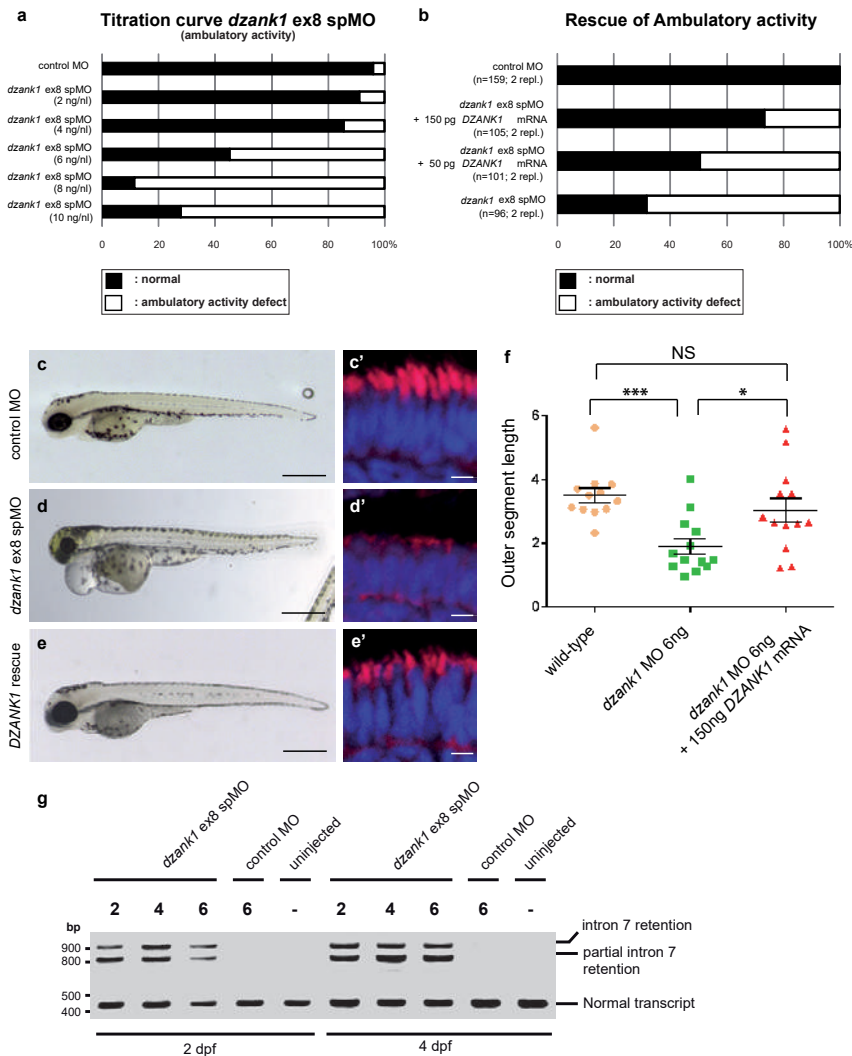
S1 Fig. Specificity of the *dzank1* ex8 spMO.

Titration curve of the dzank1 ex8 spMO scored on ambulatory activity shows an increased incidence of the phenotype with an increasing dose (a). (b) Co-injection of 6 ng dzank1 ex8 spMO with 150 pg capped MO-resistant mRNA encoding human DZANK1 reduced the incidence of phenotypes including ambulatory activity, small eyes (c, d, e) (n>95/group, p<0.0001 (two-tailed Fisher's exact test) and restored photoreceptor outer segment lengths (n = 13, P<0.001 (two-tailed, unpaired Student's t-test), c', d', e', f). (f) Quantification of photoreceptor outer segment lengths revealed a significant increase in length in the DZANK1 rescue group (3.0+/-0.4 µm) as compared to dzank1 morphants (6ng/nl; 1.9+/-0.25 µm) (P<0.001; two-tailed, unpaired Student's t-test). Bars indicate mean OS length per group and Standard error of the mean (SEM) (g) Characterization of the effect of the dzank1 ex8 spMO at 2 and 4 dpf by RT-PCR analysis. Injection of various amounts of MO resulted in the (partial) retention of intron7, leading to a premature termination of translation. PCR fragments were analyzed by Sanger sequencing. Scale bars represent 500 µm (c-e) and 15 µm (c'-e').
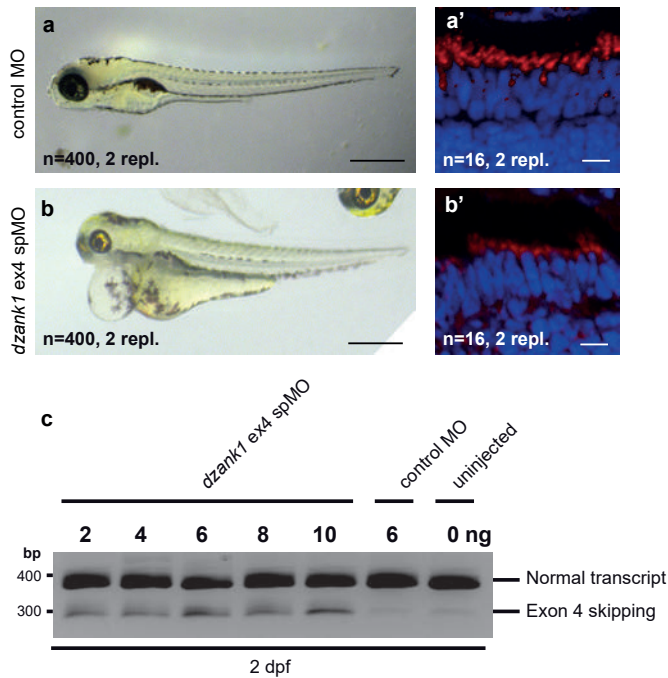
S2 Fig. Recapitulation of the phenotype by a second *dzank1* spMO targeting exon4.

Injection of a dzank1 ex4 spMO-injected larvae completely recapitulates the phenotype observed in dzank1 ex8 spMO-injected larvae, including pericardial edema, small eyes, defects in ambulatory activity (b) and shortened photoreceptor outer segments (b') as compared to control MO-injected larvae from the same clutch (a,a'). (c) Characterization of the effect of the dzank1 ex4 s pMO at 2 dpf by non-quantitative RT-PCR analysis. Injection of various amounts of MO resulted in the (partial) skipping of exon4, leading to a premature termination of translation. PCR fragments were analyzed by Sanger sequencing. Scale bars represent 500 μm (a-b) and 15 μm (a'-b').
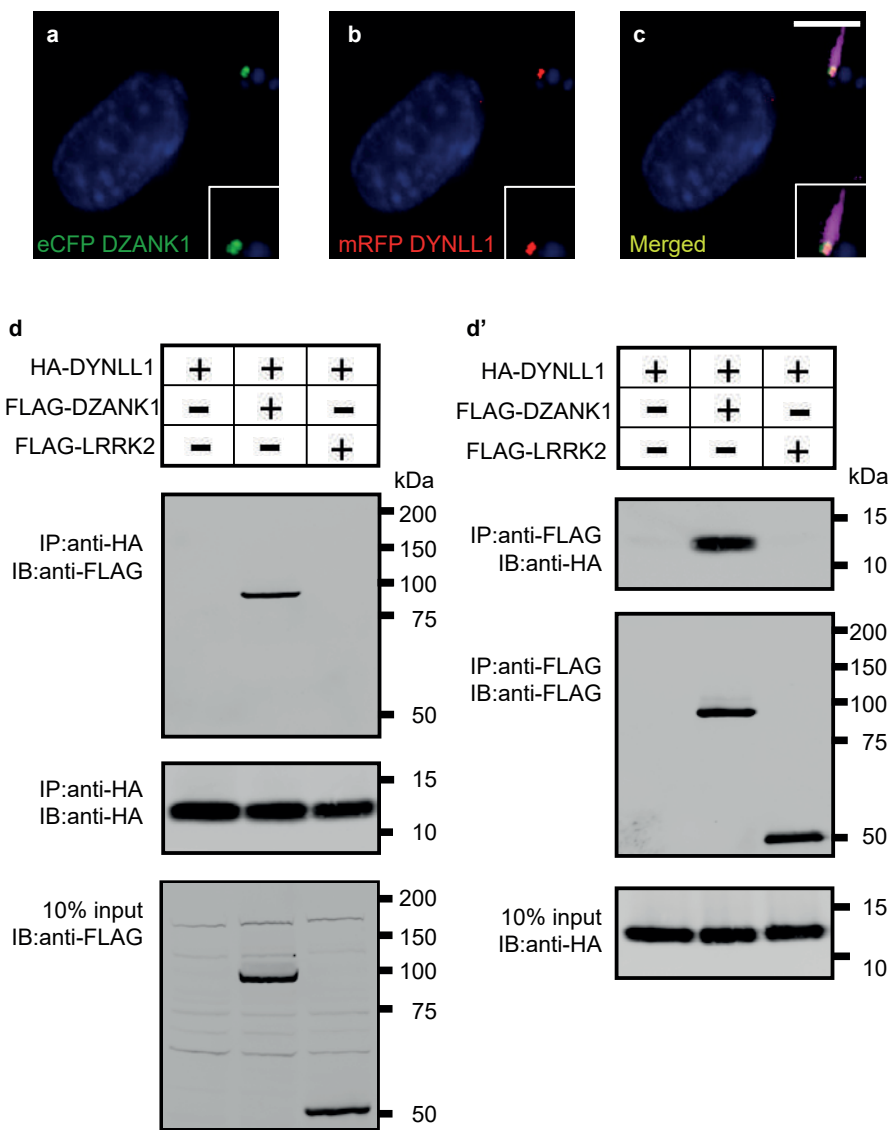
S3 Fig. DZANK1 co-localizes with DYNLL1 at the base of the cilia.

(a-c) eCFP-DZANK1 (green signal) and mRFP-DYNLL1 (red signal) localized to both centrioles of the centrosome and to the basal body of the cilia marked by GT335 (Cyanid signal). After co-expression, both proteins localized at the basal body of the cilia at the centrosome. c; yellow signal). Nuclei are stained with DAPI (blue signal). (d) Co-immunoprecipitation of DZANK1 FL with DYNLL1, but not with LRRK2. The immunoblot (IB) in the top panel shows that HA-tagged DYNLL1 co-immunoprecipitated with Strep/FLAG-tagged DZANK1 (lane 2), whereas unrelated FLAG-tagged LRRK2 (lane 3) did not. The anti-HA immunoprecipitates are shown in the middle panel; protein input is shown in the bottom panel. (d') Reciprocal IP experiments using anti-FLAG antibodies confirmed the co-immunoprecipitation of HA-tagged DYNLL1 with Strep/FLAG-tagged DZANK1 (lane 2) and not with LRRK2 (lane 3) shown in the top panel. The anti-FLAG immunoprecipitates are shown in the middle panel; protein input is shown in the bottom panel. Scale bars represent 10 μm (a-c).

2.1

a	b	c
eCFP DZANK1	mRFP DYNLL2	Merged

d

3xHA-DYNLL2	+	+	+
FLAG-DZANK1	−	+	−
FLAG-LRRK2	−	−	+

IP:anti-HA
IB:anti-FLAG

kDa
200
150
100
75
50

IP:anti-HA
IB:anti-HA

25
20

10% input
IB:anti-FLAG

200
150
100
75
50

d'

3xHA-DYNLL2	+	+	+
FLAG-DZANK1	−	+	−
FLAG-LRRK2	−	−	+

IP:anti-FLAG
IB:anti-HA

kDa
25
20

IP:anti-FLAG
IB:anti-FLAG

200
150
100
75
50

10% input
IB:anti-HA

25
20
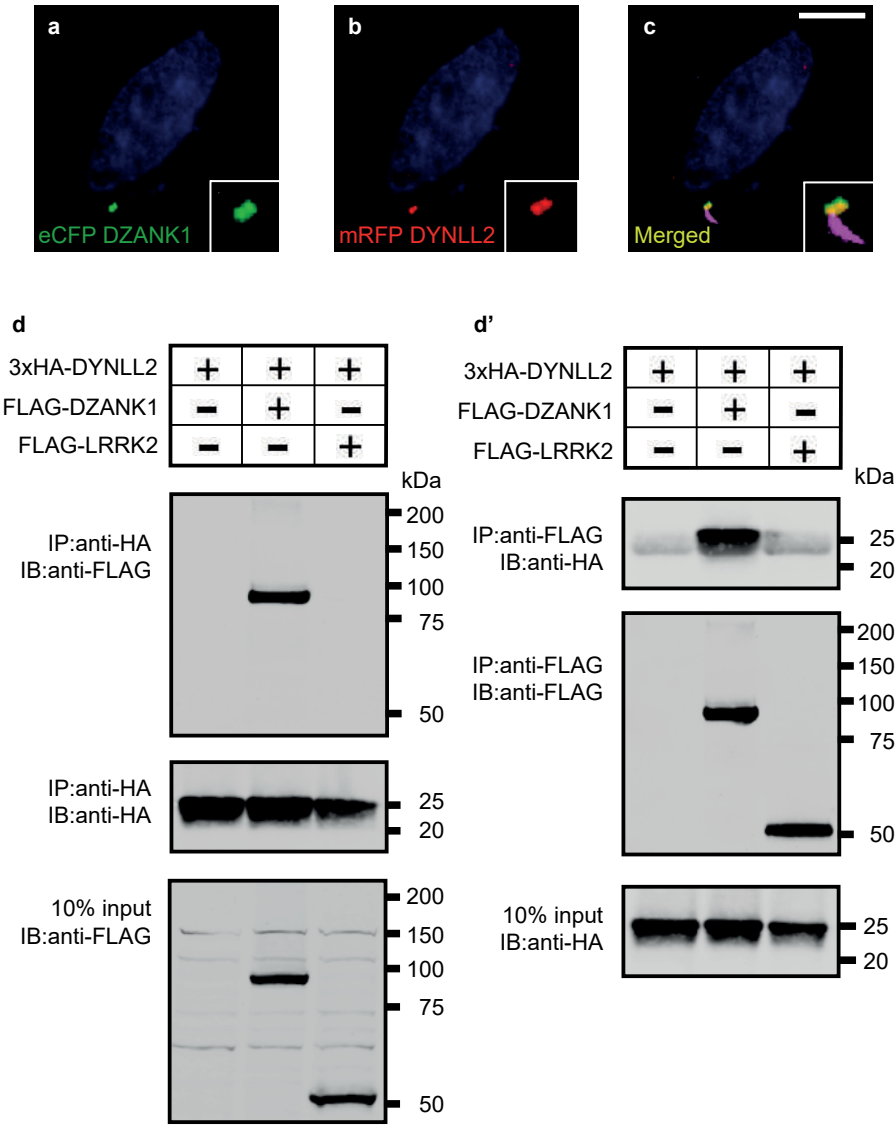
S4 Fig. DZANK1 co-localizes with DYNLL2 at the base of the cilia.

(a-c) eCFP DZANK1 (a; green signal) and mRFP-DYNLL2 (b; red signal) co-localizes at the basal body of the cilia in the centrosome (c; yellow signal). Nuclei were stained with DAPI (blue signal). (d-d') Co-immunoprecipitation of DZANK1 FL with DYNLL2, but not with LRRK2. The immunoblot (IB) in the top panel shows that 3xHA-tagged DYNLL2 co-immunoprecipitates with Strep/FLAG-tagged DZANK1 (lane 2), whereas unrelated FLAG-tagged LRRK2 (lane 3) does not. The anti-HA immunoprecipitates are shown in the middle panel; protein input is shown in the bottom panel. (d') Reciprocal IP experiments using anti-FLAG antibodies confirm the co-immunoprecipitation of 3xHA-tagged DYNLL2 with Strep/FLAG-tagged DZANK1 (lane 2) but not with LRRK2 (lane 3) shown in the top panel. The anti-FLAG immunoprecipitations are shown in the middle panel; protein input is shown in the bottom panel. Scale bars represent 10 μm (a-c).
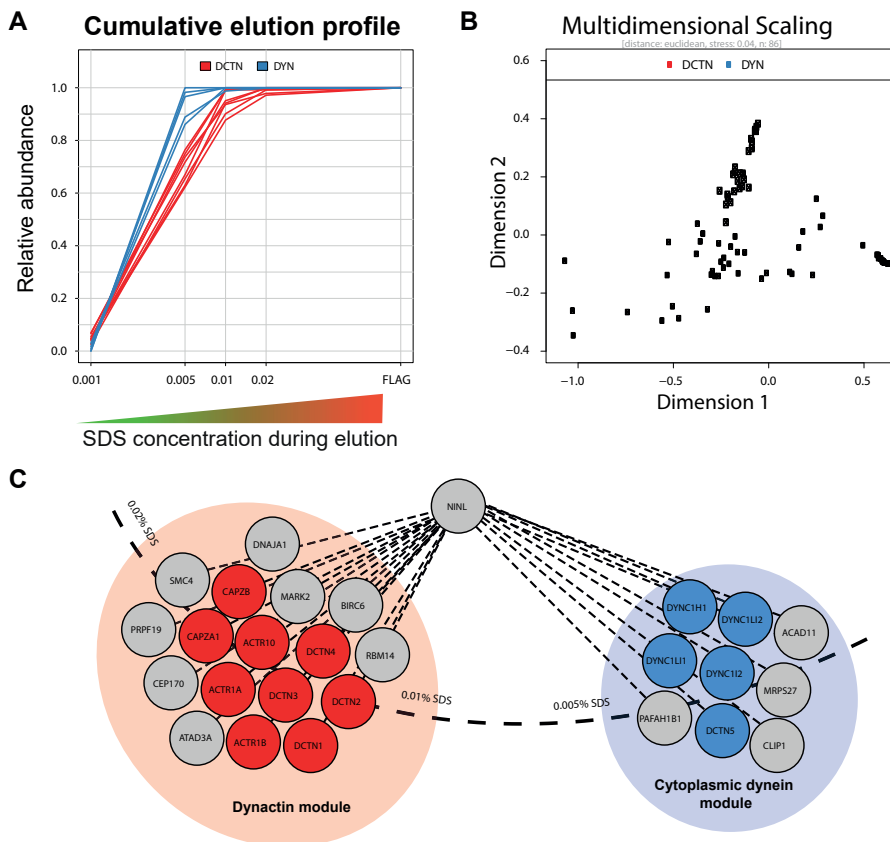
S5 Fig. EPASIS of the NINL protein complex.

(a) Visualization of the elution profiles of the known consensus protein groups, dynactin (DCTN, red), cytoplasmic dynein 1 module (DYN, blue), after analysis by liquid chromatography coupled to tandem mass spectrometry (LC-MS/MS) and label-free quantification. On the y-axis the cumulative relative abundance is plotted against the stepwise increasing SDS concentration on the x-axis. (b) Nonmetric multidimensional scaling ordination plot based on the Euclidean distances of elution profiles (stress 0.04). Data points (n = 86) present the average of replicated data (n = 7). (c) Sub-module organization of the NINL interactome, showing its putative sub-structure as determined by EPASIS. The respective modules are highlighted by colored clouds, the known members of the sub-modules are shown in full color, the new members in grey. Additionally to the known members of the dynactin module, several, potentially new candidates could be assigned to the dynactin module (ACTR10, RBM14, BIRC6, SMC4, MARK2, DNAJA1, CEP170, ATAD3A and PRPF19) with an Elution Profile Distance (EPD) ≤ 0.077. The second sub-module consists of proteins from the cytoplasmic dynein 1 motor complex and eluted between a SDS concentration of 0.001 and 0.01% from the NINL protein complex. Four further proteins were determined as potential new candidates to this module (MRPS27, ACAD11, PAFAH1B1 and CLIP1; EPD ≤ 0.015). Interestingly, the dynactin "pointed-end complex" protein DCTN5 was in our experiments clearly assigned to the dynein module. The distance of the modules from the bait, along the curved, dashed line, reflects the resistance of the interaction to SDS and correlates with stability of association.

2.1
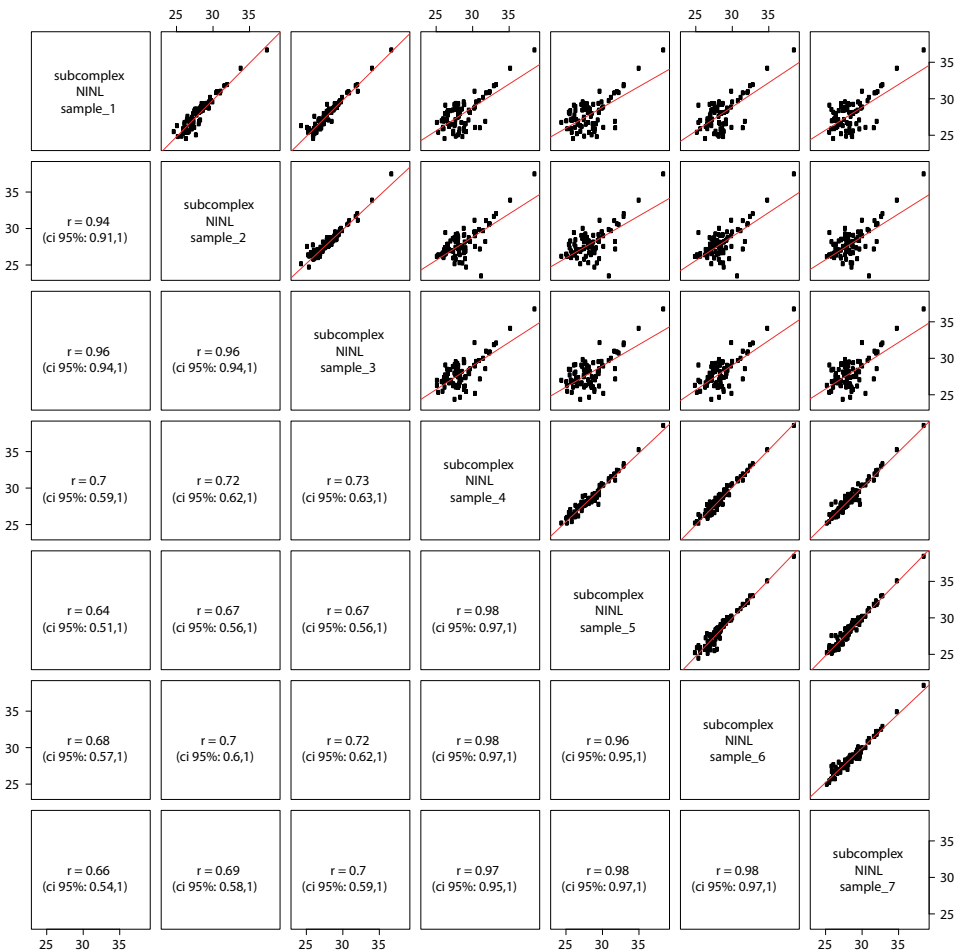
S6 Fig. Reproducibility of the NINL EPASIS.

Scatter plots of log2-transformed protein (n = 86) intensities from replicated experiments (experiment 1–7). Orthogonal regression lines are shown in red; Pearson correlation coefficients (r) and their 95% confidence intervals (ci) are shown.
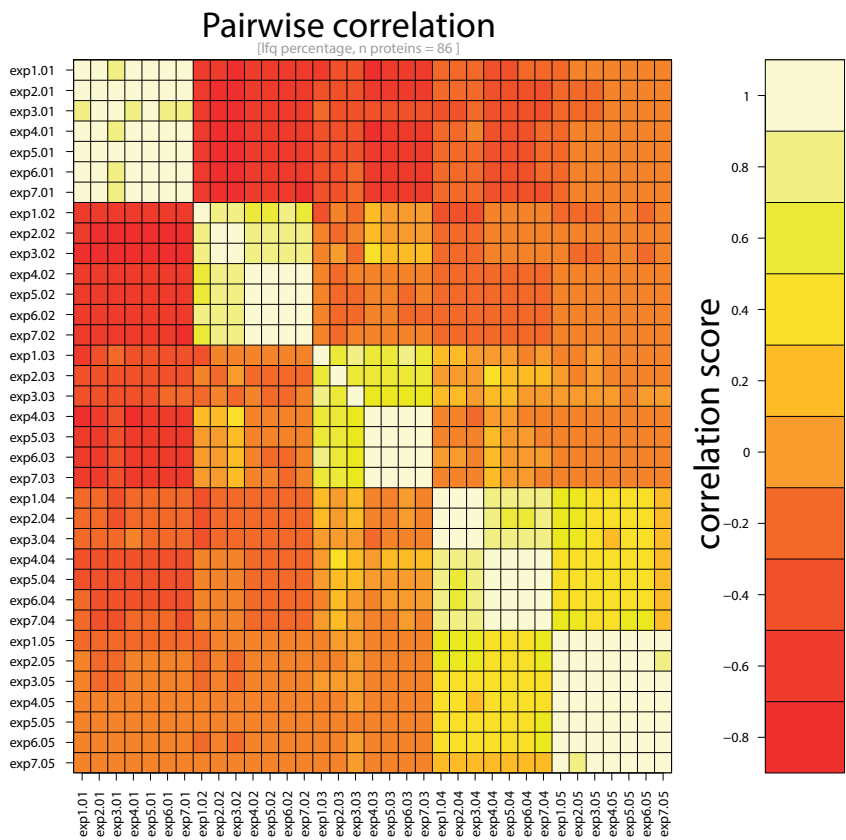
S7 Fig. Correlation matrix plot of the NINL EPASIS.

Correlation matrix plot of log2-transformed protein (n = 86) intensities for all concentration steps. Correlation scores of Spearman's test statistic are displayed and color-coded.
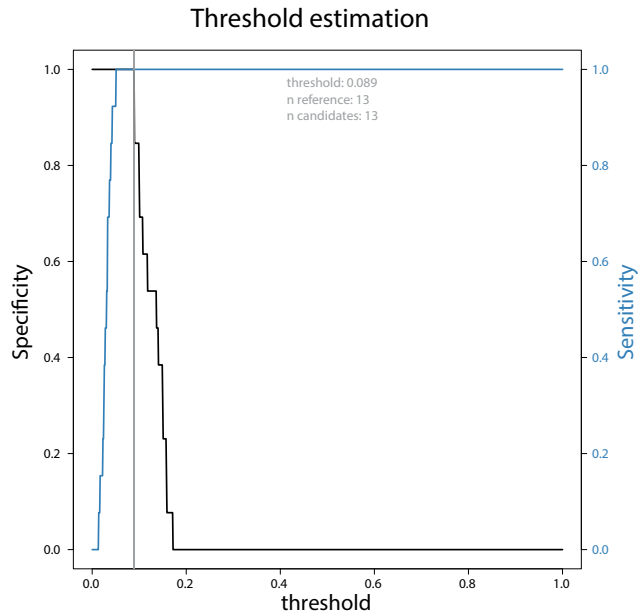
S8 Fig. Threshold estimation for the elution profile distance (EPD) of the NINL EPASIS.

For stepwise increasing thresholds (n = 1000), the specificity (black line) and sensitivity (blue line) to detect known consensus profile members are displayed. The grey line represents the selected threshold of 0.089 leading to the selection of 13 candidate proteins and 13 reference group proteins.
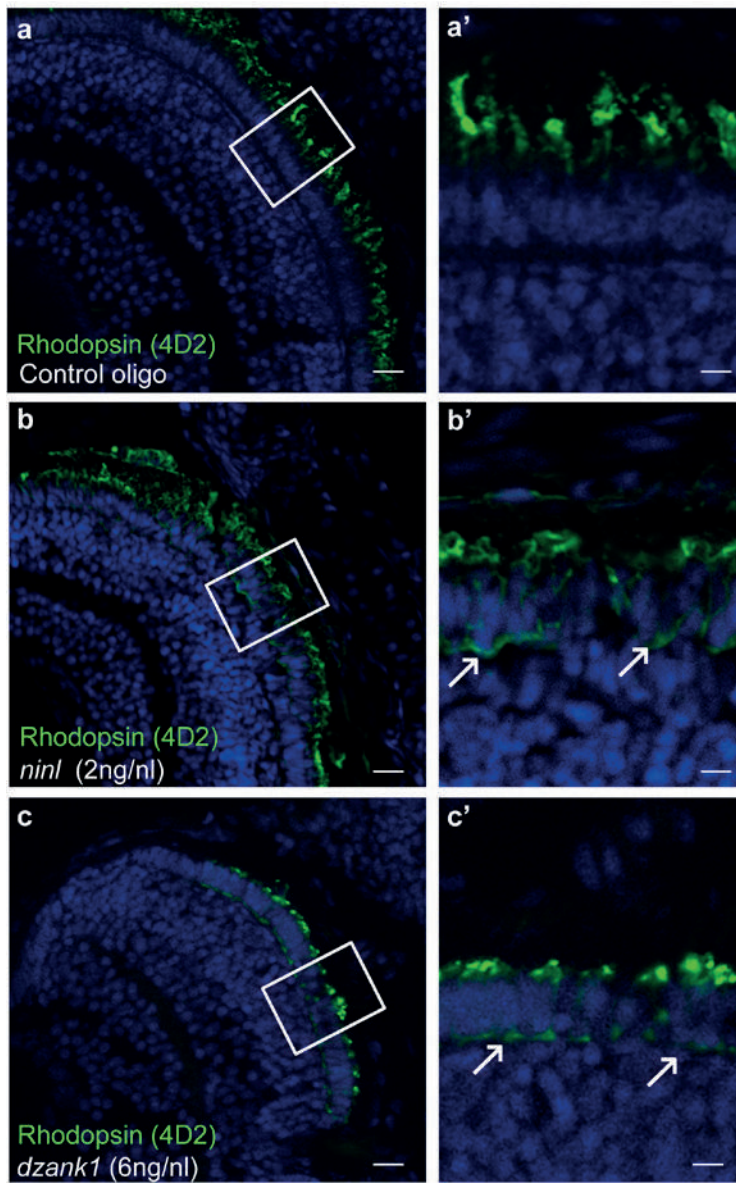
S9 Fig. *Ninl* or *Dzank1* knockdown in zebrafish leads to mis-localization of rhodopsin.

Immunofluorescence with anti-opsin antibody 4D2 demonstrated mislocalization of opsins (indicated by arrows) in the photoreceptor cell body in ninl (b-b') and dzank1 (c-c') morphants, compared to controls, where opsins are restricted to the outer segments (a-a'). (a'-c') are the white boxed areas of (a-c). Larvae are 4 dpf. Scale bars represent 50 μm (a-c) and 15 μm (a'-c').

Zebrafish Group	Eyes (n)	Fields of view (n)	Photoreceptor cells (n)
Wildtype	10	21	102
Control Oligo (10ng/nl)	8	18	111
Ninl (2ng/nl)	6	18	115
Ninl (0.5ng/nl)	8	11	80
Dzank1 (6ng/nl)	9	18	139
Dzank1 (1ng/nl)	8	12	134
Combi (dzank1 + ninl) (1 ng/nl + 0.5ng/nl)	7	20	142

S1 Table. GST pull-down from retinal extracts.

GST pull-down analysis from bovine retinal extracts with N-terminally GST-fused NINLisoB_aa538-825 (n = 4) or GST alone (n = 3) as a control. Shown are the number of unique peptides that were identified for each protein detected by mass spectrometry. Proteins identified in less than three out of four experiments and/or in GST-control experiments were removed. https://doi.org/10.1371/journal.pgen.1005574.s010

S2 Table. TAP-data and SILAC data.

SF-TAP analysis with over-expressed N-terminally SF-TAP-tagged proteins in HEK293T cells. Shown are the number of unique identified peptides as well as the sequence coverage for each protein detected by mass spectrometry. Proteins identified in the SF-TAP analysis of empty vector control experiments were removed. SILAC analysis with over-expressed N-terminally SF-TAP-tagged proteins in HEK293T cells. Shown are the ratios and significance value for WT/SF-control experiments.
https://doi.org/10.1371/journal.pgen.1005574.s011

S3 Table. EPD-values for EPASIS of the NINL protein complex.

EPD to consensus profiles were calculated for each protein displayed. Proteins with an EPD equal or less than 0.089 were assigned to a consensus profile. DCTN: dynactin module, DCTN_cand: proteins with EPD-value in the range of DCTN, DYN: Cytoplasmic dynein 1 module, DYN_cand: proteins with EPD-value in the range of DYN, unknown: unassigned proteins.
https://doi.org/10.1371/journal.pgen.1005574.s012

S4 Table. Consensus protein groups NINL interactome for EPASIS.

In the first column the corresponding sub-modules are depicted, the second column indicates the Uniprot accession number, in the third column the gene names are shown and the last column indicated the reference for the module association. The assignment to the different modules was done according to literature and by interpretation of the SF-TAP and SILAC data.
https://doi.org/10.1371/journal.pgen.1005574.s013

Zebrafish Group	Eyes (n)	Fields of view (n)	Photoreceptor cells (n)
Wildtype	10	21	102
Control Oligo (10ng/nl)	8	18	111
Ninl (2ng/nl)	6	18	115
Ninl (0.5ng/nl)	8	11	80
Dzank1 (6ng/nl)	9	18	139
Dzank1 (1ng/nl)	8	12	134
Combi (dzank1 + ninl) (1 ng/nl + 0.5ng/nl)	7	20	142

S5 Table. Specimens (central retina) analyzed for ultrastructural TEM analysis.

Ruxandra Bachmann-Gagescu[1,2,#,*], Margo Dona[3,4,*], Lisette Hetterschijt[3,4], Edith Tonnaer[3], Theo Peters[3], Erik de Vrieze[3,4], Dorus A. Mans[4,6], Sylvia E.C. van Beersum[4,6], Ian G. Phelps[7], Heleen H. Arts[4,6,8], Jan E. Keunen[5], Marius Ueffing[9], Ronald Roepman[4,6], Karsten Boldt[9], Dan Doherty[7], Cecilia B. Moens[10], Stephan C.F. Neuhauss[1], Hannie Kremer[3,4,6], Erwin van Wijk[3,4,#]

[1] Institute for Molecular Life Sciences, University of Zurich, Zurich, Switzerland; [2] Institute of Medical Genetics, University of Zurich, Zurich, Switzerland; [3] Department of Otorhinolaryngology, Radboud University Medical Centre, Nijmegen, the Netherlands; [4] Radboud Institute for Molecular Life Sciences, Radboud University Nijmegen, the Netherlands; [5] Department of Ophthalmology, Radboud University Medical Centre, Nijmegen, the Netherlands; [6] Department of Human Genetics, Radboud University Medical Centre, Nijmegen, the Netherlands; [7] Department of Pediatrics, University of Washington, Seattle, WA, USA; [8] Department of Biochemistry, University of Western Ontario, London, Ontario, Canada; [9] Division of Experimental Ophthalmology and Medical Proteome Center, Centre for Ophthalmology, Eberhard Karls University Tuebingen, Germany; [10] Fred Hutchinson Cancer Research Center, Seattle, WA, USA

* Authors contributed equally to the work

Chapter 2.2

The ciliopathy protein CC2D2A associates with NINL and functions in RAB8-MICAL3-regulated vesicle trafficking

2.2
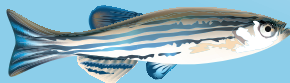
ABSTRACT

Ciliopathies are a group of human disorders caused by dysfunction of primary cilia, ubiquitous microtubule-based organelles involved in transduction of extra-cellular signals to the cell. This function requires the concentration of receptors and channels in the ciliary membrane, which is achieved by complex trafficking mechanisms, in part controlled by the small GTPase RAB8, and by sorting at the transition zone located at the entrance of the ciliary compartment. Mutations in the transition zone gene *CC2D2A* cause the related Joubert and Meckel syndromes, two typical ciliopathies characterized by central nervous system malformations, and result in loss of ciliary localization of multiple proteins in various models. The precise mechanisms by which CC2D2A and other transition zone proteins control protein entrance into the cilium and how they are linked to vesicular trafficking of incoming cargo remain largely unknown. In this work, we identify the centrosomal protein NINL as a physical interaction partner of CC2D2A. NINL partially co-localizes with CC2D2A at the base of cilia and *ninl* knockdown in zebrafish leads to photoreceptor outer segment loss, mislocalization of opsins and vesicle accumulation, similar to *cc2d2a-/-* phenotypes. Moreover, partial *ninl* knockdown in *cc2d2a-/-* embryos enhances the retinal phenotype of the mutants, indicating a genetic interaction in vivo, for which an illustration is found in patients from a Joubert Syndrome cohort. Similar to zebrafish *cc2d2a* mutants, *ninl* morphants display altered Rab8a localization. Further exploration of the NINL-associated interactome identifies MICAL3, a protein known to interact with Rab8 and to play an important role in vesicle docking and fusion. Together, these data support a model where CC2D2A associates with NINL to provide a docking point for cilia-directed cargo vesicles, suggesting a mechanism by which transition zone proteins can control the protein content of the ciliary compartment.

1. INTRODUCTION

Primary cilia are microtubule-based organelles protruding from the apical surface of most differentiated vertebrate cell types where they play a crucial role in transduction of extra-cellular signals to the cell [1]. Cilia achieve this function by concentrating and regulating receptors and channels that are required for sensing these signals in their membrane domain. Consequently, the ciliary membrane has a distinct composition from that of the adjacent plasma membrane, despite them being continuous with each other [2]. The tight regulation required to maintain the specificity of the ciliary membrane composition is achieved by complex trafficking and sorting mechanisms at the entry point to the ciliary compartment, as well as by a diffusion barrier present at the base of the cilium [3,4]. The transition zone, at the base of the ciliary axoneme, plays a crucial role in this sorting mechanism [5,6]. Indeed, dysfunction of proteins normally localized at the transition zone leads to both abnormal access to the ciliary compartment for proteins that should not localize there and loss of normal localization for ciliary proteins [5,7]. The actual mechanism, by which these transition zone proteins contribute to this sorting of ciliary proteins, remains however largely unknown.

Mutations in transition zone proteins in humans lead to several ciliopathies such as Joubert syndrome. Ciliopathies are a group of human disorders caused by dysfunction of primary cilia and characterized by overlapping genetics and phenotypes [8]. As cilia are present on most vertebrate cells, their dysfunction can manifest as a wide array of phenotypic features affecting most organs systems [9]. Retinal dystrophy is a common finding in ciliopathies given that retinal photoreceptor outer segments, which are the site of the phototransduction cascade, are highly specialized primary cilia [10]. Joubert syndrome (JBTS) (OMIM 213300) is a prototypical ciliopathy with a phenotypic spectrum that can encompass most of the typical ciliopathy phenotypes [11,12]. It is characterized by a specific hindbrain malformation termed the molar tooth sign (MTS), in addition to which affected individuals may have retinal dystrophy, tubulo-interstitial kidney disease, liver fibrosis, skeletal dysplasia and polydactyly [13–15]. To date, mutations in over 27 different genes have been reported as an underlying cause for JBTS [12,16–20]. Most of these genes encode proteins associated in multi-protein complexes localized at the transition zone of the primary cilium [7,21].

Mutations in *CC2D2A* (Coiled-coil and C2-domains containing protein 2A) are the second most common genetic cause for JBTS, accounting for almost 9% of affected individuals [22,12]. Moreover, mutations in *CC2D2A* can also result in the genetically related and more severe Meckel syndrome, which is a perinatal-lethal disorder characterized by encephalocele, polydactyly, cystic kidneys and liver fibrosis [23]. CC2D2A is part of one of the ciliary transition zone complexes with several other JBTS proteins [7,21]. Two *Cc2d2a* mouse mutants have been described, presenting with severe brain

malformation (holoprosencephaly), microphthalmia, curved body axis and randomized left-right axis, all typical ciliopathy-associated phenotypes [7,24]. Interestingly, mouse embryonic fibroblasts from one of the reported *Cc2d2a*^{-/-} mice appear to lack cilia entirely [24] whereas disruption of CC2D2A function in the other reported mutant does not compromise ciliogenesis in mouse embryonic fibroblasts [7]. Instead, the ciliary localization of several proteins (including ARL13B, Adenylyl Cyclase III, Smoothened and Polycystin2) is lost, suggesting that presence of CC2D2A at the transition zone is required for appropriate targeting of proteins to the ciliary compartment [7]. The zebrafish *cc2d2a* mutant *sentinel* demonstrates a curved body axis, pronephric cysts and a striking retinal phenotype with short and dysmorphic photoreceptor outer segments [25]. In addition, the photoreceptors of *cc2d2a* mutants also show mislocalization of opsins in the cell body and cytoplasmic accumulation of vesicles in the apical portion of the cells and around the connecting cilium (equivalent of the transition zone in photoreceptors), suggesting a defect in opsin trafficking. Opsins are the photosensitive pigment molecules concentrated at high levels in the outer segments and required for sensing the light signal. Trafficking of opsins from the cell body towards the ciliary compartment is (at least in part) controlled by the small GTPase Rab8, which coats rhodopsin-carrier vesicles allowing their docking and fusion at the ciliary base [26]. Expression of a dominant-negative form of Rab8a leads to accumulation of rhodopsin-containing vesicles in photoreceptors [27]. In addition, RAB8A is also involved in ciliary membrane biogenesis in other cell types and thus appears to play a general role in orchestrating trafficking towards the ciliary compartment [28,29]. The trafficking defect observed in *cc2d2a*^{-/-} photoreceptors appears to be mediated by loss of normal Rab8 localization [25] but the precise mechanism by which loss of this transition zone protein affects the localization of Rab8 and the trafficking of ciliary-directed opsins remains unclear.

In the current work, we identify a chain of physical interactions linking CC2D2A to RAB8A through NINL and MICAL3. Using a zebrafish model, we demonstrate that loss of Ninl function leads to a similar retinal phenotype as loss of Cc2d2a, including short outer segments, mislocalization of opsins and accumulation of vesicles. Based on the physical and genetic interactions that we identify, we propose a model in which CC2D2A provides a docking point at the photoreceptor ciliary base, allowing RAB8A-positive vesicles to bind through a series of interactions involving CC2D2A-NINL-MICAL3-RAB8A.

2. RESULTS

2.1 CC2D2A associates with NINL

In order to shed light on the function of CC2D2A we performed a dedicated ciliary yeast two-hybrid assay with different fragments of CC2D2A against a panel of 164 proteins, containing most of the ciliopathy-associated proteins [30]. A direct binary interaction between CC2D2A and both isoforms (A and B) of the centrosome- and basal body-associated protein NINL (Ninein-like protein) was identified (Figure 1a). NINL isoforms A and B are distinguished by the fact that isoform B is 349 amino acids shorter due to skipping of the large exon 17 (Figure S1a). Both isoforms share predicted EF-hand domains in the N-terminal region as well as coiled-coil domains in the more C-terminal portion. Both isoforms display similar broad expression patterns, with the strongest expression patterns in cochlea, brain, testis, kidney and retina [31].

By generating deletion constructs for CC2D2A and subsequent evaluation of the interaction with NINL, we could pinpoint the interaction to the two predicted coiled-coil domains (433-637aa) present in CC2D2A (Figure 1a). Since CC2D2A and NINL isoform B demonstrated the strongest interaction (Figure 1a), we focused on NINL isoform B (NINL^{isoB}) for confirmation and further investigation of this interaction. Co-immunoprecipitation assays performed using full-length tagged-constructs for NINL^{isoB} and CC2D2A, showed co-precipitation of the two proteins. FLAG-tagged LRRK2 that was used as a negative control did not co-precipitate with HA-tagged NINL^{isoB}, which confirmed the specificity of the interaction between NINL^{isoB} and CC2D2A in this assay (Figure 1b). A reciprocal co-immunoprecipitation experiment confirmed the interaction between NINL^{isoB} and CC2D2A (Figure 1c).

2.2 CC2D2A and NINL co-localize at the base of cilia independently of each other

To further validate the interaction between CC2D2A and NINL^{isoB} in ciliated mammalian cells, we transfected hTERT-RPE1 cells (human telomerase reverse transcriptase retinal pigment epithelium cells) with expression-constructs of wild-type mRFP-tagged NINL^{isoB}, eCFP-tagged CC2D2A or a combination of both. When expressed alone, eCFP-tagged CC2D2A localizes to the ciliary base (basal body, accessory centriole) and also (partly) to the ciliary transition zone, which was visualized using anti-RPGRIP1L as a marker (Figure 2a-b). mRFP-tagged NINL isoform B was localized at the ciliary base adjacent to the ciliary transition zone (Figure 2c-d). When co-expressed, NINL^{isoB} and CC2D2A co-localized at the base of the primary cilium (Figure 2e-e").

To investigate the localization and function of endogenous Ninl, we turned to the zebrafish model. The zebrafish genome harbors a single *ninl* orthologue (Genbank
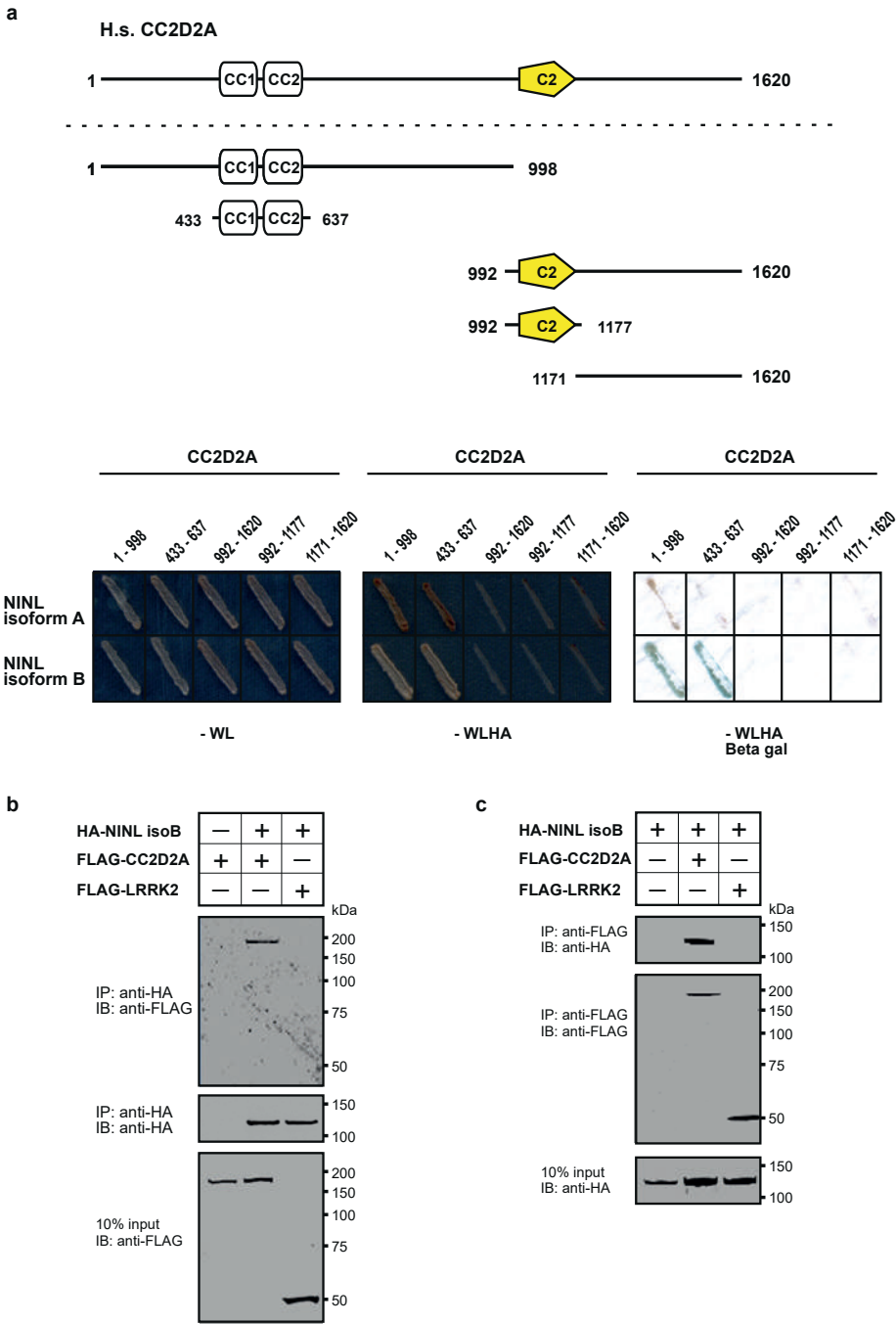
Figure 1. CC2D2A associates with NINL.

(**a**) Yeast two-hybrid interaction assays were performed with different fragments of CC2D2A fused to the GAL4 DNA binding domain (BD) and full length NINL isoform A and B, fused to the GAL4 activation domain (AD). Activation of the reporter genes, which indicates a physical interaction, was dependent on coiled-coil (CC) domains 1 and 2 of CC2D2A and either NINL isoform A or B. (**b**) The top panel of the immunoblot (IB) shows that FLAG-tagged CC2D2A, but not the FLAG-tagged LRRK2 that was included as a negative control, was co-precipitated with HA-tagged NINL isoform B using a rat monoclonal antibody directed against the HA-epitope. Protein input is shown in the lower panel; anti-HA precipitates are shown in the middle panel. (**c**) In a reciprocal experiment, HA-tagged NINL[isoB] was co-precipitated with FLAG-tagged CC2D2A, but not with FLAG-tagged LRRK2. Protein input is shown in the lower panel; anti-FLAG precipitates are shown in the middle panel.

2.2

NP_001268727) that has 45% similarity with human *NINL*. Conserved domains include the predicted EF-hand domains and multiple coiled-coil domains. Cloning of zebrafish *ninl* from whole embryo mRNA at 5dpf revealed that all identified zebrafish transcripts lack the large exon 17 which is present only in human NINL isoform A but not in isoform B (Figure S1a). Therefore, zebrafish *ninl* is most similar to the shorter human NINL isoform B. RNA *in situ* hybridization with two different antisense probes derived from the 5'-end and the 3'-end of the zebrafish *ninl* transcript revealed broad expression at 14-18 somites in neural tube, inner ear, developing eye and pronephros. Expression persists in the retina at least up to 6 dpf (days post fertilization; last developmental stage assessed) (Figure S1b). Antibody staining showed punctate localization of endogenous Ninl in zebrafish retina at the base of the cilium in 4dpf larvae (Figure 2g). While co-staining with Cc2d2a antibodies was not possible due to different fixation conditions, co-staining of serial sections with anti-centrin and anti-Ninl or anti-Cc2d2a antibodies respectively revealed that both endogenous proteins partially co-localize at the base of the photoreceptor cilium of 4 dpf old zebrafish larvae (Figure 2f-g). We observed that Cc2d2a localizes slightly more apically with respect to Centrin than Ninl, consistent with Cc2d2a localization at the connecting cilium, while Ninl localization is overlapping more broadly with the basal body (Figure 2f-g, schematized in j).

In order to determine whether Cc2d2a localization is dependent on the presence of Ninl, we performed morpholino-induced knockdown studies in zebrafish. Injection of 2 ng/nl of *ninl* translation-blocking morpholino (atgMO) led to efficient knockdown of Ninl, as demonstrated by substantially decreased antibody staining in cryosections through morphant retina (Figure S2a-b"). On Western blots of whole 5dpf larval extracts, a single strong band of 80 kDa is present in wild-type fish (Figure S2d), which is consistent with results from immunoprecipitation from retinal bovine extracts with a previously published antibody against human *NINL* (Figure S2 [31]). This band is strongly reduced in *ninl* atgMO injected larvae (Figure S2d), supporting the specificity of the morpholino and of the antibody.

Ninl knockdown led to typical ciliopathy-associated phenotypes, including curved body shape, enlarged brain ventricle and pronephric cysts (Figure S3a-g). The specificity of
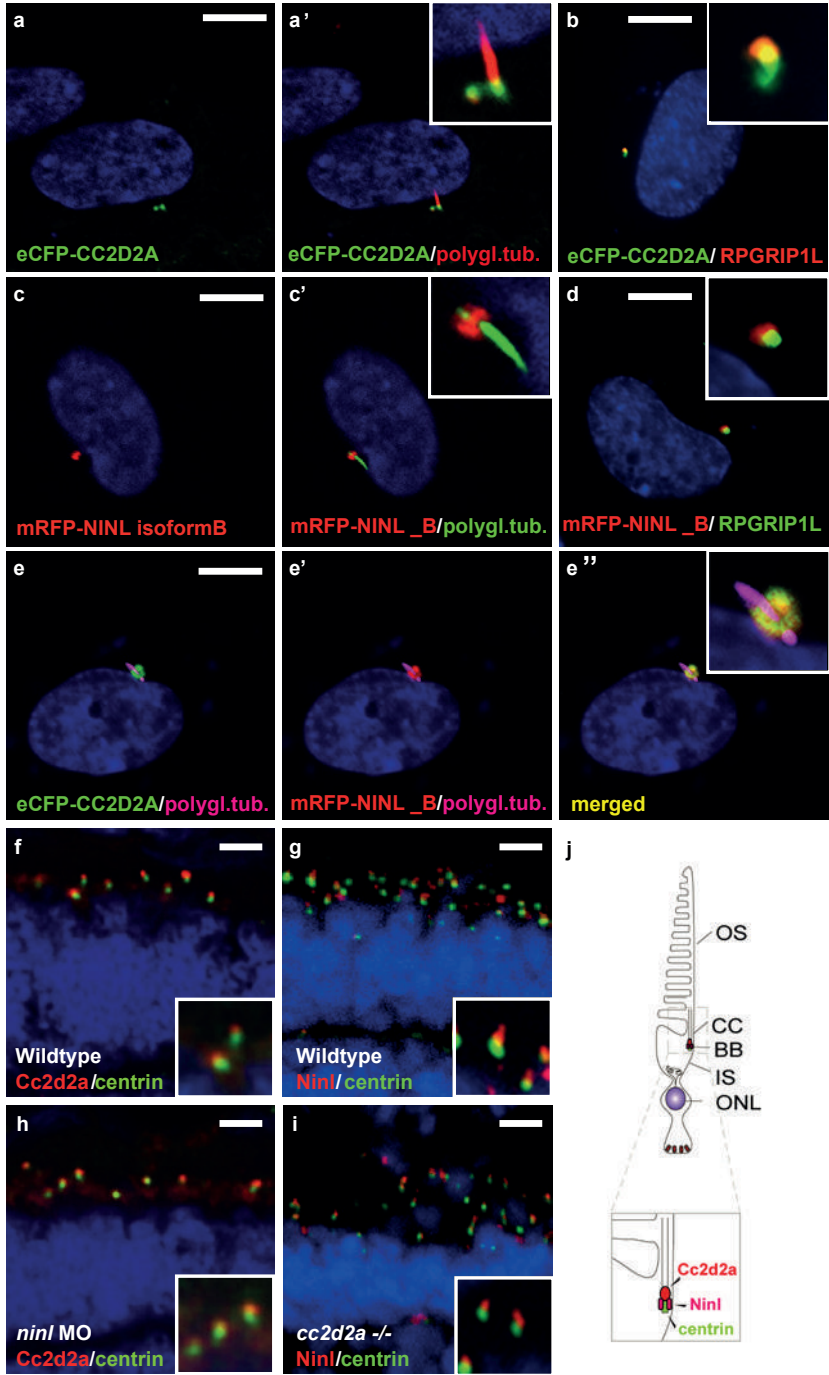
Fig. 2. CC2D2A and NINL co-localize at the ciliary base in hTERT-RPE1 cells and in zebrafish retina.

(**a, a'** and inset) When expressed alone, eCFP-tagged CC2D2A (green signal) localizes to the ciliary base (basal body, accessory centriole). The cilium is marked by anti-polyglutamylated tubulin (red signal, **a'** and inset). eCFP-tagged CC2D2A (green signal; **b**) also (partly) localizes to the ciliary transition zone, which was visualized using anti-RPGRIP1L as a marker (red signal; **b**). (**c, c'** and inset) mRFP-tagged NINL isoform B was localized at the ciliary base (cilium in green, **c'** and inset). (**d** and inset) mRFP-tagged NINL isoform B (red signal) localizes adjacent to the ciliary transition zone (anti-RPGRIP1L; green signal). (**e-e''** and inset) Co-expression of mRFP-tagged NINL isoform B (red signal) and eCFP-tagged CC2D2A showed co-localization of both proteins around the ciliary base (yellow signal). (**f**) In wild-type larval zebrafish retina (4 dpf), Cc2d2a marked by anti-Cc2d2a antibodies (red signal) is localized apically to the photoreceptor basal body (marked by anti-centrin antibodies, green signal). (**g**) Ninl, stained with anti-Ninl antibodies, (red signal) is localized at the zebrafish photoreceptor ciliary base, partially overlapping with and apical to the green centrin signal. (**h**) Cc2d2a localization is unaffected by *ninl* knockdown and (**i**) Ninl localization is normal in *cc2d2a*^{-/-} larvae. (**j**) Schematic representation of the localization of Ninl and Cc2d2a in zebrafish photoreceptor cells. (**f-i**) are immunostainings on cryosections from 4 dpf larvae. Nuclei were stained with DAPI (blue signal) in all panels. Scale bars are 10 μm in a-e, and 4 μm in f-i.

2.2

the observed phenotype was confirmed by rescue experiments, in which co-injection of 2 ng/nl *ninl* MO with capped MO-resistant human *NINL*-mRNA reduced the prevalence of the curved body phenotype in a dose-dependent manner (curved body shape in 71% of *ninl* atgMO injected larvae (n=207) versus 36% in *ninl* atgMO + *ninl* mRNA injected larvae (n=203), data pooled from 2 biological replicates, *P*<0.0001, two-tailed Fisher's exact test; Figure S4a-d). Finally, the specificity of the observed phenotypes was further confirmed by a second morpholino against *ninl* targeting the splice site at the intron14/exon15 junction and thus causing aberrant splicing with premature truncation (Figure S5c). This splice morpholino led to similar phenotypes as the atgMO, including ventriculomegaly and abnormal photoreceptor outer segments (Figure S5a-b). The body curvature phenotype was absent in the splice morphants, which may be explained either by rescue of this early phenotype by maternal *ninl* mRNA, which remains unaffected by splice morpholinos (as seen in some ciliopathy zebrafish mutants such as *talpid3* where only the maternal zygotic mutants have a curved body shape [32]), or by less efficient gene knockdown with this morpholino, as normal transcript persists in addition to the aberrant transcript (Figure S5c). Indeed, using the anti-NINL antibody, we observed a milder decrease of Ninl protein on Western blots and on immuno-histochemistry of retinal cryosections at 5dpf for the *ninl* ex15 spMO as compared to the atgMO (Figure S2c-d).

Localization of Cc2d2a at the connecting cilium, shown by anti-Cc2d2a immunostaining, was unaffected by Ninl knockdown (Figure 2h). Conversely, immunostainings using anti-Ninl antibodies revealed no clear mislocalization of Ninl in the retina of *cc2d2a*^{-/-} larvae (Figure 2i). Taken together, these data indicate that Cc2d2a and Ninl co-localize at the ciliary base independently of each other.

2.3   NINL knockdown in zebrafish leads to outer segment loss, opsin mislocalization and vesicle accumulation

Since *cc2d2a*^{-/-} zebrafish have prominent retinal abnormalities [25], we focused our phenotypic analysis on the retina of *ninl* morphants. Retinal lamination was unaffected in *ninl* morphants (Figure 3a-b). In contrast, photoreceptors demonstrated shortened axonemes and abnormal outer segments, as seen on retinal cryosections at 4 dpf stained with boron-dipyrromethene (bodipy) to mark the outer segment membrane discs (Figure 3c-d') and anti-acetylated alpha-tubulin and anti-Ift88 antibodies to mark the axoneme (Figure 3e-f). Measurement of outer segment (OS) length of early 4dpf larvae, performed in a blinded manner as to injection status, revealed a significant shortening (mean OS length 1.6 +/- 0.26 µm in *ninl* atgMO morphants compared to 3.9 +/- 0.32 µm in wild-type, $P<0.0001$, unpaired Student's t-test, n>10 larvae from each group in each of 2 biological replicates; Figure S4e). This retinal phenotype was observed with both the *ninl* translation-blocking and the splice-blocking morpholinos (Figure S5b'). Little to no photoreceptor cell death was observed with TUNEL assay on cryosections of 4dpf morphant larvae (Figure S3i-j) compared to *ift88*-/- retinas that are known to display prominent photoreceptor cell death at the same stage (and were thus used as positive controls; Figure S3k). In general, minimal cell death was observed at 4dpf throughout the embryo, including in brain of larvae with overt ventriculomegaly (Figure S3l). Co-injection of 150pg of capped human *NINL* mRNA with 2ng/nl *ninl* atgMO restored normal outer segment length (mean OS length in rescued larvae 3.8 +/- 0.25 µm, $P<0.0001$, unpaired Student's *t*-test, n= 10 larvae; Figure S4 a'-c' and e).

Immuno-staining with anti-opsin antibodies (4D2 antibody) demonstrated significant accumulation of opsins in the inner segment and throughout the cell body of *ninl*-depleted photoreceptors (Figure 3g-i; mean intracellular fluorescence was significantly increased in *ninl* morphants compared to controls, $P<0.0001$, unpaired Student's *t*-test, n=15 morphant larvae and 7 control larvae, 2 replicate experiments). At the ultra-structural level, two types of abnormal membrane-bound structures were observed by transmission electron microscopy in *ninl* morphants: large vacuole-like structures were present in the cell body and small vesicular structures accumulated around the Golgi complex and below the connecting cilium (Figure 3j-m; vacuolar and/or vesicular structures were present in 45/112 photoreceptors from 6 morphant eyes compared to 13/192 photoreceptors from 4 uninjected and 4 Control Oligo injected eyes; $P<0.0001$, Fisher's exact test). These phenotypes are partially reminiscent of those observed in *cc2d2a*^{-/-} embryos [25], supporting a common or coordinated function for Cc2d2a and Ninl in the process of vesicular trafficking towards the ciliary compartment.
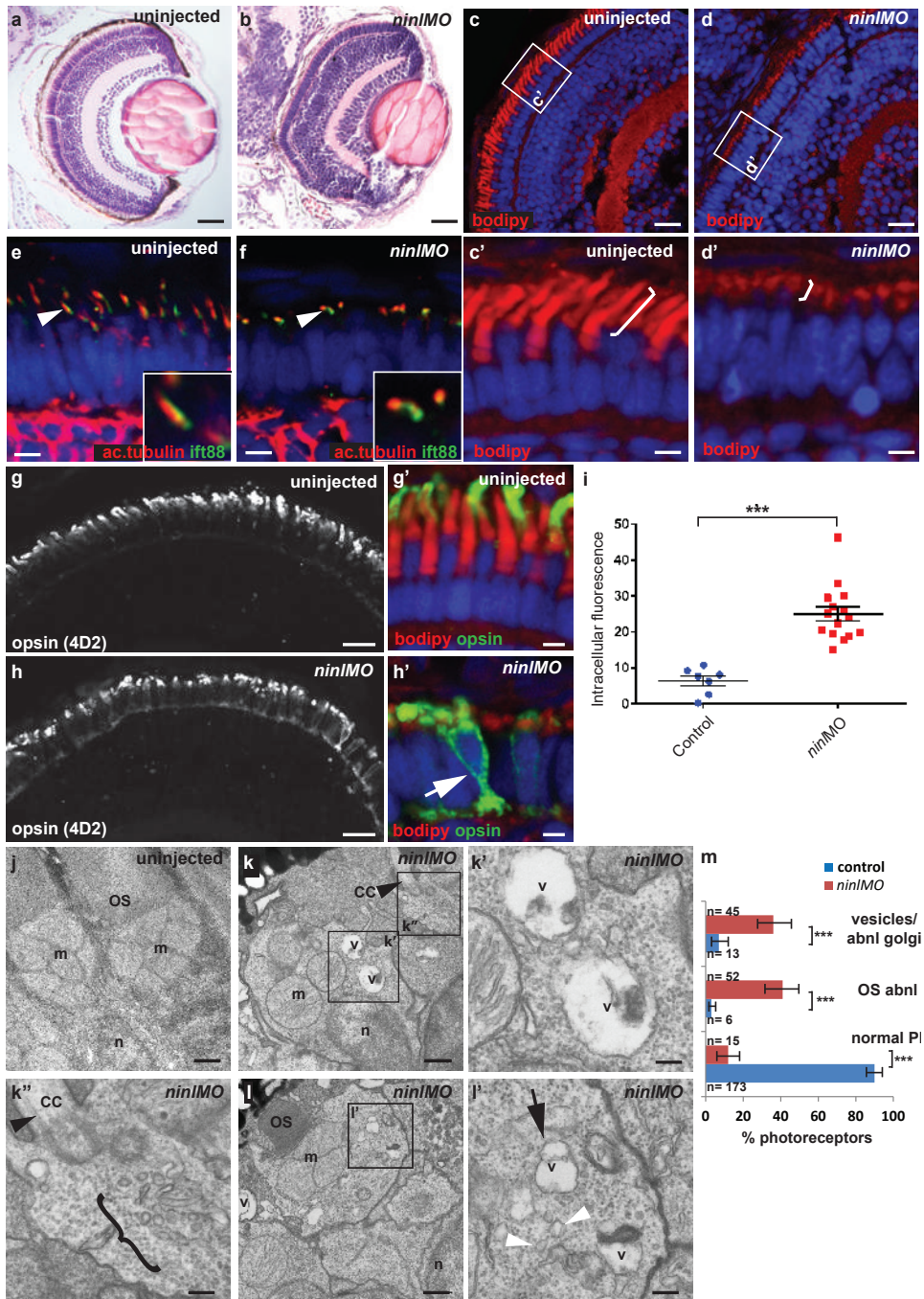
Figure 3. Zebrafish *ninl* knockdown causes loss of axonemes and outer segments, opsin mislocalization and vesicle/vacuole accumulation.

(**a-b**) Paraffin sections stained with Hematoxylin/Eosin of control (**a**) and *ninl* knockdown larvae (**b**) demonstrating shortened outer segments and grossly preserved retinal lamination in the morphants. (**c-d'**) Bodipy-stained cryosections highlight the shortened (brackets **c'-d'**) and dysmorphic outer segments of ninl knockdown larvae (**d** and **d'**) compared to the long cone- or rod-shaped outer segments of controls (**c** and **c'**). (**e-f**) Axonemes and connecting cilia marked with anti-acetylated alpha-tubulin and anti-Ift88 antibodies are severely shortened and reduced in numbers in *ninl* knockdown larvae (arrowhead in f). (**g-h'**) Immunofluorescence with anti-opsin antibody 4D2 demonstrates mislocalization of opsins within the cell body in *ninl* knockdown larvae (arrow in **h'**) compared to controls (**g**) where opsins are restricted to the outer segment. (**i**) Quantification of the intracellular opsin accumulation in *ninl* morphant photoreceptors compared to control: each single datapoint in the scatter graph displays the averaged mean grey value from one larva. The mean value and the Standard Error of the Mean (SEM) are displayed as bars. The difference is statistically significant (*** = $p < 0.0001$, Student's *t*-test). (**j-l'**) Transmission electron microscopy of control (**j**) and *ninl* knockdown larvae (**k-l'**) demonstrates absent or shortened and dysmorphic outer segments (OS) and accumulation of large vacuoles (v, arrow in **l'**) and smaller vesicular structures (bracket in **k"** and white arrowheads in **l'**) in morphants. Black arrowheads point to the connecting cilium in k and k". k' and k" are the boxed areas in k and l' is the boxed area in l. (**m**) Quantification of the % of photoreceptors displaying these phenotypes. Absolute numbers of photoreceptors are also indicated. Error bars indicate 95% Confidence Intervals. The differences between morphant (red bars) and controls (blue bars) are statistically significant (*** = $p < 0.0001$, Fisher's exact test). Larvae in all panels are 4 dpf old. Scale bars are 30 µm in **a-b**, 15 µm in **c-d and g-h**, 3 µm in **c'-d' and g'-h'**, 4 µm in **e-f**, 0.5 µm in **j-k and l** and 150nm in **k'-k"** and **l'**. OS outer segment, CC connecting cilium, m mitochondria, n nucleus, v vacuole.

2.4 *Ninl* genetically interacts with *cc2d2a* and may act as a genetic modifier for *CC2D2A*-associated Joubert Syndrome

To further delineate the relationship between *cc2d2a* and *ninl*, we tested whether a synergistic effect was detectable between the two genes by using partial *ninl* knockdown in the *cc2d2a* mutant background. We observed that injection of a sub-phenotypic dose of *ninl* MO (0.75 ng/nl), which causes no discernible phenotype in wild-type larvae, significantly increased the penetrance and severity of pronephric cysts in *cc2d2a* mutants: 89% of *ninlMO-cc2d2a*-/- zebrafish developed cysts compared to 40% of uninjected *cc2d2a*-/- larvae ($p < 0.0001$, Fisher's exact test) and the size of these cysts was significantly increased (as measured by the area of the dilated glomerulus and proximal tubules: 0.044 +/-0.004 mm^2 for *cc2d2a*-/- + *ninl*MO (n=16) as compared to 0.016 +/-0.002 mm^2 for uninjected *cc2d2a*-/- (n=8, $P < 0.0001$, unpaired Student's *t*-test) (Figure 4a-d). Importantly, the *cc2d2a*+/- and *cc2d2a*+/+ siblings from the same injection clutch did not develop pronephric cysts at these sub-phenotypic *ninl* MO doses (Figure 4a and d). In the retina, the opsin mislocalization phenotype in *cc2d2a*-/- larvae (5 dpf) was enhanced by the addition of the same sub-phenotypic dose of *ninl*MO (Figure 4 e-h; $P < 0.0001$, Student's *t*-test, n=19 *cc2d2a*-/- + *ninl*MO and n=16 *cc2d2a*-/- uninjected, 2 replicates). These findings support a genetic interaction between *cc2d2a* and *ninl* and suggest that *NINL* could be a genetic modifier for *CC2D2A*-caused disorders or even contribute to the genetic spectrum underlying Joubert/Meckel syndrome. Following this rationale, we sequenced *NINL* in a cohort of 346 individuals with Joubert syndrome (from 291 families) using a molecular inversion probes (MIPs) capture method followed by next-generation sequencing [33] but did not identify any individuals carrying bi-allelic

rare deleterious *NINL* variants. We did however find 3 individuals with heterozygous *NINL* mutations predicted to be deleterious. Individual UW48-3 carried the homozygous missense *CC2D2A* mutation c. 3364C>T (p.P1122S), previously shown to be causal for Joubert syndrome, and a heterozygous *NINL* frameshift mutation leading to a stop codon after 43 amino acids (c.3020delC, p.P1007Lfs*43) (Figure 4i) (and no other rare deleterious variant in any of the known JS genes). Phenotypically, this subject had a severe form of JBTS with retinal dystrophy, hearing loss, ventriculomegaly in addition to the MTS and renal failure leading to death at age 7 years. In comparison, subject UW 36-3 carried the same homozygous *CC2D2A* c.3364C>T (p.P1122S) mutation but no additional *NINL* variants (or rare deleterious variants in other JBTS genes) and presented with the "pure JBTS" phenotype, consisting only of the MTS with associated ataxia, developmental delay and respiratory rhythm disturbance (Figure 4j). Subject UW07-3 carried a heterozygous *NINL* nonsense mutation (c.2446 G>A, p.R816X) in addition to causal, compound heterozygous *C5ORF42* frameshift mutations (c.8726delG; p.A2909Qfs*4 and c.493delA, p.I165Yfs*17). This subject presented a classical Joubert phenotype without extra-neuronal manifestations, suggesting that the additional *NINL* frameshift had no effect on the clinical manifestations (Figure 4k). Finally, subject UW57-3 carried a heterozygous *NINL* missense mutation (c.1631A>T, p.E544V), predicted to be deleterious by Polyphen2, along with bi-allelic causal *TMEM67* mutations (c.2825T>G, p.F942C and c.978+3 A>G). This individual had Joubert syndrome with coloboma but no retinal, renal or hepatic involvement (Figure 4l). Given the known association between *TMEM67* mutations and coloboma [34,12], this additional feature is most likely explained by the causal gene mutations, while the additional *NINL* variant appears to have no obvious effect on the phenotype in individual UW57-3. While it remains possible that additional sequence variants in non-JBTS genes also contributed to the enhanced phenotype in individual UW48-3 and while our findings from a large human cohort remain of anecdotal nature given the rarity of this highly heterogeneous genetic disorder, taken together with the zebrafish experiments, they suggest that *NINL* may act as a genetic modifier specifically for *CC2D2A*-caused Joubert syndrome.

2.5   Ninl is required for correct Rab8a localization

Previous work on the *cc2d2a^{uw38}* zebrafish mutant demonstrated that loss of Cc2d2a leads to abnormal Rab8a localization in retinal photoreceptors [25]. Given the opsin mislocalization and vesicle accumulation phenotypes observed in *ninl* morphants, the known role of Rab8a in opsin trafficking [27,35,36] and the interaction with *cc2d2a* demonstrated here, we next determined whether loss of Ninl function also had an effect on Rab8a localization. For this purpose, we used a transgenic construct that drives expression of mCherry-tagged Rab8a in wild-type zebrafish photoreceptors in a
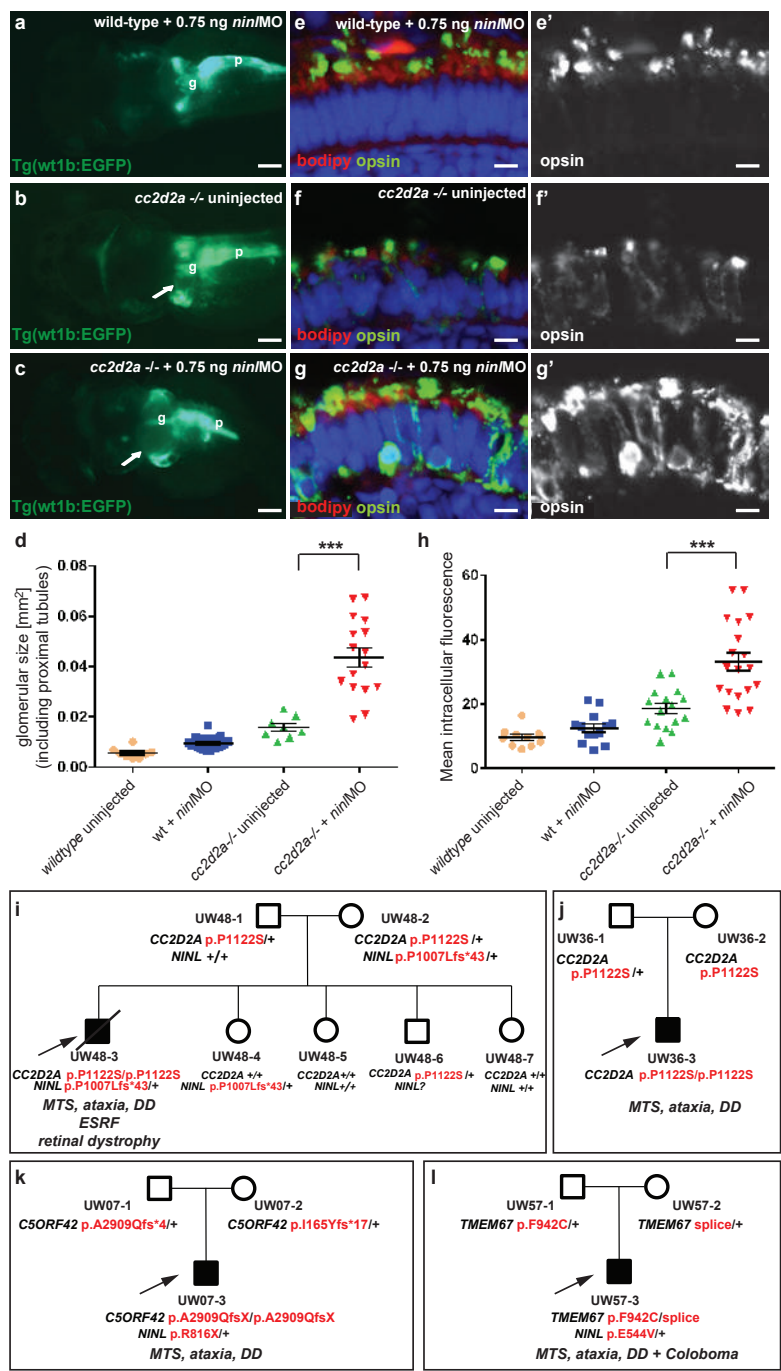
Figure 4. Genetic interaction between *ninl* and *cc2d2a*.

(**a-c**) Partial *ninl* knockdown enhances the cystic kidney phenotype of *cc2d2a* mutants. (**a-c**) Glomerulus and proximal pronephric tubules highlighted in the transgenic line Tg(wt1b-EGFP). (**a**) Injection of a low dose of *ninl* atgMO (0.75 ng/nl) causes no cysts in wild-type larvae. (**b**) *cc2d2a-/-* larvae display small dilatations of the proximal tubules (arrow) in ~40% of cases. (**c**) Injection of this low dose of *ninl* atgMO in the *cc2d2a-/-* background leads to large dilatations of the proximal tubules and glomerular space (arrow) in 89% of mutants. *g* glomerulus, *p* pancreas (**d**) Quantification of the glomerular + proximal tubular area displayed as a scatter plot, demonstrating a significant increase in proximal pronephric area in *cc2d2a-/-* larvae injected with low-dose *ninl* atgMO. The bars represent the mean and standard error of the mean (SEM) for each treatment group and each datapoint is an individual fish. (**e-g'**) Immunohistochemistry with anti-opsin antibody (4D2, green) on retinal cryosections of 4dpf *cc2d2a-/-* uninjected larvae (**f-f''**) and *cc2d2a-/-* larvae injected with subphenotypic doses of *ninl* MO (**g'g'''**), that cause no mislocalization in wild-type fish (**e-e'**), demonstrates that partial *ninl* knockdown increases the mislocalization of opsins (**e'-g'**). (**h**) Quantification of the mean intracellular fluorescence displayed as a scatter plot shows significant increase in intracellular fluorescence in *cc2d2a-/-* larvae injected with low dose of *ninl* atgMO. The bars represent the mean and standard error of the mean (SEM) for each treatment group and each datapoint represents the mean intracellular fluorescence from 10 photoreceptors in one individual fish. Cell membrane and outer segments are stained with bodipy (red in **e-**g). Nuclei are counterstained with DAPI. Scale bars are 100 μm in (a-c) and 4 μm in (e-g'). (**i**) Pedigree of a consanguineous family with one affected boy (UW48-3) and 4 unaffected siblings. UW48-3 carried a homozygous missense *CC2D2A* mutation as well as a frameshift mutation in *NINL* leading to premature truncation. (**j**) Pedigree of a family where the affected individual (UW36-3) carries the same homozygous *CC2D2A* mutation as in (**i**) but no additional rare deleterious variants. (**k**) Pedigree of a family where the affected individual (UW07-3) carries compound heterozygous *C5ORF42* frameshift mutations and a nonsense mutation in *NINL*. (**l**) Pedigree of a family where the affected individual (UW57-3) carries compound heterozygous *TMEM67* mutations and a missense *NINL* mutation. The phenotype of the affected individuals is detailed in *italic* on each pedigree under the corresponding mutations. *MTS* Molar Tooth Sign, *DD* Developmental Delay, *ESRF* End-Stage Renal Failure.

punctate manner [25]. When expressed in *ninl* morphants (atgMO), mCherry-tagged Rab8a localized in significantly fewer puncta than when expressed in controls (42% of expressing photoreceptors displayed Rab8 puncta in *ninl* morphants (n=38/87 from 14 larvae) compared to 73% in uninjected controls (n=48/66 from 13 larvae), *p*=0.0005, two-tailed Fisher's exact test; Figure 5a-c). Instead, expression of the transgene was mostly diffuse throughout the photoreceptor cell body of *ninl* morphants. A similar result was obtained using an anti-Rab8a antibody that recognizes endogenous small Rab8a puncta, which are found throughout the cell body, concentrated at the synapse and in the inner and outer segments in controls (Figure 5 d-d'). In *ninl*-knockdown larvae, the number of endogenous Rab8a puncta was significantly reduced (Figure 5e-e' and quantification in f: the average number of puncta per μm^2 was reduced to 0.04 +/- 0.01 (or 1 puncta per 25 μm^2) in *ninl* morphants as compared to 0.09 +/- 0.01 (or 1 puncta per 11 μm^2) in uninjected wild-type, *P*=0.01, unpaired Student's t-test), supporting a role for Ninl in Rab8 localization.
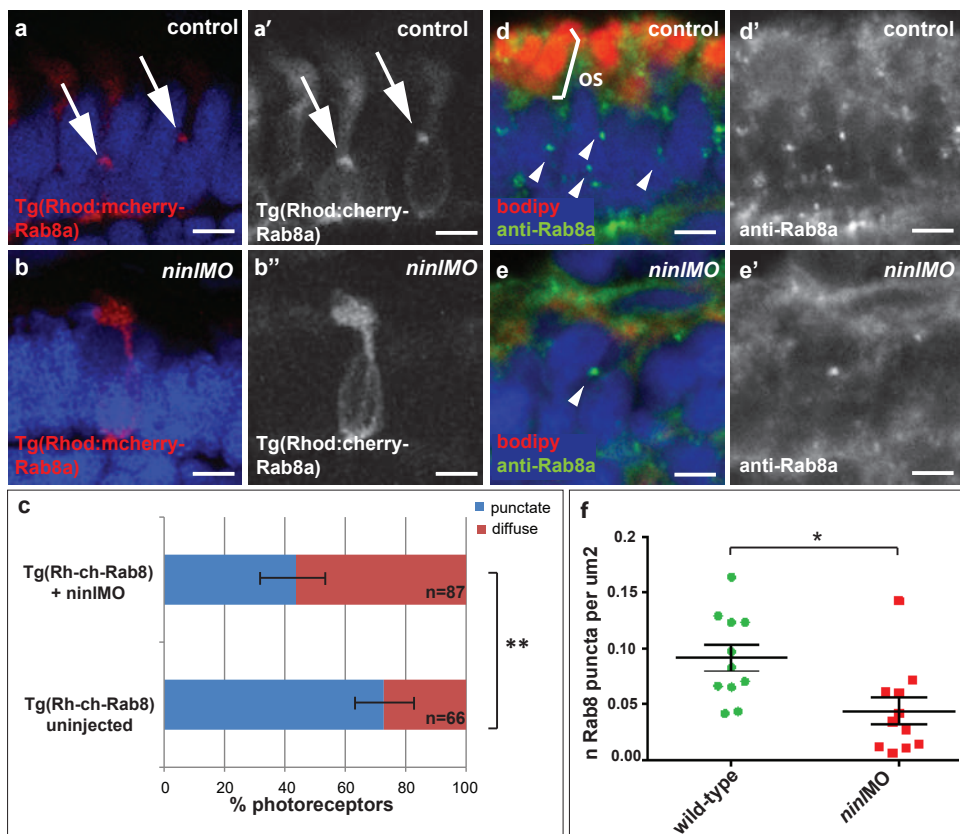
Figure 5. Ninl is required for correct Rab8A localization.

(**a-a'**) Expression of a rhodopsin-promoter driven cherry-tagged Rab8a in wild-type photoreceptors is mostly concentrated in one or several puncta (arrows **a-a'**) whereas it is diffuse in the majority of *ninl* morphant photoreceptors (**b-b'**). (**c**) Proportion of Rab8a-cherry expressing photoreceptors with punctate expression versus diffuse expression (bars represent 95% confidence interval; ** $P<0.001$, *Fisher's* exact test). (**d-d'**) Endogenous Rab8a localization as seen by immunohistochemistry using an anti-Rab8a antibody (green) displays similar puncta (arrowheads) in wild-type photoreceptors, while the number of puncta is decreased in *ninl* morphant photoreceptors (**e-e'**). (**f**) Quantification of the number of Rab8a puncta displayed in the form of a scatter plot indicating that significantly fewer endogenous Rab8 puncta per μm^2 are present in *ninl* morphants compared to uninjected controls (*$P=0.01$, unpaired Student's *t*-test; bars represent standard error of the mean). Scoring was performed blinded as to injection status for (**c**) and (**f**). Outer segments are counterstained with bodipy in (**d-e**). Nuclei are counterstained with DAPI. All images are cryosections of 4 dpf larvae. Scale bars are 4 μm in all panels.

2.6 MICAL3 associates with NINL and is mislocalized in NINL and CC2D2A-depleted cells

In order to unravel the underlying molecular cause of the observed vesicle accumulation and to identify proteins that interact with NINL, we next generated N-terminal Strep/FLAG-tagged fusion proteins of NINL isoA and isoB. A single-step affinity purification combined with quantification by stable isotope labeling of amino acids in cell culture (SILAC) and tandem affinity purification (TAP) [37] were applied to isolate the protein complexes in their native functional states from human embryonic kidney 293T (HEK293T) cells. The complexes were subsequently analyzed by liquid chromatography coupled with tandem mass spectrometry (LC-MS/MS). The identified interactome consisted of 174 unique proteins (Figure 6a, Supplementary table 1). An important association was found with multiple subunits of the cytoplasmic dynein 1-dynactin motor complex (DYNC1H1, DYNC1LI1, DYNC1LI2, DYNCI2, DYNLRB1, DCTN1-4, and DCTN6) which is involved in minus end–directed microtubule-associated transport. In addition, six actin-binding proteins (ARP1, ARP1B, ARP10, CAPZA1, CAPZA2 and CAPZB) and three subunits of Ca^{2+}/calmodulin-dependent protein kinase II (CaMKII) (CAMK2A, CAMK2D, and CAMK2G), involved in non-canonical Wnt5a signaling, synaptic plasticity and kidney development [38], were found to associate with NINL. An additional relevant NINL interaction partner identified was MICAL3 (Microtubule-associated Monooxygenase, Calponin and LIM domain containing 3 protein), which is known to participate in a protein complex with RAB6 and RAB8 that is involved in the fusion of exocytotic vesicles [39], a process that appears to be deficient in the retina of *cc2d2a* mutants and *ninl* morphants. We validated the interaction between NINL[isoB] and MICAL3 by reciprocal co-immunoprecipitations (Figure 6b) and confirmed that endogenously expressed MICAL3 is present at the photoreceptor connecting cilium in rat retina (P20), partially overlapping with the cilium and basal body marker polyglutamylated tubulin (Figure 7b-d'). In hTERT-RPE1 cells, mRFP-tagged NINL[isoB] (Figure 7e-e") and eCFP-tagged CC2D2A (Figure 7f-f") partially overlapped with tagged MICAL3.

To evaluate the role of NINL and CC2D2A in MICAL3 localization, we silenced the expression of *NINL* and *CC2D2A* in ciliated hTERT-RPE1 cells using siRNA, which was quantified by qPCR analysis (Figure 7j-k). Subsequent immunohistochemical stainings showed predominant MICAL3 localization at the ciliary base in non-targeting siRNA-treated cells (Figure 7g) whereas silencing of *NINL* expression resulted in a dispersed distribution of MICAL3 throughout the cell body (Figure 7h). Downregulation of *CC2D2A* expression in hTERT-RPE1 cells had a less pronounced effect on MICAL3 localization, resulting in partial mislocalization to the cell body (Figure 7i). These findings support a link between CC2D2A and MICAL3-RAB8-mediated vesicle trafficking/fusion through NINL.

2.2
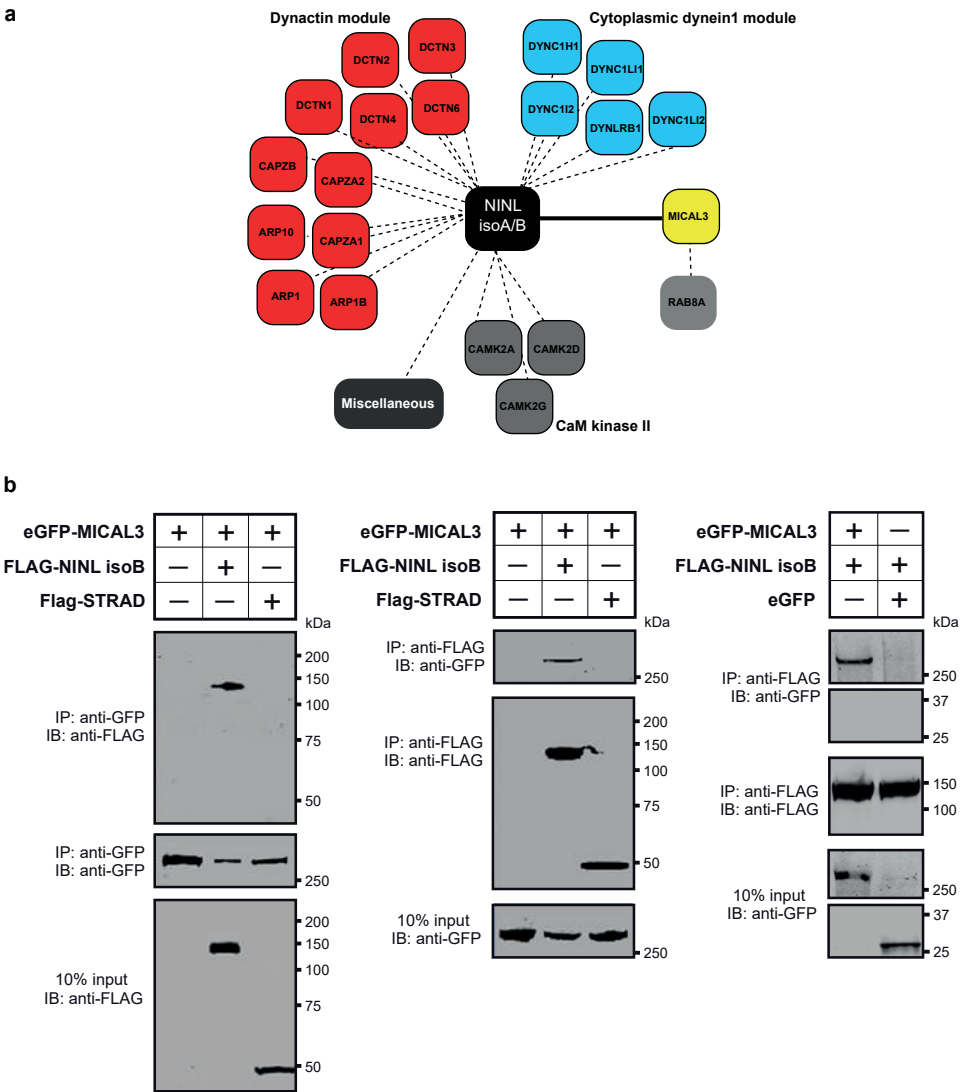
Figure 6. NINL interactome screen identifies MICAL3.

(**a**) Strep-SILAC and TAP (tandem affinity purification) experiments show that NINL interacts specifically with MICAL3 (Yellow). The solid line between NINL and MICAL3 symbolizes a direct interaction, whereas the dashed lines indicate interactions determined by IP. (**b**) Co-immunoprecipitation of eGFP-MICAL3 with FLAG-NINL[isoB], but not with FLAG-STRAD. The immunoblot (IB) in the top panel shows that eGFP-tagged MICAL3 co-immunoprecipitated with FLAG -tagged NINL (lane 2), whereas FLAG-tagged STRAD used as a negative control (lane 3) did not. The anti-GFP immunoprecipitates are shown in the middle panel; protein input is shown in the bottom panel. Reciprocal IP experiments using anti-FLAG antibodies confirmed the co-immunoprecipitation of eGFP-tagged MICAL3 with FLAG-tagged NINL[isoB] (lane 2) and not with STRAD (lane 3) shown in the top panel. The anti-FLAG immunoprecipitations are shown in the middle panel; protein input is shown in the bottom panel. A co-immunoprecipitation experiment using untagged eGFP as a negative control (right panel) showed that eGFP-tagged MICAL3 immunoprecipitates with FLAG-tagged NINL[isoB] but not with untagged eGFP.

Figure 7. NINL and CC2D2A co-localize with MICAL3 and are required for correct MICAL3 localization.

(**a**) Schematic of a photoreceptor for orientation. (**b-d'**) Co-localization of endogenous MICAL3 (green signal; **b**) and polyglutamylated tubulin (red signal; c) in rat retina (P20) by co-immunostaining radial cryosections. The yellow signal in the merged image (**d'**) indicates co-localization at the base of 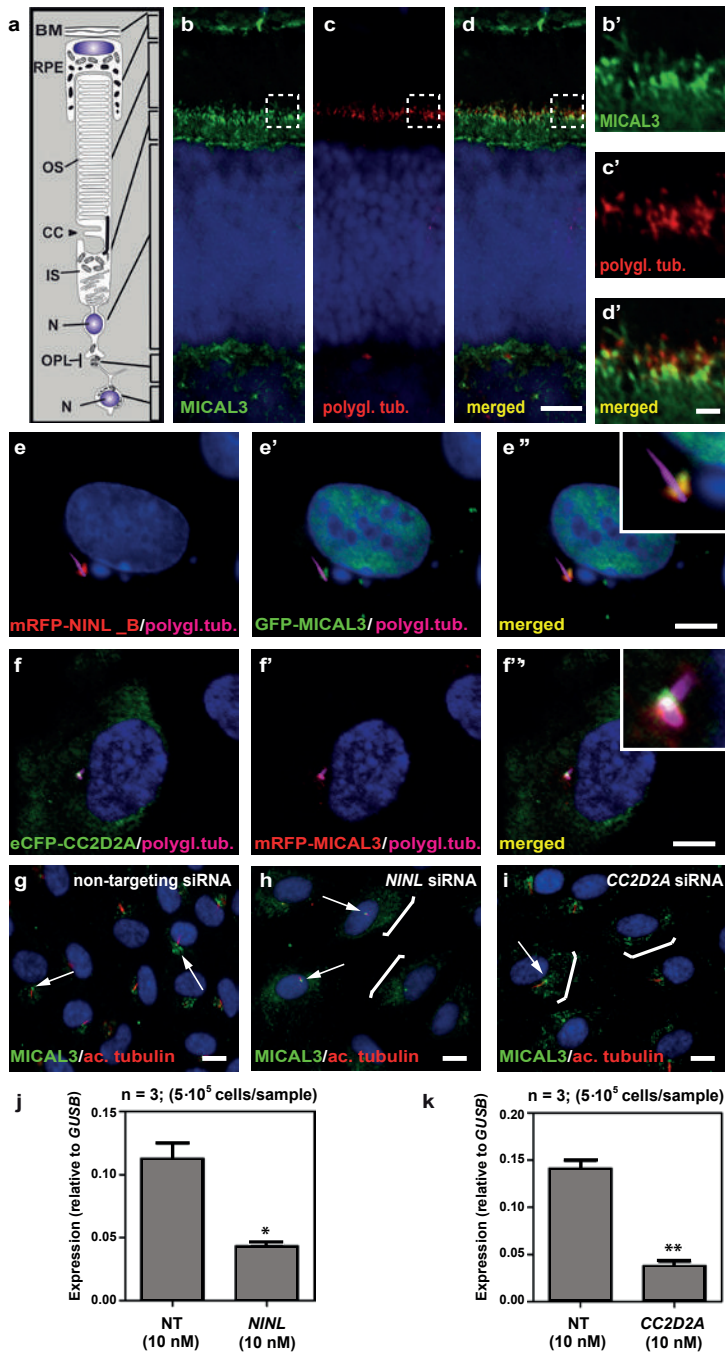the photoreceptor connecting cilium. (**b'-d'**) are high magnification images of the boxed areas in (b-d). (**e-f''**) Centrosomal co-localization of NINL[isoB], CC2D2A and MICAL3 in hTERT-RPE1 cells. mRFP-NINL[isoB] (red signal, **e**) localizes to the basal body of the cilia marked with polyglutamylated tubulin (cyanid signal; **e**) and overlaps with GFP-tagged MICAL3 (green signal, **e'**) at the ciliary base when co-expressed (yellow signal, **e''**). Co-expression of eCFP-CC2D2A (green signal, **f**) and mRFP-MICAL3 (red signal, f') resulted in partial overlap at the base of the cilia (yellow signal, **f''**). (**g**) Endogenous MICAL3 (green signal) detected by immunostaining clusters at the ciliary base (white arrows; cilium marked with anti-acetylated tubulin in red) of hTERT-RPE1 cells treated with non-targeting siRNA. (**h, i**) Knockdown of *NINL* (**h**) or *CC2D2A* (**i**) expression by siRNA results in dispersed distribution of MICAL3 throughout the cell body (brackets) with retention of some MICAL3 puncta at the ciliary base (arrows). qPCR analysis of *NINL* (**j**) and *CC2D2A* (**k**) siRNA treated hTERT-RPE1 cells. Cells were transfected with 10nM siRNA and all qPCR data were normalized against *GUSB* levels. Bar and error bars refer to mean and standard deviation, respectively (n=3, on two biological replicates). *: P<0.05; **: P<0.01 versus non targeting siRNA (NT) (student's *t*-test). Nuclei are counter stained with DAPI in all panels (blue signal). Scale bars: are 5 μm in d, 1 μm in d' and 10 μm in e-i.

3. DISCUSSION

Dysfunction of transition zone proteins causes several ciliopathies such as Joubert syndrome, Meckel syndrome, nephronophthisis or Usher syndrome [16,21,40–43]. Previous work suggests that transition zone proteins in general, and CC2D2A in particular, are required for correct localization of transmembrane proteins to the ciliary membrane [7,25]. The mechanism by which transition zone proteins exert this function and the link to upstream ciliary-directed vesicular trafficking mechanisms remain however largely unknown. In this work, we identify NINL as a novel physical interaction partner for the transition zone protein CC2D2A and propose a model linking CC2D2A to RAB8A-controlled vesicle trafficking through a dual role for NINL in microtubule-based vesicle transport (Figure 8). The association of NINL with both the cytoplasmic dynein 1-dynactin motor complex (Dona et al, co-submitted manuscript) and MICAL3 supports a role for NINL in the initial transport of trans-Golgi network-derived RAB8A-MICAL3 coated vesicles towards the base of the photoreceptor cilium, while the association of NINL with CC2D2A provides a docking point for these incoming vesicles at the entrance of the ciliary compartment.

Ciliary transmembrane proteins are synthesized in the cell body and travel from the Golgi towards the cilium in vesicles which move along microtubules using a cytoplasmic dynein motor [44]. Once at the entrance of the ciliary compartment, these vesicles must dock and fuse with the periciliary membrane to deliver their cargo into the ciliary membrane [45]. This path has been particularly well studied in photoreceptors, where large quantities of opsins and membrane continuously have to replenish the discs which constitute this photo-sensitive structure [26,46,35]. Opsin trafficking is severely affected in both zebrafish *cc2d2a* mutants and *ninl* morphants, suggesting that both proteins

play an important role in this transport which is crucial for the correct morphogenesis and homeostasis of the outer segments. Their co-localization at the base of the photoreceptor cilium could suggest that Cc2d2a and Ninl play a similar or combined role in opsin transport or that one protein is required to localize the other. However, since we found that each protein localizes independently of the other, and that *ninl* knockdown enhances the *cc2d2a* null mutant phenotype, the relationship between them is likely more complex than a simple linear pathway. At the ultrastructural level, the loss of function phenotypes of these two proteins also slightly diverge from each other: although vesicles accumulate in both cases in the affected photoreceptors, small vesiculo-tubular structures accumulate mostly apically around the connecting cilium in *cc2d2a* mutants [25], while this work shows that small vesicles and larger vacuoles are also present more basally and closer to an abnormal Golgi apparatus in *ninl* morphants. This suggests that both proteins are important for vesicular trafficking but play different roles in this process.
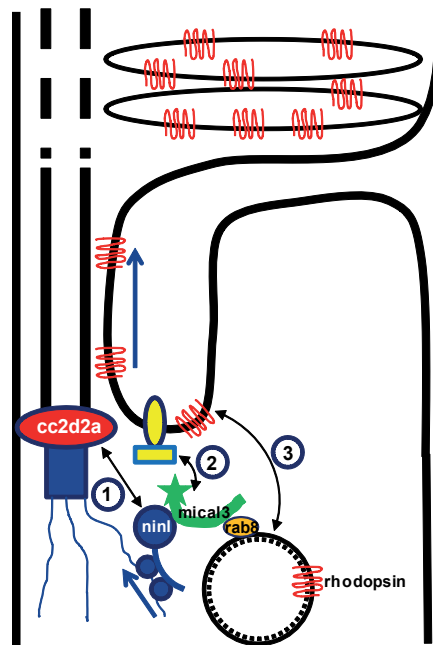
Figure 8. Proposed model for CC2D2A and NINL function in trafficking, docking and fusion of rhodopsin-carrier vesicles.

1) CC2D2A binds NINL and thus provides a docking point at the base of the connecting cilium for incoming vesicles. 2) NINL binds MICAL3 which in turn binds RAB8 that is coating the rhodopsin-carrier vesicles. Since NINL also associates with the cytoplasmic dynein1 motor complex, it provides a link between the carrier vesicles and the motor generating the movement along the microtubules. 3). MICAL3 subsequently interacts with ELKS and its redox activity promotes remodeling of the docking complex resulting in fusion of the vesicle at the periciliary region.

NINL has been previously shown to bind several other ciliopathy proteins present at the base of cilia, specifically LCA5 and USH2A [31], suggesting that it may play a more pivotal role in vesicular trafficking in photoreceptors than CC2D2A. Given that the zebrafish *ninl* morphant phenotype is more severe than the *cc2d2a* mutant phenotype, this further suggests a more central role for Ninl than for Cc2d2a in cilium-directed trafficking. This hypothesis is also supported by the lack of bi-allelic *NINL* mutations in a large human cohort of Joubert syndrome. Indeed, this may be interpreted as lack of tolerance to loss-of-function mutations in *NINL*, as these would lead to more severe phenotypes or early embryonic lethality. The direct interaction between NINL and the dynein 1-dynactin complex [47] which we confirmed and expanded in the associated study by Dona et al, suggests that NINL might be involved in minus end–directed microtubule-associated transport of organelles and cargo towards the base of the cilium. An appealing model would thus propose that NINL functions both more upstream in ciliary-directed vesicular trafficking than CC2D2A as well as at the base of the cilium where it interacts with several different proteins including CC2D2A.

While no bi-allelic rare deleterious *NINL* variants were identified in our JBTS cohort, we did find heterozygous *NINL* mutations in individuals with Joubert syndrome. Interestingly, only the individual with causal bi-allelic *CC2D2A* mutations and a heterozygous truncating *NINL* mutation had a severe phenotype with retinal and terminal renal disease. In comparison, the individuals with causal mutations in other JBTS genes and a heterozygous deleterious *NINL* mutation (or with the same causal *CC2D2A* mutation alone) had the classical "pure Joubert" phenotype without retinal or renal involvement. While bi-allelic *CC2D2A* mutations can result in a wide range of JBTS-associated phenotypes, the majority of individuals with causal *CC2D2A* mutations and JBTS display the "pure JBTS" phenotype [22]. The more severe phenotype only of the individual carrying causal *CC2D2A* mutations and an additional *NINL* truncating variant suggest that deleterious variants in *NINL* may act as genetic modifiers specifically of *CC2D2A*-caused ciliopathies such as Joubert syndrome. Unfortunately, the rarity of this disorder and its prominent genetic heterogeneity with over 27 associated genes prevent identification of multiple individuals sharing the same combination of causal and additional genetic variants, precluding identification of a statistically significant effect of rare variants as genetic modifiers using human genetics alone. Our findings from a large Joubert cohort therefore remain of anecdotal nature. However, the physical and genetic interaction in zebrafish identified in this work substantially strengthen the significance of this finding and suggest that deleterious variants in *NINL* may indeed enhance the retinal and renal phenotype in individuals with *CC2D2A*-associated Joubert syndrome. The effect on the retinal phenotype may be explained by the importance of NINL function in photoreceptors as highlighted in the present study. Enhancement

of the renal phenotype by the additional *NINL* mutation may be explained by the association identified in this study between NINL and the PKD2-target CaMKII, which is important for renal development [38].

The identification of MICAL3 as an interaction partner for NINL is of particular relevance in the context of vesicular trafficking given that MICAL3 binds RAB8A and plays a role in exocytotic vesicle fusion [39]. MICAL3 is part of the MICAL family of flavoprotein monooxygenases which regulate the actin cytoskeleton by disassembling the actin filaments. The redox function of MICAL3 is required to promote vesicle fusion, possibly by destabilizing protein complexes and remodeling the docking-fusion complexes in which it is engaged [39]. The role of RAB8A in vesicle fusion at the ciliary base has been abundantly documented in various cell types including photoreceptors [27,28]. While RAB8A was found to bind several ciliopathy proteins directly including CEP290 and RGPR [48,49], no direct interaction has been demonstrated between CC2D2A and RAB8A, despite a functional interaction in zebrafish photoreceptors and a requirement for CC2D2A in RAB8A localization in mouse embryonic fibroblasts [25,24]. Our findings now provide a model explaining the link between CC2D2A and RAB8A (Figure 8): RAB8A-coated vesicles destined to the ciliary compartment are bound by MICAL3 which in turn binds NINL that is associated to the cytoplasmic dynein 1 motor complex (Dona et al, co-submitted manuscript), allowing the movement along the microtubules. Once at the base of the cilium, NINL interacts with CC2D2A, providing the specificity of the docking point at the entrance to the ciliary compartment. Finally, the redox activity of MICAL3 promotes remodeling of the complex allowing fusion of the vesicle and release of cargo into the peri-ciliary membrane.

A role for CC2D2A in promoting the assembly of ciliary subdistal appendages was recently suggested whereby CC2D2A would be required for docking of transport vesicles [24]. This is compatible with our model which also provides a possible mechanism to explain how transition zone proteins may regulate ciliary protein composition by providing specific docking points at the entry to the ciliary compartment. Dysfunction of transition zone proteins can lead to a variety of ciliopathies and it is likely that abnormal ciliary protein composition is at least in part responsible for the observed disease phenotypes even in the absence of ciliogenesis defects. This provides an opportunity for the development of pathway-specific therapies aiming at modulating trafficking routes and restoring normal ciliary protein content. In this perspective, unraveling the cell biological function of disease genes such as *CC2D2A* as presented in the current study is a prerequisite for the future development of pharmacological treatments for patients with ciliopathies.

4.   MATERIAL AND METHODS

4.1   Zebrafish

Zebrafish (*Danio Rerio*) were maintained as described [50]. The *cc2d2a*[w38]/*sentinel* mutant (referred to as *cc2d2a* mutant or *cc2d2a*-/-) was previously described [25,51,52]. The transgenic Tg(wt1b:EGFP) line was previously described [53]. Embryos were raised at 28°C in embryo medium and pigment development was inhibited by phenylthiourea as described in Westerfield [50]. *ninl* translation-blocking (5'-CATCCTCGTCCATCCCAC CACATAC-3') morpholino (MO) and splice blocking (5'-CCCAACACTAAAGAGATACACCA AT-3') morpholinos were designed by Gene Tools Inc. (USA) and 1nl was injected into zebrafish embryos at the one-cell stage. After a titration curve, we established that 2ng/nl was the optimal phenotypic dose consistently causing the major phenotypes without significant cell death, while at the low dose of 0.75ng/nl, no phenotypes were observed (therefore called the "sub-phenotypic dose"). For the splice morpholino, the optimal phenotypic dose was 4ng/nl. For rescue experiments, cDNA encoding full length human *NINL* isoform B was cloned into a pCS2+ vector made compatible with the Gateway system (Invitrogen, USA), pCS2+/DEST, and subsequently transcribed with the SP6 Message Machine kit (Ambion, USA) according to manufacturer's instructions. The cherry-Rab8a construct was previously described [25]. All quantifications were performed blinded as to injection status. All animal protocols were in compliance with internationally recognized guidelines for the use of fish in biomedical research and experiments and were approved by the local authorities (Veterinäramt Zürich TV4206).

4.2   Plasmids

pDONR201 vectors containing cDNA encoding human NINL isoform A and B as well as aa 1-998, aa 433-637, aa 992-1177 of human *CC2D2A* were previously described [31,52]. Using Gateway cloning technology, cDNA fragments encoding aa 992-1620 and aa 1171-1620 of human *CC2D2A* (NM_001080522) were cloned in pDONR201 according to manufacturer's instructions. pEGFP-C1-MICAL3 was kindly provided by Dr. A. Akhmanova (Utrecht University, The Netherlands).

4.3   Yeast two-hybrid interaction assay

The direct interaction between CC2D2A and other ciliary proteins was tested using a GAL4-based yeast two-hybrid system (Hybrizap, Stratagene, USA) as previously described [30]. The DNA binding domain (GAL4-BD) fused to full length CC2D2A was used as a bait to test the interaction with previously described ciliopathy and cilium-associated proteins fused to an activation domain (GAL4-AD). Constructs encoding GAL4-BD and GAL4-AD fusion proteins were co-transformed in yeast strain PJ69-4A. The

direct interaction between baits and preys induced the activation of the reporter genes, resulting in the growth of yeast colonies on selective media (deficient of histidine and adenine) and induction of α-galactosidase and β-galactosidase colorimetric reactions [54].

4.4 Affinity purification of protein complexes

HEK293T cells transiently expressing the SF-TAP tagged NINL[isoB] were grown in SILAC DMEM (PAA) supplemented with 3 mM l-glutamine (PAA), 10% dialyzed fetal bovine serum (PAA), 0.55 mM lysine, and 0.4 mM arginine. Light SILAC medium was supplemented with $^{12}C_6,^{14}N_2$ lysine and $^{12}C_6,^{14}N_4$ arginine. Heavy SILAC medium was supplemented with either $^{13}C_6$ lysine and $^{13}C_6,^{15}N_4$ arginine or $^{13}C_6,^{15}N_2$ lysine and $^{13}C_6,^{15}N_4$ arginine. 0.5 mM proline was added to all SILAC media to prevent arginine-to-proline conversion [55]. All amino acids were purchased from Silantes. For one-step Strep purifications, SF-TAP–tagged proteins and associated protein complexes were purified essentially as described previously [37,56]. HEK293T cells transiently expressing the SF-TAP tagged constructs were lysed in lysis buffer containing 0.5% Nonidet-P40, protease inhibitor cocktail (Roche), and phosphatase inhibitor cocktails I and II (Sigma-Aldrich) in TBS (30 mM Tris-HCl, pH 7.4, and 150 mM NaCl) for 20 minutes at 4°C. After sedimentation of nuclei at 10,000 g for 10 minutes, the cleared lysates were transferred to Strep-Tactin-Superflow beads (IBA) and incubated for 1 hour before the resin was washed 3 times with wash buffer (TBS containing 0.1% NP-40 and phosphatase inhibitor cocktails I and II). The protein complexes were eluted by incubation for 10 minutes in Strep-elution buffer (IBA). After purification, the samples were precipitated with chloroform and methanol and subjected to in-solution tryptic cleavage as described previously [57]. LC-MS/MS analysis was performed on an Ultimate3000 nano HPLC system (Dionex) coupled to a LTQ OrbitrapXL mass spectrometer (Thermo Fisher Scientific) by a nanospray ion source. The raw data were analyzed using Sequest (Thermo Fisher Scientific) or Mascot and Scaffold (Proteome Software) as described previously [57]. Proteins were considered to be specific protein complex components if they were not detected in the control and were detected at least twice with two or more peptides (peptide probability >80%) in three experiments. The protein probability threshold was set to 99%.

4.5 Knockdown of *NINL* and *CC2D2A* in cultured hTERT-RPE1 cells by RNAi

Three Silencer Select siRNAs targeting *NINL* and *CC2D2A* were purchased from Life Technologies (targeting sequences are listed in Supplementary Table 2). For transfection, a pool of three siRNAs per gene (45 nM final concentration) were plated in MW12 plates with or without glass slides. Lipofectamine RNAiMax (LifeTechnologies) and Opti-MEM (LifeTechnologies) were added to the duplexes and incubated for 10-20 minutes

according to manufacturer's protocol to allow the formation of transfection complexes. Human telomerase reverse transcriptase-transformed retinal pigment epithelium (hTERT-RPE1) cells from American Type Culture Collection (ATCC) were then plated in MW12 plates. Per plate, non-targeting Silencer Select duplexes (LifeTechnologies) were included as negative controls. After 24 hours of transfection, cells were serum-starved to induce ciliogenesis. After 72 hours of transfection, knockdown-efficiency was determined by isolating total RNA from one 12-well with Trizol (Invitrogen, USA), followed by first-strand cDNA synthesis (iScript; Bio-Rad, USA). Quantitative PCRs using GoTaq (Promega), with validated *NINL-, CC2D2A-* and *GUSB*-specific primers (sequences are listed in Supplementary Table 3), were performed as previously described [31]. The second 12-well of cells were fixed with 2% paraformaldehyde, permeabilized with 1% Triton-X-100/PBS and stained with anti-MICAL3 antibodies (kindly provided by Dr. A. Akhmanova). Images were taken with an Axioplan2 Imaging fluorescence microscope (Zeiss, Germany) equipped with a DC350FX camera (Zeiss, Germany).

4.6   Co-immunoprecipitation in HEK293T cells

HA-tagged NINL isoform B was expressed by using the mammalian expression vector pcDNA3-HA/DEST, FLAG-tagged CC2D2A, LRRK2 and STRAD by using p3xFLAG-CMV/DEST and strep-FLAG-tagged NINL isoform B by using pNTAPe5/DEST from the Gateway cloning system (Invitrogen, USA). eGFP and eGFP-tagged MICAL3 were expressed from pEGFP-C1 (Clontech, USA). All plasmids contain a CMV promoter. HEK293T cells were co-transfected using Effectene (Qiagen, USA) according to manufacturer's instructions. Twenty-four hours after transfection cells were washed with PBS and subsequently lysed on ice in lysis buffer (50 mM Tris-HCl pH 7.5, 150 mM NaCl, 1% Triton-X-100 supplemented with complete protease inhibitor cocktail (Roche, Germany)). HA-tagged NINL isoform B was immunoprecipitated from cleared lysates overnight at 4°C by using rat monoclonal anti-HA-beads (Roche, Germany), while FLAG-tagged CC2D2A, LRRK2, STRAD and NINL isoform B were immunoprecipitated by using monoclonal anti-FLAG M2 Agarose beads (Sigma, Germany) and eGFP-tagged MICAL3 was immunoprecipitated using anti-GFP polyclonal antibodies (Abcam) coupled to ProtA/G beads (Santa Cruz, USA). After 4 washes in lysis buffer, the protein complexes were analyzed on immunoblots using the Odyssey Infrared Imaging System (LI-COR, USA). Tagged molecules were detected by anti-HA, anti-FLAG or anti-GFP mono- or polyclonal antibodies. As secondary antibody IRDye800 goat-anti-mouse IgG (Rockland Antibodies and Assays) and Alexa Fluor 680 goat-anti-rabbit IgG (Life Technologies) were used.

4.7 Immunohisto- and immunocytochemistry

Zebrafish larvae were fixed in 4% paraformaldehyde (PFA) overnight at 4°C, embedded in OCT and cryosectioned following standard protocols. Sections were blocked using PBDT (PBS, 1% DMSO, 0.1% Triton X, 2mg/ml BSA) with 10% goat serum for 30 minutes at RT before incubation with primary antibodies overnight. Primary antibodies were mouse monoclonal anti-acetylated alpha tubulin (1:500, clone 6-11B-1, Sigma), mouse monoclonal anti-polyglutamylated tubulin GT335 (1:500, gift from C. Janke, Institut Curie, France), mouse anti-zebrafish Cc2d2a (1:20, [25]), rabbit anti-NINL (1:100; LSBio Cat# LS-C201509), mouse anti-*pan* centrin 20H5 (1:200, clone 20H5 Millipore), mouse anti-Rab8a (1:100, clone 3G1 Novus Biologicals), mouse anti-opsin 4D2 (1:100, gift from R. Molday, University of British Columbia) and rabbit anti-Ift88 (gift from B. Perkins [58], Cleveland Clinic), mouse monoclonal anti-FLAG (1:1000, Sigma), rabbit polyclonal anti-human MICAL3 [39]. Secondary antibodies were Alexa Fluor goat anti-rabbit or goat anti-mouse IgG (Life Technologies) used at 1:300. Bodipy (1:300, Invitrogen) was applied for 20 minutes after the secondary antibodies and nuclei were counterstained with DAPI. Rab8 puncta detected by immuno-staining using the mouse anti-Rab8 antibody were analyzed blinded as to injection status in ImageJ. A region of interest was manually determined on single confocal sections and was thresholded (always with the same parameters); the "analyze particles" function of ImageJ was then used to determine the number of puncta per μm^2. For quantification of intracellular fluorescence after 4D2 (opsin) immuno-staining, a region of interest including 10-15 photoreceptor cell bodies was determined on single confocal sections using ImageJ and the mean grey value was measured. For quantification of the proximal pronephric area, the fluorescent region corresponding to the glomerulus and the proximal tubules up to the curved part of the tubule was outlined manually in ImageJ and the "measure" function was used to determine the area of the outlined region. All quantifications were performed blinded as to injection status. Confocal imaging was performed on a Leica HCS LSI.

4.8 Paraffin sections and Transmission Electron Microscopy

For paraffin sections, 4 dpf old *ninl* morphant larvae were fixed in 4% PFA overnight at 4°C, embedded in paraffin and sectioned following standard protocols. For Transmission Electron Microsopy, *ninl* morphant and control larvae were fixed overnight at 4°C in a freshly prepared mixture of 2,5 % glutaraldehyde and 2% paraformaldehyde in 0.1 M sodiumcacodylate buffer (pH 7.4). After rinsing in buffer, specimens were post-fixed in a freshly prepared mixture, containing 1% osmiumtetroxide and 1% potassiumferrocyanide in 0.1 M sodiumcacodylate buffer (pH 7.4), during 2 h at room temperature. After rinsing, tissues were dehydrated through a graded series of ethanol and embedded in epon. Ultrathin (rostrocaudally) sections (70nm), comprising zebrafish

eyes at the optic nerve level, were collected on formvar coated grids, subsequently stained with 2% uranyl acetate and Reynold's lead citrate, and examined with a Jeol1010 electron microscope.

4.9 Sequencing of *NINL* in a cohort of Joubert syndrome patients

346 individuals (from 291 families) with Joubert syndrome (JBTS) from the University of Washington Joubert Research Center were examined for mutations in *NINL*. Minimal enrollment criteria included clinical findings of JBTS (intellectual impairment, hypotonia, ataxia) and diagnostic or supportive brain imaging findings, or presence of a sibling with JBTS along with supportive clinical or imaging features. Procedures were approved by the Institutional Review Boards at the UW and Seattle Children's Hospital, and all participants or their legal representatives provided written informed consent. Genomic DNA from peripheral blood or saliva was extracted and all *NINL* exons were captured by Molecular Inversion Probes (MIPS) [33]. Captured DNA was PCR amplified and sequenced on either the Illumina HiSeq or MiSeq platform. Sequence reads were mapped using the Burrows-Wheeler Aligner (BWA v.0.5.9). Variants were called using the Genome Analysis Tookit (GATK v2.5-2) and annotated with SeattleSeq (http://snp.gs.washington.edu/SeattleSeqAnnotation138/). Minimal quality criteria for analyzed variants were DP (Depth) ≥ 8, QD (Quality by Depth) > 5, and ABHet (Heterozygous Allele Balance) <0.8. The variant list was then filtered for rare and deleterious variants. Only variants with minor allele frequency of <1% were considered given the rarity of JBTS (estimated prevalence 1/80'000 [11]). All non-sense, frameshift and canonical splice-site variants, as well as missense variants with Polyphen2 scores >0.8 were considered deleterious. Selected variants were Sanger confirmed.

4.10 Statistical Analyses

For all quantifications of zebrafish experiments, the Graphpad Prism6 software (http://www.graphpad.com/scientific-software/prism/) was employed to generate scatter plots, calculate mean values and SEM values, and perform statistical tests. Continuous data was analyzed using two-tailed, unpaired Student's t-test and categorical data was analyzed using Fisher's exact test.

ACKNOWLEDGEMENTS

2.2

REFERENCES

1. Goetz SC, Anderson KV (2010) The primary cilium: a signalling centre during vertebrate development. Nat Rev Genet 11 (5): 331–344.

2. Tyler KM, Fridberg A, Toriello KM, Olson CL, Cieslak JA et al. (2009) Flagellar membrane localization via association with lipid rafts. Journal of Cell Science 122 (6): 859–866.

3. Hu Q, Milenkovic L, Jin H, Scott MP, Nachury MV et al. (2010) A Septin Diffusion Barrier at the Base of the Primary Cilium Maintains Ciliary Membrane Protein Distribution. Science 329 (5990): 436–439.

4. Nachury MV, Seeley ES, Jin H (2010) Trafficking to the Ciliary Membrane: How to Get Across the Periciliary Diffusion Barrier. Annu. Rev. Cell Dev. Biol. 26 (1): 59–87.

5. Williams CL, Li C, Kida K, Inglis PN, Mohan S et al. (2011) MKS and NPHP modules cooperate to establish basal body/transition zone membrane associations and ciliary gate function during ciliogenesis. The Journal of Cell Biology 192 (6): 1023–1041.

6. Reiter JF, Blacque OE, Leroux MR (2012) The base of the cilium: roles for transition fibres and the transition zone in ciliary formation, maintenance and compartmentalization. EMBO reports 13 (7): 608–618.

7. Garcia-Gonzalo FR, Corbit KC, Sirerol-Piquer MS, Ramaswami G, Otto EA et al. (2011) A transition zone complex regulates mammalian ciliogenesis and ciliary membrane composition. Nat Genet 43 (8): 776–784.

8. Hildebrandt F, Benzing T, Katsanis N (2011) Ciliopathies. N Engl J Med 364 (16): 1533–1543.

9. Badano JL, Mitsuma N, Beales PL, Katsanis N (2006) The Ciliopathies: An Emerging Class of Human Genetic Disorders. Annu. Rev. Genom. Human Genet. 7 (1): 125–148.

10. Insinna C, Besharse JC (2008) Intraflagellar transport and the sensory outer segment of vertebrate photoreceptors. Dev. Dyn. 237 (8): 1982–1992.

11. Parisi MA, Glass I (2003) Joubert syndrome and related disorders.

12. Bachmann-Gagescu R, Dempsey JC, Phelps IG, O'Roak BJ, Knutzen DM et al. (2015) Joubert syndrome: a model for untangling recessive disorders with extreme genetic heterogeneity. J Med Genet 52(8):514-22.

13. Maria BL, Hoang KBN, Tusa RJ, Mancuso AA, Hamed LM et al. (1997) "Joubert Syndrome" Revisited: Key Ocular Motor Signs With Magnetic Resonance Imaging Correlation. Journal of Child Neurology 12 (7): 423–430.

14. Romani M, Micalizzi A, Valente EM (2013) Joubert syndrome: congenital cerebellar ataxia with the molar tooth. Lancet Neurol. 12 (9): 894–905.

15. Doherty D (2009) Joubert Syndrome: Insights Into Brain Development, Cilium Biology, and Complex Disease. Developmental Disorders of the Central Nervous System: Bench to Bedside and Back Again 16 (3): 143–154.

16. Romani M, Micalizzi A, Valente EM (2013) Joubert syndrome: congenital cerebellar ataxia with the molar tooth. Lancet Neurol. 12 (9): 894–905.

17. Romani M, Micalizzi A, Kraoua I, Dotti M, Cavallin M et al. (2014) Mutations in B9D1 and MKS1 cause mild Joubert syndrome: expanding the genetic overlap with the lethal ciliopathy Meckel syndrome. Orphanet Journal of Rare Diseases 9 (1): 72.

18. Tuz K, Bachmann-Gagescu R, O'Day DR, Hua K, Isabella CR et al. (2014) Mutations in CSPP1 Cause Primary Cilia Abnormalities and Joubert Syndrome with or without Jeune Asphyxiating Thoracic Dystrophy. The American Journal of Human Genetics 94 (1): 62–72. Available: http://www.sciencedirect.com/science/article/pii/S000292971300534X.

19. Thauvin-Robinet C, Lee JS, Lopez E, Herranz-Perez V, Shida T et al. (2014) The oral-facial-digital syndrome gene C2CD3 encodes a positive regulator of centriole elongation. Nat Genet 46 (8): 905–911.

20. Thomas S, Wright KJ, Le Corre S, Micalizzi A, Romani M et al. (2014) A Homozygous PDE6D Mutation in Joubert Syndrome Impairs Targeting of Farnesylated INPP5E Protein to the Primary Cilium. Hum. Mutat. 35 (1): 137–146.

21. Sang L, Miller JJ, Corbit KC, Giles RH, Brauer MJ et al. (2011) Mapping the NPHP-JBTS-MKS Protein Network Reveals Ciliopathy Disease Genes and Pathways. Cell 145 (4): 513–528.

22. Bachmann-Gagescu R, Ishak GE, Dempsey JC, Adkins J, O'Day D et al. (2012) Genotype–phenotype correlation in CC2D2A-related Joubert syndrome reveals an association with ventriculomegaly and seizures. Journal of Medical Genetics 49 (2): 126–137.

23. Mougou-Zerelli S, Thomas S, Szenker E, Audollent S, Elkhartoufi N et al. (2009) CC2D2A mutations in Meckel and Joubert syndromes indicate a genotype–phenotype correlation. Hum. Mutat. 30 (11): 1574–1582.

24. Veleri S, Manjunath SH, Fariss RN, May-Simera H, Brooks M et al. (2014) Ciliopathy-associated gene Cc2d2a promotes assembly of subdistal appendages on the mother centriole during cilia biogenesis. Nat Commun 5: http://dx.doi.org/10.1038/ncomms5207.

25. Bachmann-Gagescu R, Phelps IG, Stearns G, Link BA, Brockerhoff SE et al. (2011) The ciliopathy gene cc2d2a controls zebrafish photoreceptor outer segment development through a role in Rab8-dependent vesicle trafficking. Human Molecular Genetics 20 (20): 4041–4055.

26. Deretic D, Wang J (2012) Molecular assemblies that control rhodopsin transport to the cilia. Retina Ciliopathies: From Genes to Mechanisms and Treatment 75 (0): 5–10.

27. Moritz OL, Tam BM, Hurd LL, Peränen J, Deretic D et al. (2001) Mutant rab8 Impairs Docking and Fusion of Rhodopsin-bearing Post-Golgi Membranes and Causes Cell Death of TransgenicXenopus Rods. Molecular Biology of the Cell 12 (8): 2341–2351.

28. Nachury MV, Loktev AV, Zhang Q, Westlake CJ, Peränen J et al. (2007) A Core Complex of BBS Proteins Cooperates with the GTPase Rab8 to Promote Ciliary Membrane Biogenesis. Cell 129 (6): 1201–1213.

29. Westlake CJ, Baye LM, Nachury MV, Wright KJ, Ervin KE et al. (2011) Primary cilia membrane assembly is initiated by Rab11 and transport protein particle II (TRAPPII) complex-dependent trafficking of Rabin8 to the centrosome. Proceedings of the National Academy of Sciences 108 (7): 2759–2764.

30. Cevik S, Sanders AAWM, van Wijk E, Boldt K, Clarke L et al. (2013) Active Transport and Diffusion Barriers Restrict Joubert Syndrome-Associated ARL13B/ARL-13 to an Inv-like Ciliary Membrane Subdomain. PLoS Genet 9 (12): e1003977 EP.

31. van Wijk E, Kersten FFJ, Kartono A, Mans DA, Brandwijk K et al. (2009) Usher syndrome and Leber congenital amaurosis are molecularly linked via a novel isoform of the centrosomal ninein-like protein. Human Molecular Genetics 18 (1): 51–64.

2.2

32. Ben J, Elworthy S, Ng ASM, van Eeden F, Ingham PW (2011) Targeted mutation of the talpid3 gene in zebrafish reveals its conserved requirement for ciliogenesis and Hedgehog signalling across the vertebrates. Development 138 (22): 4969–4978.

33. O'Roak BJ, Vives L, Fu W, Egertson JD, Stanaway IB et al. (2012) Multiplex Targeted Sequencing Identifies Recurrently Mutated Genes in Autism Spectrum Disorders. Science 338 (6114): 1619–1622.

34. Doherty D, Parisi MA, Finn LS, Gunay-Aygun M, Al-Mateen M et al. (2010) Mutations in 3 genes (MKS3, CC2D2A and RPGRIP1L) cause COACH syndrome (Joubert syndrome with congenital hepatic fibrosis). Journal of Medical Genetics 47 (1): 8–21.

35. Wang J, Deretic D (2014) Molecular complexes that direct rhodopsin transport to primary cilia. Progress in Retinal and Eye Research 38 (0): 1–19.

36. Wang J, Morita Y, Mazelova J, Deretic D (2012) The Arf GAP ASAP1 provides a platform to regulate Arf4- and Rab11–Rab8-mediated ciliary receptor targeting. The EMBO Journal 31 (20): 4057–4071.

37. Gloeckner CJ, Boldt K, Schumacher A, Roepman R, Ueffing M (2007) A novel tandem affinity purification strategy for the efficient isolation and characterisation of native protein complexes. Proteomics 7 (23): 4228–4234.

38. Rothschild SC, Francescatto L, Drummond IA, Tombes RM (2011) CaMK-II is a PKD2 target that promotes pronephric kidney development and stabilizes cilia. Development 138 (16): 3387–3397.

39. Grigoriev I, Yu KL, Martinez-Sanchez E, Serra-Marques A, Smal I et al. Rab6, Rab8, and MICAL3 Cooperate in Controlling Docking and Fusion of Exocytotic Carriers. Current Biology 21 (11): 967–974.

40. Wolfrum U1 LXSAUIWD (1998) Myosin VIIa as a common component of cilia and microvilli. Cell Motil Cytoskeleton 40 (3): 261–271.

41. Maerker T, van Wijk E, Overlack N, Kersten FFJ, McGee J et al. (2008) A novel Usher protein network at the periciliary reloading point between molecular transport machineries in vertebrate photoreceptor cells. Human Molecular Genetics 17 (1): 71–86.

42. van Wijk E, van der Zwaag B, Peters T, Zimmermann U, te Brinke H et al. (2006) The DFNB31 gene product whirlin connects to the Usher protein network in the cochlea and retina by direct association with USH2A and VLGR1. Human Molecular Genetics 15 (5): 751–765.

43. Kremer H, van Wijk E, Märker T, Wolfrum U, Roepman R (2006) Usher syndrome: molecular links of pathogenesis, proteins and pathways. Human Molecular Genetics 15 (suppl 2): R262.

44. Madhivanan K, Aguilar RC (2014) Ciliopathies: The Trafficking Connection. Traffic 15 (10): 1031–1056. Available: http://dx.doi.org/10.1111/tra.12195.

45. Hsiao Y, Tuz K, Ferland R (2012) Trafficking in and to the primary cilium. Cilia 1 (1): 4.

46. Kennedy B, Malicki J (2009) What drives cell morphogenesis: A look inside the vertebrate photoreceptor. Dev. Dyn. 238 (9): 2115–2138.

47. Casenghi M, Barr FA, Nigg EA (2005) Phosphorylation of Nlp by Plk1 negatively regulates its dynein-dynactin-dependent targeting to the centrosome. Journal of Cell Science 118 (21): 5101–5108.

48. Kim J, Krishnaswami SR, Gleeson JG (2008) CEP290 interacts with the centriolar satellite component PCM-1 and is required for Rab8 localization to the primary cilium. Human Molecular Genetics 17 (23): 3796–3805.

2.2

49. Murga-Zamalloa CA, Atkins SJ, Peranen J, Swaroop A, Khanna H (2010) Interaction of retinitis pigmentosa GTPase regulator (RPGR) with RAB8A GTPase: implications for cilia dysfunction and photoreceptor degeneration. Human Molecular Genetics 19 (18): 3591–3598.

50. Westerfield M The Zebrafish Book. A Guide for the Laboratory Use of Zebrafish (Danio rerio). University of Oregon Press, Eugene, OR.

51. Owens KN, Santos F, Roberts B, Linbo T, Coffin AB et al. (2008) Identification of Genetic and Chemical Modulators of Zebrafish Mechanosensory Hair Cell Death. PLoS Genet 4 (2): e1000020 EP.

52. Gorden NT, Arts HH, Parisi MA, Coene KLM, Letteboer SJF et al. (2008) CC2D2A Is Mutated in Joubert Syndrome and Interacts with the Ciliopathy-Associated Basal Body Protein CEP290. The American Journal of Human Genetics 83 (5): 559–571.

53. Perner B, Englert C, Bollig F (2007) The Wilms tumor genes wt1a and wt1b control different steps during formation of the zebrafish pronephros. Developmental Biology 309 (1): 87–96.

54. Letteboer SF, Roepman R (2008) Versatile Screening for Binary Protein-Protein Interactions by Yeast Two-Hybrid Mating. In: Thompson J, Ueffing M, Schaeffer-Reiss C, editors. Functional Proteomics: Humana Press. pp. 145-159.

55. Bendall SC, Hughes C, Stewart MH, Doble B, Bhatia M et al. (2008) Prevention of Amino Acid Conversion in SILAC Experiments with Embryonic Stem Cells. Molecular & Cellular Proteomics 7 (9): 1587–1597.

56. den Hollander AI, Koenekoop RK, Mohamed MD, Arts HH, Boldt K et al. (2007) Mutations in LCA5, encoding the ciliary protein lebercilin, cause Leber congenital amaurosis. Nat Genet 39 (7): 889–895.

57. Gloeckner CJ, Boldt K, Ueffing M (2001) Strep/FLAG Tandem Affinity Purification (SF-TAP) to Study Protein Interactions. Current Protocols in Protein Science: John Wiley & Sons, Inc.

58. Krock BL, Perkins BD (2008) The intraflagellar transport protein IFT57 is required for cilia maintenance and regulates IFT-particle–kinesin-II dissociation in vertebrate photoreceptors. Journal of Cell Science 121 (11): 1907–1915.

SUPPLEMENTAL DATA

A
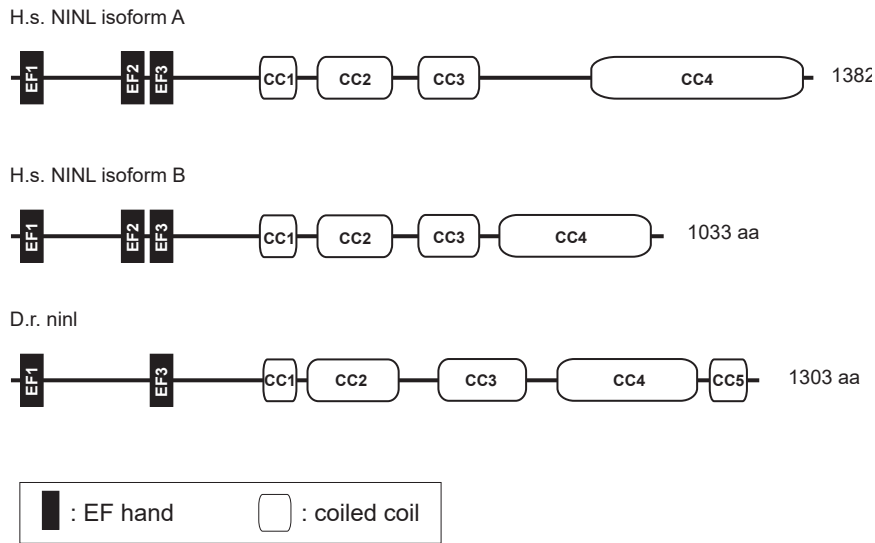
B
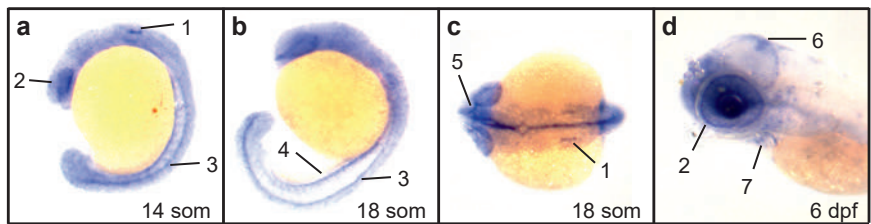
Figure S1. Cloning and characterization of zebrafish *ninl*.

(**a**) Schematic representation of the protein structure of human NINL[isoA] and NINL[isoB] (*H.s.* NINL[isoA] and *H.s.* NINL[isoB]) and zebrafish ninl (*D.r.* ninl) as predicted by using the Pfam homepage (http://pfam.xfam.org/). (**b**) *Ninl* expression during zebrafish development by whole mount RNA *in situ* hybridization. Specific expression was found in the following structures as indicated by numbers and arrows: (**a**) 14 somite stage: otic placode (1); developing eye (2); neural tube (spinal cord) (3); (**b**) 18 somite stage: neural tube (3); pronephros (4); (**c**) 18 somite stage: inner ear (1); optic nerve (5). (**d**) At 6 dpf, expression was observed in the tectum (6), the heart (7) and in the eye (2), predominantly in the photoreceptor cell layer. *H.s.*: *homo sapiens*; *D.r.*: *danio rerio*; CC: coiled-coil; som: somites; dpf: days post-fertilization.
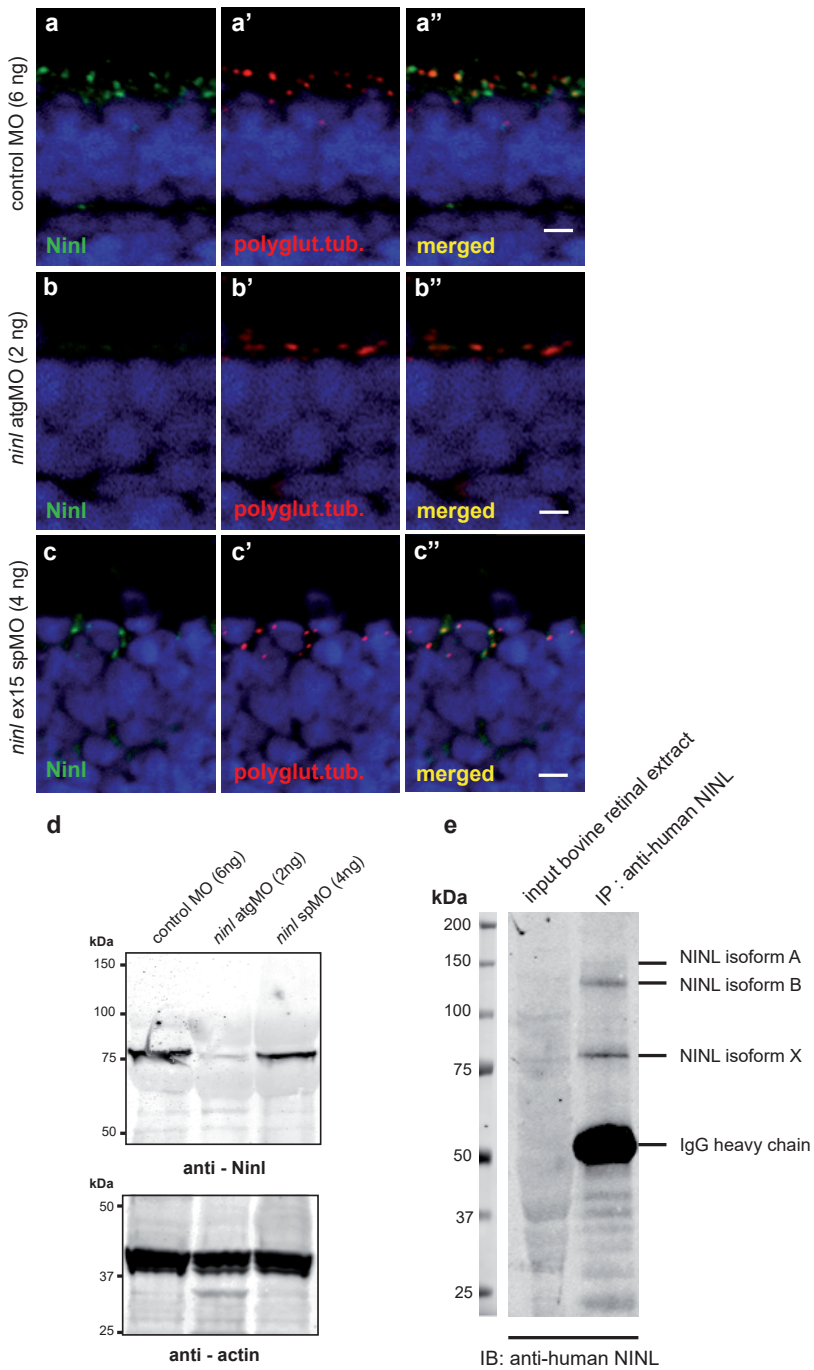
Figure S2. Specificity of the anti-Ninl antibody.

(**a**) Indirect immunohistochemical staining using anti-Ninl antibody on 4 dpf retinal cryosections of control MO-injected larvae (green signal) shows punctate staining, partially overlapping with the ciliary marker anti-polyglutamylated tubulin (**a′, a″**, red signal). (**b**) Indirect immunohistochemical staining using anti-Ninl antibody on 4 dpf retinal cryosections of *ninl* atgMO-injected larvae (**b**, green signal) along with the ciliary marker anti-polyglutamylated tubulin (**b′, b″**, red signal). Specific Ninl-immunofluorescence is largely abolished in *ninl* morphants, whereas the polyglutamylated tubulin signal is still detected. (**c**) Indirect immunohistochemical staining of anti-Ninl on 4 dpf retinal cryosections of *ninl* ex15 spMO-injected larvae (green signal) along with the ciliary marker anti-polyglutamylated tubulin (c′, c″, red signal). Specific Ninl-immunofluorescence was still detected but at a diminished level in *ninl* morphants whereas the polyglutamylated tubulin signal was unaltered. Nuclei are stained with DAPI (blue signal). Scale bars: 4 μm. (**d**) Western blot analysis using protein extracts obtained from 100 zebrafish larvae injected with either control MO (6ng), *ninl* atgMO (2ng) or *ninl* ex15 spMO (4ng). A specific product was detected with a molecular weight of ~80kDa in control MO-injected larvae (left panel). This band was almost completely abolished in the *ninl* atgMO-treated larvae, but was still detected in *ninl* spMO-injected larvae although with a slightly diminished intensity. Anti-actin antibodies were used as a loading control (right panel). (**e**) Immunoprecipitation from bovine retinal extracts with anti-human NINL antibody detects 3 bands, the strongest being of the same size as the band found on Western blot of zebrafish lysates (~80 kDa).
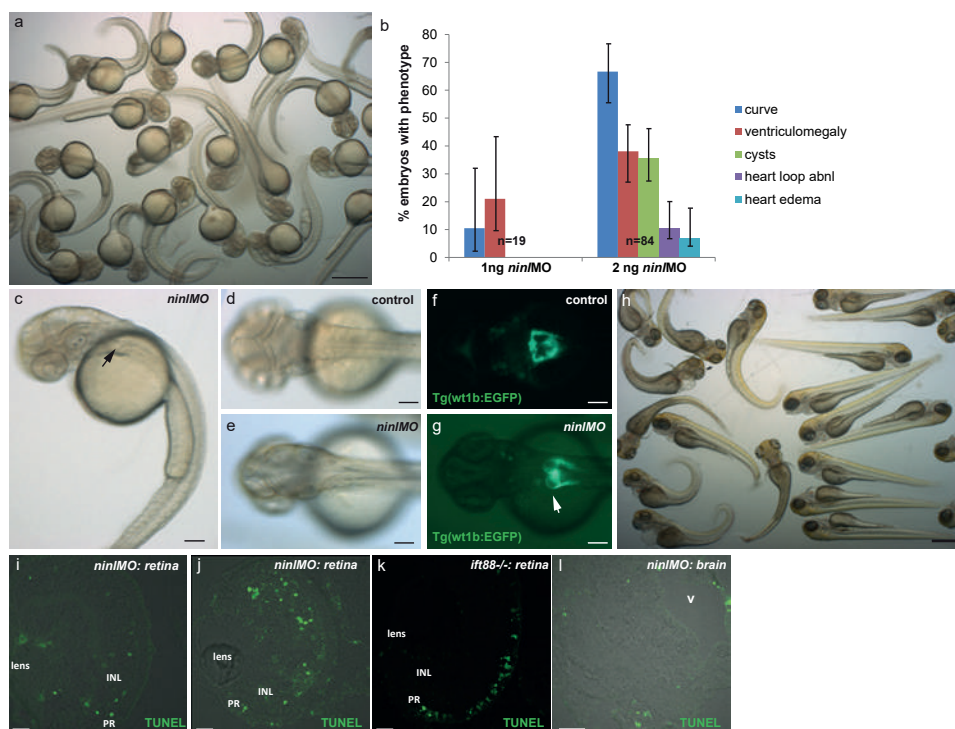
Figure S3. Phenotypes of the *ninl* atgMO.

(**a**) Representative clutch of zebrafish larvae at 2dpf injected with the phenotypic dose of *ninl* atgMO (2ng/nl). (**b**) Titration curve for the *ninl* atgMO illustrating the distribution of phenotypes in 2dpf larvae at two different concentrations: at 1ng/nl, a minority of injected larvae present a curved body shape (10%) and/or ventriculomegaly (20%) (n=19). At ~2ng/nl, on average 66% of injected larvae present a curved body shape and ~40% present ventriculomegaly and/or pronephric cysts (n=84). 95% Confidence Interval bars are shown. (**c**) Representative 2dpf-old *ninl* atg-morphant displaying curved body shape, ventriculomegaly and pronephric cyst (arrow). (**d-e**) Dorsal view of 2dpf larvae showing the normal morphology of the brain folds in

wild-type (**d**) and the enlarged ventricle in morphants (**e**). (**f-g**) Transgenic Tg(wt1b:EGFP) zebrafish line used to highlight the larval pronephros, shows the morphology of the fused glomerulus and proximal tubules in wild-type (**f**) and the dilatation of the region in *ninl* morphants ("kidney cysts", white arrow in **g**). (**h**) A clutch of *ninl* morphants at 4dpf. (**i-j**) TUNEL assay on 4dpf cryosections through retinas from *ninl* morphants shows the range of cell death detected (curved larvae in (h) were sectioned for the TUNEL assay). Note the absence of TUNEL-positive cells in the photoreceptor (PR) cell layer in the morphants. The *ift88*-/- retina is used as a positive control, given the known death of photoreceptors in this mutant at 4dpf. (**l**) Cryosection through a 4dpf brain in a morphant larva displaying a dilated brain ventricle (v) shows no significant neuronal cell death. Scale bars represent 500 µm in (a) and (h), 100 µm in (c-g), 10 µm in (i-k) and 30 µm in (l). PR PhotoReceptors, INL Inner Nuclear Layer.

Figure S4. Rescue of the morphant phenotype supports its specificity.

(**a-d**) Co-injection of 2 ng/nl *ninl* atgMO with 150 pg capped MO-resistant mRNA encoding human *NINL* isoform B reduced the incidence of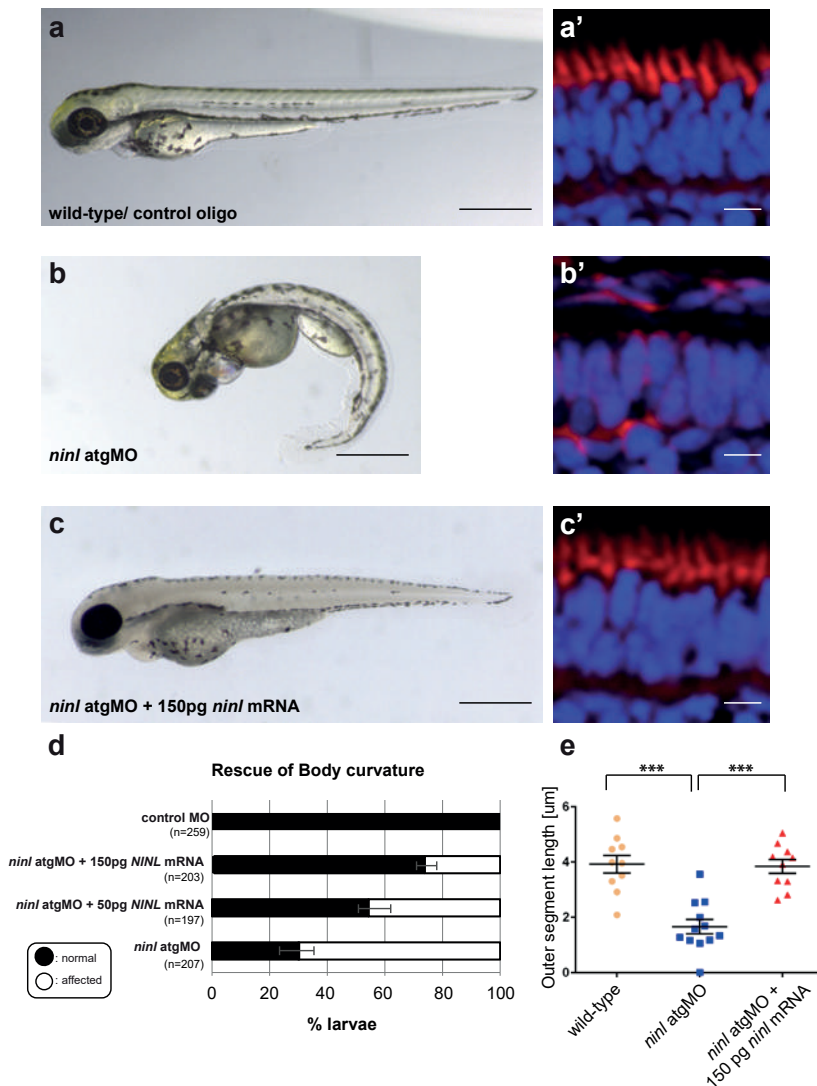 body curvature defects from 71% in *ninl* atgMO injected larvae (n=207) to 36% in *ninl* atgMO + *NINL* mRNA injected larvae (n=203) (*P*<0.0001, two-tailed Fisher's exact). A subset of these larvae were sectioned and a perfect correlation was observed in rescue between body curvature defects and defects in photoreceptor outer segment formation (**a'-c'**). (**e**) Quantification of the rescue of retinal outer segment length showing that mean OS length was rescued from 1.6 +/- 0.26 μm in *ninl* morphants to 3.8 +/- 0.25 μm with co-injection of *NINL* mRNA (P<0.0001, unpaired Student's *t*-test).
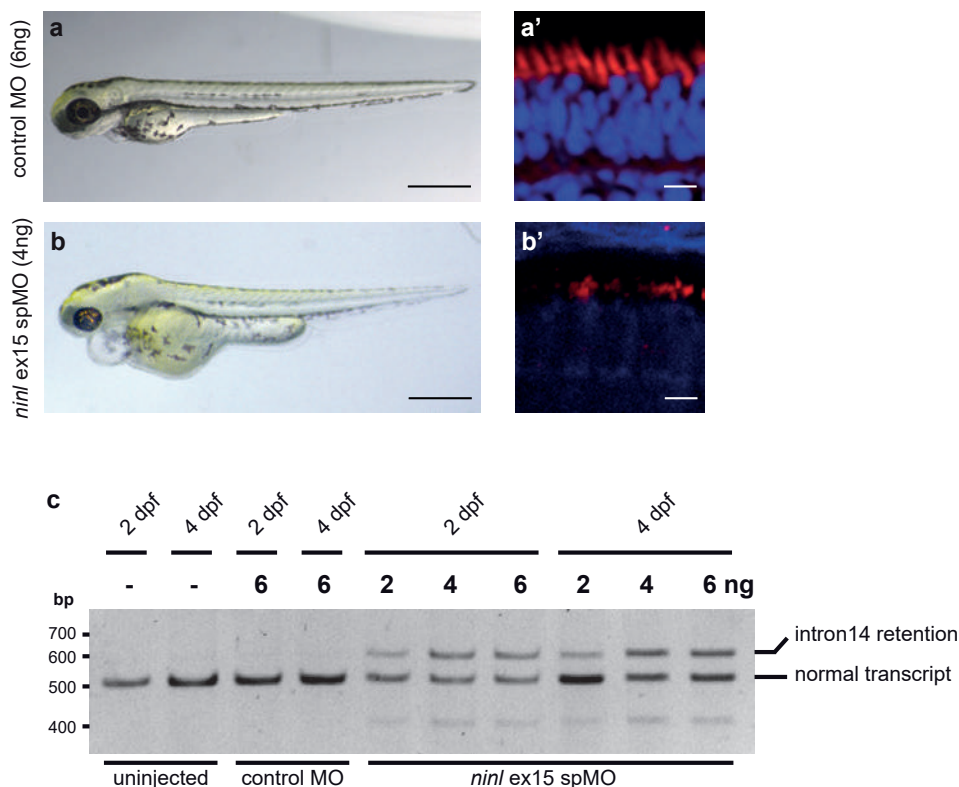
Figure S5. Recapitulation of phenotype by a *ninl* ex15 spMO (4 dpf).

(**a-b**) Injection of 4ng *ninl* ex15 spMO (n>100) results in heart edema and small eyes. No defects in body curvature were observed in comparison to control MO-injected larvae. (**a', b'**) Analyses of bodipy-stained retinas of *ninl* ex15 spMO-injected larvae (n=10) revealed defects in photoreceptor outer segment formation (10 of 10) similar to those observed in *ninl* atgMO-treated larvae, whereas stained retinas of control MO-injected larvae (n=10) appeared normal (10 of 10). Scale bars represent 500μm (a-b) and 5μm (a'-b'). (c) RT-PCR analysis on RNA isolated from 25 larvae that were either uninjected, injected with control MO (6ng) or injected with various amounts of *ninl* ex15 spMO (2, 4, 6ng), collected at two different time points after injection (2 dpf and 4 dpf). One PCR product of the expected length (~500bp) was obtained from RNA from uninjected and control MO-injected larvae. Sequence analysis revealed that this was the predicted transcript including exons 13-16. RT-PCR analysis on RNA obtained from the morphant larvae resulted in two products: Sequence analysis of both fragments revealed that the shorter product is the predicted wild-type transcript (ex13-16) and that the longer transcript in addition includes the entire intron14 (85 bp), resulting in premature termination of translation already after two codons in intron14. This aberrant splicing persists at 4dpf.

Supplementary Table 1. TAP-data and SILAC data SF-TAP analysis with over-expressed N-terminally SF-TAP-tagged NINL in HEK293T cells.

Shown are the number of unique identified peptides as well as the sequence coverage for each protein detected by mass spectrometry. Proteins identified in the SF-TAP analysis of empty vector control experiments were removed. SILAC analysis with over-expressed N-terminally SF-TAP-tagged NINL in HEK293T cells. Shown are the ratios and significance value for WT/SF-control experiments.
https://doi.org/10.1371/journal.pgen.1005575.s006

Supplementary Table 2. siRNA sequences

RefSeq Accession Number	Gene Symbol	Gene ID	siRNA ID	Sense siRNA Sequence	Antisense siRNA Sequence
NM_025176	NINL	22981	s22764	GGAGCAUCGUGUGACCAUUtt	AAUGGUCACACGAUGCUCCtc
NM_025176	NINL	22981	s22763	GCCUGAAUCAGGAACAUCAtt	UGAUGUUCCUGAUUCAGGCat
NM_025176	NINL	22981	s22765	CAGUGAGUAUAGAAACGGAtt	UCCGUUUCUAUACUCACUGga
XM_940346	CC2D2A	57545	s33278	GCCUAUUCCUGAGACUACUtt	AGUAGUCUCAGGAAUAGGCag
XM_940346	CC2D2A	57545	s33277	GAAUCAGUGAUAAAUCGUUtt	AACGAUUUAUCACUGAUUCtc
XM_940346	CC2D2A	57545	s33279	CCAUGAUUCUGCACGAAAAtt	UUUUCGUGCAGAAUCAUGGaa

Supplementary Table 3. Primer sequences

Name	Fw Primer sequence (5'-3')	Rv primer sequence (5'-3')
NINL#1	GGAAGGTTTTGTGGCTGTG	AGGCAGCTGATTCCAAAG
NINL#2	CTGGGACAGGAGGCTTCTAC	ATTTGGTCACTCTGCTGCTG
CC2D2A#1	AGGAAGCGTAACACCCAATG	CCTGGACACCTCCTTGTTG
CC2D2A#2	AGGGTCCAACTGCCTATGTG	ACAGCCCACATTTTTCAAGG
GUSB	AGAGTGGTGCTGAGGATTGG	CCCTCATGCTCTAGCGTGTC

2.2

Margo Dona[a,b*], Ralph Slijkerman[a,b*], Kimberly Lerner[c], Sanne Broekman[d,e], Jeremy Wegner[c], Taylor Howat[c], Theo Peters[c,e], Lisette Hetterschijt[a,e], Nanda Boon[d], Erik de Vrieze[a,e], Nasrin Sorusch[f], Uwe Wolfrum[f], Hannie Kremer[a,d,e], Stephan Neuhauss[g], Jingjing Zang[g], Maarten Kamermans[h,i], Monte Westerfield[c,#], Jennifer Phillips[c,#] and Erwin van Wijk[a,e,#,$]

[a] Department of Otorhinolaryngology, Radboud University Medical Center, Geert Grooteplein 10, 6525 GA Nijmegen, the Netherlands; [b] Radboud Institute for Molecular Life Sciences, Geert Grooteplein Zuid 28, 6525 GA Nijmegen, the Netherlands; [c] Institute of Neuroscience, 1254 University of Oregon, Eugene (OR), 97403-1254, USA; [d] Department of Human Genetics, Radboud University Medical Center, Geert Grooteplein 10, 6525 GA Nijmegen, the Netherlands; [e] Donders Institute for Brain, Cognition, and Behavior, Montessorilaan 3, 6525 HR Nijmegen, the Netherlands; [f] Institute of Molecular Physiology, Johannes Gutenberg University, Johannes-von-Muellerweg 6, D-55099 Mainz, Germany; [g] University of Zürich, Institute of Molecular Life Sciences, Winterthurerstrasse 190, Zürich, CH - 8057, Switzerland; [h] Retinal Signal Processing Lab, Netherlands Institute for Neuroscience, Meibergdreef 47, 1105 BA Amsterdam, The Netherlands; [i] Department of Biomedical Physics, Academisch Medisch Centrum, Meibergdreef 9, 1105 AZ Amsterdam, The Netherlands.

* The first two authors are co-first authors.
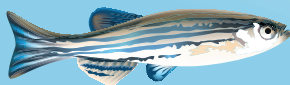# The last three authors are co-last authors.

Chapter 3

Usherin defects lead to early-onset retinal dysfunction in zebrafish

3

ABSTRACT

Mutations in *USH2A* are the most frequent cause of Usher syndrome and autosomal recessive nonsyndromic retinitis pigmentosa. To unravel the pathogenic mechanisms underlying *USH2A*-associated retinal degeneration and to evaluate future therapeutic strategies that could potentially halt the progression of this devastating disorder, an animal model is needed. The available *Ush2a* knock-out mouse model does not mimic the human phenotype, because it presents with only a mild and late-onset retinal degeneration. Using CRISPR/Cas9-technology, we introduced protein-truncating germline lesions into the zebrafish *ush2a* gene (*ush2a^rmc1^*: c.2337_2342delinsAC; p.Cys780GlnfsTer32 and *ush2a^b1245^*: c.15520_15523delinsTG; p.Ala5174fsTer). Homozygous mutants were viable and displayed no obvious morphological or developmental defects. Immunohistochemical analyses with antibodies recognizing the N- or C-terminal region of the *ush2a*-encoded protein, usherin, demonstrated complete absence of usherin in photoreceptors of *ush2a^rmc1^*, but presence of the ectodomain of usherin at the periciliary membrane of *ush2a^b1245^*-derived photoreceptors. Furthermore, defects of usherin led to a reduction in localization of USH2 complex members, whirlin and Adgrv1, at the photoreceptor periciliary membrane of both mutants. Significantly elevated levels of apoptotic photoreceptors could be observed in both mutants when kept under constant bright illumination for three days. Electroretinogram (ERG) recordings revealed a significant and similar decrease in both a- and b-wave amplitudes in *ush2a^rmc1^* as well as *ush2a^b1245^* larvae as compared to strain- and age-matched wild-type larvae. In conclusion, this study shows that mutant *ush2a* zebrafish models present with early-onset retinal dysfunction that is exacerbated by light exposure. These models provide a better understanding of the pathophysiology underlying *USH2A*-associated RP and a unique opportunity to evaluate future therapeutic strategies.

1.   INTRODUCTION

Usher syndrome is a rare genetic condition characterized by hearing impairment and a progressive loss of visual function as a consequence of Retinitis Pigmentosa (RP). The latter often results in legal blindness by the sixth decade of life [1]. Currently there are no treatments for retinal degeneration in patients with Usher syndrome, although they benefit from hearing aids or cochlear implants. Usher syndrome is classified into three types (USH1, USH2 and USH3), varying in severity of hearing impairment, age at which RP is diagnosed, and presence or absence of vestibular dysfunction [2]. Approximately two-thirds of USH patients present with USH2 [3], up to 85% of whom can be explained by mutations in *USH2A* [4,5]. Mutations in *USH2A* are also the most frequent cause of autosomal recessive RP (arRP), accounting for 7-23% of arRP cases [4]. Approximately 600 different, mostly private, mutations are evenly distributed over the gene and include point-nonsense, frame-shift, splice-modulating, and missense variants [6]. However, there are a number of mutations that originate from a common ancestor and are therefore observed more frequently [6-8]. The two most commonly found *USH2A* mutations are c.2299delG; p.Glu767fs and c.2276G>T; p.Cys759Phe, both residing in exon 13. Bi-alellic truncating defects of *USH2A* (nonsense mutations, frameshift mutations, or mutations that affect splicing), most often result in USH2, whereas the presence of at least one hypomorphic *USH2A* allele generally results in non-syndromic arRP [9]. The distribution of known mutations and neutral variants from the LOVD database for *USH2A* does not reveal a particular mutation tolerant or intolerant region of the gene that could pinpoint particularly important functional domains [7]. Despite ongoing efforts, little is known about either the physiological role(s) of the usherin protein in photoreceptors or the pathophysiological mechanism underlying *USH2A*-associated RP [4,10].

The *USH2A* transcript in retina consists of 72 exons and encodes a protein of 5,202 amino acids (usherin) [11,12]. Moreover, a cochlea-specific exon has been identified between exons 70 and 71 that encodes 24 additional amino acids [11]. Usherin contains an N-terminal signal peptide, a Lam-G like domain, a LamNT domain, 10 EGF-lam domains, 4 FN3 domains, two laminin G (LamG) domains, 28 FN3 domains, a transmembrane domain, and a short intracellular region with a C-terminal class I PDZ-binding motif. It is generally thought that usherin has a structural role at the periciliary region of the photoreceptor, where it is held in place via its interactions with harmonin (*USH1C* encoded), SANS (*USH1G* encoded) and whirlin (*WHRN* encoded, USH2d) [13-18]. At the periciliary region, usherin possibly stabilizes the photoreceptor connecting cilium by an extracellular interaction with Adhesion G protein-coupled receptor V1 (ADGRV1; previously known as GPR98 or VLGR1) [11,19-21].

Understanding the molecular mechanisms underlying photoreceptor dysfunction in *USH2A*-associated RP and the development of treatment strategies have been severely

hampered by the absence of suitable cellular or animal models mimicking the human phenotype. Although mutant mouse models are commonly used to study RP and test therapeutic strategies, for USH and several other types of RP the retinal phenotypes in mouse models do not mimic that of patients with defects in the orthologous genes [22]. In contrast, retinal dysfunction from a very young age is observed in zebrafish USH1 gene mutants [23]. Zebrafish larvae lacking Myo7aa (USH1b), harmonin (USH1c) or Pcdh15b (USH1f) function show reduced electroretinogram (ERG) traces by 5 to 7 days post fertilization (dpf) [24-26]. Additionally, photoreceptor-specific degeneration has been shown to occur in *ush2a* depleted morphant larvae [27], as well as in *myo7aa* mutant larvae exposed to elevated light levels [26].

In this study, we generated and characterized two *ush2a* mutant zebrafish models (*ush2a^rmc1*: c.2337_2342delinsAC; p.Cys780GlnfsTer32 and *ush2a^b1245*: c.15520_15523delinsTG; p.Ala5174fsTer) to study usherin function in the retina. Subsequent functional analyses showed that usherin is absent from photoreceptors in *ush2a^rmc1*, but that the extracellular domain of usherin can still be detected at the periciliary membrane of *ush2a^b1245*-derived photoreceptors. The levels of usherin interaction partners Whrna and Whrnb (whirlin) are reduced at the photoreceptor periciliary membrane of homozygous *ush2a^rmc1* larvae, whereas in homozygous *ush2a^b1245* larvae only the level of Whrna is affected. Furthermore, mutant zebrafish display elevated levels of apoptotic cells in the outer retina as compared to strain and age-matched wild-type zebrafish upon constant light rearing. We further found that ERG traces are notably attenuated in both mutants, indicating impaired outer retinal function. These mutants are the first genetic animal models for *ush2a* that present with early-onset retinal dysfunction.

2.   MATERIAL AND METHODS

2.1   Zebrafish maintenance and husbandry

Experimental procedures were conducted in accordance with international and institutional guidelines (Dutch guidelines, protocol #RU-DEC 2012-301; Swiss guidelines, Veterinäramt Zürich TV4206 and University of Oregon IACUC guidelines). Wild type adult Tupfel Long fin (TLF) or Oregon AB* zebrafish were used. The zebrafish eggs were obtained from natural spawning of wild-type or mutant breeding fish. Larvae were maintained and raised by standard methods [28].

2.2   CRISPR/Cas9 design and microinjection

For the *ush2a^rmc1* allele, oligos for generating guide RNAs were designed using the ZiFiT targeter software [29]. Oligos were subsequently ordered from Integrated DNA

Technologies. Annealing of oligos was performed in a buffer (1 M NaCl, 10 mM EDTA and 100 mM Tris-HCl pH7.5) by incubation at 90°C for four minutes, followed by a ten minute-incubation step at 70°C and gradual cooling (5°C per two minutes) to 16°C. The annealed oligos were immediately ligated into the a BsaI (New England Biolabs, #R0535S) linearized pDR271 vector (Addgene plasmid #42250) using T4 ligase (New England Biolabs, #M0202). The oligo and surrounding sequences were excised from the pDR274 vector using DraI (New England Bioloabs, #R0129S). The excised DNA band (284 basepairs) was subsequently used as a template for *in vitro* transcription using the MAXIscript® T7 Transcription Kit (Ambion life technologies, #AM1314) according the manufacturer's protocol. Obtained transcripts were purified using the MEGAclear™ Transcription Clean-Up Kit (Ambion life technologies, #AM1908). For the *ush2a*[b1245] allele, gene specific oligos were designed by flanking the 20 bp target sequence with T7 promoter and gRNA sequence: 5`-AATTAATACGACTCACTATA-[20 bp Target Sequence]-GTTTTAGAGCTAGAAATAGC-3`. The templates for gRNA syntheses were PCR amplified using the gene specific oligo with a gRNA scaffolding primer: 5`-GATCCGCACCGACTC GGTGCCACTTTTTCAAGTTGATAACGGACTAGCCTTATTTTAACTTGCTATTTCTAGCTCTAAA AC-3`. As input 13.4 µl water, 4ul 5x Phusion DNA polymerase buffer, 0.4 µl dNTPs (10 µM), 1 µl of gene specific oligo (10 µM), 1 µl of gRNA scaffold oligo (10 µM), 0.2 µl Phusion DNA polymerase. The cycling conditions were as follows: 98°C 30 seconds, 40 cycles of 98°C 10 seconds, 60°C 10 seconds, 72°C 15 seconds and 72°C 10 minutes. PCR products were column purified and used to prepare gRNA with the Ambion T7 megascript kit (AM1344) as per manufacturer's instructions. A zebrafish codon-optimized Cas9 containing vector (pT3TS-nCas9n; Addgene plasmid #46757) was used to generate Cas9 mRNA. The vector was linearized using XbaI (NEB, #R0145S) and used as a template for an *in vitro* transcription reaction using the mMESSAGE mMACHINE® T3 Transcription Kit (Ambion life technologies, #AM1348) according to manufacturer's instructions. Transcripts were purified using the MEGAclear™ Transcription Clean-Up Kit (#AM1908). Zebrafish embryos at a 1-cell stage were injected with 1 nl of a mixture containing gRNA (6 ng/µl), Cas9 mRNA (150 ng/µl), KCl (0.2 M) and phenol red (0.05%) using a Pneumatic PicoPump pv280 (World Precision Instruments) for the generation of the *ush2a*[rmc1] allele. To generate the *ush2a*[b1245] allele, one-cell stage zebrafish embryos were injected with 1 nl of a mixture containing gRNA (100 ng/µl), Cas9 mRNA (150 ng/µl), KCl (0.2 M) and phenol red (0.05%) using an MPPI-2 Pressure Injector with a BP-15 Back Pressure Unit (Applied Scientific Instrumentation, Oregon USA). After injection, embryos were raised at 28.5°C in E3 embryo medium (5 mM NaCl, 0.17 mM KCl, 0.33 mM $CaCl_2$, 0.33 mM $MgSO_4$), supplemented with 0.1% (v/v) methylene blue. At 2.5 days post fertilization, part of the injected embryos were analyzed for the presence of desired mutational events. When mutations could be detected, the remainder of injected embryos was raised.

2.3 Genotyping

Genomic DNA was isolated from pools of 15 larvae after incubation in 75 µl lysis buffer (10 mM Tris HCl pH=8.2, 10 mM EDTA, 100 mM NaCl and 0.5 % SDS) supplemented with freshly added proteinase K (final concentration of 0.20 mg/ml, Invitrogen #25530049) at 55°C for two hours. The isolated genomic DNA was subsequently used as a template in a PCR. Primers used for the amplification of *ush2a* exon13 are 5'-TCCACCAACAGAATCTAAATCTTTC-3' and 5'-CTGATTTGTAAATGGTGTTGGG-3' and primers used for the amplification of *ush2a* exon71 are 5'-CATGTTTTGGTTATCTGTT-CTTCT-3' and 5'-GACAGCGGAATGGTGAGATAAAC-3'. The obtained amplicons were cloned into a pCR®4-TOPO® vector (Invitrogen, #450030) according to manufacturer's instructions. Individual clones were analyzed for the presence of mutational events using the ABI PRISM Big Dye Terminator Cycle Sequencing V2.0 Ready Reaction kit and the ABIPRISM 3730 DNA analyzer (Applied Biosystems).

2.4 Transcript analysis

Pools of 15 larvae were snap frozen in liquid nitrogen and subsequently homogenized in 500 µl QIAzol (Qiagen, #79306) using a 25 gauge 16 mm needle. Total RNA was isolated using phenol:chloroform extraction and precipitated using isopropanol. Extracted total RNA was further purified and DNAse treated using a NucleoSpin® RNA II Isolation kit (Macherey-Nagel, #740955.50, Düren, Germany) according to manufacturer's protocol. Subsequently, 0.5-1.0 µg of total RNA was used as a template for cDNA synthesis using SuperScript III RT (Life Technologies, #11755050, Carlsbad (California) - United States). An *ush2a* amplicon (1096 bp) of homozygous *rmc1* larvae was amplified using with primers located in exon11 (5'-AGCGCTGTCGGAGTCTCTTC-3') and exon14 (5'-CCATCACTGACCGGTCACAG-3'). An *ush2a* amplicon (710 bp) of homozygous *b1245* larvae was amplified using primers located in exon68 (5'-TGGACTGGAGTGGCTCTTTC-3') and exon73 (5'-GATGAGGACTTTGGAGAGACCA-3').

2.5 Antibodies and Immunohistochemistry

Dissected adult eyes (12-18 mpf) and larval zebrafish (4-6 dpf) from homozygous *ush2a^rmc1* and *ush2a^b1245* mutants and their age and strain-matched wild-type controls were cryoprotected with 10% sucrose in PBS for 30 minutes prior to embedding in OCT compound (Tissue-Tek, 4583, Sakura). After embedding, samples were slowly frozen down using melting isopentane. To assess retinal morphology, cryosections (7 µm thickness along the lens/optic nerve axis) were fixed for 10 minutes with paraformaldehyde (PFA) 4%, stained with hematoxylin and eosin and analysed on a Zeiss Axioskop light microscope. For analysis by scanning confocal microscope, embryos were

fixed in 4% PFA overnight at 4°C, washed 3x in PBS-T, dehydrated in 100% methanol, rehydrated in descending methanol series and washed several times in PBS-T before being cryoprotected in 30% sucrose for several hours at room temperature. Larvae were then embedded in molten agarose blocks, frozen, and sectioned on a cryomicrotome. For immunofluorescence on unfixed cryosections (7 μm thickness) were permeabilised for 20 minutes with 0.01% Tween20 in PBS. Sections were rinsed 3 times for 5 minutes with PBS and blocked for 1 hour with blocking buffer (10% normal goat serum and 2% bovine serum albumin in PBS). Antibodies diluted in blocking buffer were incubated overnight at 4 °C. Secondary antibodies were also diluted in blocking buffer and incubated together with DAPI (1:8000; D1306; Molecular Probes) for 1 hour. Sections were post fixed with PFA 4% for 10 minutes and mounted with Prolong Gold Anti-fade (P36930; Molecular Probes). For immunofluorescence on fixed cryosectioned tissue (16μm thickness), slides were hydrated 10 minutes in PBS-T, then immersed in Sodium Citrate solution at pH 8.5 and heated in a pressure cooker for 10 minutes. After cooling to 37°C, slides were washed twice in PBS-T, blocked in 10% NFDM in PBS-T and incubated with primary antibodies. The following primary antibodies and dilutions were used: rabbit anti-active caspase 3 (1:500; #559565; BD Pharmingen), rabbit anti-Whrnb (1:300; #42690002 Cip98a; Novus Biological), rabbit anti-Whrna (1:300; #42700002 Cip98b; Novus Biological), rabbit anti-usherin-C (1:500; #27640002; Novus Biological), rabbit anti-Adgrv1 (1:1000) [27] and as marker for connecting cilium region in photoreceptor cells we used mouse anti-centrin (1:500; # 04-1624; Millipore) or acetylated α-tubulin (Sigma T7451). Secondary antibodies (Alexa Fluor 568 goat anti-rabbit (A11011), Alexa Fluor 488 goat anti-guinea pig (A11073) and Alexa Fluor 488 goat anti-mouse (A11029)), derived from Molecular Probes, were used in a 1:800 dilution. Images were taken using a Zeiss Axio Imager fluorescence microscope equipped with an AxioCam MRC5 camera (Zeiss) or a Zeiss LSM5 Confocal. The intensity of Whrna and Whrnb immunofluorescence was measured in FIJI version 1.47v [58] . First, the outer segment layer was isolated based on the centrin immunostaining. Subsequently, a mask was made based on the centrin staining using the "Find Maxima" option (noise=50), and dilated five times. To find the exact location of Whrna or Whrnb staining, the centrin mask and Whrn layer were combined. Find Maxima (noise=10) was used to identify the Whrn staining within the Centrin mask. The resulting mask was dilated three times and touching objects were separated using the watershed option. Subsequently, the maximum gray value of the identified regions was measured on the original image of Whrn immunofluorescence (Analyze Particles option; size=0-50, pixel circularity=0.00-1.00). Active caspase-3 labeled cells were analyzed on a Zeiss fluorescence microscope by manually counting positively stained cells in the ONL.

2.6 Constant light rearing

For constant light treatment, embryos were raised in transparent 10-cm petri dishes under normal conditions and were placed under constant light from 5-8 dpf. From 5 dpf onwards, *ush2a^rmc1* larvae were either maintained in facility conditions of 300 lux white light in a 14/10h day/night rhythm or were exposed to continuous white light with an intensity of 3000 lux, using a 150 W LED light source (Zeiss). *ush2a^b1245* larvae were either maintained in facility conditions of 300 lux white light in a 14/10h day/night rhythm or were exposed to continuous white light with an intensity of 3000 lux using two LED strips (Westek) mounted in parallel. Light input: 12V DC, transformer input 120V ~60Hz, transformer output 12V DC, 6W max. Light intensities were measured at water level using a lumino meter (Testo 540, Lenzkirch, Germany or Advanced Light Meter 840022, Sper Scientific, Arizona, USA).

2.7 Fixation and pre-embedding labeling for immunoelectron microscopy

For immunoelectron microscopy of adult zebrafish retinas, we followed the previously published protocol for pre-embedding labeling [20,30,31]. In brief, rabbit anti-usherin C (1:500; #27640002; Novus Biological) was applied on vibratome sections of pre-fixed (4% PFA) murine eye-cups, followed by incubation with biotinylated secondary antibodies. Antibody reactions were visualized by a Vectastain ABC-Kit (Vector Laboratories) and 0.01% hydrogen peroxide to 0.05 M diaminobenzidine (DAB) solution was added. Stained retinas were fixed in 2.5% glutaraldehyde in 0.1 M cacodylate buffer (pH 7.4), followed by silver enhancement of DAB precipitates and post-fixation in cacodylate buffered 0.5% OsO4 on ice. Dehydrated specimens were flat-mounted between two sheaths of ACLAR-films (Ted Pella Inc., Redding, USA) in Araldite resin. Ultrathin sections were made using a Reichert Ultracut S ultramicrotome (Leica), collected on Formvar-coated copper or nickel grids and counterstained with 2% uranyl acetate in 50% ethanol aund aq. 2% lead citrate. Ultrathin sections were analysed in a Tecnai 12 BioTwin transmission electron microscope (FEI, Eindhoven, The Netherlands). Images were obtained with a CCD camera (charge-coupled-device camera; SIS MegaView3; Surface Imaging Systems, Herzogenrath, Germany) and processed with Adobe Photoshop CS (Adobe Systems).

2.8 Electroretinogram (ERG) recordings

ERG recordings were performed on isolated larval eyes (5-7 dpf) as previously described [32]. Larvae were dark-adapted for a minimum of 30 min prior to the measurements and subsequently handled under dim red illumination. The isolated eye was positioned to face the light source. Under visual control via a standard microscope equipped with

red illumination (Stemi 2000C, Zeiss, Oberkochen, Germany), the recording electrode with an opening of approximately 20 μm at the tip was positioned at the center of the cornea. This electrode was filled with E3 embryo medium (5 mM NaCl, 0.17 mM KCl, 0.33 mM CaCl, and 0.33 mM MgSO$_4$). The electrode was positioned using a micromanipulator (M330R, World Precision Instruments Inc., Sarasota, USA). A custom-made stimulator was invoked to provide light pulses of 100 ms duration, with a light intensity of 6000 lux. It uses a ZEISS XBO 75W light source and a fast shutter (Uni-Blitz Model D122, Vincent Associates, Rochester, NY, USA) driven by a delay unit interfaced to the main ERG recording setup. Electronic signals were amplified 1000 times by a pre-amplifier (P55 A.C. Preamplifier, Astro-Med. Inc, Grass Technology) with a band pass between 0.1 and 100 Hz, digitized by DAQ Board NI PCI-6035E (National Instruments) via NI BNC-2090 accessories and displayed via a self-developed NI Labview program [33]. Statistical analysis was performed using SPSS Statistics 22 (IBM All the experiments were performed at room temperature (~22°C).

2.9 Statistical analyses

The Graphpad Prism software (version 5.03 for Windows, GraphPad Software, La Jolla California USA, www.graphpad.com) was used to generate scatter plots, calculate mean values, and perform statistical analysis using two-tailed unpaired Student's t-tests or two-tailed Mann-Whitney tests.

3. RESULTS

3.1 Zebrafish and human usherin are highly conserved

Bioinformatic analyses of the zebrafish and human usherin protein sequence revealed that the proteins have a high degree of sequence similarity (52% identity; 68% similarity) and share a similar protein domain architecture (Fig. 1). We characterized the subcellular localization of usherin in the zebrafish retina with an antibody directed against the intracellular C-terminal region of usherin (anti-usherin-C). In adult zebrafish retina, usherin is not only present at the periciliary membrane of both cones and rods, but also apical to the cone connecting cilium (Fig. 2A, B and C; Fig. S1). Subsequent immunoelectron microscopy identified these structures as cone accessory outer segments (AOS) (Fig. 2D and E). AOS are structures that run along the photoreceptor outer segment and are predominantly found in cone photoreceptors of adult frogs and teleost fish [34].
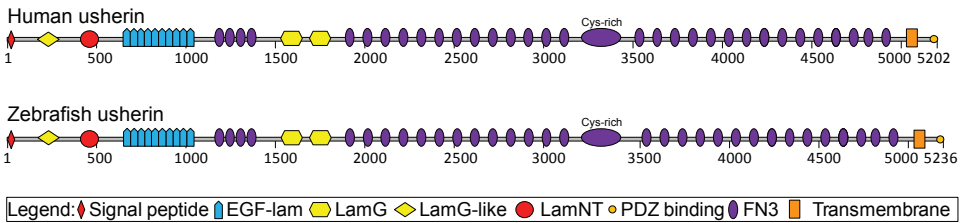
Figure 1. Schematic presentation of zebrafish usherin.

Motif alignment of human and zebrafish usherin. Both proteins have an identical predicted domain architecture. EGF-lam, laminin-type epidermal growth factor-like domain; LamG, laminin G domain; LamG-like, LamG-like jellyroll fold domain; LamNT, laminin N-terminal domain; FN3, fibronectin type 3 domain.
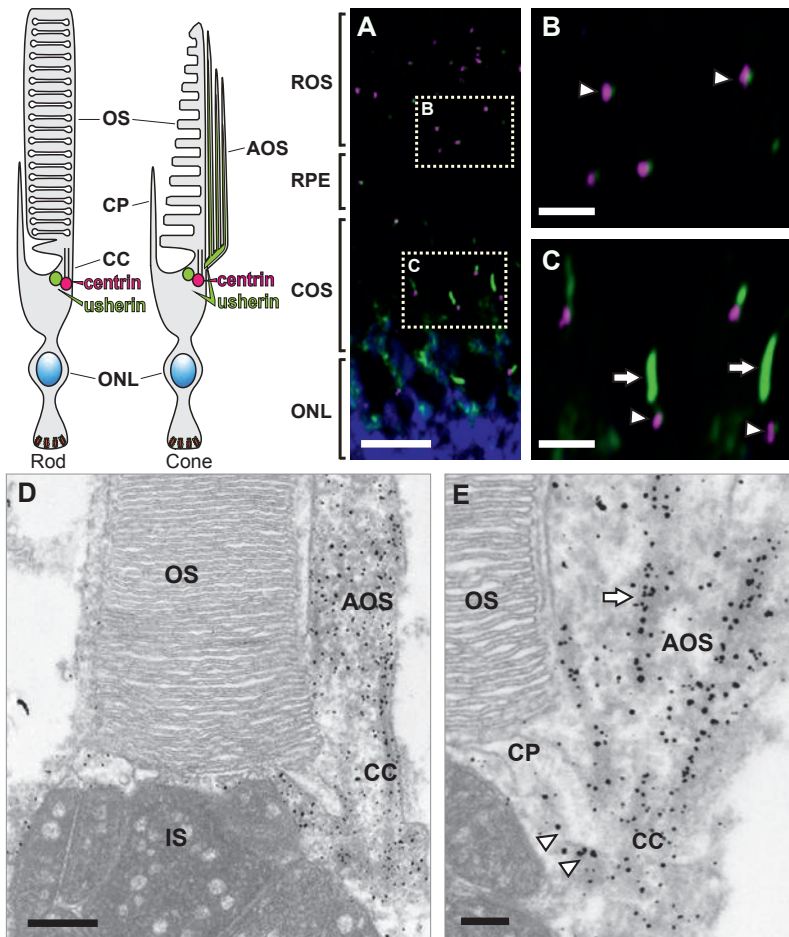
Figure 2. Usherin localizes at the periciliary membrane and accessory outer segments of adult zebrafish photoreceptor cells.

(A) Retinal sections of wild-type adult zebrafish are labeled for usherin (green signal) and the connecting cilium marker centrin (magenta signal). **(B)** Usherin labeling at the periciliary region of rod photoreceptors is present adjacent to the connecting cilium marked by centrin (indicated by an arrow head). **(C)** In cones, usherin is also detected at the periciliary region (arrow heads) as well as apical to the connecting cilium marked by centrin labeling (arrows). Nuclei were stained with DAPI (blue signal). **(D, E)** Electron microscopy images of adult zebrafish retinas show that usherin localizes at the periciliary membrane (arrowheads) as well as in the accessory outer segments (AOS; arrow) of cone photoreceptors. Scale bars in A: 10 µm; B: 3 µm; C: 3 µm; D: 1 µm E: 0.1 µm. CC: connecting cilium, COS: cone outer segment, CP: calyceal processes, ONL: outer nuclear layer, OS: outer segment, ROS: rod outer segment, RPE: retinal pigment epithelium.

3.2   Generation of zebrafish *ush2a^rmc1^* and *ush2a^b1245^* mutants

Using CRISPR/Cas9 technology, we generated two *ush2a* mutant alleles (sequences in Fig. S3). *ush2a^rmc1^* contains a frameshift mutation in *ush2a* exon13 (c.2337_2344delinsAC; p.Cys780GlnfsTer32), that is predicted to result in the premature termination of translation of usherin (Fig. 3A). *ush2a^b1245^* harbors a frameshift mutation in *ush2a* exon71 (ENSDART00000086201.4; c.15520_15523delinsTG; p.Ala5174fsTer), predicted to encode an usherin protein that retains the transmembrane domain but lacks the C-terminal 62 amino acids of the intracellular region including the class I PDZ binding motif. This allele provides an opportunity to assess the functional importance of the intracellular region, including the PDZ-binding motif, relative to the ectodomain of usherin (Fig. 3A). Both homozygous mutants were viable and no abnormalities in morphology, development, or swimming behavior were observed.

3.3   *ush2a^rmc1^* and *ush2a^b1245^* do not affect *ush2a* pre-mRNA splicing

In patient-derived fibroblasts, the *USH2A* c.2299delG mutation results in skipping of *USH2A* exon12 and exon13 in some transcripts, or in skipping of exon13 only [35]. Recent studies showed that CRISPR/Cas9-induced exonic lesions could also induce an (in-frame) skipping of the targeted exon thereby preventing generation of a functional knock-out model [36]. If the lesion introduced in the *ush2a^rmc1^* mutant causes an in-frame skipping of exon 13, this could potentially result in expression of a shortened usherin with residual function. Similarly, the c.15520_15523delinsTG (*ush2a^b1245^*) mutation is predicted to disrupt an exonic splice enhancer site and potentially induce skipping of exon71, thereby also leaving the *ush2a* open reading frame intact. We, thus, analyzed *ush2a* transcripts in homozygous *ush2a^rmc1^* and *ush2a^b1245^* larvae to assess whether the introduced lesions would result in alternative *ush2a* pre-mRNA splicing events. Amplicons spanning exon13 or exon71 and their surrounding exons were amplified by RT-PCR. Because no alternatively spliced *ush2a* transcripts were amplified from cDNA derived from homozygous *ush2a^rmc1^* or *ush2a^b1245^* larvae (Fig. 3B and C), we expect that the introduced mutations in the *rmc1* and *b1245* alleles result in premature termination of usherin translation.
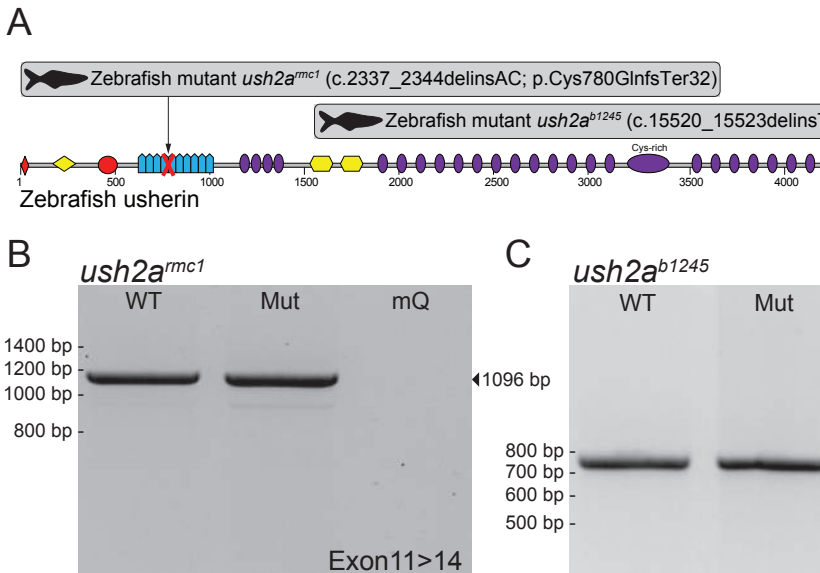
3

A

Zebrafish mutant *ush2a^rmc1* (c.2337_2344delinsAC; p.Cys780GlnfsTer32)

Zebrafish mutant *ush2a^b1245* (c.15520_15523delinsT

Zebrafish usherin

B

ush2a^rmc1

C

ush2a^b1245

Figure 3. *ush2a* transcript analyses in homozygous *ush2a^rmc1* and *ush2a^b1245* mutant zebrafish.

(A) The locations of the mutations in *ush2a^rmc1* and *ush2a^b1245* are schematically depicted. **(B)** RT-PCR analyses of *ush2a* transcripts derived from homozygous *ush2a^rmc1* or **(C)** homozygous *ush2a^b1245* larvae (5 dpf) provided no indications for an effect of the introduced lesions on pre-mRNA splicing. WT: wild-type, Mut: homozygous mutant, mQ: milliQ water.

3.4 *ush2a^rmc1* leads to absence of usherin, whereas *ush2a^b1245* results in truncated usherin at the periciliary region

Using zebrafish-specific anti-usherin antibodies directed against the N- or C-terminus of the protein, we evaluated the presence of usherin in the retina of homozygous *ush2a^rmc1* and *ush2a^b1245* larvae and strain-matched (TLF or AB*, respectively) wild-type larvae at 5 dpf. Anti-usherin-N is directed against an amino acid sequence present at the N-terminus of usherin. In wild-type larvae, both antibodies detected usherin adjacent to the basal body and connecting cilium marker, centrin (Fig. 4). In contrast, no usherin signal was detected in the retina of *ush2a^rmc1* mutant larvae using either anti-usherin antibody. Also in the retina of *ush2a^b1245* larvae, no signal was detected when using anti-usherin-C antibodies (Fig. 4A and B). However, a signal at the photoreceptor periciliary region of homozygous *ush2a^b1245* larvae was obtained when using anti-usherin-N antibodies. These results suggest that the truncated usherin protein still localizes appropriately at the membrane even though it lacks the C-terminal intracellular region and the PDZ binding motif (Fig. 4A and B). We conclude that *ush2a^rmc1* mutants completely lack usherin at the photoreceptor periciliary region and the mutation should be considered a true null allele, whereas *ush2a^b1245* should be considered a hypomorphic allele with potential residual function.
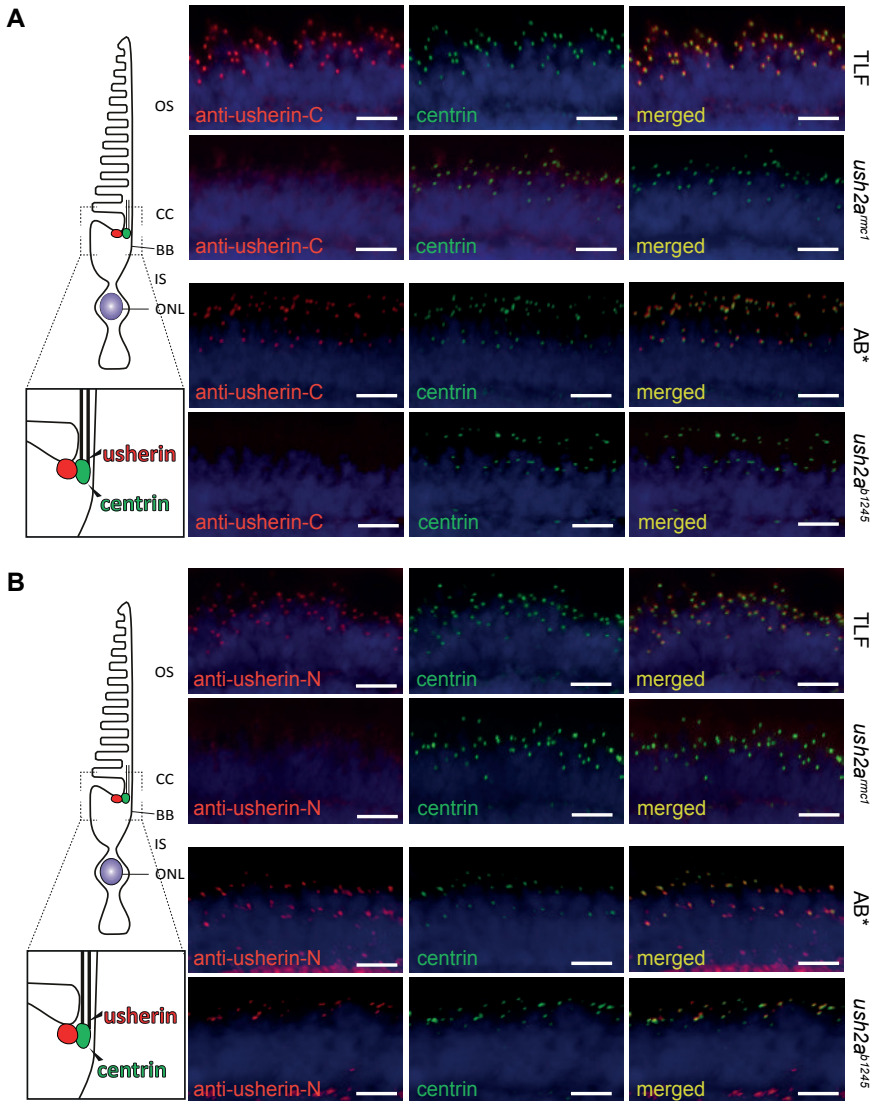
Figure 4. Localization of usherin in frontal cryosections of wild-type and mutant zebrafish retinas (5 dpf).

Zebrafish-specific anti-usherin-C **(A)** or anti-usherin-N **(B)** antibodies are employed (red signal). **(A)** In *ush2a^rmc1* as well as *ush2a^b1245* homozygous mutant larvae no signal was detected with the anti-usherin-C antibody, whereas in both TLF and AB* wild-type controls usherin was present adjacent to the connecting cilium marked by centrin (green signal). **(B)** No signal was detected in the retina of homozygous *ush2a^rmc1* mutants using the anti-usherin-N antibody, however, a signal at the photoreceptor periciliary region was observed in the retina of homozygous *ush2a^b1245* larvae when this antibody was used. In wild-type controls, the anti-usherin-N antibody also detected usherin at the photoreceptor periciliary region. (n= 35 larvae, from 5 biological replicates with TLF and *ush2a^rmc1* larvae, n= 64, from 8 biological replicates with AB* and *ush2a^b1245* larvae). Nuclei are stained with DAPI (blue signal). Scale bars: 10 μm.

3.5 Ablation of usherin affects the localization of Whrna and Whrnb in the retina

Human Usherin was previously shown to interact directly with whirlin *in vitro* [16]. The biological relevance of this interaction was confirmed by the absence of whirlin at the photoreceptor periciliary membrane of *Ush2a* knock-out mice [17]. Here, we determined whether or not whirlin localization was also affected in the retina of homozygous *ush2a*[rmc1] and *ush2a*[b1245] zebrafish larvae (5 dpf). The zebrafish genome harbors two whirlin-encoding orthologs. *whrna* (previously known as *dfnb31a* (ENSDARG00000075362)) encodes Whrna and *whrnb* (previously known as *dfnb31b* (ENSDARG00000068166)) encodes Whrnb. Whrna was found to be located at the photoreceptor periciliary region in wild-type larvae (Fig. 5A, Fig. S2). Reduced intensity of the Whrna signal was observed in the retinas of homozygous larvae of both *ush2a* mutants, which was further confirmed by quantification of fluorescence signal intensities (Fig. 5A). The same results were observed in homozygous *ush2a*[rmc1] larvae when an anti-Whrnb antibody was employed (Fig. 5B, Fig. S2). In contrast, the intensity of the Whrnb signal was unaltered in photoreceptors of homozygous *ush2a*[b1245] larvae as compared to AB* wild-type larvae (Fig. 5B).

3.6 Zebrafish *ush2a* mutants exhibit elevated levels of photoreceptor apoptosis

Based on the assumption that usherin is required for long-term maintenance of photoreceptor cells, we assessed whether absence of usherin in the zebrafish retina would lead to increased levels of apoptosis in the outer nuclear layer (ONL). Larvae were raised under a 14/10 hours light/dark cycle until 5 dpf. After 5 dpf, they were either raised for an additional 72 hours in regular facility conditions of 300 lux light intensity of a 14hr/10hr light/dark cycle, or exposed to constant light with an intensity of 3000 lux for 72 hours. A slight but significant increase in the amount of apoptotic photoreceptor cells was observed in 8 dpf *ush2a*[rmc1] larvae raised in normal facility conditions (Fig. 6A). These results were consistent with our previously reported data on photoreceptor degeneration in larvae treated with a morpholino targeting an early splice junction in *ush2a* [27]. Subsequently, we assessed the number of apoptotic events in *ush2a*[b1245] mutant larvae. No significantly elevated levels of cell death in the ONL were observed when these larvae were raised under normal facility conditions (Fig. 6B). Constant light rearing with an elevated light intensity of 3000 lux significantly increased the amount of apoptotic cells in the ONL of both mutant alleles as compared to their strain-matched wild-type controls (Fig. 6A and B). Variations in the genetic backgrounds of the *rmc1* and *b1245* alleles, variances in the light sources used in the elevated light exposure assay, and other environmental differences between the two facilities where these experiments were conducted could contribute to the observed difference in the absolute number of apoptotic cells.
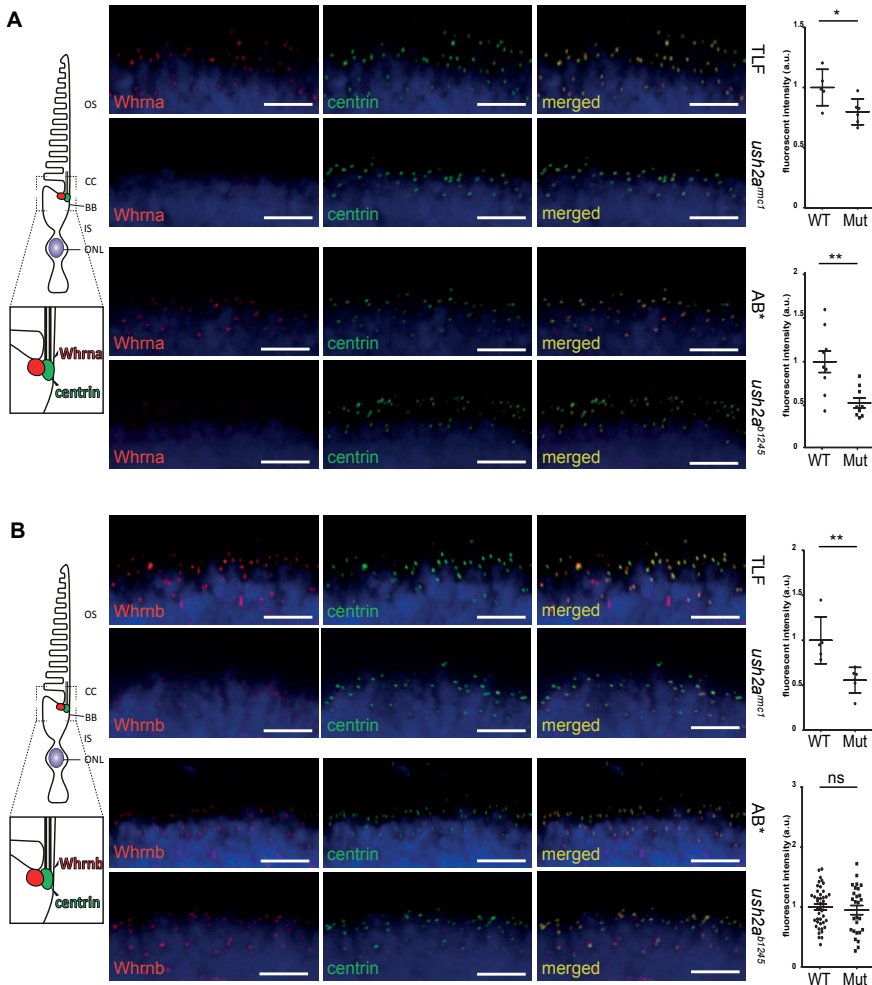
Figure 5. Ablation of usherin affects the localization of Whrna and Whrnb in the zebrafish retina (5 dpf).

(A) Intensity of Whrna labeling was significantly reduced in both *ush2a^rmc1^* and *ush2a^b1245^* mutants as compared to corresponding wild-types (n=35 larvae from 5 biological replicates with *ush2a^rmc1^* mutant larvae and TLF larvae, and n=54 larvae from 7 biological replicates with *ush2a^b1245^* mutant larvae and AB* larvae). Intensities of fluorescence using antibodies directed against Whrna (red signal) were quantified and plotted as scatter plots next to the corresponding images. Each dot represents the average grey-value per eye (n=5 *ush2a^rmc1^* eyes and n=6 TLF larvae eyes, *p*<0.05 and n=10 *ush2a^b1245^* and n=9 AB* eyes, *p*=<0.01, two-tailed unpaired Student's *t*-test). **(B)** Whrnb labeling was reduced in *ush2a^rmc1^* mutants, but unaltered in *ush2a^b1245^* mutants compared to corresponding wild-types (n=35 larvae from 5 biological replicates with *ush2a^rmc1^* mutant larvae and TLF larvae, and n=54 larvae from 7 biological replicates with *ush2a^b1245^* mutant larvae and AB* larvae). Intensity of Whrnb labeling (red signal) was significantly reduced in *ush2a^rmc1^* larvae as compared to wild-type (TLF) larvae (n=5 *ush2a^rmc1^* eyes and n=6 TLF eyes, *p*<0.01, two-tailed unpaired Student's *t*-test). In *ush2a^b1245^* larvae, the intensity of Whrnb labeling appeared unaltered as compared to wild-type (AB*) larvae (n=27 eyes for both *ush2a^b1245^* and AB* wild-type; *p*=0.57, two-tailed unpaired Student's *t*-test). Nuclei were stained with DAPI (blue signal) and anti-centrin (green signal) was used as a marker for the connecting cilium. Scale bars: 10 µm, dpf: days post fertilization, a.u.: arbitrary units, * indicates *p*<0.05, ** indicates *p*<0.01, and ns: not significant.
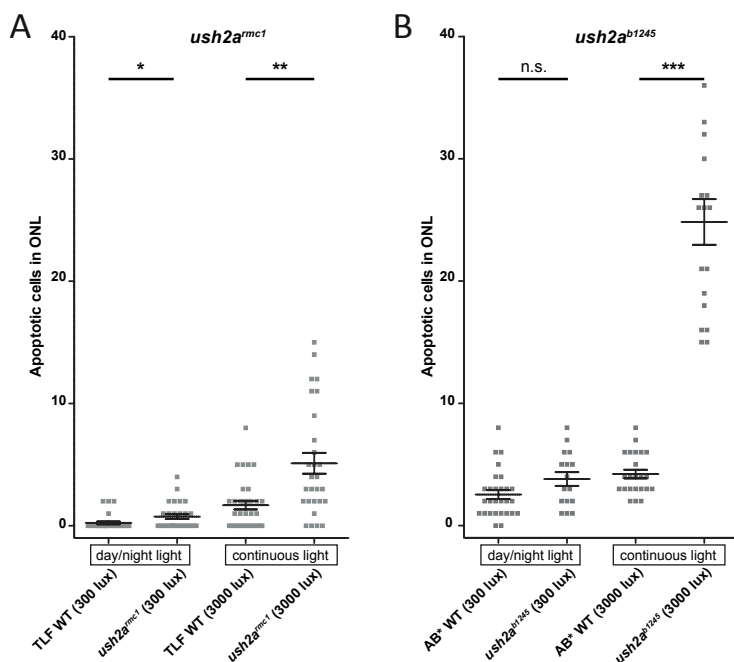
Figure 6. Quantification of apoptotic events in the ONL of zebrafish *ush2a* mutants (8 dpf). Homozygous *ush2a^rmc1* and *ush2a^b1245* larvae were exposed either to 300 lux in a (14/10h) day/night rhythm or to continuous light at 3000 lux from 5-8 dpf. Individual dots represent the number of apoptotic cells in the ONL per eye. Strain matched wild-type TLF or AB* zebrafish were used as controls. **(A)** TLF and *ush2a^rmc1* larvae kept at 300 lux with a day/night cycle showed on average 0.2 (± 0.1; 30 eyes) and 0.8 (± 0.2; 28 eyes) apoptotic cells per eye, respectively ($p<0.05$). When kept under 3000 lux of continuous light, 1.7 (± 2.0; 34 eyes) and 5.1 (± 4.5; 28 eyes) apoptotic cells per eye were observed in TLF and *ush2a^rmc1*, respectively ($p<0.01$). **(B)** AB* and *ush2a^b1245* larvae maintained at 300 lux with a day/night cycle showed on average 2.5 (± 1.9; 28 eyes) versus 3.8 (± 2.3; 16 eyes) apototic cells per eye, respectively (n.s.). When kept under 3000 lux of continuous light, on average 4.2 (± 1.7; 23 eyes) versus 24.8 (± 7.9; 18 eyes) apoptotic cells per eye were observed in AB* and *ush2a^b1245*, respectively ($p<0.0001$). Each point represents the number of apoptotic cells in the ONL per eye and the standard error of the mean are given as error bars. * indicates $p<0.05$, ** indicates $p<0.01$, *** indicates $p<0.0001$, n.s.: not significant (two-tailed Mann-Whitney test); ONL: outer nuclear layer; dpf: days post fertilization.

Because significantly elevated levels of apoptotic events were seen in the ONL of *ush2a^rmc1* mutant larvae when kept at facility conditions, we examined whether retinal degeneration was progressive under these conditions. Retinal histology was analyzed for both homozygous *ush2a* mutants at 5 dpf and at 18 months of age, which revealed that cellular organization and retinal lamination in mutants was indistinguishable from those in wild-type controls. Moreover, photoreceptor outer segments of both *ush2a* mutants had a normal morphology (Fig. S4). The observed lack of progressive retinal degeneration in these mutants suggests that the rate of photoreceptor apoptosis might be compensated by the rate of photoreceptor regeneration when fish are raised in low-intensity light.
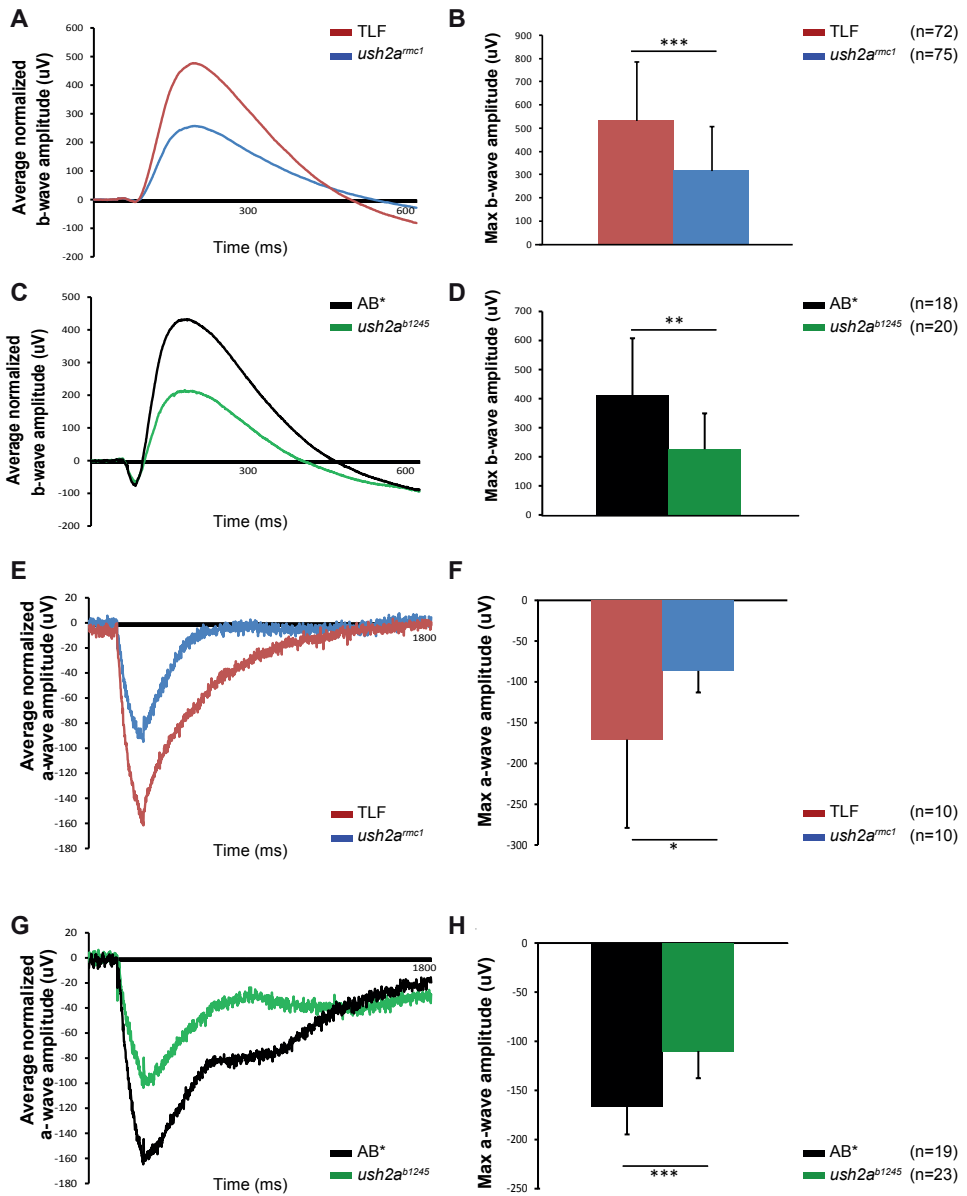
Figure 7. *ush2a* mutants show reduced retinal function.

Average ERG traces from a cohort of homozygous *ush2a^rmc1* and *ush2a^b1245* larvae (5 dpf) with age- and strain-matched wild-type controls are depicted. Averages of the maximum ERG amplitudes are plotted as bar graphs ± standard deviation. **(A-D)** Normalized b-wave amplitudes recorded in both mutants are significantly reduced compared to ERG-traces from wild-type controls (n=72 TLF and n=75 *ush2a^rmc1*, from 3 biological replicates, *p*<0.001, two-tailed unpaired Student's *t*-test, and n=20 *ush2a^b1245* larvae and n=18 wild-type larvae, from 3 biological replicates, *p*<0.01, two-tailed unpaired Student's *t*-test). **(E-H)** In both *ush2a* mutants, the a-wave amplitudes are significantly reduced as compared to strain-matched wild-type controls (n=10 for TLF

and *ush2a^rmc1*, from 2 biological replicates, *p*<0.05, two-tailed unpaired Student's *t*-test, and n=19 for AB* and n=23 for *ush2a^b1245*, from 2 biological replicates, *p*<0.001, two-tailed unpaired Student's *t*-test). * indicates *p*<0.05, ** indicates *p*<0.01 and *** indicates *p*<0.001.

3.7 *ush2a* mutants show reduced visual function

To assess whether absence of usherin has implications for visual function in the *ush2a^rmc1* and *ush2a^b1245* mutants, electroretinograms (ERGs) were recorded in 5 dpf *ush2a* mutant larvae and strain- and age-matched wild-type controls that were raised under normal facility conditions. In the zebrafish retina, a small negative a-wave generated by photoreceptor hyperpolarization is immediately followed by a large positive b-wave, generated largely by the depolarization of second-order ON-bipolar cells in response to photoreceptor hyperpolarization [37]. The ERG maximum b-wave amplitudes were significantly reduced in homozygous *ush2a^rmc1* larvae as compared to age- and strain-matched wild-type controls (Fig. 7A and 7B). The same result was observed in homozygous *ush2a^b1245* larvae (5 dpf) (Fig. 7C and 7D). To investigate whether the decreased inner retinal function was primarily mediated by a decrease in photoreceptor function, we recorded pharmacologically isolated a-waves by abolishing b-waves with glutamate receptor antagonists t-APB and TBOA. Maximum a-wave amplitudes in homozygous *ush2a^rmc1* larvae were significantly reduced compared to wild-type larvae (Fig. 7E and 7F). Again, a similar defect was detected in homozygous *ush2a^b1245* larvae, in which the maximum a-wave amplitudes were also significantly decreased compared to wild-type controls (Fig. 7G and 7H). Despite the absence of detectable retinal morphological defects, early-onset retinal photoreceptor dysfunction was recorded in both *ush2a* mutants.

4. DISCUSSION

In this study we generated and characterized two zebrafish *ush2a* mutant models, *ush2a^rmc1* and *ush2a^b1245*, in which different domains of usherin were ablated. No signal was detected in photoreceptors of either *ush2a^rmc1* or *ush2a^b1245* larvae when using an antibody targeting the intracellular C-terminal region. In contrast, truncated usherin was detected at the photoreceptor periciliary region of homozygous *ush2a^b1245* larvae when using an N-terminal usherin antibody, but not in *ush2a^rmc1*. Absence of full length usherin resulted in reduced whirlin levels at the photoreceptor periciliary region. Furthermore, the *rmc1* allele showed mild levels of photoreceptor degeneration at 8 dpf raised under normal facility conditions, whereas constant light rearing from 5-8 dpf with a light intensity of 3000 lux exacerbated photoreceptor degeneration in both mutants. Finally, both models presented with early-onset retinal dysfunction, as evidenced by significantly reduced ERG a- and b-wave responses recorded at 5 dpf. After complete

phenotypic evaluation of both alleles we conclude that the intracellular region of usherin is the most critical region in usherin required for visual function in zebrafish larvae.

Prior to this study, several USH mouse models were generated, which all presented with early-onset hearing defects, with or without vestibular dysfunction, closely resembling human inner ear USH defects [38]. These models have contributed significantly to understanding the molecular pathology underlying USH-associated hearing loss [17,39,40]. Unfortunately, these mouse models only sporadically recapitulated retinal degeneration seen in USH patients. A spontaneous mutant mouse model, *Kunming*, was described for Usher syndrome type IIa [41]. This model shows a rapid, early-onset retinal degeneration, but contains mutations in two genes known to be involved in inherited retinal dystrophies: *Ush2a* and *Pde6b*. A targeted *Ush2a* knock-out mouse demonstrates only mild retinal degeneration with late age of onset [19]. A likely explanation for the discrepancy in phenotypic outcome between mice and humans lies within the anatomical differences between human and mouse photoreceptor cells. The most prominent subcellular locations in human photoreceptor cells where USH1 and USH2 proteins have been found are the calyceal processes and the periciliary membrane [15,20,42,43]. In rodents, photoreceptor calyceal processes and periciliary membranes are absent or underdeveloped, respectively, compared to humans. In contrast, these structures are well-developed and present in frogs and teleost fish [22]. Zebrafish mutants or morphants for USH1-associated genes *myo7aa* [26,44], *cdh23* [45,46], *pcdh15* [25] and *ush1c* [24,47] have been described in the literature, most of them showing early-onset retinal dysfunction [23]. Furthermore, we showed that morpholino-induced knock-down of *ush2a* expression induces photoreceptor cell death in zebrafish larvae [27]. In this study we generated and characterized two zebrafish mutant models that will allow us to continue to investigate the molecular pathology underlying *ush2a*-associated retinal dysfunction and future therapeutic strategies.

Although the anatomical similarities between human and zebrafish photoreceptor cells are numerous, some differences have also been noted. Cone photoreceptors of adult teleost fish contain a cilium-like structure with a 9+0 arrangement of microtubule-doublets. This structure, the accessory outer segment (AOS), protrudes from the connecting cilium and projects apically alongside the outer segment, eventually associating with the retinal pigment epithelium (RPE) [48]. The function of the AOS is still unclear, but previous reports have suggested that the AOS provides structural support to the outer segment [49] and that it is involved in exchange of metabolites between RPE and cones [48-50]. Moreover, in response to changes in ambient light conditions and to circadian signals during light-to-dark adaptation of the teleost retina, reversible retinomotor movements take place that result in contraction and elongation of rods

and cones to expose the outer segment optimally to incoming light [51,52]. It has been postulated that by anchoring the cones to the pigment epithelium, the AOS may preserve the highly organized arrangement of the various types of cones in the fish retina [49]. Previous experiments showed that the USH1b protein, myosin VIIa, is localized in the cone AOS [48], and we now discovered that usherin is present in these structures as well. It has been shown that myosin VIIa and usherin, together with Adgrv1 and whirlin, physically interact to form the ankle-link complex in cochlear hair cells [53]. It is therefore tempting to speculate that within the AOS, myosin VIIa and usherin also form a complex that could be of importance for alignment and connection of the AOS to cone outer segments.

In humans, usherin and the other known USH2 proteins, whirlin and ADGRV1, form a dynamic protein complex that is mainly mediated by PDZ-PBM-based interactions [16,17]. Previous research using knockout mice showed that usherin, whirlin, and Adgrv1 are mutually dependent on each other for their localization at the photoreceptor periciliary membrane [13,17]. Whereas *ush2a* and *adgrv1* are present as single copy genes, there are two zebrafish whirlin orthologs (*whrna* and *whrnb*). In larvae of the *ush2a^rmc1* allele, in which no usherin could be detected, we observed reduced levels of both Whrna and Whrnb at the periciliary membrane. In *ush2a^b1245* larvae, however, Whrna is significantly reduced at the periciliary membrane, whereas Whrnb appears unaffected. These observations fit a model in which the ectodomains of usherin and Adgrv1 interact while the intracellular regions of both proteins are anchored by whirlin (Fig. 8), as was previously proposed by Maerker and co-workers [15,20]. Based on the results of the current study, Whrna seems to bind the intracellular region of usherin preferentially, whereas Whrnb predominantly associates with the intracellular region of Adgrv1. Complete absence of usherin (*rmc1* allele) results in absence of both Whrna and Whrnb at the periciliary membrane and probably the complete USH2 complex including Adgrv1, similar to what was observed in the *Ush2a* knockout mouse [17]. Immunohistochemical analyses using anti-Adgrv1 antibodies corroborated this hypothesis (Fig. S5). Absence of the C-terminal cytoplasmic region of usherin (*b1245* allele) apparently affects the association with only the intracellular binding partner Whrna, leaving the remainder of the USH2 complex (Adgrv1 and Whrnb) intact (Fig. 8; Fig. S5). Thus, absence of zebrafish usherin affects localization of interaction partner whirlin. The observed differences in localization of both whirlin co-orthologs in the *rmc1* and *b1245* alleles suggest that Whrna and Whrnb have high binding-affinities for usherin and Adgrv1, respectively, and that they most probably have acquired divergent functions during evolution, consistent with the subfunctionalization hypothesis [54].

The presence of usherin at the periciliary region suggests a role in providing the connecting cilium with structural support. It has been proposed that the periciliary

membrane is physically connected to the connecting cilium by means of interactions between the ectodomains of usherin and Adgrv1 (Fig. 8) [15,20]. The photoreceptor apical inner segment and periciliary region are also thought to be involved in docking of trans-Golgi-derived vesicles that contain cargo essential for outer segment formation, maintenance, and function [55]. The USH protein complex, including usherin, has been proposed to play a role in this process [20]. Based on our functional and immunohistochemical data, we propose a dual role for usherin in zebrafish photoreceptors: providing the connecting cilium with (ectodomain-mediated) structural support and participating in vesicle docking and/or signaling mediated by the intracellular region. Moreover, reduced retinal function and increased cell death in the retinal outer nuclear layer combined with the localization of truncated usherin at the periciliary membrane of the *ush2a*[b1245] mutant, point towards a critical role for the intracellular region of usherin in retinal function, a significant finding for future therapeutic interventions.

3
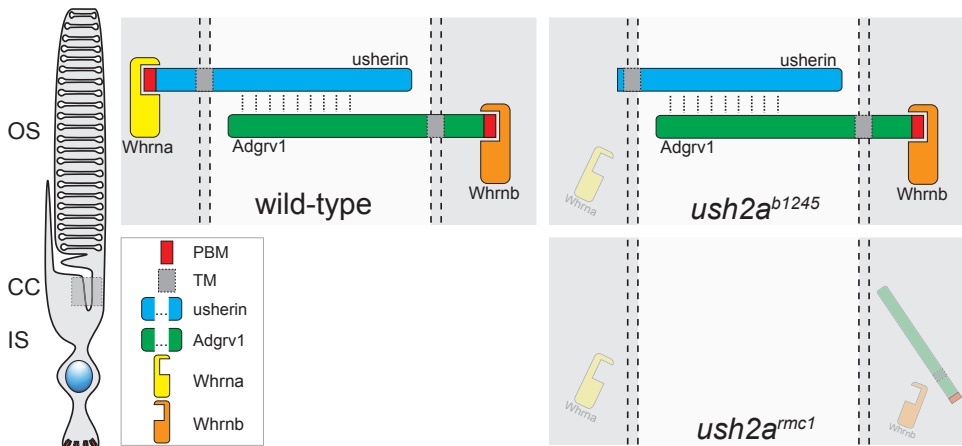
Figure 8. Schematic model of molecular consequences for other USH2 proteins in *ush2a* mutants. The ectodomain of wild-type usherin associates with the ectodomain of Adgrv1 (indicated by dashed lines). Whrna and Whrnb bind via a PDZ-PBM-mediated interaction to usherin and Adgrv1, respectively. The *ush2a*[rmc1] allele results in the complete absence of usherin at the periciliary region. As a consequence, localization of Adgrv1, Whrna and Whrnb at the periciliary membrane is also affected. The *ush2a*[b1245] allele, however, generates a truncated usherin protein that lacks only the C-terminal 62 amino acids and that is still located at the proper subcellular location in the photoreceptor cell. Because Whrna is mislocalized in this mutant and Whrnb localization is largely unaffected, we propose a model in which Whrna has a higher binding affinity for usherin, and Whrnb a higher binding affinity for Adgrv1. IS: inner segment, OS: outer segment, PBM: PDZ-binding motif.

The first clinical sign of retinal dysfunction in patients with Usher syndrome is typically night blindness, indicative of rod dysfunction. In zebrafish, rod photoreceptors contribute little to visual function before about 14 dpf [56,57]. In both *ush2a* mutants, however, we observed impaired ERGs at 5 dpf, which is suggestive of early-onset cone

dysfunction. Although ERG data of pre-symptomatic patients are typically not available, a recent study demonstrated markedly reduced ERG responses for both rods and cones in adolescent Usher syndrome type 2a patients [58], consistent with our observations of cone defects by the onset of vision in zebrafish *ush2a* mutants. Furthermore, *USH2A*-associated retinal degeneration in humans has a slow, progressive pathology. Zebrafish, unlike humans, have the ability to regenerate retinal cells lost to injury or disease. Steady cell proliferation from stem-like populations in the ciliary marginal zone persists throughout adult stages [59]. Acute damage to the retina triggers the reprogramming of Müller glial cells into retinal progenitor cells that are able to differentiate into all major types of retinal neurons including photoreceptors [60]. Either or both of these regenerative pathways could explain the finding that *ush2a* mutants showed no progressive loss of retinal photoreceptor cells (Fig. S4) under normal light conditions, although increased levels of photoreceptor apoptosis and impaired visual function were observed within the first week of life when larvae were challenged by exposure to constant illumination with 3000 lux of white light. These observations suggest that sustained exposure to higher light levels throughout life might disrupt the homeostasis between slow degeneration and steady repopulation by regeneration in these mutants. Importantly these observations may have significant implications for light exposure and the use of sunglasses or high-energy wavelength filtering lenses as treatments in Usher syndrome patients. In conclusion, we have shown that zebrafish *ush2a* mutants show an early onset retinal dysfunction, mainly in the absence of photoreceptor degeneration. Not only will these mutants avail our studies of the retinal function of usherin, but the quantified phenotypes of USH2 protein mislocalization, defects in visual function and increased photoreceptor degeneration in elevated light conditions in *ush2a* mutants can all be used as measures for evaluation of therapeutic strategies that are currently being developed for the future treatment of *USH2A*-associated retinal degeneration.

3

REFERENCES

1. Sandberg, M. A. *et al.* Disease course in patients with autosomal recessive retinitis pigmentosa due to the USH2A gene. *Invest Ophthalmol Vis Sci* 49, 5532-5539 (2008).

2. Tazetdinov, A. M., Dzhemileva, L. U. & Khusnutdinova, E. K. [Molecular genetics of Usher syndrome]. *Genetika* 44, 725-733 (2008).

3. Millan, J. M. *et al.* An update on the genetics of usher syndrome. *Journal of ophthalmology* 2011, 417217 (2011).

4. McGee, T. L., Seyedahmadi, B. J., Sweeney, M. O., Dryja, T. P. & Berson, E. L. Novel mutations in the long isoform of the USH2A gene in patients with Usher syndrome type II or non-syndromic retinitis pigmentosa. *J Med Genet* 47, 499-506 (2010).

5. Yan, D. & Liu, X. Z. Genetics and pathological mechanisms of Usher syndrome. *Journal of human genetics* 55, 327-335 (2010).

6. Aller, E. *et al.* The USH2A c.2299delG mutation: dating its common origin in a Southern European population. *Eur J Hum Genet* 18, 788-793 (2010).

7. Baux, D. *et al.* Enrichment of LOVD-USHbases with 152 USH2A genotypes defines an extensive mutational spectrum and highlights missense hotspots. *Hum Mutat* 35, 1179-1186 (2014).

8. Pennings, R. J. *et al.* USH2A mutation analysis in 70 Dutch families with Usher syndrome type II. *Hum Mutat* 24, 185 (2004).

9. Lenassi, E. *et al.* A detailed clinical and molecular survey of subjects with nonsyndromic USH2A retinopathy reveals an allelic hierarchy of disease-causing variants. *Eur J Hum Genet* 23, 1318-1327 (2015).

10. Hartong, D. T., Berson, E. L. & Dryja, T. P. Retinitis pigmentosa. *Lancet* 368, 1795-1809 (2006).

11. Adato, A. *et al.* Usherin, the defective protein in Usher syndrome type IIA, is likely to be a component of interstereocilia ankle links in the inner ear sensory cells. *Hum Mol Genet* 14, 3921-3932 (2005).

12. van Wijk, E. *et al.* Identification of 51 novel exons of the Usher syndrome type 2A (USH2A) gene that encode multiple conserved functional domains and that are mutated in patients with Usher syndrome type II. *Am J Hum Genet* 74, 738-744 (2004).

13. Chen, Q., Zou, J., Shen, Z., Zhang, W. & Yang, J. Whirlin and PDZ domain-containing 7 (PDZD7) proteins are both required to form the quaternary protein complex associated with Usher syndrome type 2. *J Biol Chem* 289, 36070-36088 (2014).

14. Reiners, J. *et al.* Scaffold protein harmonin (USH1C) provides molecular links between Usher syndrome type 1 and type 2. *Hum Mol Genet* 14, 3933-3943 (2005).

15. Sorusch, N. *et al.* Characterization of the ternary Usher syndrome SANS/ush2a/whirlin protein complex. *Hum Mol Genet* (2017).

16. van Wijk, E. *et al.* The DFNB31 gene product whirlin connects to the Usher protein network in the cochlea and retina by direct association with USH2A and VLGR1. *Hum Mol Genet* 15, 751-765 (2006).

17. Yang, J. *et al.* Ablation of whirlin long isoform disrupts the USH2 protein complex and causes vision and hearing loss. *PLoS genetics* 6, e1000955 (2010).

18. Zou, J. *et al.* Whirlin replacement restores the formation of the USH2 protein complex in whirlin knockout photoreceptors. *Invest Ophthalmol Vis Sci* 52, 2343-2351 (2011).

19. Liu, X. *et al.* Usherin is required for maintenance of retinal photoreceptors and normal development of cochlear hair cells. *Proc Natl Acad Sci U S A* 104, 4413-4418 (2007).

20. Maerker, T. *et al.* A novel Usher protein network at the periciliary reloading point between molecular transport machineries in vertebrate photoreceptor cells. *Hum Mol Genet* 17, 71-86 (2008).

21. Overlack, N. *et al.* Direct interaction of the Usher syndrome 1G protein SANS and myomegalin in the retina. *Biochim Biophys Acta* 1813, 1883-1892 (2011).

22. Slijkerman, R. W. *et al.* The pros and cons of vertebrate animal models for functional and therapeutic research on inherited retinal dystrophies. *Progress in retinal and eye research* 48, 137-159 (2015).

23. Blanco-Sanchez, B., Clement, A., Phillips, J. B. & Westerfield, M. Zebrafish models of human eye and inner ear diseases. *Methods in cell biology* 138, 415-467 (2017).

24. Phillips, J. B. *et al.* Harmonin (Ush1c) is required in zebrafish Muller glial cells for photoreceptor synaptic development and function. *Disease models & mechanisms* 4, 786-800 (2011).

25. Seiler, C. *et al.* Duplicated genes with split functions: independent roles of protocadherin15 orthologues in zebrafish hearing and vision. *Development* 132, 615-623 (2005).

26. Wasfy, M. M., Matsui, J. I., Miller, J., Dowling, J. E. & Perkins, B. D. myosin 7aa(-/-) mutant zebrafish show mild photoreceptor degeneration and reduced electroretinographic responses. *Exp Eye Res* 122, 65-76 (2014).

27. Ebermann, I. *et al.* PDZD7 is a modifier of retinal disease and a contributor to digenic Usher syndrome. *J Clin Invest* 120, 1812-1823 (2010).

28. Kimmel, C. B., Ballard, W. W., Kimmel, S. R., Ullmann, B. & Schilling, T. F. Stages of embryonic development of the zebrafish. *Dev Dyn* 203, 253-310 (1995).

29. Sander, J. D., Zaback, P., Joung, J. K., Voytas, D. F. & Dobbs, D. Zinc Finger Targeter (ZiFiT): an engineered zinc finger/target site design tool. *Nucleic acids research* 35, W599-605 (2007).

30. Sedmak, T. & Wolfrum, U. Intraflagellar transport molecules in ciliary and nonciliary cells of the retina. *J Cell Biol* 189, 171-186 (2010).

31. Sedmak, T., Sehn, E. & Wolfrum, U. Immunoelectron microscopy of vesicle transport to the primary cilium of photoreceptor cells. *Methods in cell biology* 94, 259-272 (2009).

32. Sirisi, S. *et al.* Megalencephalic leukoencephalopathy with subcortical cysts protein 1 regulates glial surface localization of GLIALCAM from fish to humans. *Hum Mol Genet* 23, 5069-5086 (2014).

33. Rinner, O., Makhankov, Y. V., Biehlmaier, O. & Neuhauss, S. C. Knockdown of cone-specific kinase GRK7 in larval zebrafish leads to impaired cone response recovery and delayed dark adaptation. *Neuron* 47, 231-242 (2005).

34. Januschka, M. M., Burkhardt, D. A., Erlandsen, S. L. & Purple, R. L. The ultrastructure of cones in the walleye retina. *Vision Res* 27, 327-341 (1987).

35. Lenassi, E., Saihan, Z., Bitner-Glindzicz, M. & Webster, A. R. The effect of the common c.2299delG mutation in USH2A on RNA splicing. *Exp Eye Res* 122, 9-12 (2014).

36. Mou, H. *et al.* CRISPR/Cas9-mediated genome editing induces exon skipping by alternative splicing or exon deletion. *Genome biology* 18, 108 (2017).

37. Dowling, J. E. What can a zebrafish see with only an off-pathway and other fish stories? *Journal of ophthalmic & vision research* 7, 97-99 (2012).

38. Slijkerman, R. W. Molecular Genetics of Usher Syndrome: Current State of Understanding. *eLS* John Wiley & Sons (2017).

39. Schwander, M. *et al.* A novel allele of myosin VIIa reveals a critical function for the C-terminal FERM domain for melanosome transport in retinal pigment epithelial cells. *J Neurosci* 29, 15810-15818 (2009).

40. Tian, C. *et al.* Ush1c gene expression levels in the ear and eye suggest different roles for Ush1c in neurosensory organs in a new Ush1c knockout mouse. *Brain Res* 1328, 57-70 (2010).

41. Yao, L. *et al.* The Time Course of Deafness and Retinal Degeneration in a Kunming Mouse Model for Usher Syndrome. *PLoS One* 11, e0155619 (2016).

42. May-Simera, H., Nagel-Wolfrum, K. & Wolfrum, U. Cilia - The sensory antennae in the eye. *Progress in retinal and eye research* 60, 144-180 (2017).

43. Sahly, I. *et al.* Localization of Usher 1 proteins to the photoreceptor calyceal processes, which are absent from mice. *J Cell Biol* 199, 381-399 (2012).

44. Ernest, S. *et al.* Mariner is defective in myosin VIIA: a zebrafish model for human hereditary deafness. *Hum Mol Genet* 9, 2189-2196 (2000).

45. Glover, G., Mueller, K. P., Sollner, C., Neuhauss, S. C. & Nicolson, T. The Usher gene cadherin 23 is expressed in the zebrafish brain and a subset of retinal amacrine cells. *Mol Vis* 18, 2309-2322 (2012).

46. Sollner, C. *et al.* Mutations in cadherin 23 affect tip links in zebrafish sensory hair cells. *Nature* 428, 955-959 (2004).

47. Blanco-Sanchez, B., Clement, A., Fierro, J., Jr., Washbourne, P. & Westerfield, M. Complexes of Usher proteins preassemble at the endoplasmic reticulum and are required for trafficking and ER homeostasis. *Disease models & mechanisms* 7, 547-559 (2014).

48. Hodel, C. *et al.* Myosin VIIA is a marker for the cone accessory outer segment in zebrafish. *Anatomical record* 297, 1777-1784 (2014).

49. Yacob, A., Wise, C. & Kunz, Y. W. The accessory outer segment of rods and cones in the retina of the guppy, Poecilia reticulata P. (Teleostei). An electron microscopical study. *Cell Tissue Res* 177, 181-193 (1977).

50. Burnside, B., Wang, E., Pagh-Roehl, K. & Rey, H. Retinomotor movements in isolated teleost retinal cone inner-outer segment preparations (CIS-COS): effects of light, dark and dopamine. *Exp Eye Res* 57, 709-722 (1993).

51. Hodel, C., Neuhauss, S. C. & Biehlmaier, O. Time course and development of light adaptation processes in the outer zebrafish retina. *The anatomical record. Part A, Discoveries in molecular, cellular, and evolutionary biology* 288, 653-662 (2006).

52. Wagner, B., Wagner, M. & Ryc, M. Morphological evidence for different types of IgG-Fc receptors in group A streptococci. *Zentralblatt fur Bakteriologie, Mikrobiologie, und Hygiene. Series A, Medical microbiology, infectious diseases, virology, parasitology* 256, 61-71 (1983).

53. Michalski, N. *et al.* Molecular characterization of the ankle-link complex in cochlear hair cells and its role in the hair bundle functioning. *J Neurosci* 27, 6478-6488 (2007).

54. Force, A. *et al.* Preservation of duplicate genes by complementary, degenerative mutations. *Genetics* 151, 1531-1545 (1999).

55. Falk, N., Losl, M., Schroder, N. & Giessl, A. Specialized Cilia in Mammalian Sensory Systems. *Cells* 4, 500-519 (2015).

56. Bilotta, J., Saszik, S. & Sutherland, S. E. Rod contributions to the electroretinogram of the dark-adapted developing zebrafish. *Dev Dyn* 222, 564-570 (2001).

57. Moyano, M., Porteros, A. & Dowling, J. E. The effects of nicotine on cone and rod b-wave responses in larval zebrafish. *Visual neuroscience* 30, 141-145 (2013).

58. Sengillo, J. D. *et al.* Electroretinography Reveals Difference in Cone Function between Syndromic and Nonsyndromic USH2A Patients. *Scientific reports* 7, 11170 (2017).

59. Wan, Y. *et al.* The ciliary marginal zone of the zebrafish retina: clonal and time-lapse analysis of a continuously growing tissue. *Development* 143, 1099-1107 (2016).

60. Wan, J. & Goldman, D. Retina regeneration in zebrafish. *Curr Opin Genet Dev* 40, 41-47 (2016).

3

SUPPLEMENTAL FIGURES
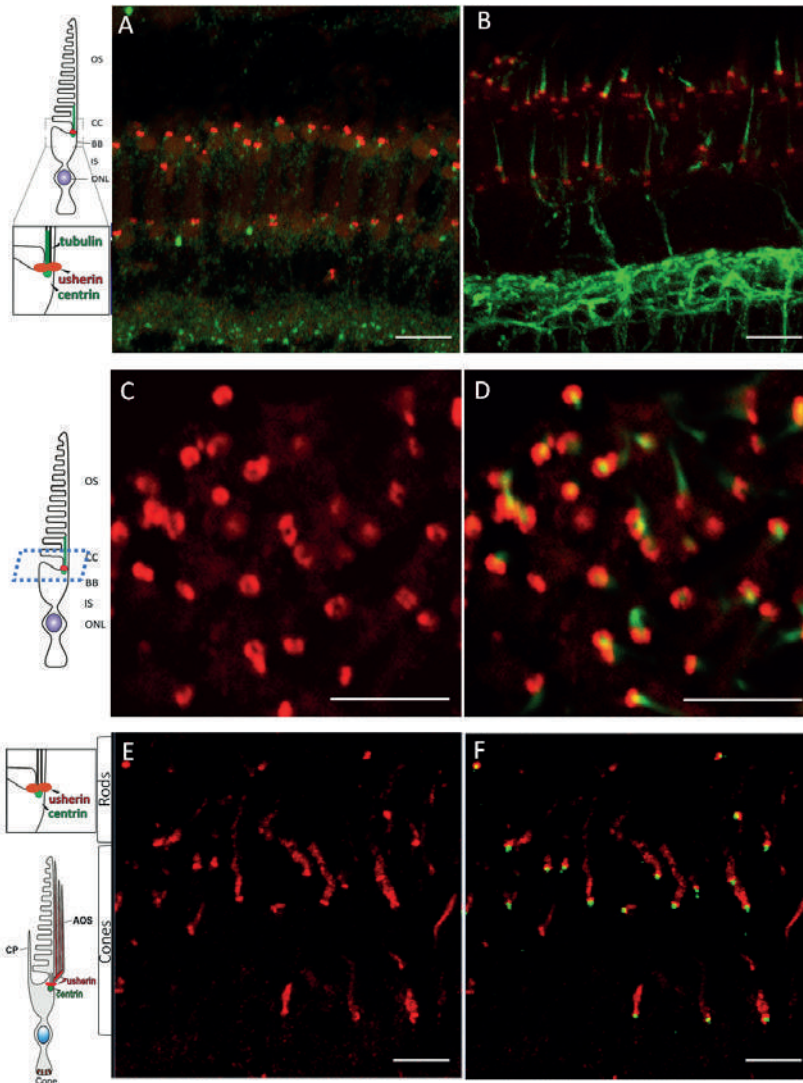
Supplemental Figure 1. Specific organization of usherin within wild-type photoreceptors is revealed by scanning confocal microscopy.

(A,B) Anti-usherin antibody localizes in a flattened disc pattern spanning the photoreceptor periciliary region in cross sections of 6dpf wild-type retinas. Tissue co-labeled sequentially with anti-centrin (A) to mark the basal body or acetylated α-tubulin to mark the connecting cilium (B) further defines the region of usherin enrichment between these two structures. (C,D) Transverse sections through the 6dpf larval retina (dotted line on schematic) reveal the usherin localization pattern as a ring at the periciliary region (cilia labeled green in panel D). (E,F) Cross sections of adult retinas labeled for usherin and centrin (F only) show the persistance of the ring structure superior to the basal body in addition to the localization within the accessory outer segments of cone photoreceptors. Scale bars: 5μm.
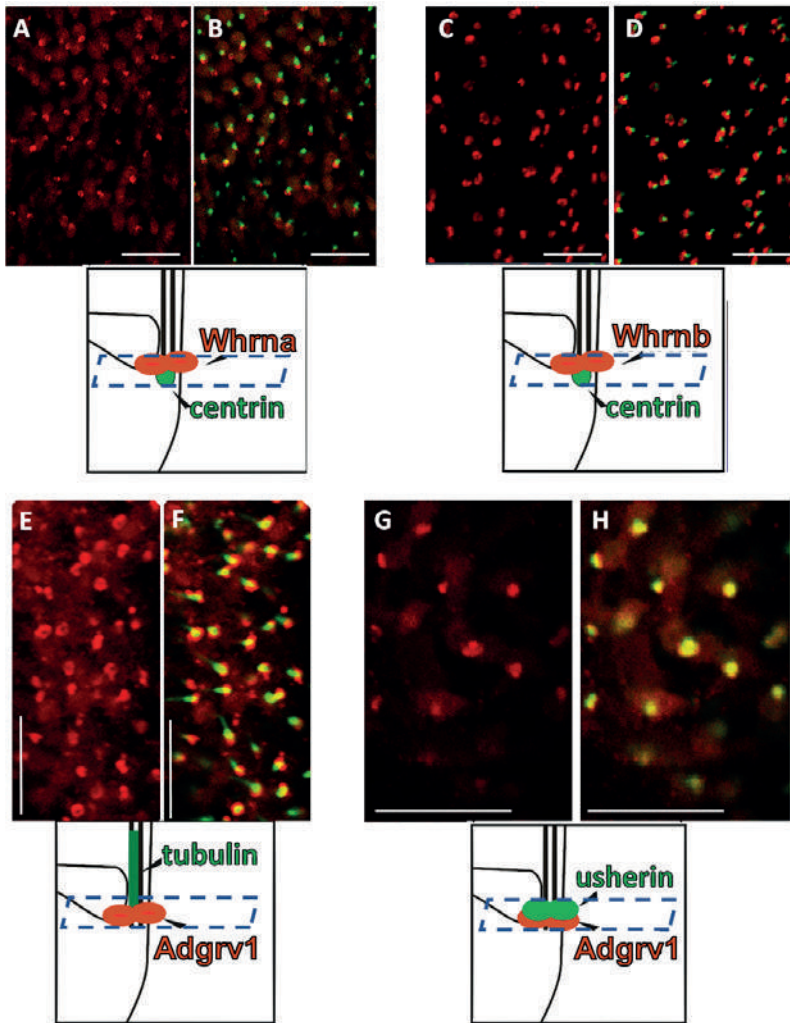
Supplemental Figure 2. Zebrafish USH2 proteins encircle the base of the connecting cilium.

(A-D) Transverse sections through the inner-outer segment boundary of 6dpf larval photoreceptors shows whirlin proteins (red; WhrnA: **A**, **B**, WhrnB: **C**, **D**) at the periciliary region. Centrin marks the basal body/ connecting cilium in green. **(E-H)** In transverse sections of 6dpf larval retinas, Adgrv1 (red) organizes into a concentric ring **(E, F)** surrounding the connecting cilium (acetylated α-tubulin, green in **F**); Adgrv1 (red) and usherin (green) localization overlaps in this region **(G, H)**. Scale bars: 5μm. Plane of sectioning shown in schematics.

A

ush2a^rmc1 (c.2337_2342delinsAC; p.Cys780GlnfsTer32)

```
wt:  ACTGGACAGTGTGAGTGCAAAGCTGGTGTGCGGG
mut: ACTGGACAGTGTGA     ACAGCTGGTGTGCGGG
```
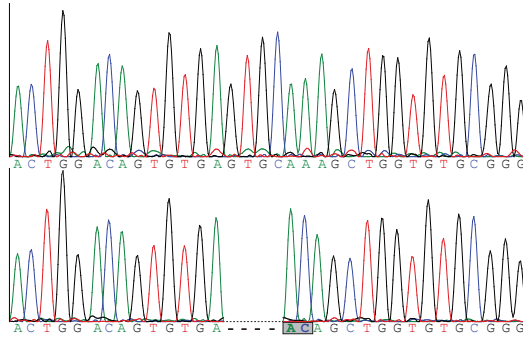

B

ush2a^b1245 (c.15520_15523delinsTG; p.Ala5174fsTer)

```
wt:  GCCAGCTGAGCCATGCCTACTCCCAGAATTCC
mut: GCCAGCTGAGCCAT     TGACTCCCAGAATTCC
```
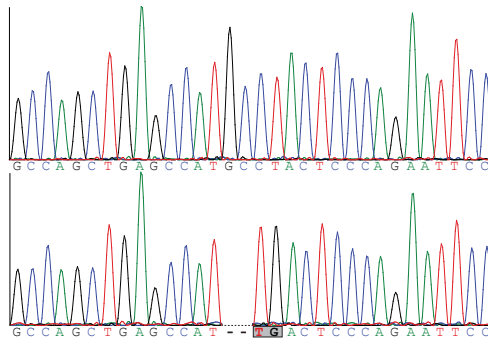

Supplemental Figure 3. DNA sequence traces of homozygous *ush2a^rmc1* and *ush2a^b1245* alleles.

(A) The *ush2a^rmc1* allele contains a six basepair deletion ('GTGCAA') and a two basepair insertion ('AC') in *ush2a* exon13 (c.2337_2342delinsAC; p.Cys780GlnfsTer32). Lower sequence traces are derived from larvae homozygous for the *ush2a^rmc1* allele, whereas the upper sequence traces are derived from strain-matched wild-type larvae. **(B)** Zebrafish homozygous for the *ush2a^b1245* allele have a four basepair-deletion ('GCCT') and a two basepair insertion ('TG') in *ush2a* exon71, creating an instant TGA termination codon (c.15520_15523delinsTG; p.Ala5174fsTer). Lower sequence traces are derived from larvae homozygous for the *ush2a^b1245* allele, whereas the upper sequence traces are derived from strain-matched wild-type larvae.
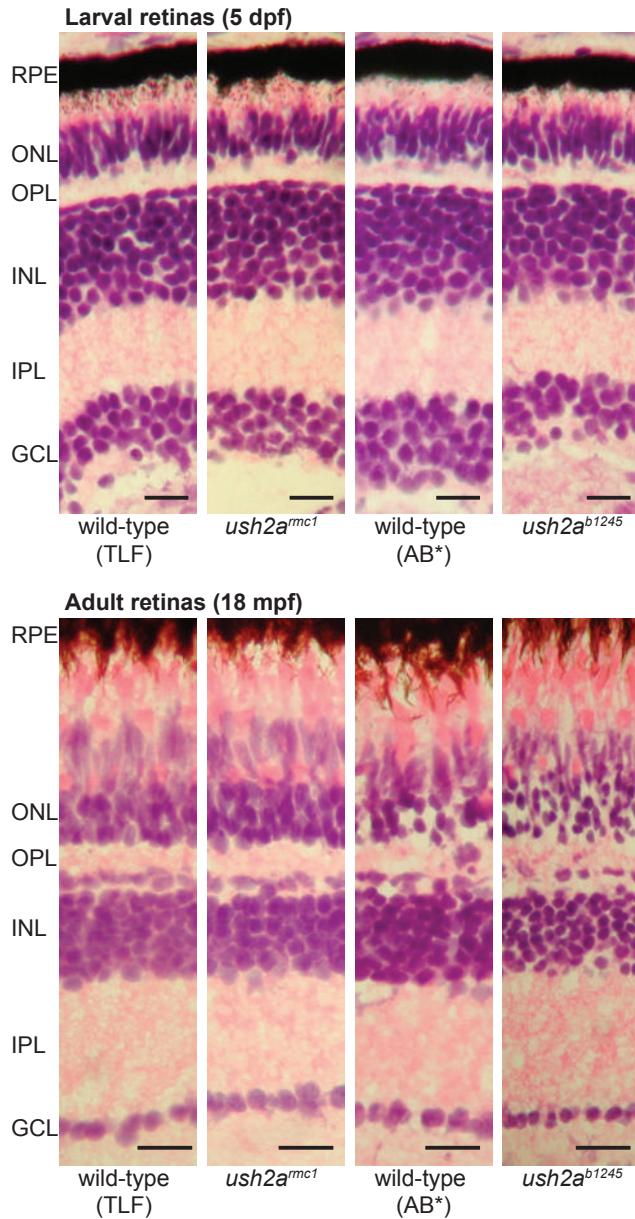
Supplemental Figure 4. Histological examination of *ush2a^{rmc1}* and *ush2a^{b1245}* zebrafish retinas.

Light microscopy of retinal sections from larval (5 dpf) and adult (18 mpf) zebrafish stained with hematoxylin and eosin. Retinas of wild-type and both mutant alleles are morphologically indistinguishable from wild-type retinas at both ages. (n=7 larvae and n=4 adult eyes (18 mpf) with *ush2a^{rmc1}* mutant, *ush2a^{b1245}* mutant, TLF and AB* fish). Dpf: days post fertilization, mpf: months post fertilization, GCL: ganglion cell layer, IPL: inner plexiform layer, OPL: outer plexiform layer, ONL: outer nuclear layer, RPE: retinal pigment epithelium. Scale bars: 10 μm.
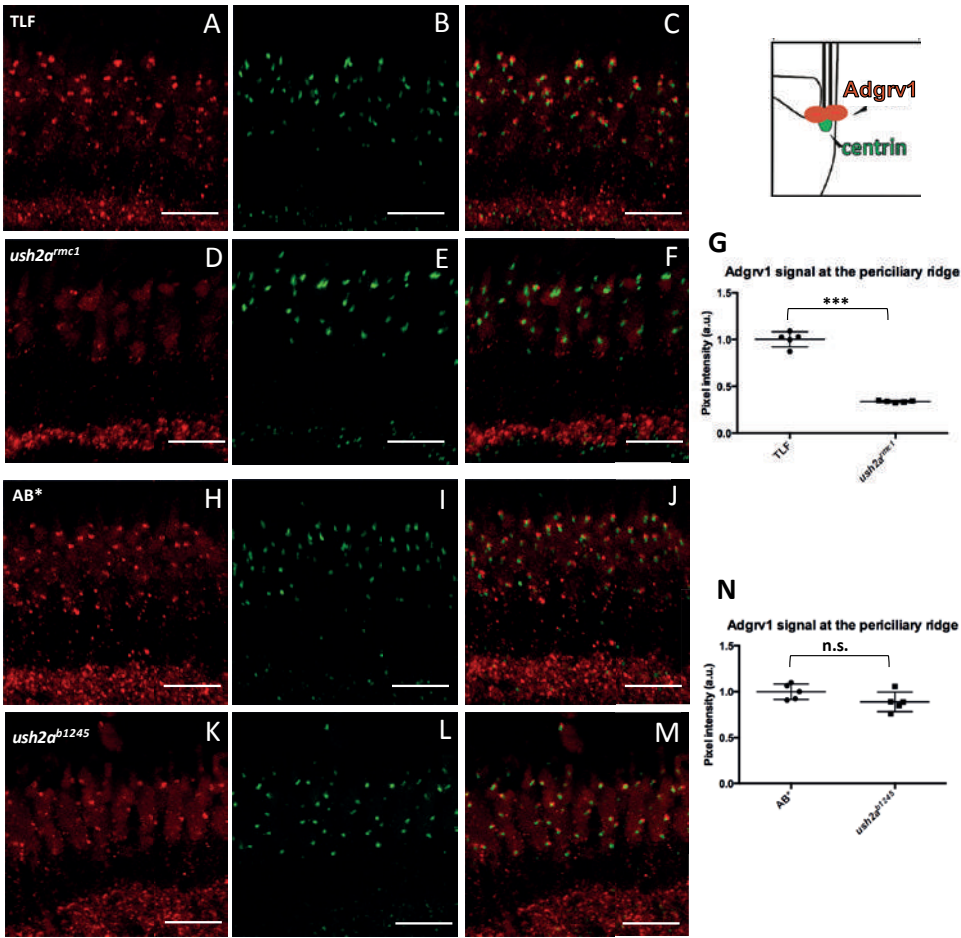
Supplemental Figure 5. Ablation of usherin affects the localization of Adgrv1 in the zebrafish retina (5 dpf).

M. Dona[1,3], T. Peters[1,4], L. Hetterschijt[1,4], S. Broekman[2], E. de Vrieze[1,4], J. Oostrik[1,4], M.A. Huynen[5], R.W.N. Slijkerman[1,3], H. Kremer[1,2,4] and E. van Wijk[1,4]

[1] Department of Otorhinolaryngology, Radboudumc, Nijmegen, the Netherlands; [2] Department of Human Genetics, Radboudumc, Nijmegen, the Netherlands; [3] Radboud Institute for Molecular Life Sciences, Nijmegen, the Netherlands; [4] Donders Institute for Brain, Cognition, and Behaviour, Nijmegen, the Netherlands; [5] Centre for Molecular and Biomolecular Informatics, Radboudumc, Nijmegen, The Netherlands

Chapter 4

Gene therapy using *miniUSH2A* genes improves visual function in a zebrafish *ush2a* knock-out model

4

ABSTRACT

Mutations in *USH2A* are among the most frequent causes of recessively inherited syndromic and non-syndromic retinitis pigmentosa, for which no treatment options are available. The absence of a suitable cellular or animal model that mimics the *USH2A*-associated retinal phenotype for long hampered the development and evaluation of novel therapeutic strategies. Recently, the first *ush2a* knock-out zebrafish models were generated that presented with early-onset retinal dysfunction. Another critical roadblock in the development of a genetic therapy for *USH2A* is the size of the coding sequence, which by far exceeds the packaging capacities of the currently available viral vectors for gene delivery. In this study we report the identification and characterization of two human *miniUSH2A* genes that are amenable to viral delivery and improve retinal function of the *ush2a^rmc1* zebrafish mutant when expressed. For this purpose, *Tol2*-based transgenic *ush2a^rmc1* zebrafish lines that stably express miniUSH2A-1 or -2 under the control of a photoreceptor-specific promoter were generated. Expression of either miniUSH2A rescued the levels of interaction partner Whrna at the photoreceptor periciliary region. Furthermore, electroretinogram (ERG) traces and visual motor responses (VMR) were fully restored after expression of miniUSH2A-1 and significantly improved after expression of miniUSH2A-2. In conclusion, this study shows the potential of using shortened *USH2A* genes for the future treatment of *USH2A*-associated retinitis pigmentosa.

1.   INTRODUCTION

The *USH2A* gene is mutated in patients with Usher syndrome type IIa (USH2a). Patients suffer from congenital hearing impairment and a progressive loss of visual function, as a consequence of retinitis pigmentosa (RP) [1,2]. Besides causing USH2a, mutations in *USH2A* are also among the most common cause of autosomal recessively inherited non-syndromic RP [2,3]. *USH2A*-associated RP is generally diagnosed after puberty. The initial clinical sign is often night blindness, which is followed by a progressive loss of peripheral vision that often results in legal blindness in the sixth or seventh decade of life [4]. While hearing loss can be partially compensated by providing patients with hearing aids or cochlear implants [5], currently no treatment options are available to compensate for the progressive loss of visual function.

Up to now, two protein-encoding *USH2A* transcripts have been identified in the retina. A transcript encoding usherin[isoA] consists of 21 exons and encodes a presumably secreted protein of 1,551 amino acids [6]. The transcript encoding usherin[isoB] is built up by 51 additional exons, and encodes a transmembrane protein of 5,202 amino acids [7]. Usherin[isoB] has been proposed to be the predominant isoform in murine and zebrafish retina and is required for long-term maintenance of photoreceptor cells [8]. It has been proposed to fulfil a structural role at the periciliary membrane of the photoreceptor and to possibly function in vesicle docking and/or outside-in signalling [9,10]. Together with other known USH proteins, harmonin (USH1C), whirlin (USH2D), SANS (USH1G) and ADhesion G protein-coupled Receptor V1 (ADGRV1), usherin forms a dynamic protein complex that is mainly mediated by highly conserved PDZ domain-PDZ binding motif-based interactions [9,11-19]. However, the exact function of this complex and the molecular mechanism underlying photoreceptor dysfunction in *USH2A*-associated RP remains elusive. Until recently, no suitable animal model was available to study the function of usherin in the retina. The major reason was that the retinal phenotype of patients with USH was not faithfully mimicked in the available *Ush2a* knock-out mouse models for Usher syndrome. The *Ush2a* knock-out mouse only manifests a mild retinal degeneration with a very late age of onset [18]. Recently, zebrafish models having mutations in Usher syndrome-associated genes, such as   *myo7aa* (USH1b), *ush1c* (USH1c) and *pcdh15b* (USH1f), have been shown to exhibit early-onset retinal dysfunction [20-22]. More recently, we generated and characterized the first known *ush2a* knock-out zebrafish models that presented with early-onset retinal dysfunction [8]. These zebrafish mutants therefore provide an excellent opportunity to study the pathogenic mechanism underlying *USH2A*-associated retinal degeneration *in vivo* and to evaluate the potential of future therapeutic strategies.

Several pre-clinical therapeutic strategies have already been explored to restore or overcome the consequences of *USH2A* mutations. Antisense oligonucleotides (AONs)

4

have been successfully used *in vitro* to correct aberrant splicing as a consequence of deep-intronic *USH2A* mutations [23,24]. Using CRISPR/Cas9 technology in patient-derived fibroblasts, the frequently found c.2299delG mutations could be repaired [25]. Furthermore, translational read-through inducing drugs (TRIDs) were demonstrated to lead to read-through of the common nonsense mutation p.Arg3955Ter mutation *in vitro* [26]. AON-based splice modulation, CRISPR/Cas9-based genome editing and translational read-through are largely mutation-specific approaches [23]. As more than 600 different *USH2A* mutations have been identified, which are mostly private and evenly distributed over the gene and include many nonsense, frame-shift inducing, splice-modulating, and missense variants [27], a mutation-independent therapeutic approach would be preferred.

A promising mutation-independent strategy is gene augmentation using viral vectors for delivery. Initially, lentiviral (LV) vectors were often used because of their relatively high packaging capacity of ~8.5 kb. Subretinal injections of LV vectors expressing the USH1b gene, *Myo7a*, in the *shaker1* mouse model rescued the mutant phenotype by restoring the α-transducin translocation in photoreceptors and decreasing the level of photoreceptor apoptosis [28,29]. These results showed the potential of a LV-based delivery of transgenes for the future treatment of retinal dystrophies. However, biosafety poses a concern due to the integrative nature of LV vectors potentially leading to insertional mutagenesis. In contrast, adeno-associated virus (AAV)-based gene therapy vectors form episomal concatemers in the host cell nucleus, which have been shown to be stable in terminally differentiated (photoreceptor) cells [30]. More importantly, the AAV-mediated delivery of a transgene into the subretinal space has proven to be safe and effective in treating photoreceptor degenerative diseases [28,31-35]. However, AAVs have a limited cargo packaging capacity of ~4.8 kb [36], which hampered the progress in the development of gene augmentation therapies for large genes such as *USH2A*. Recent studies have focused on developing methods that enable the delivery of large genes, such as *MYO7A* (USH1b) and *ABCA4* (Stargardt disease), to retinal cells [37]. Augmentation of these genes using dual AAVs resulted in, albeit with low efficiencies, the rescue of the retinal phenotype in the corresponding mouse and pig models [30,38-42]. However, the length of the *USH2A* coding sequence (~15.6 kb) exceeds also the capacity of a dual AAV approach [18].

A potential solution for this critical roadblock is to engineer AAV-amenable minigenes that encode proteins capable of preventing or delaying the clinical symptoms seen in patients. This method has been successfully employed for the *CEP290* and *dystrophin* genes [43-46]. AAV-mediated delivery of a *miniCEP290* gene was proven to be effective in slowing down the severe progression of retinal degeneration in the *Cep290rd16* mouse model for Leber Congenital Amaurosis (LCA) [44]. In addition, reduced muscle

degeneration was observed after the delivery of a mini-*dystrophin* gene using dual AAV vectors in a canine model for Duchenne Muscular Dystrophy (DMD) [45]. Moreover, for patients with Duchenne muscular dystrophy, a phase I/IIa is started with rAAV2.5-CMV-mini-Dystrophin gene vector (www.clinicaltrials.gov).

In this study, we generated two different *Tol2*-based transgenic zebrafish lines that express human *miniUSH2A* genes in the *ush2a^rmc1* background. We show that expression of either *miniUSH2A* gene resulted in significant rescue of the retinal phenotype observed in *ush2a^rmc1* larvae, thereby demonstrating the potential of using *miniUSH2A* genes for the future treatment of *USH2A*-associated RP.

2. MATERIAL AND METHODS

2.1 Zebrafish maintenance and husbandry

Experimental procedures were conducted in accordance with international and institutional guidelines (Dutch guidelines, protocol #RU-DEC 2012-301 and #RU-DEC 2016-0091). Wild type adult Tupfel Long fin (TLF) zebrafish and the previously described *ush2a^rmc1* mutants were used [8]. The zebrafish eggs were obtained from natural spawning of Tuebingen Long-Fin (TLF) breeding fish. Larvae were maintained and raised by standard methods [47].

2.2 Plasmid constructs

Fragments encoding human usherin^isoB amino acid residues (aa) 1-744, aa 1682-1871, aa 2912-3955 and aa 4919-5202 (*miniUSH2A-1*) or usherin^isoB aa 1-47, aa 2912-3955 and aa 4919-5202 (*miniUSH2A-2*) were amplified from Human Retina Marathon®-Ready cDNA (Clontech, #639349) using Phusion® High-Fidelity DNA polymerase (New England Biolabs, #E0553), assembled and cloned in pUC19L using the GeneArt™ Seamless Cloning and Assembly Enzyme Mix (Thermo Fisher, #A14606) according to manufacturer's instructions (primers are listed in Supplemental Table 1). Using Gateway® cloning technology the 3xPRE-ZOP promoter (kindly provided by Dr. Breandán Kennedy [48]) was cloned in the pDONR™P4-P1r vector in order to generate a p5'E vector. *MiniUSH2A-1* and *-2* were cloned in pDONR™221 in order to generate a pME vector. The p5'E-3xPRE-ZOP, pME-*miniUSH2A-1* or *-2* and p3'E-IRES-EGFPpA (Multisite Tol2kit clone 389; generously provided by Prof. Dr. Koichi Kawakami [49]) were cloned in the pDestTol2CG2 (Multisite Tol2kit clone 395) vector using the MultiSite Gateway® Three-Fragment Vector Construction Kit (Thermo Fisher, #12537-023), according to manufacturer's instruction and sequence verified.

2.3   Generation of Tol2 transposase mRNA

Transposase mRNA was generated using the pCS2FA-transposase plasmid as a template. After a phenol:chloroform extraction, the vector was linearized using NotI (NEB, #R0189S), and subsequently purified with DNA clean & Concentrator™ 5-kit (Zymo Research, #D4003T). Capped RNA synthesis was performed using the mMESSAGE mMACHINE™ SP6 Transcription Kit (ThermoFisher, #AM1340) according to manufacturer's protocol. Obtained transcripts were purified using the NucleoSpin® RNA kit (MACHEREY-NAGEL, #740955.250).

2.4   Micro-injections

Zebrafish eggs were obtained from natural spawning. 1 nl of a mixture containing *Tol2* transposase mRNA (250ng/ul), *miniUSH2A* expression construct (250ng/ul), KCL (0.2 M) and phenol red (0.05%) was injected into 1-cell-stage embryos of the *ush2a^{rmc1}* line using a Pneumatic PicoPump pv280 (World Precision Instruments). After injection, embryos were raised at 28°C in E3 embryo medium (5 mM NaCl, 0.17 mM KCl, 0.33 mM $CaCl_2$, 0.33 mM $MgSO_4$) supplemented with 0.1 % v/v methylene blue. At 4 days post fertilization (dpf), embryos were selected for heart-specific EGFP expression. EGFP-positive larvae were raised and subsequently outcrossed with homozygous *ush2a^{rmc1}* mutants to determine germline transmission of the *miniUSH2A* gene.

2.5   Genotyping transgenic *miniUSH2A* zebrafish

Genomic DNA was isolated from 5 pooled EGFP-positive larvae after a two hour incubation step at 55 °C in lysis buffer (10 mM Tris-HCl pH 8.2, 10 mM EDTA, 100 mM NaCl, 0.5 % SDS) supplemented with freshly added proteinase K to a final concentration of 0.20 mg/ml (Invitrogen, #25530049). Isolated genomic DNA (40 ng) was used as input in a PCR to detect *miniUSH2A-1* and *-2*. For this purpose, the Phusion® High-Fidelity PCR Kit (New England Biolabs, E0553) with forward primer 5'-AGACACTCTGCAGTATTCAC-3' (3xPRE-ZOP promoter) and reverse primer 5'-CAGAACTGAATACTTTCAGC-3' (*miniUSH2A-1*) or 5'-GAGTCGTTTGAGGTAGCAGA-3' (*miniUSH2A-2*) were employed. The cycling conditions were as follows: 98°C 60 seconds, 30 cycles of 98°C 10 seconds, 56°C 30 seconds, and 72°C 30 seconds and a final 72°C 5 minutes. Amplified fragments were gel-extracted using the NucleoSpin® Gel and PCR Clean-up kit (MACHERY-NAGEL, #740609.250) and sequence verified.

2.6   Immunohistochemistry

Zebrafish larvae (4-6 dpf) were positioned (ventral side downwards) in Tissue-Tek (4583, Sakura), frozen in melting isopentane and cryosectioned following standard protocols

(7 μm thickness along the lens/optic nerve axis). Sections were permeabilized using 0.01% Tween-20 in PBS followed by a blocking step using blocking solution (10% normal goat serum, 2% BSA in PBS). Primary antibodies diluted in blocking solution were incubated overnight at 4 °C. The following primary antibodies were used: rabbit anti-zebrafish Whrna (1:300; Novus Biological, #42700002), rabbit anti-zebrafish usherin-C (1:500; Novus Biological, #27640002), and mouse anti-centrin (1:500; Novus Biological, #2712468/2677126). The secondary antibodies were goat anti-mouse Alexa Fluor 488 and goat anti-rabbit Alexa Fluor 568 (1:600, Molecular Probes-Invitrogen Carlsbad, CA, USA), diluted in blocking buffer supplemented with DAPI (1:8000) and incubated for 1 hour. Sections were post-fixed in 4% PFA for 5-10 minutes and embedded with Prolong Gold Anti-fade (Thermo Fisher). For the immunofluorescence analyses using rabbit anti-human usherin-C (1:500, kindly provided by Prof. Dr. D. Cosgrove [50]), two adaptations to the protocol were made. The sections were permeabilized in PBS with 0.1% Triton-X for 20 minutes and the used blocking solution consisted of 10% normal goat serum, 2% BSA, 0.1% Triton-X-100 in PBS. Images were taken with an Axioplan2 Imaging fluorescence microscope (Zeiss) equipped with a DC350FX camera (Zeiss, Germany). For quantification of fluorescence after anti-Whrnb and anti-usherin labelings, microscope sections were analyzed using ImageJ. The region of interest was determined in the Alexa Fluor 488 (anti-centrin signal) channel using the "find maxima" option. The 488 channel layer was projected onto the Alexa Fluor 568 (anti-Whrnb or anti-usherin signal) channel after using the 'substract background' function. Next, the 'set measurements', 'analyze particles' and 'measure' tools were used in the Alexa Fluor 568 channel, respectively, to determine the mean gray intensity. *P*-values were calculated using a two-tailed unpaired Student's *t*-test.

2.7   Genomic qPCR analysis

Genomic DNA was isolated from single larvae or adult zebrafish finclips using the QIAamp DNA Mini Kit (Qiagen, #51304) following the manufacturer's protocol. Genomic qPCRs were performed to quantify copy numbers of *miniUSH2A-1* and *-2* using 6ng genomic DNA as input. Specific primers were designed with Primer3Plus (fwd= 5'-TGCCTCGTTTCTTCACAGTC-3' and rev= 5'- GAGCCCAATGAAAGAACTGG -3') covering the transition between the opsin promoter and the start of both miniUSH2A-*1* and -*2*. As an internal reference gene gusb (ENSDART00000091932.5) was employed using fwd= 5'-GTCGTCCCGTCACATTTATTAC-3' and rev= 5'- ATCATGCAGTCCTACTCTGACAC-3'. All reaction mixtures were prepared with the GoTaq qPCR Master Mix (Promega A6001) in accordance with the manufacturer's protocol. All reactions were performed in triplicate with the Applied Biosystems Fast 7900 system. MiniUSH2A/gusb ratios were calculated using the ΔCt method to obtain relative miniUSH2A copy numbers.

2.8 Adaptor-Ligation PCR

To determine the genomic integration sites of *miniUSH2A-1* and *-2* and validate the number of genomic insertions an adaptor-ligation PCR strategy was used, as previously described [51]. As input ~150 ng of genomic DNA extracted from single larvae was used. Amplified fragments were gel-extracted using the NucleoSpin® Gel and PCR Clean-up kit (MACHERY-NAGEL, #740609.250) and sequence verified.

2.9 GST pull-down

In order to produce GST (glutathione S-transferase) fusion proteins, *Escherichia coli* BL21-DE3 was transformed with plasmid pDEST15-usherin_icd (aa 5064-5202). After induction with IPTG, GST fusion proteins were isolated as described before [11]. HA-tagged Whrna was produced by transfecting HEK293T cells with pcDNA3-HA-Whrna, using the transfection reagent polyethylenimine (PEI, PolySciences), according to the manufacturer's instructions. Twenty-four hours after transfection, cells were washed with PBS and subsequently lysed on ice using lysisbuffer (50 mM Tris-HCL pH7.5, 150 mM NaCl, 0.5% Triton-X-100) supplemented with Complete protease inhibitor cocktail (Roche, Germany). GST pull-down assays were performed as described previously [11]. Proteins were resolved on 4-12% NuPage gradient gels (Thermo Fisher #NP0321BOX) and analyzed on immunoblots. Bands were visualized by using the Odyssey Infrared Imaging System (LI-COR, USA). HA-tagged Whrna was detected by anti-HA monoclonal antibodies (Sigma, #H9658). As secondary antibody, Alexa Fluor 680 goat-anti-rabbit IgG was used (Molecular Probes, USA).

2.10 Visual Motor Response assay (VMR)

Locomotor activity was tracked and analyzed using EthoVision XT 11.0 software (Noldus Information Technology BV, Wageningen, The Netherlands), as previously described [8,52]. Larvae (5dpf) were individually positioned into a 48-wells plate, containing 200µl of E3 medium per well. The 48-wells plate was placed in the observation chamber of the DanioVision™ tracking system (Noldus Information Technology BV, Wageningen, The Netherlands). After 20 minutes of dark adaption, the larvae were exposed to 3 cycles of 10 minutes dark/10 minutes light. In all experiments, larvae were subjected to locomotion analyses between 13:00-18:00 in a sound- and temperature-controlled (28°C) behavioral testing room.

2.11 Electroretinograms (ERG)

ERG measurements were performed on isolated larval eyes (5-7 dpf) as previously described [53]. Larvae were dark-adapted for a minimum of 30 min prior to the

measurements and subsequently handled under dim red illumination. Isolated eyes were positioned to face the light source. Under visual control via a standard microscope equipped with red illumination (Stemi 2000C, Zeiss, Oberkochen, Germany), the recording electrode with an opening of approximately 20 *μ*m at the tip was placed against the center of the cornea. This electrode was filled with E3 medium (5 mM NaCl, 0.17 mM KCl, 0.33 mM $CaCl_2$, and 0.33 mM $MgSO_4$). The electrode was moved with a micromanipulator (M330R, World Precision Instruments Inc., Sarasota, USA). A custom-made stimulator was invoked to provide light pulses of 100 ms duration, with a light intensity of 6000 lux. For the light pulses a ZEISS XBO 75W light source was employed and a fast shutter (Uni-Blitz Model D122, Vincent Associates, Rochester, NY, USA) driven by a delay unit interfaced to the main ERG recording setup. Electronic signals were amplified 1000 times by a pre-amplifier (P55 A.C. Preamplifier, Astro-Med. Inc, Grass Technology) with a band pass between 0.1 and 100 Hz, digitized by DAQ Board NI PCI-6035E (National Instruments) via NI BNC-2090 accessories and displayed via a self-developed NI Labview program [54]. Statistical analyses were performed using SPSS Statistics 22 (IBM), and graphs were generated in Excel (Microsoft). Statistical significance was set at p < 0.05. All experiments were performed at room temperature (22°C).

3. RESULTS

3.1 Design and construction of *miniUSH2A* genes

Human usherin is predicted to contain multiple copies of the Laminin-type EGF-like (EGF Lam) domain, the Laminin G (LamG) domain and the Fibronectin type 3 (FN3) domain. To decide which domains of those should be included in the *miniUSH2A* genes, we examined which ones were evolutionary best conserved and therewith likely most critical to the proteins' function. Analysis of the Treefam database (http://www.treefam. org) showed that full length orthologs or usherin, with identical domain composition, arose early in metazoan evolution and can also be found in prebilaterian metazoa like sponges and anemones. We determined the conservation per residue using consurf [55] based on a sequence alignment [56] created from the metazoan orthologs available in 2012. Subsequently averaging the conservation per domain did not reveal any domains with significantly higher scores than the other domains in that family (**Suppl. Fig. 1**). We therefore decided that to construct the *miniUSH2A* genes, there was, based on sequence conservation, no reason not to include the domain combination that was most practical from a cloning point of view.

Considering the transgene packaging capacity of the conventional LV and AAV vectors [30], we constructed two human *USH2A* minigenes (**Fig. 1A**). *MiniUSH2A-1* (~6.8 kb) encodes a polypeptide of 2,262 amino acids containing the signal sequence (S), the

laminin G-like domain (LamGL), the laminin N-terminal domain (LamNT), four EGF Lam domains, one LamG domain, the cysteine-rich region flanked by two and five FN3 domains at the N- and C-terminal side respectively, the transmembrane domain (TM) and the intracellular region containing the class I PDZ-binding motif (PBM). *MiniUSH2A-2* (~4.1 kb) encodes a polypeptide of 1,375 amino acids that contains the usherin signal sequence (S), two FN3 domains, the cysteine-rich region, five additional FN3 domains, the transmembrane domain (TM) and the intracellular region containing the class I PDZ-binding motif (PBM). We cloned the coding sequences of *miniUSH2A-1* and *miniUSH2A-2* in the Tol2 transposon vector pDestTol2CG2, between an enhanced zebrafish opsin promoter and the internal ribosomal entry site (IRES) EGFP. This vector further contains the coding sequences of EGFP under the control of a heart-specific *cmcl2* promoter (**Fig. 1B and C**). The complete expression cassette was flanked by *Tol2* sites.
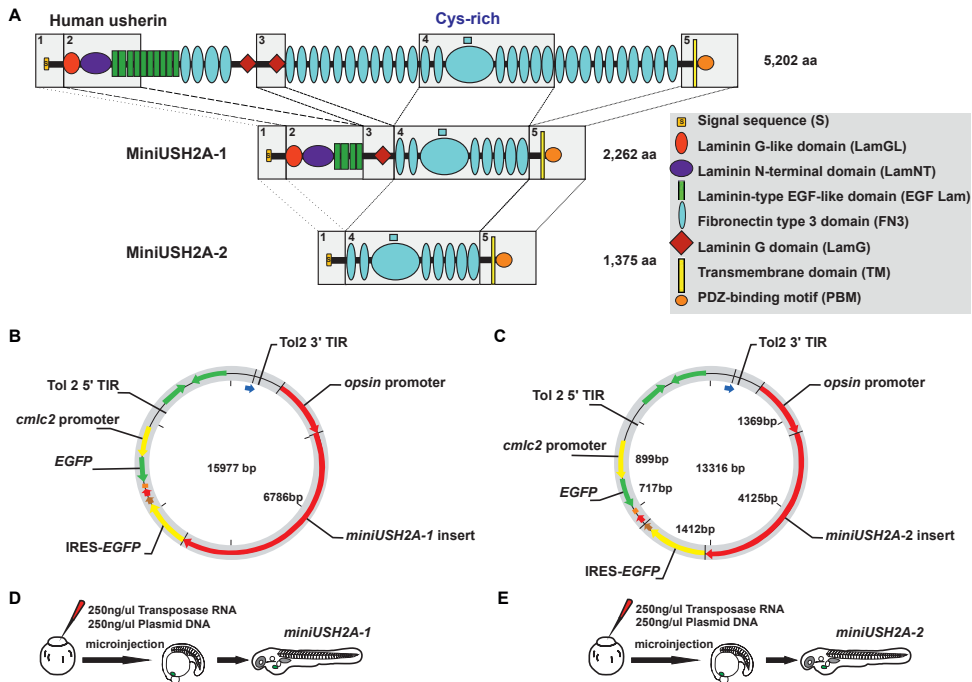
Figure 1. Construction of *miniUSH2A* fragments and generation of *Tg(3xPRE-1_-1.2ZOP:Hsa. miniUSH2A-1 and -2, EGFP, cmcl2:EGFP);ush2a^rmc1^.*

(**A**) Schematic presentation of the domain architecture of human usherin[isoB], miniUSH2A-1 and miniUSH2A-2. The fragments of usherin[isoB] that are encoded in the *miniUSH2A* genes are boxed. *Tol2*-based vectors containing an enhanced zebrafish opsin promoter (*3xPRE-1_-1.2ZOP*) driving the expression of *miniUSH2A-1* (6786 bp) (**B**), *miniUSH2A-2* (4125 bp) (**C**) and IRES-*EGFP* in zebrafish photoreceptors, were generated. The vector further contains the heart-specific *cmcl2* promoter driving the expression of *EGFP*. (**D-E**) The *miniUSH2A*-containing plasmids were co-injected with *Tol2* transposase mRNA into one-cell staged *ush2a^rmc1^* embryos. At 4 dpf, heart-specific EGFP expression could be observed for which the larvae were selected.

3.2 *MiniUSH2A-1* and *miniUSH2A-2* insertion into the genome of *ush2a^rmc1* zebrafish

We injected the minigene-containing vectors together with *Tol2* transposase mRNA into homozygous one-cell staged *ush2a^rmc1* embryos (**Fig. 1D and E**). *ush2a^rmc1* mutants contain a frameshift-inducing mutation in *ush2a* exon 13 (c.2337_2344delinsAC; p.Cys780GlnfsTer32) that leads to a premature termination of translation and, as a consequence, absence of zebrafish usherin. Injected larvae (F0) that were positive for heart-specific EGFP expression at 4 dpf were raised and outcrossed with homozygous *ush2a^rmc1* fish in order to test for germline transmission of the *miniUSH2A* expression cassettes. Again, larvae (F1) with heart-specific EGFP expression were selected. Tol2 transposase induces a random integration of (multiple) transposable elements into the genome. Therefore we performed a genomic qPCR analysis to determine the number of *miniUSH2A* copies that were integrated in the genome of the transgenic F1 larvae. This revealed that for both *USH2A* minigenes multiple copies were present in the genomes of F1 larvae. The same analyses were performed after a second outcross with *ush2a^rmc1* mutants. F2 larvae contained either one or two copies of the *miniUSH2A-1* gene, whereas for *miniUSH2A-2* only larvae were identified with a single copy insertion (**Suppl. Fig**. **2**). This was corroborated by an adaptor ligation assay. This assay also revealed the exact genomic position of minigene insertions. Single copies of *miniUSH2A-1* were found to be integrated at two distinct genomic loci: approximately 70 bp upstream of the zinc-finger CCCH-type containing 4 (*zc3h4*) gene at chromosome 15 (**Fig. 2A; Suppl. Fig. 3**) and in an intergenic region at chromosome 18, approximately 800 bp upstream of *lsm14ab* (**Fig. 2A; Suppl. Fig. 4**). So far, *ZC3H4* mutations have not been associated with a human disease and also no animal models for *ZC3H4* are available. Deletion of *ZC3H4* in patients with the 19q13.32 microdeletion syndrome has also not been reported to be associated with retinal dysfunction [57]. A single copy of *miniUSH2A-2* was found to be integrated within the 5'-UTR of the *zgc:154061* gene at chromosome 17 (**Fig. 2B; Suppl. Fig. 5**). Mutations of *C15ORF41*, the human orthologue of *zgc:154061*, are associated with congenital dyserythropoietic anemia (OMIM: 615631), an inherited disorder that affects the development of red blood cells. Although no retinal phenotype has been described to be associated with *C15ORF41* or *ZC3H4* mutations, we questioned whether disruption of these genes due to the integration of an *USH2A* minigene would affect retinal morphology.

4
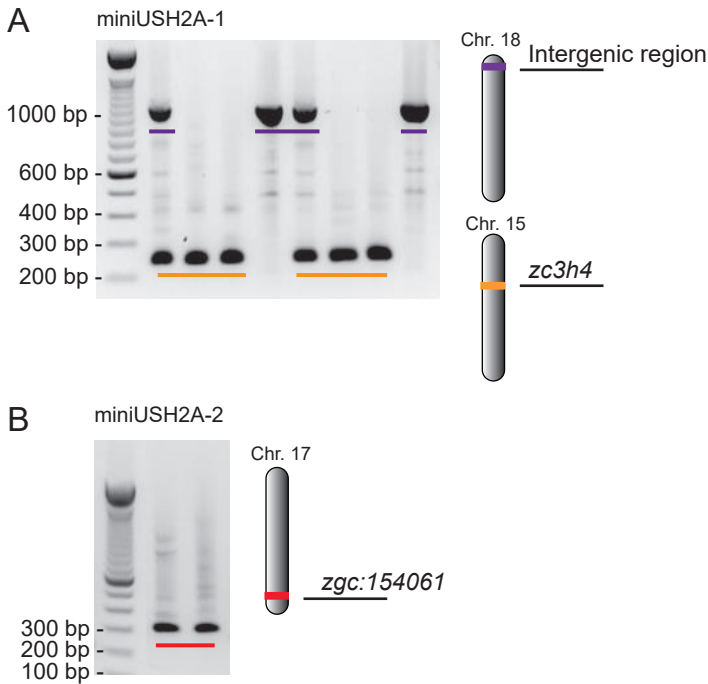
Figure 2. Analysis of *Tol2*-based *miniUSH2A-1* **and -*2* genomic insertions in transgenic** F2 larvae. (**A**) Genomic DNA of transgenic F2 larvae was fragmented and adaptor-ligated. Nested PCR and Sanger sequencing revealed that *miniUSH2A-1* is incorporated in chromosome 15 (larvae 2 and 3, ~250 bp fragment), in chromosome 18 (larva 4, ~1.1 kb fragment), or at both genomic loci (larvae 1 and 5). (**B**) A single copy of *miniUSH2A-2* was incorporated in chromosome 17 (~300 bp fragment).

3.3 MiniUSH2A- 1 and -2 are expressed and localize to the photoreceptor periciliary region

We first determined whether the *USH2A* minigenes are expressed in photoreceptor cells and whether miniUSH2A-1 and -2 localize to the photoreceptor periciliary region in transgenic zebrafish larvae. For this purpose, we performed immunofluorescence assays with an antibody that specifically recognizes the intracellular region of human usherin. As expected, no anti-usherin signal was observed in retina of wild-type and *ush2a^{rmc1}* larvae (**Fig. 3D** and **3E**). In the retina of transgenic larvae, miniUSH2A-1 and -2 were detected adjacent to the connecting cilium/basal body marker centrin (**Fig. 3B** and **3C**). We next assessed whether the expression of the *miniUSH2A* genes had an adverse effect on retinal morphology. Histological analysis of transgenic fish expressing miniUSH2A-1 or -2 showed a normal retinal lamination and cellular organization in both larvae and adults as compared to wild-type controls (5 dpf: n=21; 5 months post fertilization (mpf) n=2; **Suppl. Fig. 6**). Also, no other abnormalities in overall

body morphology or swimming behavior were observed. Therefore, we conclude that the genomic integration and expression of *miniUSH2A-1* or *-2* has no gross negative consequences for zebrafish development and function of adult fish in the presented transgenic zebrafish lines.
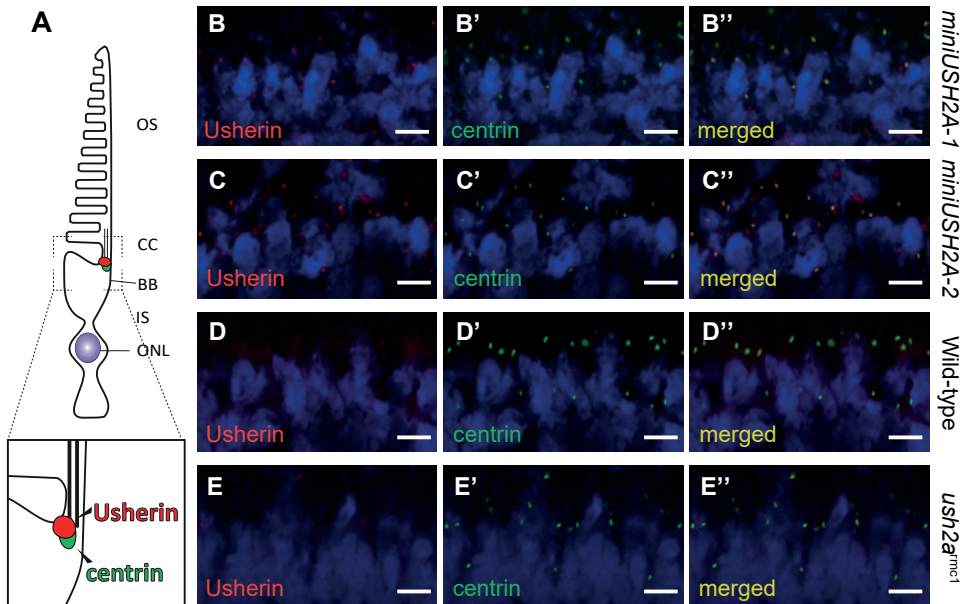
Figure 3. Localization of miniUSH2A-1 and -2 in the retina of transgenic zebrafish (5 dpf). (**A**) Schematic presentation of a cone photoreceptor cell with the expected localization of centrin and miniUSH2A. (**B-C**) In the transgenic zebrafish larvae, miniUSH2A-1 or -2 is detected using an anti-human usherin antibody (red signal), while in wild-type larvae (**D**) and *ush2a^{rmc1}* mutants (**E**) no signal is observed. (n=14 for all groups, from 2 biological replicates). In all images the nuclei are stained with DAPI (blue signal) and anti-centrin is used as a marker for the connecting cilium and basal body (green signal). Scale bars: 5µm.

3.4 Expression of miniUSH2A restores Whrna levels at the photoreceptor periciliary region

Usherin and whirlin interact and are mutually dependent on each other for their localization at the photoreceptor periciliary membrane [11,8,15]. Therefore, we questioned whether the expression of *miniUSH2A-1* or *-2* would result in the restoration of Whrna localization in *ush2a^{rmc1}* zebrafish photoreceptor cells. We first confirmed that the intracellular region of human usherin and zebrafish Whrna indeed interact. In a glutathione S-transferase (GST) pull-down assay, full length HA-tagged Whrna was pulled down from HEK293T cell lysates by GST-fused usherin aa 5064-5202 but not by GST alone (**Fig. 4C**). Subsequently, we performed immunohistochemistry using anti-Whrna antibodies. Anti-centrin antibodies were employed as a marker for the basal
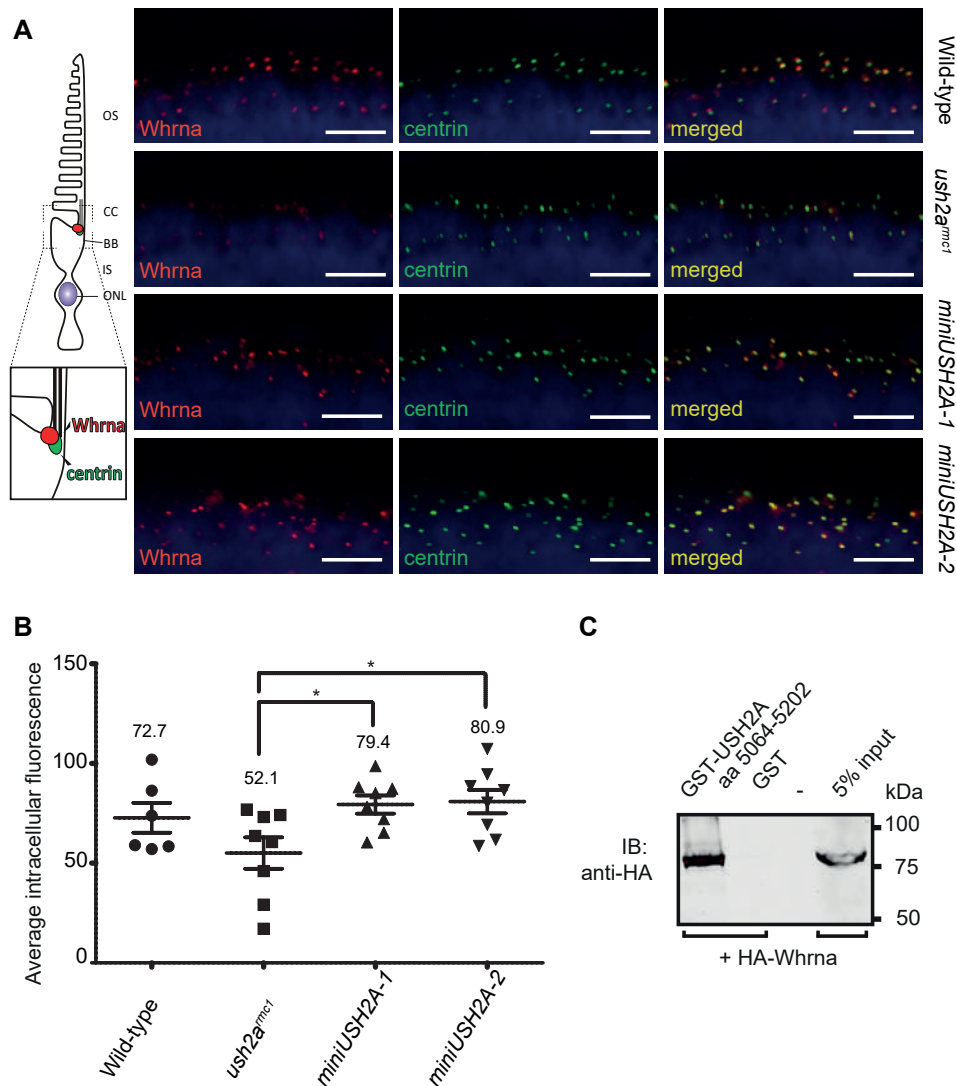
Figure 4. Association of miniUSH2A-1 and -2 with Whrna.

(**A**) Whrna labeling (red signal) at the photoreceptor periciliary region was significantly decreased in *ush2a^rmc1* larvae as compared to wild-type larvae (5 dpf). In transgenic larvae expressing miniUSH2A-1 and miniUSH2A-2, Whrna labeling at the periciliary region was restored (5 dpf) (n= 14 larvae for each group from 2 biological replicates). Nuclei are counterstained with DAPI (blue signal), and anti-centrin (green signal) was used as a basal body and connecting cilium marker. Scale bars: 10 μm. (**B**) Quantification of Whrna localization (red signal) at the photoreceptor periciliary region in both transgenic zebrafish lines as compared to wild-type and *ush2a^rmc1* larvae. Each single datapoint in the scatter graph displays the averaged mean grey value from the eye of one larva. The mean value and the Standard Error of the Mean (SEM) are displayed as bars. Expression of either *miniUSH2A* leads to a significant increase of fluorescence intensity compared to *ush2a^rmc1* mutants. (* indicates *P*<0.05, two-tailed unpaired Student's *t*-test). (**C**) GST pull down assay, showing that HA-tagged zebrafish Whrna was efficiently pulled down by GST-fused usherin (aa5064- aa5202), but not by GST alone. The third line shows 5% input of the protein extract.

body and connecting cilium. In transgenic larvae expressing miniUSH2A-1 or -2, Whrna levels at the photoreceptor periciliary regions were significantly increased as compared to those in *ush2a^{rmc1}* larvae (**Fig. 4A** and **4B**). This demonstrates that expression of *miniUSH2A-1* and *miniUSH2A-2* leads to the formation of an USH2A-Whrna complex at the photoreceptor periciliary region, potentially resulting in the (partial) functional rescue.

3.5 Expression of miniUSH2A rescues the visual motor response

The next step was to assess whether supplementing *ush2a^{rmc1}* zebrafish with human miniUSH2A-1 or -2 (partially) restores retinal function. As shown before, the visual motor response (VMR) is a semi high-throughput behavioral assay by which defects in visual function can be detected in a sensitive and robust way. *ush2a^{rmc1}* larvae have a decreased light-ON VMR as compared to wild-type controls (**Fig. 5**). Recording the light-ON VMR of transgenic *miniUSH2A-1* or *-2 ush2a^{rmc1}* larvae demonstrated that expression of either miniUSH2A protein restored the VMR. The maximum velocity during the first 2 seconds after the light-ON stimulus, which is regarded to be the eye-specific response, was significantly improved in *ush2a^{rmc1}* larvae expressing miniUSH2A-1 or -2 as compared to *ush2a^{rmc1}* mutant larvae ($P<0.01$ for transgenic *miniUSH2A-1* and $P<0.05$ for *miniUSH2A-2* larvae, two-tailed unpaired Student's *t*-test. Furthermore, the recorded VMRs in transgenic *miniUSH2A-1* or *-2* larvae was not significantly different from the VMR recorded in age-matched wild-type larvae ($P=0.39$, two-tailed unpaired Student's *t*-test).
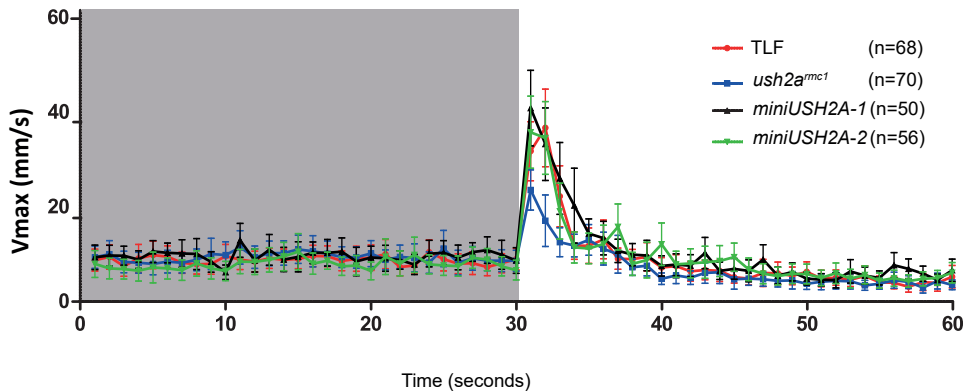
Figure 5. Visual Motor Responses in transgenic zebrafish expressing miniUSH2A-1 or -2 (5 dpf). (**A**) The eye-specific Light-ON Visual Motor Response (VMR) presented as the maximum velocity (mm/s) is shown for the time frame of 30 seconds prior and after light alternation. The average Vmax of wild-type larvae (red line), *ush2a^{rmc1}* larvae (blue line), *miniUSH2A-1*-expressing *ush2a^{rmc1}* larvae (black line), *miniUSH2A-2*-expressing *ush2a^{rmc1}* larvae (green line) is shown. A clear increase in VMR is observed in both *miniUSH2A-1* and *miniUSH2A-2*-expressing *ush2a^{rmc1}* larvae as compared to *ush2a^{rmc1}* mutants (5 dpf; n=56 minimum per group; minimum of 2 biological replicates).

3.6 MiniUSH2A expression enhances b-wave amplitudes of the electro-retinogram

We next recorded electroretinograms (ERGs) to determine the functionality of the retina of transgenic larvae expressing miniUSH2A-1 or -2 (5 dpf). Average ERGs from dark-adapted individual wild-type, *ush2a^rmc1*, *miniUSH2A-1* and *miniUSH2A-2* larvae are shown in **Figure 6A**, together with the maximum average amplitudes plotted as bar-graphs (**Fig. 6B**). Analysis of retinal function by ERG revealed a significant improvement of the b-wave amplitudes of the miniUSH2A-1 (37%) and -2 (57%) expressing larvae at 5dpf compared to the *ush2a^rmc1* larvae (**Fig. 6**). Statistical analyses revealed no significant differences in b-wave amplitudes recorded in *ush2a^rmc1* larvae expressing *miniUSH2A-1* or *-2*. Also the b-wave amplitudes of wild-type control larvae and larvae expressing the *miniUSH2A-1* gene were not significantly different. Overall, our results suggest that the expression of miniUSH2A-1 or miniUSH2A-2 both improves retinal function of *ush2a^rmc1* larvae.
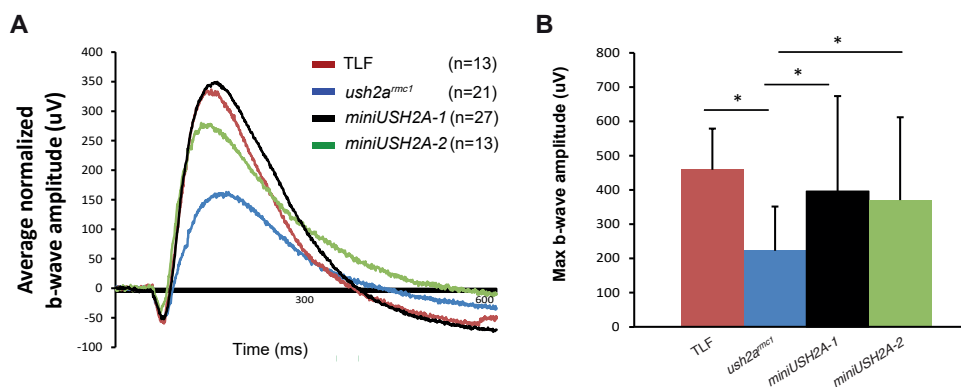
Figure 6. Physiological rescue potential of miniUSH2A-1 and miniUSH2A-2.

(**A**) The average normalized b-wave amplitude (µV) was significantly reduced in *ush2a^rmc1* mutants as compared to strain-matched wild-type larvae (5dpf). B-wave amplitudes recorded in *ush2a^rmc1* larvae expressing miniUSH2A-1 or miniUSH2A-2 were significantly improved as compared to *ush2a^rmc1* larvae. (**B**) Statistical analysis of the maximum b wave amplitudes was performed using at least 13 larvae per experiment. (*$P<0.05$; two-tailed unpaired Student's t-test; n=13 wild-type, n=21 *ush2a^rmc1*, n=27 *miniUSH2A-1* and n=13 *miniUSH2A-2* larvae, from minimal 2 biological replicates).

4. DISCUSSION

Development of gene augmentation therapy for the future treatment of *USH2A*-associated RP has been severely hampered by the enormous size of the usherin-encoding sequence. In this study, we generated different transgenic zebrafish lines to evaluate the therapeutic potential of human *miniUSH2A* genes. We provided evidence for the (partial) restoration of retinal function of *ush2a^rmc1* mutants after expression of

two human *miniUSH2A* genes of different lengths. First of all, using an antibody directed against the intracellular C-terminal region of human usherin, miniUSH2A-1 and -2 were detected at the photoreceptor periciliary region of transgenic larvae. Furthermore, the level of Whrna at the periciliary region was increased in both transgenic lines as compared to *ush2a^{rmc1}* mutants. Finally, expression of *miniUSH2A-1* leads to a complete restoration of visual function as determined by ERG recordings and VMR assays, while expression of *miniUSH2A-2* partially restored visual function.

A Tol2-based strategy was adopted to generate transgenic zebrafish lines that express miniUSH2A. Tol2 transposase catalyzes the excision of the transposon from the donor plasmid, resulting in the stable integration of (multiple copies of) the transposable element at random positions in the genome. As a result, the level of minigene expression can vary significantly between individual larvae. To minimize this variability, we performed all functional analyses on F2 larvae derived from a single transgenic fish in which a single copy of the minigene is inserted at a known position in the genome. Still, to better control minigene expression levels and to enable comparative analyses between different minigene-expressing transgenic lines, integration of a single copy at the same pre-determined genomic locus is preferred. The observed difference in rescue efficiency after expression of either *miniUSH2A-1* or *-2* may be the consequence of the composition of the minigene or can be caused by a difference in expression level resulting from the different genomic loci where the minigenes are integrated. The unknown consequence of the differential genomic integration makes comparison of therapeutic efficacy of different *miniUSH2A* genes extremely difficult. Site-directed zebrafish transgenesis into a single genomic landing site can be achieved with the phiC31 integrase system [58]. A single site-specific integration of minigenes could result in reduced variability, however, the visual performance of transgenic zebrafish containing the phiC31 integrase-mediated genomic landing site still needs to be determined [59].

Prior to the application of minigenes in human subjects, more research is needed to determine the most efficient method of gene delivery and the optimal level of gene expression. Adeno-associated viruses (AAV) are currently the most frequently used vehicles for retinal gene delivery. So far, subretinal injections with viral vehicles such as AAV2, AAV8 and AAV2tYF, have been performed to transduce photoreceptor cells [60]. The major disadvantage of this method is that only cells around the injection site are being transduced. Recently, transduction of mouse photoreceptors after intravitreal injection using an AAV7m8 vector that is capable of penetrating all retinal layers was demonstrated [61]. AAVs have a packing capacity of ~4.7 kb. However, due to the inclusion of necessary regulatory elements, like a promoter and polyadenylation signal, the practical limit for a cDNA that can be packaged in AAV is ~3 kb [60]. This implicates that both *miniUSH2A* genes, respectively ~4.1 kb and ~6.8 kb in length, are still too large to

be incorporated into a single AAV particle. A possible solution is to use a dual or triple AAV approach albeit this will result in a significantly lower therapeutic potential due to the low recombination efficiency [42,62]. Another option is the use of a lentiviral (EIAV) vector with a capacity of ~8.5 kb. Lentiviruses have already been successfully used for augmenting the *Myo7a* gene in the retina of the *shaker1* mouse [28], and are currently being used as the vehicles for delivery in the UshStat® clinical trial Usher syndrome 1b patients. Lentivirus-mediated gene delivery is generally effective for targeting cells of the retinal pigment epithelium (RPE), although it may not be very efficient in transducing differentiated photoreceptors [63]. Future studies therefore need to address whether even smaller *miniUSH2A* genes, that would fit within the range of the packaging capacity of AAV vectors, could also ameliorate the retinal phenotype of zebrafish *ush2a* mutant larvae.

Extensive studies on evolutionary conservation did not identify clearly critical regions for usherin function. From our previous studies it is evident that *ush2a^{b1245}* larvae, which exclusively lack the 62 C-terminal amino acids including the class I PDZ binding motif (PBM), have a retinal phenotype that is comparable to the phenotype of *ush2a^{rmc1}* larvae that completely lack usherin [8]. Furthermore, the dynamic Usher protein complex consisting of Usher syndrome type 1 and 2-associated proteins, is largely mediated by highly conserved intracellular PDZ-PBM-based interactions. Together these data point into the direction that at least the presence of the intracellular region of usherin^{isoB} is essential for zebrafish retinal function.

So far, more than 200 human eyes have been injected with recombinant AAV or lentiviral vectors in clinical trials over the past 10 years using different strategies, vectors and routes of delivery [60]. In general, the safety record of the published retinal gene transfer trials has been excellent. However, direct comparison between studies is challenging due to fundamental differences between the trials. As the success of each approach is gene specific and influenced by many factors, this will also need to be tested for the *USH2A* minigenes. Levels of gene expression and the efficiency of transduction need to be balanced and tested to prevent ineffective treatment or even potential toxic side effects. As usherin is expressed in both rods and cones [64], targeting both types of photoreceptor cells is preferred. Some photoreceptor-specific promoters are used in clinical trials, although more research is needed to determine whether or not these are more suitable than for example a ubiquitously active chicken beta actin (CBA) promoter [60]. Alternatively, the endogenous *USH2A* promoter, which is expected to express the right amount of usherin in the correct cells, could be used.

For now, the ultimate goal of *USH2A* minigene therapy is to stop or slow down the progression of the retinal degeneration. As such, timing of intervention is crucial, since the presence of (partly) viable photoreceptors is essential for this therapeutic approach.

Patients with *USH2A*-associated RP are born with grossly intact and functional photoreceptor cells and only develop the initial signs of visual dysfunction after puberty. The diagnosis Usher syndrome type 2a is nowadays often given before the onset of retinal dysfunction as these children fail the neonatal hearing test and subsequently often undergo genetic testing. This enables the future treatment of young individuals, and might prevent any irreversible disease symptoms. Patient-specific iPSC-derived retinal cells may be useful in unraveling the potential difference in pathogenic mechanisms caused by different mutations [65]. Based on studies in iPSC-derived retinal progenitor cells of an Usher syndrome type 2A patient, it has been postulated that protein-truncating mutations might act via a different mechanism of action than missense mutations [65]. Elucidation of the pathogenic mechanisms underlying RP caused by different types of *USH2A* mutations will reveal whether or not *USH2A* minigene augmentation will be beneficial for all patients with *USH2A*-associated RP or that it will only be suitable for patients with protein-truncating mutations.

ACKNOWLEDGEMENTS

4

REFERENCES

1. Yan, D. & Liu, X. Z. Genetics and pathological mechanisms of Usher syndrome. *Journal of human genetics* 55, 327-335 (2010).

2. McGee, T. L., Seyedahmadi, B. J., Sweeney, M. O., Dryja, T. P. & Berson, E. L. Novel mutations in the long isoform of the USH2A gene in patients with Usher syndrome type II or non-syndromic retinitis pigmentosa. *J Med Genet* 47, 499-506 (2010).

3. Hartong, D. T., Berson, E. L. & Dryja, T. P. Retinitis pigmentosa. *Lancet* 368, 1795-1809 (2006).

4. Sandberg, M. A. *et al.* Disease course in patients with autosomal recessive retinitis pigmentosa due to the USH2A gene. *Invest Ophthalmol Vis Sci* 49, 5532-5539 (2008).

5. Scholl, H. P. *et al.* Emerging therapies for inherited retinal degeneration. *Science translational medicine* 8, 368rv366 (2016).

6. Eudy, J. D. *et al.* Mutation of a gene encoding a protein with extracellular matrix motifs in Usher syndrome type IIa. *Science* 280, 1753-1757 (1998).

7. van Wijk, E. *et al.* Identification of 51 novel exons of the Usher syndrome type 2A (USH2A) gene that encode multiple conserved functional domains and that are mutated in patients with Usher syndrome type II. *American journal of human genetics* 74, 738-744 (2004).

8. Dona, M. *e. a.* Usherin defects lead to early-onset retinal dysfunction in zebrafish. *Experimental Eye Research, submitted* (2018).

9. Maerker, T. *et al.* A novel Usher protein network at the periciliary reloading point between molecular transport machineries in vertebrate photoreceptor cells. *Hum Mol Genet* 17, 71-86 (2008).

10. Sorusch, N. *et al.* Characterization of the ternary Usher syndrome SANS/ush2a/ whirlin protein complex. *Hum Mol Genet* (2017).

11. van Wijk, E. *et al.* The DFNB31 gene product whirlin connects to the Usher protein network in the cochlea and retina by direct association with USH2A and VLGR1. *Hum Mol Genet* 15, 751-765 (2006).

12. Reiners, J. *et al.* Scaffold protein harmonin (USH1C) provides molecular links between Usher syndrome type 1 and type 2. *Human molecular genetics* 14, 3933-3943 (2005).

13. Zou, J. *et al.* Whirlin replacement restores the formation of the USH2 protein complex in whirlin knockout photoreceptors. *Invest Ophthalmol Vis Sci* 52, 2343-2351 (2011).

14. Chen, Q., Zou, J., Shen, Z., Zhang, W. & Yang, J. Whirlin and PDZ domain-containing 7 (PDZD7) proteins are both required to form the quaternary protein complex associated with Usher syndrome type 2. *J Biol Chem* 289, 36070-36088 (2014).

15. Yang, J. *et al.* Ablation of whirlin long isoform disrupts the USH2 protein complex and causes vision and hearing loss. *PLoS genetics* 6, e1000955 (2010).

16. Sorusch, N. *et al.* Characterization of the ternary Usher syndrome SANS/ush2a/ whirlin protein complex. *Human molecular genetics* 26, 1157-1172 (2017).

17. Adato, A. *et al.* Usherin, the defective protein in Usher syndrome type IIA, is likely to be a component of interstereocilia ankle links in the inner ear sensory cells. *Hum Mol Genet* 14, 3921-3932 (2005).

18. Liu, X. *et al.* Usherin is required for maintenance of retinal photoreceptors and normal development of cochlear hair cells. *Proceedings of the National Academy of Sciences of the United States of America* 104, 4413-4418 (2007).

19. Overlack, N. *et al.* Direct interaction of the Usher syndrome 1G protein SANS and myomegalin in the retina. *Biochim Biophys Acta* 1813, 1883-1892 (2011).

20. Wasfy, M. M., Matsui, J. I., Miller, J., Dowling, J. E. & Perkins, B. D. myosin 7aa(-/-) mutant zebrafish show mild photoreceptor degeneration and reduced electroretinographic responses. *Exp Eye Res* 122, 65-76 (2014).

21. Phillips, J. B. *et al.* Harmonin (Ush1c) is required in zebrafish Muller glial cells for photoreceptor synaptic development and function. *Disease models & mechanisms* 4, 786-800 (2011).

22. Seiler, C. *et al.* Duplicated genes with split functions: independent roles of protocadherin15 orthologues in zebrafish hearing and vision. *Development* 132, 615-623 (2005).

23. Slijkerman, R. W. *et al.* Antisense Oligonucleotide-based Splice Correction for USH2A-associated Retinal Degeneration Caused by a Frequent Deep-intronic Mutation. *Molecular therapy. Nucleic acids* 5, e381 (2016).

24. Liquori, A. *et al.* Whole USH2A Gene Sequencing Identifies Several New Deep Intronic Mutations. *Hum Mutat* 37, 184-193 (2016).

25. Fuster-Garcia, C. *et al.* USH2A Gene Editing Using the CRISPR System. *Molecular therapy. Nucleic acids* 8, 529-541 (2017).

26. Neuhaus, C. *et al.* Next-generation sequencing reveals the mutational landscape of clinically diagnosed Usher syndrome: copy number variations, phenocopies, a predominant target for translational read-through, and PEX26 mutated in Heimler syndrome. *Mol Genet Genomic Med* 5, 531-552 (2017).

27. Baux, D. *et al.* Enrichment of LOVD-USHbases with 152 USH2A genotypes defines an extensive mutational spectrum and highlights missense hotspots. *Hum Mutat* 35, 1179-1186 (2014).

28. Zallocchi, M. *et al.* EIAV-based retinal gene therapy in the shaker1 mouse model for usher syndrome type 1B: development of UshStat. *PLoS One* 9, e94272 (2014).

29. Hashimoto, T. *et al.* Lentiviral gene replacement therapy of retinas in a mouse model for Usher syndrome type 1B. *Gene Ther* 14, 584-594 (2007).

30. Lopes, V. S. *et al.* Retinal gene therapy with a large MYO7A cDNA using adeno-associated virus. *Gene Ther* 20, 824-833 (2013).

31. Petit, L., Khanna, H. & Punzo, C. Advances in Gene Therapy for Diseases of the Eye. *Human gene therapy* 27, 563-579 (2016).

32. Bainbridge, J. W. *et al.* Effect of gene therapy on visual function in Leber's congenital amaurosis. *N Engl J Med* 358, 2231-2239 (2008).

33. Beltran, W. A. *et al.* Gene therapy rescues photoreceptor blindness in dogs and paves the way for treating human X-linked retinitis pigmentosa. *Proc Natl Acad Sci U S A* 109, 2132-2137 (2012).

34. Cideciyan, A. V. *et al.* Human RPE65 gene therapy for Leber congenital amaurosis: persistence of early visual improvements and safety at 1 year. *Human gene therapy* 20, 999-1004 (2009).

35. MacLaren, R. E. *et al.* Retinal gene therapy in patients with choroideremia: initial findings from a phase 1/2 clinical trial. *Lancet* 383, 1129-1137 (2014).

36. Wu, Z., Yang, H. & Colosi, P. Effect of genome size on AAV vector packaging. *Molecular therapy : the journal of the American Society of Gene Therapy* 18, 80-86 (2010).

37. Mathur, P. & Yang, J. Usher syndrome: hearing loss, retinal degeneration and associated abnormalities. *Biochim Biophys Acta* 1852, 406-420 (2015).

38. Dyka, F. M., Boye, S. L., Chiodo, V. A., Hauswirth, W. W. & Boye, S. E. Dual adeno-associated virus vectors result in efficient in vitro and in vivo expression of an oversized gene, MYO7A. *Hum Gene Ther Methods* 25, 166-177 (2014).

39. Colella, P. *et al.* Efficient gene delivery to the cone-enriched pig retina by dual AAV vectors. *Gene Ther* 21, 450-456 (2014).

4

40. Trapani, I. *et al.* Effective delivery of large genes to the retina by dual AAV vectors. *EMBO Molecular Medicine* 6, 194-211 (2014).

41. Trapani, I. *et al.* Improved dual AAV vectors with reduced expression of truncated proteins are safe and effective in the retina of a mouse model of Stargardt disease. *Hum Mol Genet* 24, 6811-6825 (2015).

42. Carvalho, L. S. *et al.* Evaluating Efficiencies of Dual AAV Approaches for Retinal Targeting. *Frontiers in neuroscience* 11, 503 (2017).

43. Warner, L. E. & Chamberlain, J. S. in *eLS* (John Wiley & Sons, Ltd, 2001).

44. Zhang, W., Li, L., Su, Q., Gao, G. & Khanna, H. Gene Therapy Using a miniCEP290 Fragment Delays Photoreceptor Degeneration in a Mouse Model of Leber Congenital Amaurosis. *Human gene therapy* (2017).

45. Kodippili, K. *et al.* Dual AAV gene therapy for Duchenne muscular dystrophy with a 7-kb mini-dystrophin gene in the canine model. *Human gene therapy* (2017).

46. Harper, S. Q. *et al.* Modular flexibility of dystrophin: implications for gene therapy of Duchenne muscular dystrophy. *Nat Med* 8, 253-261 (2002).

47. Kimmel, C. B., Ballard, W. W., Kimmel, S. R., Ullmann, B. & Schilling, T. F. Stages of embryonic development of the zebrafish. *Developmental dynamics : an official publication of the American Association of Anatomists* 203, 253-310 (1995).

48. Kennedy, B. N., Vihtelic, T. S., Checkley, L., Vaughan, K. T. & Hyde, D. R. Isolation of a zebrafish rod opsin promoter to generate a transgenic zebrafish line expressing enhanced green fluorescent protein in rod photoreceptors. *J Biol Chem* 276, 14037-14043 (2001).

49. Kwan, K. M. *et al.* The Tol2kit: a multisite gateway-based construction kit for Tol2 transposon transgenesis constructs. *Dev Dyn* 236, 3088-3099 (2007).

50. Zallocchi, M., Sisson, J. H. & Cosgrove, D. Biochemical characterization of native Usher protein complexes from a vesicular subfraction of tracheal epithelial cells. *Biochemistry* 49, 1236-1247 (2010).

51. Suster, M. L., Kikuta, H., Urasaki, A., Asakawa, K. & Kawakami, K. Transgenesis in zebrafish with the tol2 transposon system. *Methods in molecular biology* 561, 41-63 (2009).

52. Domanico, D., Fragiotta, S., Cutini, A., Grenga, P. L. & Vingolo, E. M. Psychosis, Mood and Behavioral Disorders in Usher Syndrome: Review of the Literature. *Medical hypothesis, discovery & innovation ophthalmology journal* 4, 50-55 (2015).

53. Sirisi, S. *et al.* Megalencephalic leukoencephalopathy with subcortical cysts protein 1 regulates glial surface localization of GLIALCAM from fish to humans. *Human molecular genetics* 23, 5069-5086 (2014).

54. Rinner, O., Makhankov, Y. V., Biehlmaier, O. & Neuhauss, S. C. Knockdown of cone-specific kinase GRK7 in larval zebrafish leads to impaired cone response recovery and delayed dark adaptation. *Neuron* 47, 231-242 (2005).

55. Ashkenazy, H., Erez, E., Martz, E., Pupko, T. & Ben-Tal, N. ConSurf 2010: calculating evolutionary conservation in sequence and structure of proteins and nucleic acids. *Nucleic acids research* 38, W529-533 (2010).

56. Larkin, M. A. *et al.* Clustal W and Clustal X version 2.0. *Bioinformatics* 23, 2947-2948 (2007).

57. Travan, L. *et al.* Phenotypic expression of 19q13.32 microdeletions: Report of a new patient and review of the literature. *Am J Med Genet A* (2017).

58. Mosimann, C. *et al.* Site-directed zebrafish transgenesis into single landing sites with the phiC31 integrase system. *Dev Dyn* 242, 949-963 (2013).

59. Roberts, J. A. *et al.* Targeted transgene integration overcomes variability of position effects in zebrafish. *Development* 141, 715-724 (2014).

60. Bennett, J. Taking Stock of Retinal Gene Therapy: Looking Back and Moving Forward. *Molecular therapy : the journal of the American Society of Gene Therapy* 25, 1076-1094 (2017).

61. Dalkara, D. *et al.* In vivo-directed evolution of a new adeno-associated virus for therapeutic outer retinal gene delivery from the vitreous. *Science translational medicine* 5, 189ra176 (2013).

62. Maddalena, A. *et al.* Triple Vectors Expand AAV Transfer Capacity in the Retina. *Molecular therapy : the journal of the American Society of Gene Therapy* (2017).

63. Auricchio, A. *et al.* Exchange of surface proteins impacts on viral vector cellular specificity and transduction characteristics: the retina as a model. *Hum Mol Genet* 10, 3075-3081 (2001).

64. Sengillo, J. D. *et al.* Electroretinography Reveals Difference in Cone Function between Syndromic and Nonsyndromic USH2A Patients. *Scientific reports* 7, 11170 (2017).

65. Tucker, B. A. *et al.* Patient-specific iPSC-derived photoreceptor precursor cells as a means to investigate retinitis pigmentosa. *eLife* 2, e00824 (2013).

4

SUPPLEMENTAL DATA

Minigene	Subfragment primer name	Sequence
miniUSH2A-2	pUC19L-ss_fwd	5'-AATTCGAGCTCGGTACATGAATTGCCCAGTTCT-3'
miniUSH2A-2	Ss-8xFN3_rev	5'-CGGCTCGGCTTGAAAGCTCCCACG-3'
miniUSH2A-2	Ss-8xFN3 fwd	5'-CTTTCAAGCCGAGCCGAGAAGTG-3'
miniUSH2A-2	8xFN3-TM-end rev	5'-TCGGAAGCCCACAGACTCTCCAC-3'
miniUSH2A-2	8xFN3-TM-end fwd	5'-GTCTGTGGGCTTCCGAGTGGATC-3'
miniUSH2A-2	TM-end-pUC19L rev	5'-GCCAAGCTTGCATGCCTTACAGGTGGGTGTCT-3'
miniUSH2A-2	Gateway cloning fwd	5'-GGGGACAAGTTTGTACAAAAAAGCAGGCTTCGCCGCCGCCAT-GAATTGCCCAGTTCTTTC-3'
miniUSH2A-2	Gateway cloning rev	5'-GGGGACCACTTTGTACAAGAAAGCTGGGTCTTACAGGTGGGT-GTCTGT-3'
miniUSH2A-1	pUC19L-ss_fwd	5'-AATTCGAGCTCGGTACATGAATTGCCCAGTTCT-3'
miniUSH2A-1	Ss_4xEGF-lamG rev	5'-GGATTGTAACATCCAACATCATTAAAGC-3'
miniUSH2A-1	4xEGF-LamG fwd	5'-TTGGATGTTACAATCCGTCAGCTATTT-3'
miniUSH2A-1	LamG-8xFN3 rev	5'-CGGCTCGGACCCCGTGTAAATTTAAC-3'
miniUSH2A-1	8xFN3-TM-end fwd	5'-CACGGGGTCCGAGCCGAGAAGTG-3'
miniUSH2A-1	TM-end-pUC19L rev	5'-GCCAAGCTTGCATGCCTTACAGGTGGGTGTCT-3'
miniUSH2A-1	Gateway cloning fwd	5'-GGGGACAAGTTTGTACAAAAAAGCAGGCTTCGCCGCCGCCAT-GAATTGCCCAGTTCTTTC-3'
miniUSH2A-1	Gateway cloning rev	5'-GGGGACCACTTTGTACAAGAAAGCTGGGTCTTACAGGTGGGT-GTCTGT-3'

Supplemental Table 1. Primer sequences for the construction of *miniUSH2A-1* and *-2*

A   Human *USH2A*
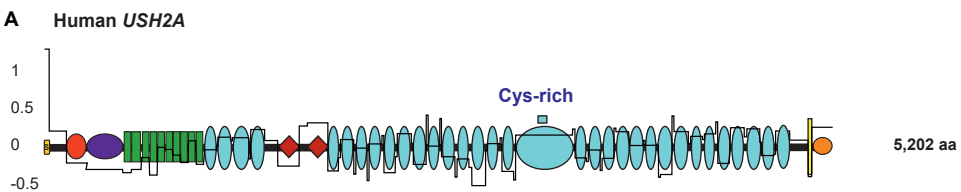
Supplemental Figure 1. Relative levels of sequence diversity among the domains and between domain regions in the USH2A protein.

Sequence diversity was calculated with consurf (consurf.tau.ac.il/2016) based on a full length alignment from 31 sequences from the deuterostomia taxon, 21 of which are from the vertebrates. Sequence variation was calculated per residue and then averaged per domain, or per inter-domain region, and shown for domains and interdomain regions that are at least 10 amino acids long. The Y-axis gives standard deviations in the per residue sequence variation. A low (negative) score indicates a relatively well conserved part of the sequence. Among each set of domains we did not detect any particularly well (or not well) conserved domain that should be included in the construct (or left out).

A
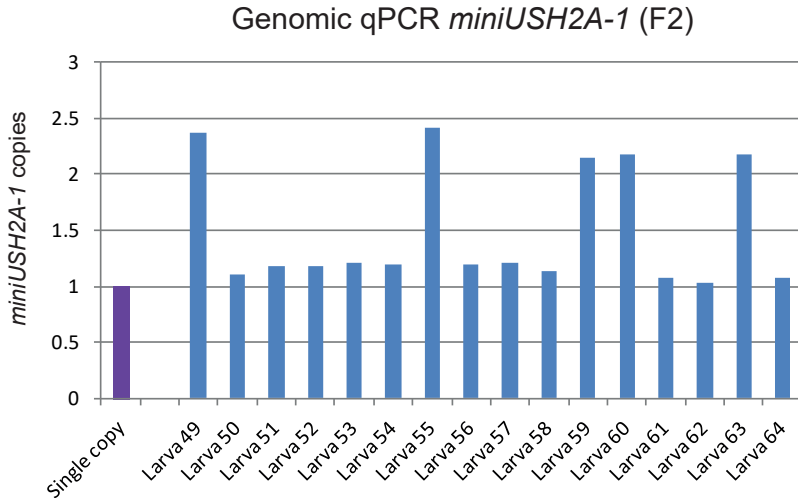
B
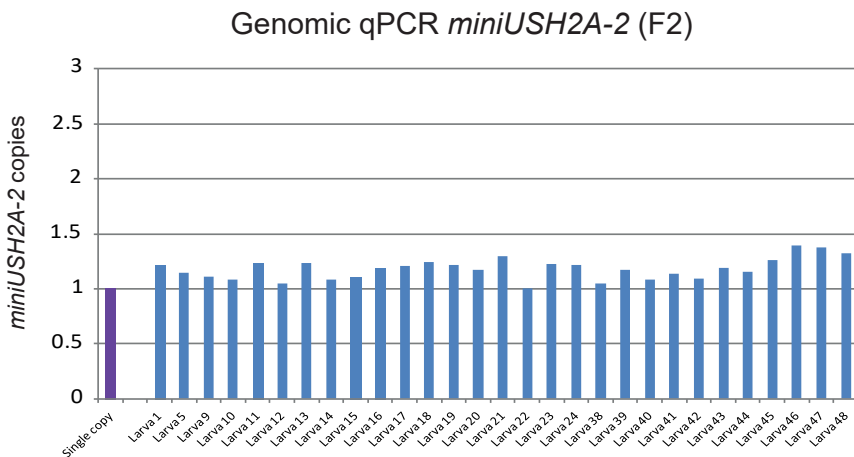
Supplemental Figure 2. Genomic qPCR for F2 larvae.

The relative amount of integrated *miniUSH2A* copies was determined by genomic qPCR analyses for larvae of the F2 generation. Transgenic *miniUSH2A-1* larvae contained either 1 or 2 copies of the minigene (**A**). (**B**) Transgenic *miniUSH2A-2* larvae all contained a single copy of the *USH2A* minigene.

A

chr15:   23,786,000 | 23,786,500 | 23,787,000 | 23,787,500 |

~70 bp
<-->

zc3h4   *sae1*

B

miniUSH2A-1

B

zc3h4   *duplication*   Tol2 5'-TIR   *miniUSH2A-1*

_ _ _.CTAAGGGTAATGTAATAG TTAAAATA CAGAGGTGTAAAGTACTTG AGTAATTTTA._ _ _
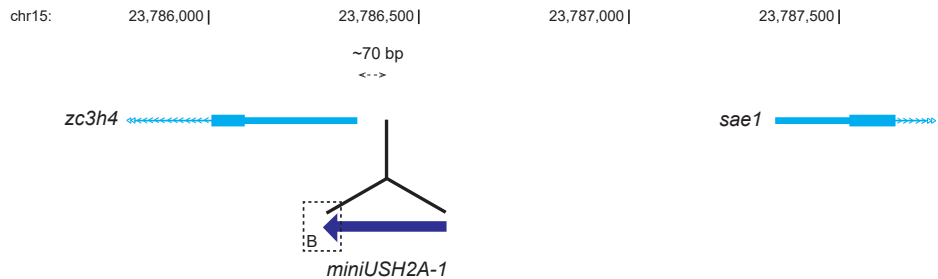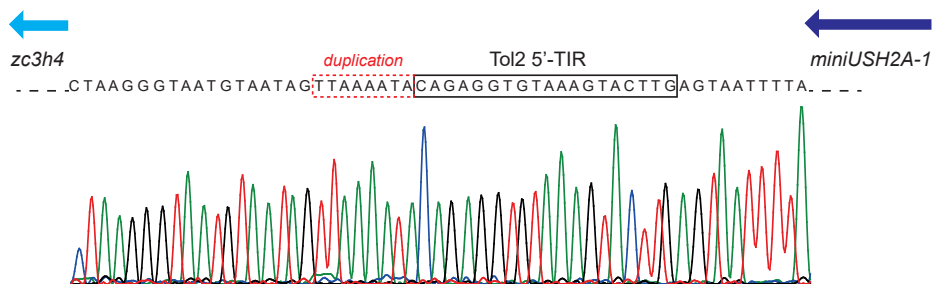
Supplemental Figure 3. Integration site of *miniUSH2A-1* (chromosome 15).

(**A**) One copy of *miniUSH2A-1* was integrated approximately 70 nucleotides upstream of the zinc-finger CCCH-type containing 4 (*zc3h4*) gene at chromosome 15. (**B**) Chromatogram of the boundary between *miniUSH2A-1* and the *zc3h4* locus. The Tol2 5'-TIR site (black solid line) and the 8 nucleotide duplication of the Tol2 target site (red dotted line) are boxed.
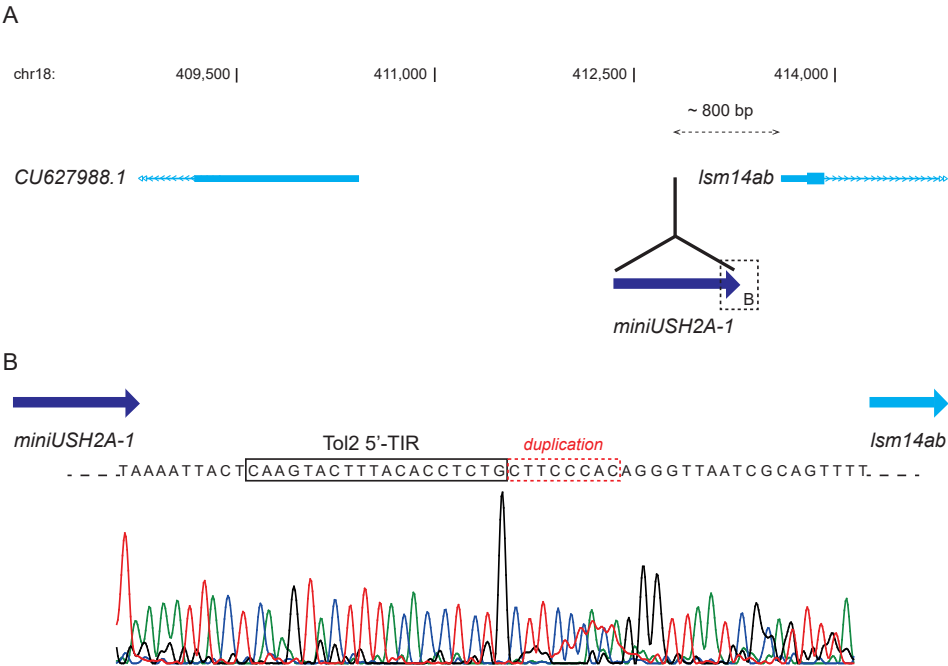
Supplemental Figure 4. Integration site of *miniUSH2A-1* (chromosome 18).

(**A**) One copy of *miniUSH2A-1* was integrated approximately 800 nucleotides upstream of the *lsm14ab* gene at chromosome 18. (**B**) Chromatogram of the boundary between *miniUSH2A-1* and the *lsm14ab* locus. The Tol2 5'-TIR site (black solid line) and the 8 nucleotide duplication of the Tol2 target site (red dotted line) are boxed.

A

B

C
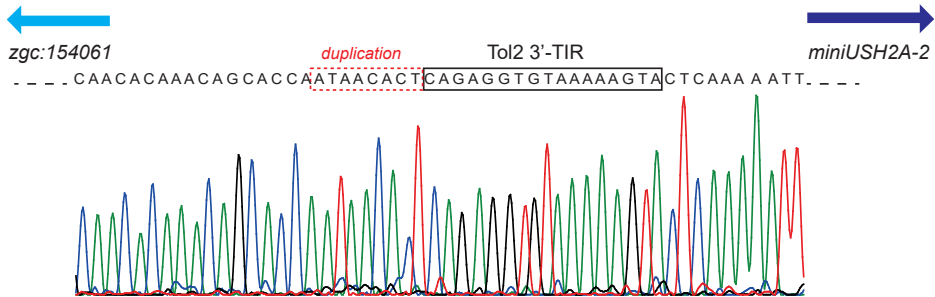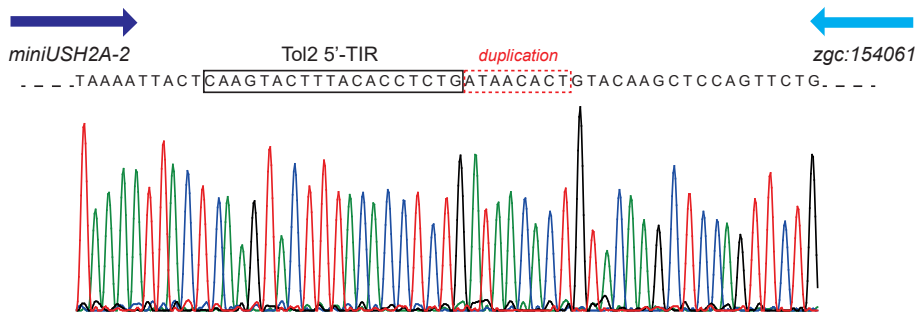
Supplemental Figure 5. Integration site of *miniUSH2A-2* (chromosome 17).

(**A**) *MiniUSH2A-2* was integrated within the 5'-UTR of the *zgc:154061* gene at chromosome 17. (**B,C**) Chromatogram of the boundaries between *miniUSH2A-1* and the *zgc:154061* locus. The Tol2 3' and 5'-TIR sites (black solid line) and the 8 nucleotide duplication of the Tol2 target site (red dotted line) are boxed.

Larval retinas (5 dpf)

RPE
ONL
OPL
INL
IPL
GCL

Wild-type   *miniUSH2A-1*   *miniUSH2A-2*

Adult retinas (5 mpf)

RPE
ONL
OPL
INL
IPL
GCL

Wild-type   *miniUSH2A-1*   *miniUSH2A-2*
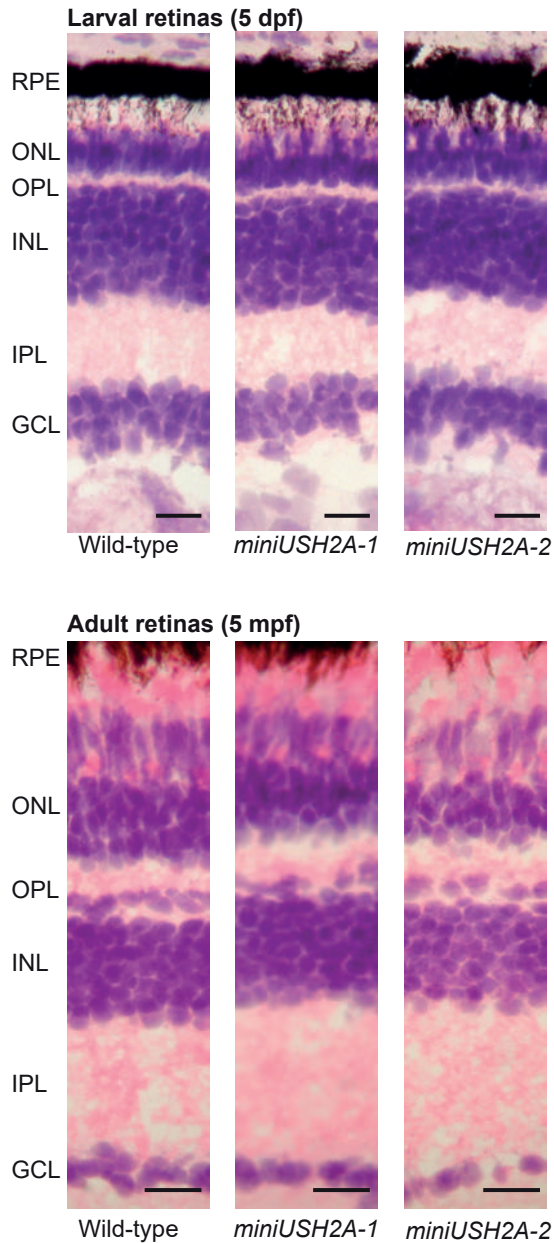
Supplemental Figure 6. Histological examination of *miniUSH2A-1* and *-2* zebrafish retinas.

Light microscopy of retinal sections from larval (5 dpf) and adult (5 mpf) zebrafish stained with hematoxylin and eosin. Retinas of wild-type and both *miniUSH2A* larvae are morphologically indistinguishable from wild-type retinas at both ages. (n=7 larvae and n=2 adult eyes (5mpf) with *miniUSH2A-1*, *miniUSH2A-2* and TLF fish). Dpf: days post fertilization, mpf: months post fertilization, GCL: ganglion cell layer, IPL: inner plexiform layer, OPL: outer plexiform layer, ONL: outer nuclear layer, RPE: retinal pigment epithelium. Scale bars: 10 μm.

Chapter 5

General discussion:
The road towards therapy for
USH2A-associated RP

5

Clinicians and geneticists have collectively spent approximately 140 years of research before the first mutations in the *MYO7A* gene were identified as the underlying cause of USH1b. Hereafter, the hunt for pathogenic mutations that could help to explain the genetic etiology of Usher syndrome started. Although mutations in *USH2A* are the most frequent cause of Usher syndrome and non-syndromic autosomal recessive RP in man [1-3], surprisingly little is known about the function of the *USH2A*-encoded protein usherin in the eye. Based on prevalence numbers it is estimated that worldwide approximately 170,000 Usher syndrome patients and 250,000 patients with non-syndromic, autosomal recessively inherited RP can be explained by mutations in the *USH2A* gene. For the progressive and irreversible loss of visual function caused by mutations in *USH2A*, currently no treatment options are available. Therefore, the main aim of the research described in this thesis was to develop and evaluate therapeutic options for the future treatment of *USH2A*-associated retinal degeneration. On this road towards therapy for *USH2A*-associated RP, several stages can be distinguished: the design phase, the pre-clinical phase and finally the clinical trials (Phase 0 – IV). This chapter reviews our main discoveries and achievements, and addresses future challenges.

1.   THE DESIGN PHASE

1.1. Strategy

Several therapeutic strategies have already been (pre-)clinically explored to restore or overcome the consequences of specific mutations in Usher syndrome-associated genes. Translational read-through inducing drugs (TRIDs) have been shown to be effective in the read-through of nonsense mutations in *USH1G in vitro* [4], and *USH1C in vitro* and *in vivo* [5]. Also splice correction strategies using antisense oligonucleotides (AONs) have been explored. AONs were shown to have great potential in *in vitro* correction of aberrant *USH2A* pre-mRNA splicing as a consequence of deep-intronic mutations [6,7]. Furthermore, treatment of neonatal mice with a single systemic dose of AONs partially corrects *Ush1c* pre-mRNA splicing in an *Ush1c* c.216G>A knock-in model. As a result, stereocilia organization in the cochlea was improved leading to a rescue of cochlear hair cells, vestibular function and low-frequency hearing in mice [8]. In addition, CRISPR/Cas9-based genome editing holds great potential for treating inherited eye diseases, however development of precise reagents that specifically target desired genomic loci, while inducing no or minimal off target modifications is still an important step that needs to be taken before this method can move towards a clinical application [8]. As more than 600 different disease-causing mutations in *USH2A* have been identified, which are evenly distributed over the gene [9], it is not cost-effective and feasible to develop mutation-specific treatments for all of them. Therefore, a mutation-independent approach would be preferred as a common treatment from which a relatively large group of patients could benefit.

A promising mutation-independent strategy is gene augmentation using viral vectors for delivery. The virus delivers a functional copy of the gene associated with the disease to the light-sensitive photoreceptor cells and/or RPE cells after a subretinal injection. *MYO7A* is effectively expressed in the retina of the *shaker1* mouse for USH1b after being packaged into a lentivirus (UshStat®) [10]. Currently UshStat® is being evaluated in phase I/II clinical trials (ClinicalTrials.gov Identifier:NCT01505062). Another strategy could be the use of minigenes (**chapter 4a**), this method has already proven its potential for the large genes *dystrophin* and *CEP290* [11-13].

The presence of photoreceptors is a pre-requisite for the application of genetic therapies to treat *USH2A*-associated retina dysfunction. Therefore slowing down the speed of retinal degeneration will enlarge the window of opportunity for a future therapeutic intervention. A possibility to slow down retinal degeneration is using a pharmacological approach with compounds that for instance inhibit apoptosis. In general, pharmacological strategies have the advantage to target common causes or mechanisms. The disadvantage of using exogenous pharmacological molecules is the

limitation of specifically targeting the retinal cells of interest after a controlled drug delivery [14].

In case the disease is already in a more advantaged stage and no (functional) photoreceptors are present anymore, alternative strategies are required. One of these strategies is stem cell transplantation [15]. Significant progress has been made in experimental stem cell applications, for which the first phase I/II clinical trials have been recently approved. The latest studies on stem cell transplantation showed that this type of therapeutic approach is promising in restoring visual function in patients with an advanced state of degenerative retinal disease [16-18].

Alternatively, patients can be provided with epiretinal prostheses. One of these epiretinal prostheses that has been generated by Second Sight Medical Products, Argus 2, has already been approved for commercial use although it still requires optimization [19]. A different strategy for restoring visual function when photoreceptors have largely degenerated is based on optogenetics. In optogenetics for the retina viable inner retina cells are genetically modified to express light-sensitive ion channels. So far, optogenetics has not been tested yet in humans.

In this thesis, we describe the development of a minigene augmentation therapy to restore visual function in RP patients with mutations in the *USH2A* gene. In order to evaluate this strategy *in vivo*, a suitable animal model is required.

1.2   Model systems

The availability of suitable animal models is crucial to determine the therapeutic effect of a certain treatment on visual function. Alternatively, iPSC-derived 3D retinal organoids generated from patient cells could be used. However, these organoids usually lack RPE cells which are essential for the proper formation, maturation and maintenance of fully functional photoreceptor outer segments. The presence of functional outer segments is essential for light capture and as such vital to determine the effect of a therapeutic intervention [20]. So far, rodents, fruit flies and zebrafish have been used as model organisms to study Usher syndrome-associated retinal degeneration (**Table 2, General introduction**). In **chapter 4**, we demonstrated that the zebrafish is a suitable model to study *USH2A*-associated retinal dysfunction and that it can be used for the *in vivo* evaluation of therapeutic strategies. As for every model system the use of zebrafish has several advantages, challenges and limitations.

One advantage of the zebrafish is that the retinal laminar organization is highly similar to the human situation. Besides rods, zebrafish have four distinct types of cone photoreceptors (ultraviolet (UV), blue, red and green cones) which all have a peak sensitivity to a specific wavelength [21]. The cone photoreceptors develop prior to the rods. By 24 dpf, the zebrafish retina is considered to be adult-like, with only the fine-

tuning of the connections left to develop. It should therefore be noted that at 5 dpf, the developmental stage at which most of our experiments have been conducted, the zebrafish retina is still immature.

Zebrafish *ush2a* mutant models do not mimic the progressive retinal degeneration as seen in man. Contrary to mammals, the zebrafish has the capacity to fully regenerate entire parts of the nervous system, including the retina. Following injury, zebrafish Müller glia cells dedifferentiate into proliferating precursor cells and subsequently differentiate into new (neuronal) cells, while mammalian Müller glia cells undergo reactive gliosis [22]. A potential explanation for the lack of a progressive *ush2a*-associated retinal phenotype in fish could therefore be that the rates of photoreceptor degeneration and subsequent regeneration are perfectly balanced. Crossing *ush2a* mutants with (temperature-sensitive) zebrafish models defective for their regenerative capabilities, like *nightcap* (*ncp*) or *no blastema* (*nbl*), could unveil the contribution of regeneration to the lack of a progressive retinal phenotype [23,24]. From a different perspective, finding the switch to activate this remarkable regeneration pathway in man could potentially hold great promise for the future treatment of *USH2A*-associated retinal degeneration [23,25].

Finally, the translational value of a zebrafish model for a human condition can be argued, although this should be considered for all types of cellular and animal models that are used. Zebrafish are evolutionarily quite distinct from man, but they still share a high degree of DNA sequence and functional homology. Although one should take into account that, due to an ancient genome duplication event in teleost fish, approximately 30% of genes are duplicated in the zebrafish genome [26]. Alternatively, pre-clinical proof of concept for a therapeutic approach could be obtained using animal models that are, both genetically and physiologically, more closely related to human than zebrafish (*e.g.* dogs, cats or pigs) [25].

2. PRE-CLINICAL PHASE

In the pre-clinical phase, the generation and characterization of the model system derived from the design phase needs to be accomplished. Subsequently, the potential of the strategy selected in the design phase can be tested in the generated animal model *in vivo*. To determine whether a therapeutic strategy is effective in restoration of visual function, consistent and sensitive read-outs are required. Therapeutic efficacy can be determined by measuring VMRs and ERG traces and by looking at bio-markers. In order to identify suitable bio-markers it is essential to understand the underlying molecular mechanisms of the retinal degeneration. The powerful combination of proteomics and knock-out animal models can attribute to unravel the retinal degeneration pathomechanisms of an *USH2A* mutation.

2.1 Proteomics

Usher syndrome-associated proteins co-function in highly dynamic protein networks at different subcellular locations and during different time points in development, as has been explained in the introduction of this thesis (**chapter 1**). In order to elucidate the cellular function of usherin and to unravel the pathogenic mechanism underlying *USH2A*-associated RP, we further investigated usherin's "social network" of proteins (**chapter 2a and 2b**).

Already in 2009, NINL was identified as a key usherin-interaction partner that connects the retinal ciliopathies Usher Syndrome and Leber congenital amaurosis at the molecular level [27]. Using a combination of proteomics and zebrafish modelling, we identified that NINL plays an important role in two consecutive steps of intracellular vesicle transport. First of all, a module consisting of NINL and DZANK1 (**chapter 2a**) was identified that plays a crucial role in the proper assembly and folding of the intracellular cytoplasmic dynein 1 motor complex in photoreceptor cells. Cytoplasmic dynein 1 has been shown to be essential for photoreceptor outer segment formation and function. Next, a complex consisting of CC2D2A-NINL-MICAL3-RAB8A (**chapter 2b**) was identified that is involved in the fusion and docking of RAB8A-coated cargo vesicles at the photoreceptor ciliary base. Although very interesting and important, the data described in these two chapters did not result in the identification of the exact function of usherin in the retina. The Cop9 signalosome associates with different members of the Usher protein network [28]. One of the eight Cop9 subunits, COPS8, directly interacts with the intracellular region of usherin. The Cop9 signalosome has different predicted roles in actin attachment/polymerization [29], DNA damage response and proteasomal degradation [30]. Future functional analyses in patient-derived cellular models or animal models will reveal to which extent an impaired Cop9 signalosome function contributes to the Usher syndrome pathogenesis.

2.2 Animal models

In **chapter 2**, the temporary downregulation of zebrafish *ninl*, *cc2d2a* and *dzank1* expression was induced by using translation or splice-blocking morpholinos (MOs) [31]. Reported toxicity, off-target effects and non-reproducibility of results in corresponding mutants have led to a strong debate around the use of MOs. Recently, novel guidelines for the proper use of MOs in a tightly controlled setting have been released [32]. However, to study the long-term effect of genetic modifications it is recommended to generate mutants by CRISPR/Cas9-based genome editing.

The availability of *ush2a* mutant zebrafish models that present with early-onset retinal dysfunction (**chapter 3a**) also provides opportunities to unravel the underlying molecular mechanisms of *USH2A*-associated retinal degeneration in more detail. In

order to sort out the cause of photoreceptor dysfunction and apoptosis, a more in depth phenotyping of the mutant is recommended. For instance, Transmission Electron Microscopy (TEM) analyses as used in **chapter 2** will provide a more detailed insight into potential morphological problems such as vesicle accumulation. Additional immunohistochemical analyses for specific photoreceptor marker proteins, such as opsins, at different time points could potentially reveal the underlying cause of the retinal dysfunction as observed in the *ush2a* knock-out larvae. Alternatively, similar to what has been observed for several other types of inherited retinal dystrophies [33], mutations in *USH2A* could affect photoreceptor proteostasis resulting in a gradual degeneration of photoreceptor cells. Autophagy is a protective mechanism used to recycle misfolded, mislocalized and/or aggregated proteins from the cytoplasm and the endoplasmic reticulum (ER) [22]. However, a prolonged increased level of autophagy could eventually induce programmed cell death. As the Usher protein network associates with the Cop9 signalosome, a complex involved in autophagosome maturation [34], investigating proteostasis in the zebrafish *ush2a* models (**chapter 3a**) could provide insight into the underlying mechanisms of photoreceptor death.

In **chapter 4** we showed the suitability of the zebrafish to model *USH2A*-associated retinal dysfunction and indicated the potential of using *USH2A* minigenes as a future treatment option for *USH2A*-associated RP. Furthermore, we demonstrated that the presence or absence of the usherin interaction partner whirlin at the photoreceptor periciliary membrane could serve as a biomarker for therapeutic efficacy in zebrafish.

3.   TOWARDS CLINICAL TRIALS

Prior to entering phase I clinical trials, three major aspects still need to be addressed: the method of delivery, toxicological screening of the therapeutic compound and patient selection criteria.

3.1   Delivery methods

Gene therapy requires a vehicle to deliver the gene of interest to the target cells. Methods for gene therapy can be broadly divided into viral and non-viral [24]. Thus far, viral vectors have been the most popular vehicles for gene delivery to the retina. AAV-mediated delivery of a gene into the subretinal space has proven to be safe and effective in treating photoreceptor degenerative diseases[35-40]. However, AAVs have a limited cargo packaging capacity of ~4.8 kb [41], which hampered the progress in the development of gene augmentation therapies for large genes such as *USH2A*. Alternatively, lentiviral (LV) vectors, which have a relatively high packaging capacity of ~8.5 kb, could be used. However, the integrative nature of LV vectors could potentially

result in insertional mutagenesis. Nanoparticles could be used as alternative non-viral vehicles for gene delivery. They have already been successfully applied in clinical trials for cystic fibrosis, and currently the use of nanoparticles as a vehicle for ocular drug delivery is under investigation [42,43]. In contrast to the limited packaging capacity of AAVs, a major advantage of the use of CK30-nanoparticles is the theoretically unlimited plasmid size that can be loaded. Sequences with a size up to 20 kb have already been successfully loaded onto nanoparticles [42,43], which is well within the range of the full length coding sequence of human *USH2A* (~15.6 kb). Nanoparticles are perfectly suited for drug delivery due to their small size and the diversity of materials that can be used to generate these particles for targeted aims. They are able to penetrate biological barriers, can deliver drugs directly at the target site and provide a sustained release profile. A successful delivery of genes to different retinal cell types such as RPE, photoreceptor cells and ganglion cells using CK30-nanoparticles after subretinal injections has already been shown. However, prior to the clinical application of nanoparticles for eye disorders, the main obstacles such as a poor delivery via eye drops, the relatively low gene expression levels during a short period of time and the side effects of the delivery method, should first be overcome [44]. Future research in cellular or animal models will determine which method will be most suitable for the delivery of *USH2A* minigenes to the human photoreceptor cells.

3.2 Toxicological screening

Toxicological testing of new genetic treatments is essential in the drug development process. The levels of toxicity can be determined by studying the accidental exposures to a substance, by *in vitro* studies using cell lines or by *in vivo* exposure of animal models. The preclinical toxicity testing helps to calculate the "No Observed Adverse Effect Level" which is needed to determine the maximal dose prior to initiating the clinical evaluation of genetic treatments that are under development [45].

3.3 Patient selection criteria

Only patients with syndromic or non-syndromic RP caused by mutations in *USH2A* are potentially eligible to be included in future clinical trials. An early genetic diagnosis of Usher syndrome is essential since therapeutic strategies will only be effective when photoreceptors are still present. Based on studies in iPSC-derived retinal progenitor cells of an Usher syndrome type 2a (USH2a) patient, it has been postulated that the mechanism of disease of protein-truncating mutations could differ from the mechanism of disease of missense mutations [46]. Elucidation of the pathogenic mechanisms caused by different types of *USH2A* mutations will reveal whether or not *USH2A* minigene augmentation will be beneficial for all patients with *USH2A*-associated RP or that it will

only be suitable for patients with protein-truncating mutations. Other selection criteria that will determine whether or not someone is eligible to be included in the initial clinical trials are the level of visual acuity (BCVA of ≤20/40), age (only adults should be included in the first trials due to ethical concerns and difficulties in performing intravitreal injections in children), absence of amblyopia and presence of photoreceptor (outer nuclear) and RPE layers on a standard OCT scan. Patients that underwent ocular surgeries or a thermal laser treatment within 6 months prior to the initiation of the clinical trial are typically excluded.

4. CLINICAL TRIALS: EXPECTATIONS AND PROSPECTS

4.1 The first clinical trial for *USH2A*-associated retinal degeneration: timeline

Taken together, the results described in **chapter 4** are very promising, but the actual implementation of this therapeutic approach as a treatment for *USH2A*-associated retinal degeneration is still far away. Only estimates can be made on expected timelines when our developments will reach the clinical phase, based on studies that have adopted the minigene approach as a therapeutic option to treat *CEP290*-associated retinal dystrophy or Duchenne Muscular Dystrophy (DMD) [11-13,47]. In 1987, mutations in *dystrophin* were identified as the underlying cause of DMD [34]. Already in 1994, Rafael and co-workers discovered that addition of a shortened version of dystrophin could prevent the observed dystrophic phenotype in *mdx* mice [30]. Thereafter, a variety of studies in mouse and dog were performed before the first phase I clinical trial was initiated in 2006, in which six participants were supplemented with rAAV2.5-CMV-minidystrophin (d3990). In 2015, another phase I clinical trial was launched in which two participants were treated with an even shorter version of the *dystrophin* gene (rAAVrh74.MCK.micro-Dystrophin). For the latter, a phase I/IIa trial was initiated in 2017 which is currently still ongoing. In total, the journey from gene discovery until clinical phase IIa already took over 30 years. Although this timeline can be highly variable between different studies, we expect that it will take at least multiple years before our minigene approach, if at all, reaches the clinical trial phase. In the coming years crucial information on timing, dosing and delivery methods needs to be gathered for the *USH2A* minigene approach. In the meanwhile, a lot can be learned from the first phase I/IIa clinical trial for *USH2A*-associated RP using an exon-skipping approach, which is expected to advance towards the clinic at the end of 2018.

5

4.2 Potential of genetic therapies to restore Usher syndrome-associated hearing loss

Although patients with Usher syndrome benefit from hearing aids and cochlear implants, yet no curative treatment is available. Usher syndrome-associated proteins have been shown to play an essential role in development of the inner ear hair bundle and cohesion in knock-out mice (**Table 2**, **general introduction**) [48,45,46,50,60-62]. Several gene replacement or splice correction strategies have been proven successful in restoring auditory and/or vestibular function in mouse models for USH1c [49-51], USH2d [52,53] USH1g [54] and USH3 [55,56], when applied prior to the completion of murine inner ear maturation at postnatal day 20. As the development of the human auditory and vestibular system is already completed during gestation, it is expected that intervention studies in man will only be beneficial when applied *in utero*.

Ush2a knock-out mice develop moderately-severe, non-progressive hearing loss, closely resembling the hearing loss observed in USH2a patients [57]. In the inner ear, usherin is part of the ankle links, a subset of lateral links that connect two adjacent stereocilia near their basal ends [57,58]. It is speculated that the enormous size of usherin (5,202 amino acids) is essential for the proper spacing between two adjacent stereocilia. Therefore it is questionable whether *USH2A* minigene augmentation, even when applied at the most optimal time-point during development, will be effective in preventing hearing impairment in USH2a patients. However, in some patients with USH2a, severe progression of hearing impairment is observed [59]. For this group of patients the introduction of an USH2A minigene into the inner ear could potentially halt the progression of the disease.

5. CONCLUDING REMARKS

The diagnosis Usher syndrome changes the lives of patients dramatically as they are all of a sudden confronted with an uncertain future. Depending on the age of the patients and the severity of the hearing and vision loss, assistive listening devices, an epiretinal prosthesis, braille instructions, low-vision services, a guide dog, auditory training or other communication methods such as sign language can be provided to the patients. Proper assistance is important to enable Usher syndrome patients to carry out daily activities, to communicate with the outer world and to maintain their independence.

In the Netherlands, five different patient-organizations are committed to support the deafblind community: Oogvereniging pg Doofblinden, Stichting Ushersyndroom, Stichting Klavertje 2, Contactgroep Ushersyndroom and Stichting Wetenschappelijk Onderzoek DoofBlindheid. The main goal of these groups is to provide support by stimulating contact between patients and providing information. In addition, they play an important role in creating societal awareness for this rare condition. Another goal of

these organizations is to raise funds in order to financially support scientific research with the ultimate aim of improving the quality of life of patients.

In line with the goal of the patient organizations, the results described in this thesis hold great promise to potentially save residual vision in patients with loss-of-function mutations in the *USH2A* gene. As a next step, we provide new directions for exiting future experiments which should focus on the delivery and safety aspects of the described therapies in the retina. Altogether, the data provided in this thesis point towards the value of the zebrafish as a model to "fish for answers" and provide new handles for breaking down the remaining barriers prior to the implementation of a treatment option for *USH2A*-associated RP.

5

REFERENCES

1. Millan, J. M. *et al.* An update on the genetics of usher syndrome. *Journal of ophthalmology* 2011, 417217 (2011).

2. Yan, D. & Liu, X. Z. Genetics and pathological mechanisms of Usher syndrome. *Journal of human genetics* 55, 327-335 (2010).

3. McGee, T. L., Seyedahmadi, B. J., Sweeney, M. O., Dryja, T. P. & Berson, E. L. Novel mutations in the long isoform of the USH2A gene in patients with Usher syndrome type II or non-syndromic retinitis pigmentosa. *J Med Genet* 47, 499-506 (2010).

4. Neuhaus, C. *et al.* Next-generation sequencing reveals the mutational landscape of clinically diagnosed Usher syndrome: copy number variations, phenocopies, a predominant target for translational read-through, and PEX26 mutated in Heimler syndrome. *Mol Genet Genomic Med* 5, 531-552 (2017).

5. Nagel-Wolfrum, K., Moller, F., Penner, I. & Wolfrum, U. Translational read-through as an alternative approach for ocular gene therapy of retinal dystrophies caused by in-frame nonsense mutations. *Visual neuroscience* 31, 309-316 (2014).

6. Liquori, A. *et al.* Whole USH2A Gene Sequencing Identifies Several New Deep Intronic Mutations. *Hum Mutat* 37, 184-193 (2016).

7. Slijkerman, R. W. *et al.* Antisense Oligonucleotide-based Splice Correction for USH2A-associated Retinal Degeneration Caused by a Frequent Deep-intronic Mutation. *Molecular therapy. Nucleic acids* 5, e381 (2016).

8. Lentz, J. J. *et al.* Rescue of hearing and vestibular function by antisense oligonucleotides in a mouse model of human deafness. *Nat Med* 19, 345-350 (2013).

9. Baux, D. *et al.* Enrichment of LOVD-USHbases with 152 USH2A genotypes defines an extensive mutational spectrum and highlights missense hotspots. *Hum Mutat* 35, 1179-1186 (2014).

10. Lopes, V. S. & Williams, D. S. Gene Therapy for the Retinal Degeneration of Usher Syndrome Caused by Mutations in MYO7A. *Cold Spring Harbor perspectives in medicine* 5 (2015).

11. Warner, L. E. & Chamberlain, J. S. in *eLS* (John Wiley & Sons, Ltd, 2001).

12. Zhang, W., Li, L., Su, Q., Gao, G. & Khanna, H. Gene Therapy Using a miniCEP290 Fragment Delays Photoreceptor Degeneration in a Mouse Model of Leber Congenital Amaurosis. *Human gene therapy* (2017).

13. Kodippili, K. *et al.* Dual AAV gene therapy for Duchenne muscular dystrophy with a 7-kb mini-dystrophin gene in the canine model. *Human gene therapy* (2017).

14. Guadagni, V., Novelli, E., Piano, I., Gargini, C. & Strettoi, E. Pharmacological approaches to retinitis pigmentosa: A laboratory perspective. *Progress in retinal and eye research* 48, 62-81 (2015).

15. MacLaren, R. E., Bennett, J. & Schwartz, S. D. Gene Therapy and Stem Cell Transplantation in Retinal Disease: The New Frontier. *Ophthalmology* 123, S98-S106 (2016).

16. Hermankova, B. & Holan, V. [Perspectives of the Cell Therapy in Ophthalmology.2. The Potential of Stem Cells for the Retinal Diseases Treatment]. *Ceska a slovenska oftalmologie : casopis Ceske oftalmologicke spolecnosti a Slovenske oftalmologicke spolecnosti* 72, 272-275 (2016).

17. Kaewkhaw, R. *et al.* Treatment Paradigms for Retinal and Macular Diseases Using 3-D Retina Cultures Derived From Human Reporter Pluripotent Stem Cell Lines. *Invest Ophthalmol Vis Sci* 57, ORSFl1-ORSFl11 (2016).

18. Oner, A. Stem Cell Treatment in Retinal Diseases: Recent Developments. *Turk J Ophthalmol* 48, 33-38 (2018).

19. Larkin, M. A. *et al.* Clustal W and Clustal X version 2.0. *Bioinformatics* 23, 2947-2948 (2007).

20. Bennett, J. Taking Stock of Retinal Gene Therapy: Looking Back and Moving Forward. *Molecular therapy : the journal of the American Society of Gene Therapy* 25, 1076-1094 (2017).

21. Saszik, S., Bilotta, J. & Givin, C. M. ERG assessment of zebrafish retinal development. *Visual neuroscience* 16, 881-888 (1999).

22. Campbell, L. J. & Hyde, D. R. Opportunities for CRISPR/Cas9 Gene Editing in Retinal Regeneration Research. *Frontiers in cell and developmental biology* 5, 99 (2017).

23. Madelaine, R. & Mourrain, P. Endogenous retinal neural stem cell reprogramming for neuronal regeneration. *Neural Regen Res* 12, 1765-1767 (2017).

24. Qin, Z., Barthel, L. K. & Raymond, P. A. Genetic evidence for shared mechanisms of epimorphic regeneration in zebrafish. *Proc Natl Acad Sci U S A* 106, 9310-9315 (2009).

25. Slijkerman, R. W. *et al.* The pros and cons of vertebrate animal models for functional and therapeutic research on inherited retinal dystrophies. *Progress in retinal and eye research* 48, 137-159 (2015).

26. Meyer, A. & Schartl, M. Gene and genome duplications in vertebrates: the one-to-four (-to-eight in fish) rule and the evolution of novel gene functions. *Curr Opin Cell Biol* 11, 699-704 (1999).

27. van Wijk, E. *et al.* Usher syndrome and Leber congenital amaurosis are molecularly linked via a novel isoform of the centrosomal ninein-like protein. *Hum Mol Genet* 18, 51-64 (2009).

28. Boldt, K. *et al.* An organelle-specific protein landscape identifies novel diseases and molecular mechanisms. *Nat Commun* 7, 11491 (2016).

29. Reiners, J., Nagel-Wolfrum, K., Jurgens, K., Marker, T. & Wolfrum, U. Molecular basis of human Usher syndrome: deciphering the meshes of the Usher protein network provides insights into the pathomechanisms of the Usher disease. *Exp Eye Res* 83, 97-119 (2006).

30. Wei, N., Serino, G. & Deng, X. W. The COP9 signalosome: more than a protease. *Trends Biochem Sci* 33, 592-600 (2008).

31. Blum, M., De Robertis, E. M., Wallingford, J. B. & Niehrs, C. Morpholinos: Antisense and Sensibility. *Dev Cell* 35, 145-149 (2015).

32. Stainier, D. Y. R. *et al.* Guidelines for morpholino use in zebrafish. *PLoS genetics* 13, e1007000 (2017).

33. Athanasiou, D. *et al.* The cell stress machinery and retinal degeneration. *FEBS Lett* 587, 2008-2017 (2013).

34. Su, H., Li, F., Ranek, M. J., Wei, N. & Wang, X. COP9 signalosome regulates autophagosome maturation. *Circulation* 124, 2117-2128 (2011).

35. Petit, L., Khanna, H. & Punzo, C. Advances in Gene Therapy for Diseases of the Eye. *Human gene therapy* 27, 563-579 (2016).

36. Bainbridge, J. W. *et al.* Effect of gene therapy on visual function in Leber's congenital amaurosis. *N Engl J Med* 358, 2231-2239 (2008).

37. Beltran, W. A. *et al.* Gene therapy rescues photoreceptor blindness in dogs and paves the way for treating human X-linked retinitis pigmentosa. *Proc Natl Acad Sci U S A* 109, 2132-2137 (2012).

38. Cideciyan, A. V. *et al.* Human RPE65 gene therapy for Leber congenital amaurosis: persistence of early visual improvements and safety at 1 year. *Human gene therapy* 20, 999-1004 (2009).

5

39. MacLaren, R. E. *et al.* Retinal gene therapy in patients with choroideremia: initial findings from a phase 1/2 clinical trial. *Lancet* 383, 1129-1137 (2014).

40. Zallocchi, M. *et al.* EIAV-based retinal gene therapy in the shaker1 mouse model for usher syndrome type 1B: development of UshStat. *PLoS One* 9, e94272 (2014).

41. Wu, Z., Yang, H. & Colosi, P. Effect of genome size on AAV vector packaging. *Molecular therapy : the journal of the American Society of Gene Therapy* 18, 80-86 (2010).

42. Date, A. A., Hanes, J. & Ensign, L. M. Nanoparticles for oral delivery: Design, evaluation and state-of-the-art. *J Control Release* 240, 504-526 (2016).

43. Konstan, M. W. *et al.* Compacted DNA nanoparticles administered to the nasal mucosa of cystic fibrosis subjects are safe and demonstrate partial to complete cystic fibrosis transmembrane regulator reconstitution. *Human gene therapy* 15, 1255-1269 (2004).

44. Trapani, I. Dual AAV Vectors for Stargardt Disease. *Methods in molecular biology* 1715, 153-175 (2018).

45. Parasuraman, S. Toxicological screening. *J Pharmacol Pharmacother* 2, 74-79 (2011).

46. Tucker, B. A. *et al.* Patient-specific iPSC-derived photoreceptor precursor cells as a means to investigate retinitis pigmentosa. *eLife* 2, e00824 (2013).

47. Harper, S. Q. *et al.* Modular flexibility of dystrophin: implications for gene therapy of Duchenne muscular dystrophy. *Nat Med* 8, 253-261 (2002).

48. Cosgrove, D. & Zallocchi, M. Usher protein functions in hair cells and photoreceptors. *Int J Biochem Cell Biol* 46, 80-89 (2014).

49. Pan, B. *et al.* Gene therapy restores auditory and vestibular function in a mouse model of Usher syndrome type 1c. *Nature biotechnology* 35, 264-272 (2017).

50. Donaldson, T. N. *et al.* Antisense oligonucleotide therapy rescues disruptions in organization of exploratory movements associated with Usher syndrome type 1C in mice. *Behav Brain Res* 338, 76-87 (2018).

51. Vijayakumar, S. *et al.* Rescue of peripheral vestibular function in Usher syndrome mice using a splice-switching antisense oligonucleotide. *Hum Mol Genet* 26, 3482-3494 (2017).

52. Isgrig, K. *et al.* Gene Therapy Restores Balance and Auditory Functions in a Mouse Model of Usher Syndrome. *Molecular therapy : the journal of the American Society of Gene Therapy* 25, 780-791 (2017).

53. Chien, W. W. *et al.* Gene Therapy Restores Hair Cell Stereocilia Morphology in Inner Ears of Deaf Whirler Mice. *Molecular therapy : the journal of the American Society of Gene Therapy* 24, 17-25 (2016).

54. Emptoz, A. *et al.* Local gene therapy durably restores vestibular function in a mouse model of Usher syndrome type 1G. *Proc Natl Acad Sci U S A* 114, 9695-9700 (2017).

55. Geng, R. *et al.* Modeling and Preventing Progressive Hearing Loss in Usher Syndrome III. *Scientific reports* 7, 13480 (2017).

56. Alagramam, K. N. *et al.* A small molecule mitigates hearing loss in a mouse model of Usher syndrome III. *Nat Chem Biol* 12, 444-451 (2016).

57. Liu, X. *et al.* Usherin is required for maintenance of retinal photoreceptors and normal development of cochlear hair cells. *Proc Natl Acad Sci U S A* 104, 4413-4418 (2007).

58. Adato, A. *et al.* Usherin, the defective protein in Usher syndrome type IIA, is likely to be a component of interstereocilia ankle links in the inner ear sensory cells. *Hum Mol Genet* 14, 3921-3932 (2005).

Chapter 6
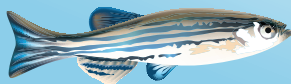
Summary | Samenvatting
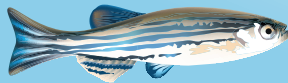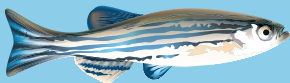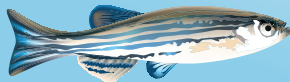
Chapter 6.1

Summary in English

6.1

Usher syndrome is a genetically and clinically heterogeneous disorder characterized by hearing impairment from birth and a progressive loss of visual function as a consequence of retinitis pigmentosa (RP) (**chapter 1**). Usher syndrome type 2 is the most common type of Usher syndrome and represents around two-third of Usher syndrome cases, of whom 57-85% can be explained by mutations in *USH2A*. Also, mutations in *USH2A* are among the most frequent causes of autosomal recessively inherited nonsyndromic RP (arRP), accounting for 7-23% of arRP cases. Currently, no treatment options exist for *USH2A*-associated retinal degeneration. The aim of the research described in this thesis was to elucidate the pathogenic mechanisms underlying Usher syndrome type 2 and to develop a pre-clinical therapeutic strategy for *USH2A*-associated RP.

Usher syndrome-associated proteins function together in a highly dynamic protein complex (**chapter 1**). So far, surprisingly little is known about the function of this protein complex in the retina. In **chapters 2a** and **2b**, we aimed to unravel part of this function by studying key interaction partners of the *USH2A*-encoded protein usherin. NINL is thought to be an important interaction partner of usherin in the retina, since this protein is connecting the retinal ciliopathies Usher syndrome and Leber congenital amaurosis at the molecular level. Using a combination of (affinity) proteomics and zebrafish as a model system, we found that NINL is part of a dynamic multi-subunit protein complex in photoreceptor cells that plays an important role in two consecutive steps in transporting trans-Golgi network (TGN)-derived cargo vesicles (**chapter 2**). First of all, a direct interaction between NINL and DZANK1 was identified. NINL and DZANK1 associate with complementary subunits of the cytoplasmic dynein 1 complex. Our results support a model in which the NINL-DZANK1 module plays a crucial role in the proper assembly of the intracellular cytoplasmic dynein 1 motor complex in photoreceptor cells (**chapter 2a**). In **chapter 2b**, we identified a series of physical interactions linking a protein complex consisting of NINL, CC2D2A and MICAL3 to vesicular trafficking. These data suggest a new model, in which CC2D2A provides a specific docking point for NINL-bound transport vesicles at the entrance to the photoreceptor ciliary compartment. NINL is proposed to bind the vesicles through MICAL3 which in turn binds RAB8 that is coating TGN-derived cargo vesicles. MICAL3 subsequently promotes remodeling of a docking complex resulting in vesicle fusion at the periciliary membrane. Interestingly, a heterozygous protein truncating mutation in *NINL* has been identified in a Joubert syndrome patient in combination with a known homozygous pathogenic mutation in the *CC2D2A* gene. Phenotypically this patient presented with a much more severe form of Joubert syndrome than was expected based on the known homozygous *CC2D2A* mutation. Together with the genetic interaction data in zebrafish, this suggests that variants of *NINL* may act as a genetic modifiers for *CC2D2A*-associated Joubert Syndrome (**chapter 2b**). With the studies described in the **chapters 2a** and **2b**, we contributed to

6.1

the knowledge of mechanisms by which transmembrane proteins such as usherin are transported from the photoreceptor inner segment towards the periciliary membrane (**chapter 2**).

Further investigations on the potential of the zebrafish model to study *USH2A*-associated retinal degeneration are described in **chapters 3** and **4**. In **chapter 3** the generation and characterization of two zebrafish *ush2a* mutants is described. Using CRISPR/Cas9-technology, we introduced protein-truncating germline lesions into the zebrafish *ush2a* gene (*ush2a^rmc1^*: c.2337_2342delinsAC; p.Cys780GlnfsTer32 and *ush2a^b1245^*: c.15520_15523delinsTG; p.Ala5174fsTer). Homozygous mutants were viable and did not display any obvious abnormalities during early development. Immunofluorescence analyses using antibodies recognizing the N- or C-terminal end of usherin demonstrated complete absence of usherin in photoreceptors of the *ush2a^rmc1^* mutant, but demonstrated the presence of the ectodomain of usherin^isoB^ at the photoreceptor periciliary membrane of *ush2a^b1245^* mutant larvae. Complete absence of usherin (*ush2a^rmc1^*) resulted in reduced levels of both paralogs of its interaction partner whirlin, Whrna and Whrnb, and of Adgrv1 at the photoreceptor periciliary membrane. In photoreceptors of *ush2a^b1245^* larvae only reduced levels of Whrna were observed, whereas the levels of Whrnb and Adgrv1 were largely unaffected. Based on these data, we proposed a model in which the ectodomains of usherin and Adgrv1 associate. We furthermore suggested that Whrna has a higher binding affinity for usherin, and Whrnb a higher binding affinity for Adgrv1. We also observed significantly elevated levels of apoptotic photoreceptors in both mutants when kept under constant illumination for three days. Electroretinogram (ERG) recordings revealed a significant and similar decrease in both a- and b-wave amplitudes in *ush2a^rmc1^* as well as *ush2a^b1245^* larvae as compared to strain- and age-matched wild-type larvae. In conclusion, this study demonstrated that mutant *ush2a* zebrafish models present with early-onset retinal dysfunction. These models are therefore instrumental in obtaining a better understanding of the pathophysiology underlying *USH2A*-associated RP and in evaluating future therapeutic strategies. **Chapter 4** describes the generation and subsequent evaluation of the therapeutic potential of two human *miniUSH2A* genes in improving retinal function of the *ush2a^rmc1^* zebrafish mutant. For this purpose, *Tol2*-based transgenic *ush2a^rmc1^* zebrafish lines were generated that stably express miniUSH2A-1 or miniUSH2A-2 under the control of a photoreceptor-specific promoter. Expression of either miniUSH2A restores the levels of interaction partner Whrna at the photoreceptor periciliary region. Furthermore, ERG traces and Visual Motor Responses (VMRs) were fully restored after expression of miniUSH2A-1 and significantly improved after expression of miniUSH2A-2. In conclusion, this study shows the potential of shortened *USH2A* genes for the development of a future treatment of *USH2A*-associated RP.

In conclusion, the research described in this thesis has resulted in some major steps forward towards the development of a future treatment for *USH2A*-associated RP. The generation of the first *ush2a* animal model with an early onset retinal dysfunction provides a unique opportunity to unravel the pathogenic mechanism(s) underlying *USH2A*-associated retinal degeneration. In addition, this zebrafish model enabled us to demonstrate the potential of the *miniUSH2A* gene approach in improving zebrafish larval visual function. Finally, in **chapter 5** the current challenges and recommendations for future studies on the road towards therapy for *USH2A*-associated RP are provided.

6.1

Chapter 6.2

Samenvatting in het Nederlands

6.2

Het Usher syndroom is een genetisch en klinisch heterogene aandoening die wordt gekenmerkt door gehoorverlies vanaf de geboorte en een progressief verlies van het gezichtsvermogen ten gevolge van retinitis pigmentosa (RP) (**hoofdstuk 1**). Usher syndroom type 2 is de meest voorkomende variant en vertegenwoordigt ongeveer twee derde van alle Usher syndroom gevallen, waarvan 57-85% kan worden verklaard door mutaties in *USH2A*. Ook zijn mutaties in *USH2A* een van de meest voorkomende oorzaken van autosomaal recessief overervende niet-syndromale RP (arRP). Mutaties in *USH2A* verklaren 7-23% van de arRP gevallen. Momenteel bestaat er geen behandeling voor *USH2A*-geassocieerde netvliesdegeneratie. Het doel van het onderzoek beschreven in dit proefschrift was om de pathogene mechanismen die ten grondslag liggen aan Usher syndroom type 2 op te helderen en om een pre-klinische behandelstrategie te ontwikkelen voor *USH2A*-geassocieerde RP.

Usher syndroom-geassocieerde eiwitten functioneren samen in een zeer dynamisch eiwitcomplex (**hoofdstuk 1**). Tot nu toe is er verrassend weinig bekend over de functie van dit eiwitcomplex in het netvlies. In de **hoofdstukken 2a** en **2b** is beschreven hoe we hebben gepoogd om een deel van deze functie te ontrafelen door een van de belangrijkste interactiepartners van het door *USH2A*-gecodeerde eiwit usherin te bestuderen. Het NINL-eiwit wordt beschouwd als een belangrijke interactiepartner van usherin in het netvlies, omdat het de retinale ciliopathieën Usher syndroom en Leber congenital amaurosis op moleculair niveau met elkaar verbindt. Door gebruik te maken van een combinatie van proteomics en het zebravismodel, ontdekten we dat NINL deel uitmaakt van een dynamisch eiwitcomplex in fotoreceptorcellen dat een belangrijke rol speelt in twee opeenvolgende stappen in het vervoeren van transportvesikels die afkomstig zijn van het trans-Golgi-netwerk (TGN) (**hoofdstuk 2**). Er werd een directe interactie tussen NINL en DZANK1 geïdentificeerd. NINL en DZANK1 associëren met complementaire eenheden van het cytoplasmische dyneïne 1-complex. Onze resultaten ondersteunen een model waarin de NINL-DZANK1 module een cruciale rol speelt bij de juiste assemblage van het intracellulaire cytoplasmische dyneïne 1-motorcomplex in fotoreceptorcellen (**hoofdstuk 2a**). In **hoofdstuk 2b** identificeerden we een reeks directe interacties die een eiwitcomplex bestaande uit NINL, CC2D2A en MICAL3 verbinden aan vesiculair transport. Deze bevindingen suggereren een nieuw inzicht, waarbij CC2D2A een specifiek landingspunt biedt voor NINL-gebonden transportvesikels aan de ingang van het ciliaire compartiment van de fotoreceptor. In dit model bindt NINL aan de vesikels via MICAL3, dat op zijn beurt interacteert met RAB8. RAB8 moleculen vormen een coating op de transportvesikels afkomstig van het TGN. MICAL3 bevordert vervolgens de herstructurering van het koppelingscomplex wat leidt tot de fusie van het vesikel met het periciliaire membraan. In een patiënt met Joubert syndroom met een bekende homozygote pathogene mutatie in het *CC2D2A*-gen hebben we een heterozygote truncerende mutatie in *NINL* geïdentificeerd. Het fenotype van deze patiënt was veel

6.2

ernstiger dan op grond van de bekende homozygote *CC2D2A*-mutatie kon worden verwacht. Deze bevinding gecombineerd met de geïdentificeerde genetische interactie tussen *ninl* en *cc2d2a* in de zebravis suggereert dat varianten in *NINL* kunnen werken als genetische modulator bij *CC2D2A*-geassocieerd Joubert syndroom (**hoofdstuk 2b**). De studies zoals beschreven in de **hoofdstukken 2a** en **2b** hebben geresulteerd in een beter inzicht in de transportmachinerie waarmee transmembraaneiwitten zoals usherin worden vervoerd van het binnenste segment van de fotoreceptor naar de periciliaire membraan (**hoofdstuk 2**).

Hoofdstukken 3 en **4** beschrijven de experimenten waarmee de potentie van de zebravis als model om *USH2A*-geassocieerde netvliesdegeneratie te bestuderen is onderzocht. In **hoofdstuk 3** wordt de ontwikkeling en karakterisering van twee zebravis *ush2a*-mutanten beschreven. Met behulp van CRISPR/Cas9-technologie introduceerden we verschillende truncerende mutaties in het *ush2a* gen van de zebravis (*ush2a^{rmc1}*: c.2337_2342delinsAC; p.Cys780GlnfsTer32 en *ush2a^{b1245}*: c.15520_15523delinsTG; p.Ala5174fsTer). Homozygote mutanten bleken levensvatbaar en vertoonden geen duidelijke morfologische afwijkingen tijdens de vroege ontwikkeling. Met behulp van immunohistochemie waarbij gebruik gemaakt is van antilichamen die het N- of C-terminale deel van usherin herkennen, is aangetoond dat usherin volledig afwezig is in fotoreceptoren van de *ush2a^{rmc1}* mutant. Echter, het ectodomein van usherin^{isoB} is nog wel aanwezig aan het periciliaire membraan van fotoreceptoren in *ush2a^{b1245}* larven. Volledige afwezigheid van usherin (*ush2a^{rmc1}*) resulteerde in een verlaagde hoeveelheid van de beide paralogen van interactiepartner whirlin, Whrna en Whrnb, en van Adgrv1 aan het periciliare membraan van de fotoreceptor. In fotoreceptoren van *ush2a^{b1245}* larven werd een verlaagde hoeveelheid van Whrna waargenomen, terwijl de niveaus van Whrnb en Adrgrv1 grotendeels onaangetast waren. Op basis van deze gegevens hebben we een model voorgesteld waarin de ectodomeinen van usherin en Adgrv1 met elkaar interacteren. We stelden bovendien voor dat Whrna een hogere bindingsaffiniteit heeft voor usherin en Whrnb een hogere bindingsaffiniteit voor Adgrv1. We hebben ook in beide mutanten significant verhoogde aantallen apoptotische fotoreceptoren waargenomen ten opzichte van wild-type controles, als de larven gedurende drie dagen in constant licht werden gehouden. Electroretinogram (ERG) metingen lieten een significante en vergelijkbare afname van de amplitude van zowel de a- als b-golf zien in *ush2a^{rmc1}* en *ush2a^{b1245}* larven in vergelijking met wildtype-larven van dezelfde leeftijd en stam. Samenvattend heeft deze studie aangetoond dat zebravis *ush2a*-mutanten al in het larvale stadium een probleem hebben met het functioneren van hun netvlies. Deze mutanten kunnen daarom een belangrijke rol spelen in het ontrafelen van de pathofysiologie die ten grondslag ligt aan *USH2A*-geassocieerde RP en in het evalueren van toekomstige therapeutische strategieën.

Hoofdstuk 4 beschrijft de ontwikkeling en daaropvolgende evaluatie van het therapeutisch potentieel van twee humane *USH2A*-minigenen ter verbetering van de visuele functie van de *ush2a^{rmc1}* zebravismutant. Voor dit doel werden met behulp van het *Tol2*-transposase systeem twee transgene *ush2a^{rmc1}* zebravislijnen gegenereerd die miniUSH2A-1 of miniUSH2A-2 stabiel tot expressie brengen onder de controle van een fotoreceptor-specifieke promoter. Expressie van miniUSH2A-1 of -2 leidde tot een herstel van de hoeveelheid Whrna in de periciliaire regio van fotoreceptoren. Daarnaast herstelden de ERG-amplitudes en Visuele Motor Response (VMR) volledig na expressie van miniUSH2A-1 en verbeterden ze significant na expressie van miniUSH2A-2. Deze studie laat derhalve de potentie zien van het gebruik van verkorte *USH2A*-genen als toekomstige behandelmethode voor *USH2A*-geassocieerde RP.

Concluderend heeft het onderzoek beschreven in dit proefschrift geresulteerd in een aantal belangrijke stappen in de richting van de ontwikkeling van een toekomstige behandeling voor *USH2A*-geassocieerde RP. De ontwikkeling van het eerste *ush2a*-diermodel met een vroeg retina fenotype biedt een unieke mogelijkheid om het pathogene mechanisme dat ten grondslag ligt aan *USH2A*-geassocieerde netvliesdegeneratie te ontrafelen. Daarnaast heeft het zebravis model ons in staat gesteld om de potentie van het gebruik van *USH2A*-minigenen te onderzoeken om de visuele functie van deze vis te verbeteren. Tenslotte worden in **hoofdstuk 5** de uitdagingen besproken die we op het pad van een verdere ontwikkeling van therapie voor *USH2A*-geassocieerde RP nog zullen tegenkomen, en doen we aanbevelingen om deze ontwikkeling te bevorderen.

6.2

List of publications
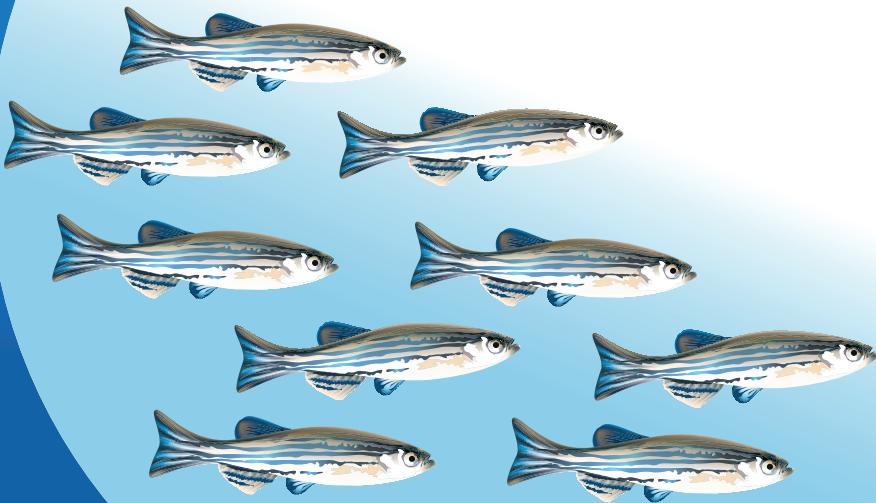
- Messchaert M., **Dona M.**, Peters T.A., Corral-Serrano J.C., Slijkerman R.W., van Wijk E., Broekman S., Collin R.W.J. (2018) Eyes shut homolog is important for maintenance of photoreceptor morphology and visual function in zebrafish.
  PLos One. 13(7): e0200789.

- Corral-Serrano J.C., Messchaert M., **Dona M.**, Peters T.A., Kamminga L.M., van Wijk E., Collin R.W.J. (2018) C2orf71a/pcare1 is important for photoreceptor outer segment morphogenesis and visual function in zebrafish.
  Scientific Reports. 8(1):9675.

- **Dona M.***, Slijkerman R.W.N.*, Lerner K.M., Broekman S., Wegner J., Howat T.A., Peters T.A., Hetterschijt L., Boon N., de Vrieze E., Sorusch N., Wolfrum U., Kremer H., Neuhauss S.C., Zang J., Kamermans M., Westerfield M.#, Phillips J.B.# and van Wijk, E.# (2018) Zebrafish *ush2a* mutant models show early-onset retinal dysfunction.
  Experimental Eye Research. 173:148-159.

- Samarut E., **Dona M**., Yoganantharjah P. (2017) Zebrafish ride the Danube's wave for the 10th European Zebrafish Meeting.
  Zebrafish. 15(1):79-83.

- Slijkerman R.W., Vaché C., Dona M., García-García G., Claustres M., Hetterschijt L., Peters TA., Hartel B.P., Pennings R.J., Millan J.M., Aller E., Garanto A., Collin R.W., Kremer H., Roux A.F., Van Wijk E. (2016) Antisense Oligonucleotide-based Splice Correction for USH2A-associated Retinal Degeneration Caused by a Frequent Deep-intronic Mutation.
  Molecular Therapy Nucleic Acids. 5(10):e381.

- Bachmann-Gagescu R.*, **Dona M.***, Hetterschijt L., Tonnaer E., Peters T., de Vrieze E., Mans D.A., van Beersum SE., Phelps I.G., Arts H.H., Keunen J.E., Ueffing M., Roepman R., Boldt K., Doherty D., Moens C.B., Neuhauss S.C., Kremer H., van Wijk E. (2015) The Ciliopathy Protein CC2D2A Associates with NINL and Functions in RAB8-MICAL3-Regulated Vesicle Trafficking.
  PloS Genetics. 11(10):e1005575.

- **Dona M**.*, Bachmann-Gagescu R.* Hetterschijt L., Tonnaer E., Peters T., Van Beersum S., Bergboer J., Van Reeuwijk J., Texier Y., Boldt K., Ueffing M., Roepman R., Kremer H., Van Wijk E. (2015) NINL and DZANK1 cooperate in assembling the cytoplasmic dynein 1 motor complex, a process essential for photoreceptor outer segment formation in zebrafish.
  PLoS Genetics. 11(10):e1005574.

- Van Wijk X., Thijssen V., Lawrence R., Van den Broek S., **Dona M.**, Naidu N., Oosterhof A., Van de Westerlo E., Kusters L., Khaled Y., Jokela T., Kremer H., Stringer S., Griffioen A., Van Wijk E., Van Delft F., and Van Kuppevelt T. (2013) Interfering with UDP-GlcNAc metabolism and heparan sulfate expression using a sugar analogue reduces angiogenesis.
  ACS Chemical Biology. 8(10):2331-8.

- Collin R., Nikopoulos K., **Dona M.**, Gilissen C., Hoischen A., Boonstra F., Poulter J., Kondo H., Berger W., Toomes C., Tahira T., Mohn L., Blokland E., Hetterschijt L., Ali M., Groothuismink J., Inglehearn C., Sollfrank, L., Strom T., Uchio E., Nouhuys C., Kremer H., Veltman J., van Wijk E. and Cremers F. (2013) *ZNF408* is mutated in familial exudative vitreoretinopathy and crucial for the development of zebrafish retinal vasculature.
  PNAS. 110(24):9856-61.

* these authors contributed equally

Dankwoord
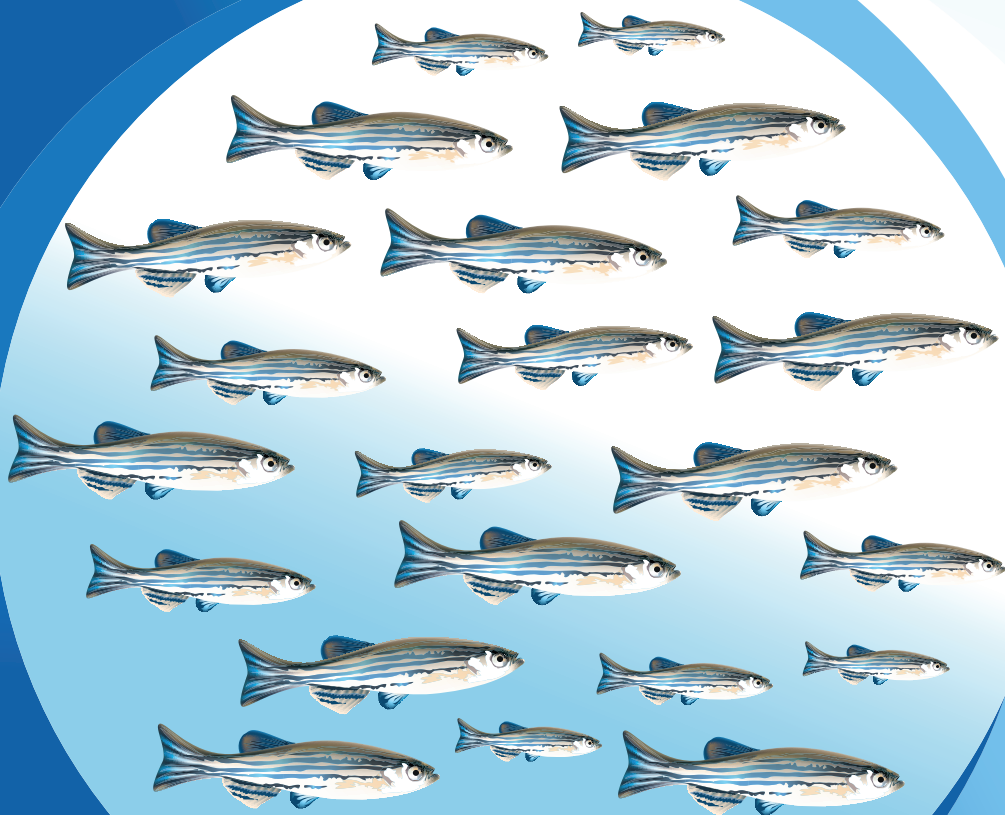
Het is zover, het moment waar ik lang naar uitgekeken heb. De rit die niet altijd even makkelijk ging, maar uiteindelijk toch gelukt is dankzij de hulp van velen die ik graag wil bedanken.

Allereerst wil ik mijn promotoren Jan en Hannie, en co-promotor Erwin bedanken. Dank voor deze mooie kans die mij geboden is. Na een uiterst leerzame en leuke stage, was ik verkocht aan de zebravisjes en het Usher onderzoek. Ik kon er echt mijn ei in kwijt, en was vaak niet meer te houden. Ik ben blij en trots dat ik het zebravis onderzoek in Nijmegen mee heb mogen opzetten, van alleen een klimaatcel met kast, tot een uitgebreid systeem met talloze waardevolle mutanten. Het allerleukst heb ik het opzetten van nieuwe assays gevonden, en dit heb ik dan ook uitgebreid mogen doen. Bedankt voor deze mogelijkheid en het vertrouwen. Qua resultaten is het ook enorm goed gegaan, ik denk dat we vooral erg trots mogen zijn dat we nu richting clinical trials gaan en het mooie patent van de minigenen zijn een kers op de taart na al het harde werk. Hannie, bedankt voor alle hulp, de altijd kritische blik en waardevolle schrijftips. Erwin, we zijn samen op het lab begonnen, jouw positieve kijk op de wereld en enthousiasme zijn zeer aanstekelijk. Han en Ad, bedankt voor al jullie hulp. Ook Henri Marres en Arjan Verhoeven van de KNO-afdeling wil ik graag bedanken voor de fijne tijd op de KNO-afdeling en de betrokkenheid bij ons mooie Usher onderzoek. Ronald Pennings, de altijd vrolijke, geïnteresseerde en vol met passie KNO-arts. Bedankt voor onze fijne gesprekken, ik waardeer je passie voor de patiënt en betrokkenheid.

Daarnaast ben ik blij dat ik veel patiënten met het Usher syndroom heb mogen leren kennen, maar vooral ook de mensen achter deze ziekte heb leren kennen. Ik bewonder jullie doorzettingsvermogen, positiviteit en ook hoe goed jullie zijn in crowdfunding. Ik wil graag alle betrokken organisaties een hart onder de riem steken, jullie doen geweldig werk en steunen ons onderzoek enorm. In het bijzonder wil ik graag Yvonne Bressers bedanken, een van de drijvende krachten achter stichting Usher syndroom. Tijdens onze gesprekken hebben we veel gelachen, ik hou van je enthousiasme en dat niets je te gek of moeilijk is, je gaat er "gewoon" voor. Daarnaast natuurlijk ook de mensen van Stichting Wetenschappelijk Onderzoek Doofblindheid (SWODB). Frank, Nicole, Hedda, Erik en Linda bedankt voor de fijne samenwerking. Mijn doel om naast het wetenschappelijk onderzoek ook mijn steentje te kunnen bijdragen en meer te leren over de wensen van de mensen met Usher syndroom was een leerzame tijd voor mij.

Door de jaren heen heb ik heel veel mensen leren kennen, met ieder heb ik een andere band opgebouwd, waar ik ontzettend dankbaar voor ben en vaak ook veel van geleerd heb. Het liefste zou ik iedereen uitgebreid persoonlijk willen bedanken, maar om

niemand te vergeten wil ik bij deze al mijn collega's van Genetica (de sensory disease groep), Oogheelkunde, KNO, Dierfysiologie en Fysiologie bedanken.

In het bijzonder; Lisette, Theo, Erik, Edith, Ralph, Sanne, Margrit, Jaap, Celia, Anne, Jeroen, Suzanne, Rob, Alex, Dyah, Lonneke, Müriel, Julio, Anita, Simon, Matthijs en Tamara. Bedankt voor de fijne samenwerking, alle waardevolle discussies, en ook de talloze grappige en leuke momenten. Ralph en Erik, de mannen van het lab, bedankt voor alle wetenschappelijke discussies en hulp bij de experimenten! Sanne, twee van onze hoogtepunten zijn zeker ons avontuur in Zürich en al onze gezellige en lekkere pizza-dates. Lisette, bedankt voor al je technische hulp, tips en tricks, en natuurlijk ook voor onze waardevolle vriendschap. Theo, bedankt dat je echt altijd voor me klaar hebt gestaan. Je bent de master van de histologie, wat een voorrecht om deze technieken en vaardigheden van je te hebben mogen leren. Ontelbare kleuringen, uurtjes (dagen) achter de mic, en ook de ontelbare uren droge humor waar we samen prima mee vooruit komen en waardoor de tijd voorbij gevlogen is. Edith, je hebt heel veel TEM en SEM werk gedaan, wat een ontzettend indrukwekkende technieken en wat een fantastische plaatjes. Bedankt voor al je hulp, de fijne samenwerking en zorgvuldigheid.

Ook een woord van dank aan Francois. Bedankt voor je kennis en het geduld om samen het ERG apparaat aan de gang te krijgen. Stiekem was ik ook heel benieuwd hoe de broer van Tom zou zijn. Ik vond het enorm leuk je te leren kennen en dank je voor je hulp! Daarnaast kon ik ook altijd bij Marty terecht voor alle technische vragen, ondersteuning en vooral ook de oplossingen, bedankt! Dirk, je hebt altijd klaargestaan voor me wat betreft de elektrofysiologie wat ik erg waardeer. In het begin waren al die knopjes en draadjes toch maar gek en verlangde ik vooral naar de pipet. Jon-Ruben ook jij bedankt voor je hulp. Uiteindelijk is het allemaal gelukt, hebben we prachtige data verkregen en vooral ook veel extra kennis in huis kunnen halen. Dyah, wellicht beginnen we ooit ons plan B met ons eigen restaurant op wielen, met jou natuurlijk als hoofd Chef. Lonneke, ik herinner me nog goed dat we beiden begonnen zijn als student toen we nog het lab deelde met de "eiwit mensen". We hebben elkaar heel goed leren kennen en het klikte meteen, bedankt dat je vandaag ook mijn paranimf wil zijn.

Wat heb ik een waanzinnig goede tijd gehad (en nog steeds) samen met de eiwitladies (en Stef). Ronald, Ideke, Ka Man, Sylvia, Brooke, Machteld, Maryam, Minh, Tess and Cenna. Dat we naar een ander lab gegaan zijn heeft geen invloed gehad op onze vriendschappen. Jullie zijn een enorm hechte groep van hele fijne mensen en ik ben ontzettend dankbaar om daar deel van uit te maken. Een heel groot woord van dank voor alle hulp, groot en klein, wetenschappelijk en vooral ook de sociale ondersteuning en vriendschap in goede en slechte tijden, enorm bedankt. Jeroen, jij hoort natuurlijk ook bij deze groep, soms zaten we een beetje in hetzelfde schuitje, bedankt voor al onze gesprekken! De tussenburen natuurlijk ook bedankt, vooral Lilian en Eveline. Bedankt

voor alle gesprekken en jullie hulp als ik weer eens iets nodig had☺! Ook regelmatig een bezoekje aan de Pre-labs, even kletsen (grappen uithalen) met Jaap, Michael, Bjorn, Ellen, Ellen, Petra, Marloes, Marlies, Masha en Remco en de andere pre-labbers, een super fijne tijd met veel fijne collega's. Jaap bedankt voor al onze fijne gesprekken, en ook voor alle hulp met de qPCRs. Een van de leukste dingen om te doen zijn natuurlijk escape-rooms en spelletjes: Alex, Bjorn, Michael, Suus, Galuh en Lonneke bedankt voor alle leuke avonden. Peer uiteindelijk hebben we wel een hele bijzonder band gekregen, wat ontzettend gaaf dat je het avontuur in Australië aangegaan bent. De plannen waren bijna rond om naar het WK in Adelaide te komen, wie weet komt er toch nog een mooie mogelijkheid. Alex Hoischen, ik ben je eeuwig dankbaar voor de hulp die je me gegeven hebt. Ik bewonder je positieve instelling en je bereidwilligheid om, hoe druk je het ook hebt, altijd tijd voor me vrij te maken, super bedankt.

Ook mijn kamergenootjes verdienen een woord van dank, ik wil speciaal Judith, Renske, Theo, Ideke, Machteld, Marjolein, Euginia, Armen, Benjamin, en Ralph noemen. De hoeveelheid grappen die getapt zijn, zijn niet te beschrijven en als ik eraan terug denk lig ik uiteraard weer dubbel, bedankt voor alle gezelligheid. Arjan ook jij bedankt voor alle gezellige gang gesprekken. Ik denk dat sommige mensen het prima vonden dat we een andere kamer kregen dan was het in de gang tenminste wat stiller.

Daarnaast een speciaal woordje van dank aan mijn studenten. Nanda, je was mijn eerste eigen student, en eigenlijk was je gewoon mijn maatje. Ik denk dat iedereen ons in de gang al van ver kon horen aankomen, wat hebben we een lol gehad en daarnaast ook hele mooie dingen bereikt. Ik ben heel blij voor je dat je nu je eigen PhD begonnen bent!! Dilys, ik denk dat je heel veel geleerd hebt bij ons in het lab. Bedankt voor alle hulp!

De ruggengraat van de Genetica afdeling; de dames van het secretariaat Ineke, Miranda en Doménique (en natuurlijk Dennis☺). Bedankt voor alle hulp bij al mijn vragen en daarnaast ook altijd een luisterend oor. Nick, de kwaliteit goeroe en daarnaast vooral grappentap maatje, bedankt voor al je bezoekjes aan 't einde van de gang en alle leuke grappen☺. Ook de dames van de celweek, bedankt voor al jullie hulp en de leerzame en fijne gesprekken. Katie, ik kan en wil jou natuurlijk niet vergeten, jij bent zeker een van de eerlijkste mensen die ik ken. Oprecht blij en oprecht verdrietig, bedankt voor al je hulp en al onze gesprekken.

Een groot woord van dank aan alle collega's van het vissenlab. Ik heb een hele goede tijd gehad op het vissenlab, en vond de ontspannen sfeer erg fijn, net als de vrijdagmiddag borrels en de jaarlijkse triatlon. Postbode, Remi en Bokito, jullie hebben alle drie het goede voorbeeld laten zien hoe dat promoveren nu moet, nu ben ik uiteindelijk ook zelf aan de beurt. Peter, Marnix en Juriaan, bedankt voor alle wetenschappelijke ondersteuning, goede tips en onze gesprekken. Daisy, Wim en Jan, bedankt dat jullie

altijd voor me hebben klaar gestaan. Ruud bedankt voor onze mooie samenwerking, op naar de volgende. Antoon, Jeroen en Tom, bedankt voor al jullie inzet met het opzetten van de visjes en alle waardevolle tips wat betreft de visjes en daarbuiten. Tom, je speciale kracht om die visjes echt altijd eitjes te laten leggen is zeer waardevol, het lijkt me nog steeds een goed idee om een grote poster af te drukken en deze bij alle visjes op te hangen, succes gegarandeerd;)! Gert, ik waardeer je enorm en vond het een fijne samenwerking met daarbij vele mooie (levens)lessen. Het mooie is dat ik de afdeling niet verlaten heb, maar in de buurt gebleven ben en verder mag gaan werken met de visjes. Paco, we zijn nu zelfs nog directere collega's geworden, ik zie een mooie samenwerking tegemoet ☺. De zebravis wereld is voor mij echt enorm gaaf en vooral ook een gezellige gemeenschap waar ik me heel goed thuis voel en mijn passie ligt. Allereerst natuurlijk dank aan onze zebravis platform in Nijmegen. Een speciaal woord van dank naar de groep van Leonie, Bilge, Marco, Naomi en Julien. Dank voor alle wetenschappelijke en niet-wetenschappelijk discussies. Julien, during our joined trip to the zebrafish congress in Buda and Pestch we got to know each other very well, I wish you and your family all the best. Bilge en Naomie, zet 'm op met de laatste loodjes, jullie kunnen het!! Leonie, ik denk dat we een hele speciale band op hebben gebouwd, bedankt voor alle theetjes, adviezen en fijne gesprekken. Selma, ook bedankt voor je hulp, uiteindelijk mag ik verder werken met de visjes die jij gemaakt hebt, hoe bijzonder. Daarnaast ook alle samenwerkingen die ik in de loop van jaren heb mogen opbouwen. Wim en Maarten uit Amsterdam. Wim, bedankt dat je altijd klaar stond voor een praatje en al je hulp. Maarten, je bent altijd positief, rustig en vol met waardevolle tips, ik heb veel van je mogen leren, bedankt. Secondly, I would greatly want to thank Stephan and his lab members for my really pleasant stay in your lab in Zürich. Next to the great atmosphere in your lab, we gathered nice data and after this collaboration I was able to set up our own system in Nijmegen. Jingjing, thank you so much for the daily supervision and Kara for taking care of the fish and all other help. Ruxandra, thanks for our collaboration and two really nice shared publications about the NINL complex. I admire the critical look and endless enthusiasm. Another great team of collaborators originated from Oregon: Monte and Jennifer. Thanks for the endless help about all kind of zebrafish related research questions and our joined effort for the zebrafish mutant paper. Monte, it was a great pleasure to meet you in person in Budapest.

Je hebt vrienden die komen en gaan, en je hebt vrienden die voor eeuwig zijn. Ons middelbare school clubje Adrienne, Elise, Evelien, Sandra en Susette. Het maakt niet uit hoe ver we uit elkaar wonen, hoe verschillend onze levens(fases) soms zijn. Als er nood aan de vrouw is, weten we elkaar te vinden. Ik waardeer jullie steun en vriendschappen enorm.

Een van mijn grootste passies en hobbies is het hockeyen. Er zijn heel wat uurtjes doorgebracht op het veld. Even de frustratie eruit slaan, heerlijk dat meppen op doel naar (de) Muur. Ik heb vanaf het begin een klik gehad met mijn nieuwe teamgenootjes van Union en voelde me enorm thuis op 't veld en daarbuiten, ik waardeer jullie enorm en ben blij jullie te hebben leren kennen. Daarnaast, is een van mijn grote hobbies het zwemmen. Wat een ontelbare uurtjes vergaderingen van spellencommissie, wedstrijdcommissie tot bestuur. Soms zag ik er wel eens tegenop, weer de zoveelste vergadering maar uiteindelijk was het altijd gezellig en zeker nuttig. Daarnaast ligt mijn passie natuurlijk bij het coachen/trainen, en ook om zelf te zwemmen. Op de zaterdag lesgeven aan de kleintjes is toch wel een van mijn favorieten (oke behalve als het buiten lekker weer is;)). Eerlijkheid en openheid van de kleintjes, dat geeft me een hoop energie en doet me goed. Wouter en Michiel, we vormen samen een goed team, en daarbij nu ook de BAM'ers maakt het compleet. Ook mijn zwemmaatjes uit Gouda wil ik niet vergeten. Ons avontuur op het EK in Allicante, Spanje is wel een van de hoogtepunten geweest. Ellis, wat was ik blij dat ik eindelijk bij die boei was, we hebben het maar mooi gedaan met die hoge grote golven!! Ons volgende avontuur wordt hopelijk het EK in Italië, op naar de kikkers!

Een speciaal woord van dank aan Fleur, Marianne, Chantal, Janneke, Wanda, Martine, Frank en aan alle E10-ers. Jullie zijn erg belangrijk voor mij geweest, nu wil ik jullie graag laten zien wat ik heb kunnen bereiken mede dankzij jullie. Ook een speciaal woord van dank aan Eveline, wat ben ik blij dat ik je heb leren kennen en gebruik mag maken van je diensten. Je hebt me geïnspireerd en zeker verder geholpen. Nanneke, ik ben blij je te leren kennen en onze nuchtere kijk op het leven te delen.

Ook een woord van dank aan de collega's van mijn nieuwe afdeling Fysiologie, het voelt als thuiskomen in een warme familie. Er wordt hard gewerkt maar tegelijkertijd heerst er een ontspannen en gezellige sfeer. Elja en Kim, mijn groepsmaatjes, we hebben nu al heel veel lol, heel veel succes nog met jullie PhD. Peter en Henri, bedankt voor het vertrouwen in mij, hopelijk volgen er nog vele mooie resultaten en momenten.
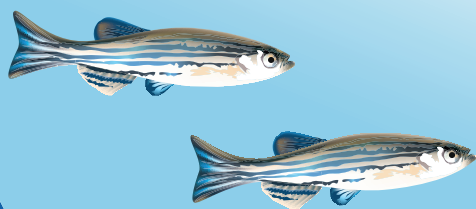
Ik wil graag al mijn mede-onderzoekers meegeven dat ons werk echt verschil kan maken. Ik hoop van harte dat alle mooie onderzoeken uiteindelijk ook de patiënt bereiken en we iedere keer weer een stapje verder komen en dat dit ons een extra boost van motivatie geeft.

Natuurlijk ook dank aan alle vrienden en familieleden voor de nodige ontspanning en gezelligheid. Ronald en Doreen, bedankt voor alle steun die ik van jullie gekregen heb. Ronald, dankzij jou ben ik lang geleden terecht gekomen op de KNO-afdeling, bedankt voor de gouden tip. Ik kon en kan echt altijd op jullie rekenen waar ik echt dankbaar

voor ben. Natuurlijk ook mijn eigen familie, bedankt voor alle hulp en alle gezellige momenten. We zijn een heel sterk team en vormen een hecht gezin. Het maakt niet uit hoe groot of klein het probleem is, er is altijd wel een oplossing en we staan altijd voor elkaar klaar. Bedankt! Amine, también eres parte de la familia, estoy muy feliz de conocerte. Quiero agradecerte por toda tu ayuda, paciencia y cordialidad. Deseo la felicidad y la suerte en nuestra nueva etapa de vida.

PhD Portfolio

RIMLS PORTFOLIO
Name PhD student: Margo Dona
Department: Otorhinolaryngology & Human Genetics
Research School: Radboud institute for Molecular Life Sciences

Promotor: Prof. Dr. J.M.J. Kremer, Prof. J.E.E. Keunen
Co-promotor: Dr. H.A.R. v. Wijk

PhD period:
01/08/2012 - 30/11/2017

TRAINING ACTIVITIES

A) COURSES & WORKSHOPS	YEAR(S)	ECTS
Graduate course	2012	2
Laboratory Animal Sciences	2012	3
Course welfare of fish	2012	0.25
Academic writing course	2013	3
Animal experiments do's and don'ts	2013	0.1
Imaging course FIJI	2013	0.75
How to manage your data	2013	0.2
Poster presentation course	2013	0.4
Management for promovendi	2013	1
Presenteren eigen onderzoek	2014	0.4
Scientific integrity course	2014	1.75
Write a data management plan	2015	0.4

B) SEMINARS & LECTURES		
RIMLS Seminar series (2013#)	2012-2017	2
RIMLS Technical forum	2012-2017	1.5
Organization technical forum nanoscience & nanomedicine	2015	1
RIMLS Symposia	2013	0.5
PhD Defenses/orations	2012-2017	1
Radboud Research rounds (2016#)	2012-2017	1

C) SYMPOSIA & CONGRESSES		
RIMLS New frontiers symposium (2015*)	2012-2017	3
European zebrafish meeting, Barcelona, Spain	2013	1.75
Vision camp, Leibertingen, Germany (2013#,2014*)	2013-2014	2
ARVO-Ned symposium	2013-2015	2
Zebrafish smart mix Leiden	2014	0.25
Dutch Ophtalmology PhD students meeting (2015#,2016*)	2015-2016	2
RIMLS PhD retreats (2014*, 2015)	2014-2015	1.5
Zebrafish disease model congress, Singapore#	2016	1.75
Oceania zebrafish meeting,Singapore#	2016	1
European zebrafish meeting, Budapest, Hungary#	2017	1.5

RIMLS PORTFOLIO
Name PhD student: Margo Dona
Department: Otorhinolaryngology & Human Genetics
Research School: Radboud institute for Molecular Life Sciences

PhD period:
01/08/2012 - 30/11/2017

Promotor: Prof. Dr. J.M.J. Kremer, Prof. J.E.E. Keunen
Co-promotor: Dr. H.A.R. v. Wijk

D) OTHER	YEAR(S)	ECTS
Literature discussion series, department of Human Genetics###	2012-2016	2
Theme discussion series, department of Human Genetics###	2012-2017	2
Co-organisation RIMLS New frontiers symposium	2016	2

TEACHING ACTIVITIES

E) LECTURING

Assistance practica for students	2012-2013	0.5
Supervision of internships master students	2012-2017	6

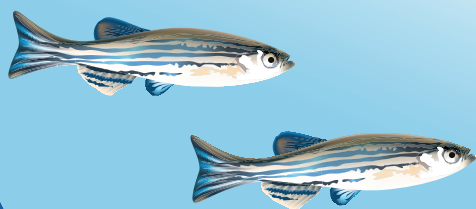| TOTAL		49.5

oral presentation, * poster presentation

About the author

Margo Dona was born on the 28th of December 1987 in 's-Hertogenbosch, the Netherlands. After finishing high school in 2006, she started her studies in Medical Biology at the Radboud University in Nijmegen. She performed her bachelor internship at the department of Molecular Animal Physiology of the Radboud Medical Center (Radboudumc), where she contributed to unravelling the pathomechanisms of schizophrenic disorder using the rat as animal model. Next, she obtained her second degree teaching qualification for Biology. During her master, she performed her first internship at the department of Integrative Physiology under supervision of Prof. Dr. Maria Hopman and Dr. Fleur Poelkens. She participated in a study on the effects of exercise on females with metabolic syndrome. During her second master internship at the Human Genetics department, she was involved in dissecting the role of ninl and c20orf12 using *Danio Rerio* as a model organism. For this study she received the RIMLS award for best scientific report. She completed her Master of Science Medical Biology in 2012. In the same year, Margo started her PhD research in the department of Otorhinolaryngology and Human Genetics. Her research was directed towards the development of therapeutic strategies for *USH2A*-associated retinitis pigmentosa using the zebrafish model with Prof. Dr. Jan Keunen, Prof. Dr. Hannie Kremer and Dr. Erwin van Wyk as (co)supervisors. Awarded with a travel grant of the Radboudumc she visited the laboratory of Prof. Dr. Stephan Neuhauss (Zürich, Switzerland) to be trained in electroretinography in zebrafish. In March 2018, she joined the group of Prof. Dr. Peter Deen as a postdoctoral researcher to study the pathomechanisms of pheochromocytomas and paragangliomas caused by mutations in the *SDHB* gene using the zebrafish as model organism.